Title
MEASUREMENT OF THE NUCLEON STRUCTURE FUNCTION USING HIGH ENERGY MUONS

Author
Meyers, P.D.

Publication Date
1983-12-01

Lawrence Berkeley Laboratory
UNIVERSITY OF CALIFORNIA

Physics Division

MEASUREMENT OF THE NUCLEON STRUCTURE FUNCTION
USING HIGH ENERGY MUONS

P.D. Meyers
(Ph.D. Thesis)

December 1983

Prepared for the U.S. Department of Energy under Contract DE-AC03-76SF00098

DISCLAIMER

LBL-17108

Measurement of the Nucleon Structure Function Using High Energy Muons

Peter Daniel Meyers
Ph.D. Thesis
Lawrence Berkeley Laboratory
University of California
Berkeley, CA 94720
December 2, 1983

Abstract

We have measured the inclusive deep inelastic scattering of muons on nucleons in iron using beams of 93 and 215 GeV muons. To perform this measurement, we have built and operated the Multimuon Spectrometer (MMS) in the muon beam at Fermilab. The MMS is a magnetized iron target/spectrometer/calorimeter which provides 5.61 kg/cm^2 of target, 9% momentum resolution on scattered muons, and a direct measure of total hadronic energy with resolution $\sigma_\nu = 1.4\sqrt{\nu\,(\mathrm{GeV})}$. In the distributed target, the average beam energies at the interaction are 88.0 and 209 GeV. Using the known form of the radiatively-corrected electromagnetic cross section, we extract the structure function $F_2(x, Q^2)$ with a typical precision of 2% over the range $5 < Q^2 < 200$ GeV$^2/c^2$. We compare our measurements to the predictions of lowest order quantum chromodynamics (QCD) and find a best fit value of the QCD scale parameter $\Lambda_{\mathrm{LO}} = 230 \pm 40^{stat} \pm 80^{syst}$ MeV/c, assuming $R = 0$ and without applying Fermi motion corrections. Comparing the cross sections at the two beam energies, we measure $R = -0.06 \pm 0.06^{stat} \pm 0.11^{syst}$. Our measurements show qualitative agreement with QCD, but quantitative comparison is hampered by phenomenological uncertainties. The experimental situation is quite good, with substantial agreement between our measurements and those of others.

Contents

Acknowledgments

Q: How many Berkeley physics graduate students does it take to change a light bulb?
A: Just one, but it takes him eight years.

Funny joke, c. 1979

This document is the closing chapter of an effort that occupied many people for the better part of a decade. Fermilab Experiment 203/391 was designed, built, and operated by a collaboration of physicists from the Lawrence Berkeley Laboratory, Fermilab, and Princeton University. The members of this group were Al Clark, George Gollin, Karl Johnson, Rol Johnson, Roy Kerth, Stew Loken, Tom Markiewicz, Craig Moore, Marshall Mugge, Bob Shafer, Frank Shoemaker, Wes Smith, Mark Strovink, Pam Surko, Bill Wenzel, and me. At LBL we were assisted by the technical skills of Fred Goozen, Tom Weber, Tim Nuzum, and Duck (aka Elaine, aka Kay) Lucas. Also instrumental were Leslie Bauman and others of the Fermilab staff. Within our group, Marshall Mugge and Stew Loken worked with me on the analysis of our deep inelastic scattering data, which forms the basis of this thesis.

The hardships involved in a small group (about 1/5 the size of a typical one for an effort of this magnitude) doing an experiment far from home should not be forgotten. The joys of working at Fermilab are related in a cycle of poems written by George Gollin and myself which is not included in this work. Suffice it to say that *somebody* had to shovel the manure out of that barn. It is this sort of direct contact with unvarnished reality that distinguishes experimental from theoretical physics.

Besides the direct collaboration with Marshall and Stew, I have been aided by many people in this endeavor. Mark Strovink advised me on many points of physics; Tom Markiewicz, fellow student, roommate, and friend, advised me on everything else. Janet Remer, Pat Bronnenberg, and Edgar Whipple are responsible for whatever is attractive in the appearance of the thesis. The experiment itself was funded by the Director, Office of Energy Research, Office of High Energy and Nuclear Physics, High Energy Physics Division of the United States Department of Energy under Contract Nos. DE-AC03-76SF00098, DE-AC02-76CH03000, and DE-AC02-76ER03072. I was supported by a National Science Foundation Graduate Fellowship during the years 1975-77. Of greater importance was the emotional support I received from family and friends, who must have wondered what was going on all this time, and from Marjorie Shapiro, who knew.

I worked on this experiment for $8\frac{1}{2}$ years. On the whole I'm quite proud of the results, something I could not have said a year ago. On the other hand, much can happen in $8\frac{1}{2}$ years, and the rest of the world has not been standing still. Many of my contemporaries have established families and careers. Against this candle of decency, the world has hurled a \$4 000 000 000 000

hurricane of military spending. Although I am grateful for the unqualified shelter provided by the University of California, my step into the world is overdue. I take that step now with some trepidation, but secure in the knowledge that, whatever the result, the cause will not be lack of schooling.

To my Mother and Father, who never made me become a real doctor.

Chapter 1

Probing the Structure of Matter

This is the last potato I have dug in my life.

E. Rutherford, 1894

When a human being wants to see an object directly, she shines a light on it. The structure of the object is revealed by the pattern of light scattered to the eye. Perhaps because we are naturally equipped to interpret such information, the extension of this process to the subatomic realm has been consistently successful in exposing the successive layers in the structure of matter. To make this kind of direct observation, the probes employed must meet several requirements. They must be pointlike: their structure must not complicate the measurement and their wavelength must be small enough, their momentum large enough, to probe the length scale of interest. They must be able to penetrate the structure under investigation down to the length scale of interest. For charged probes this requires a sufficiently large energy. Finally, the interaction of the probe with the target must be simple enough to allow an interpretation of the scattering in terms of the target's structure. Since the first decade of this century, the electromagnetic scattering of pointlike particles has shown us the structure of atoms and the (unexpected) existence of the atomic nucleus, the structure of the atomic nucleus and its size, and the structure of the nucleon and the (unexpected) existence of partons, later to be identified with quarks. The experiment recorded here continues this investigation, using the principle essentially unchanged since 1909, but at a scale 10^5 times smaller.

At the turn of the century, the current model of the atom was that of J.J. Thomson.[1] It postulated an array of light, negatively charged electrons embedded in a uniform ball of positive charge. This model was able to explain the small but measured deflections of charged particles by thin layers of matter as the result of many gentle scatters.[2] In 1909, however, Geiger and Marsden[3] working in Ernest Rutherford's laboratory at Manchester, found that there was a small ($\frac{1}{8000}$) chance that an α particle from a radioactive source would be *reflected* from a thin foil of platinum. Even this small rate of large angle scattering was impossible in Thomson's model, either through a sucession of small scatters or through a single large one. The diffuse nature of the charge distribution did not produce an electric field of sufficient intensity to turn the α particles through large angles. Rutherford[4] realized that the observed large-angle scatters could be produced only by the concentration of one sign of charge at the center of the atom. The known properties of electromagnetism allowed Rutherford to make detailed predictions of scattering probability *vs.* angle, atomic number, and velocity for his model with a pointlike nucleus. The predictions were confirmed by the subsequent experiments of Geiger and Marsden.[5]

Geiger and Marsden's α particles could only penetrate to within 3000 fm$=3 \times 10^{-10}$ cm of the center of a heavy atom. Direct measurement of nuclear sizes ($\approx$ 5 fm) had to wait for the

higher energies provided by accelerators. Measurements using beams of high energy ($\approx$ 500 MeV) electrons[6] showed suppression of large angle elastic scattering from nuclei. The interpretation was simply the inverse of Rutherford's concerning the atom: the nucleus was a finite-sized distribution of charge. The suppression of the scattering cross section is described by a "form factor" $F(\mathbf{q})$, where $\mathbf{q}$ is the momentum transferred to the target, a quantity that increases as the scattering angle increases. If the energy transfer in the collision is small, the form factor is the Fourier transform of the spatial distribution of charge. An extended charge distribution leads to an $F(\mathbf{q})$ less than one and generally decreasing with increasing $|\mathbf{q}|$.

The proton also showed a non-unit form factor, indicating a charge radius of $\approx$ 0.7 fm. This, however, represented the resolution limit of elastic electron-nucleon scattering. Demanding an elastic scatter in effect requires a momentum uncertainty in the hadron final state of less than a pion mass. The uncertainty principle then restricts spatial resolution to approximately 1 fm at large momentum transfers for which the recoiling nucleon is relativistic. To reap the benefits of higher momentum transfer (shorter wavelength), it is necessary to relax the elastic requirement and consider inelastic scattering. Early studies of inelastic eN scattering were directed primarily at the resonance region near the elastic limit,[7] but in 1969, when the SLAC-MIT group first looked at the "deep inelastic continuum," they were surprised to find very little form-factor type suppression at large momentum transfer, in clear contrast to the elastic cross section.[8]

These results were immediately interpreted[9] through a model that would have seemed familiar to Rutherford. The proposed model postulated a nucleon composed of pointlike charged "partons" which were assumed to interact with each other on a time scale longer than that characteristic of the scattering process. The parton model reproduced the weak momentum transfer suppression observed in the data and also the property of "scaling", predicted from other considerations by Bjorken[10] and confirmed by experiment.[8] For a spherically symmetric target, the elastic scattering form factor depends only on the magnitude of the momentum transfer $|\mathbf{q}|$. In inelastic scattering, the counterpart to the elastic form factor is the "structure function," which can depend on both q^2, the square of the 4-momentum transfer, and ν, the energy transfer in the target rest frame. In the parton model, the structure function depends on these variables only in the dimensionless combination $x \equiv -q^2/2M\nu$ where M is the mass of the target nucleon. The dimensionless nature of this dependence is called scaling.

The partons inferred from deep inelastic scattering were always suspected to be the quarks that Gell-Mann[11] and Zweig[12] had invoked to explain the proliferating chemistry of hadrons in the mid-1960's. However, the dynamical theory of quarks necessary to interpret scattering experiments was not developed until the mid-1970's.[13] By this time, continued experimental investigations, now using muons, had found small violations of scaling.[14] The dynamical theory, called quantum chromodynamics (QCD), was found to contain slow (logarithmic) scaling violations due to the interactions of the quarks via gluons, the postulated carriers of the strong force. Further eN and μN deep inelastic scattering experiments[15,16] qualitatively confirmed the predicted pattern of scaling violations.

The experimental task at the end of the seventies was to challenge QCD quantitatively to test its validity and if confirmed, measure its undetermined parameters. Our experiment was designed and built to make such measurements by performing a precise determination of the nucleon structure function using the deep inelastic scattering of high energy muons. By doing so, we learn not only about the structure of the nucleon, but, if QCD is valid, about the structure of the strong interaction.

Chapter 2

The Phenomenology of Deep Inelastic Scattering

ELECTRICTY, *n. The power that causes all natural phenomena not known to be caused by something else.*
Ambrose Bierce, *The Devil's Dictionary*

2.1 Kinematics

The Feynman diagram for deep inelastic scattering in the lowest order of QED is shown in Fig. 2.1, together with a summary of our kinematical notation. To this order, the process is described as the exchange of one virtual photon. QED allows us to calculate unambiguously what happens at the leptonic (upper) vertex. The goal of our experiment is to uncover what happens in the region surrounding the hadronic vertex. Simply drawing the diagram indicates an immediate simplification. The only lines entering the hadronic vertex are those representing the initial nucleon and the virtual photon. We will be studying inclusive scattering, $\mu N \to \mu X$, with no reference to any particular hadronic final state. This means that the only relevant 4-vectors are p and q, and the only Lorentz-invariant quantities are q^2 and $p \cdot q$ (and $p^2 = M_N^2$). While isolating the hadronic vertex is a productive move toward understanding the scattering process, experimentally it is important to note that these quantities can be measured using only the initial and final muons:

$$\begin{aligned} Q^2 &\equiv -q^2 = 4EE' \sin^2 \frac{\theta}{2}, \\ \nu &\equiv p \cdot q / M_N = E - E', \end{aligned} \tag{2.1}$$

where E, E', and θ are the initial and final muon energies and the muon scattering angle as measured in the laboratory frame (the target rest frame). Terms containing the lepton mass have been neglected. Another useful quantity is the invariant mass of the hadronic final state: $W^2 = (p+q)^2 = M_N^2 + 2M_N\nu - Q^2$. The elastic limit is $W^2 = M_N^2$ or $Q^2 = 2M_N\nu$. Resonances appear at fixed W^2 near this limit. Figure 2.2 shows the region of the Q^2-ν plane accessible to inelastic scattering at fixed incident energy E.

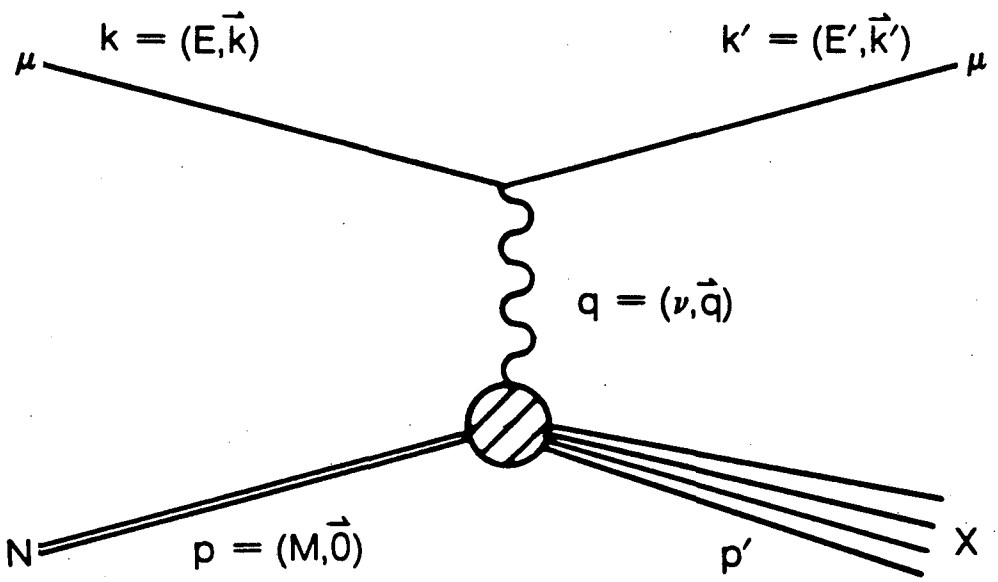

Fig. 2.1. Deep inelastic μN scattering, showing our notation for the 4-momenta and their representation in the laboratory frame.

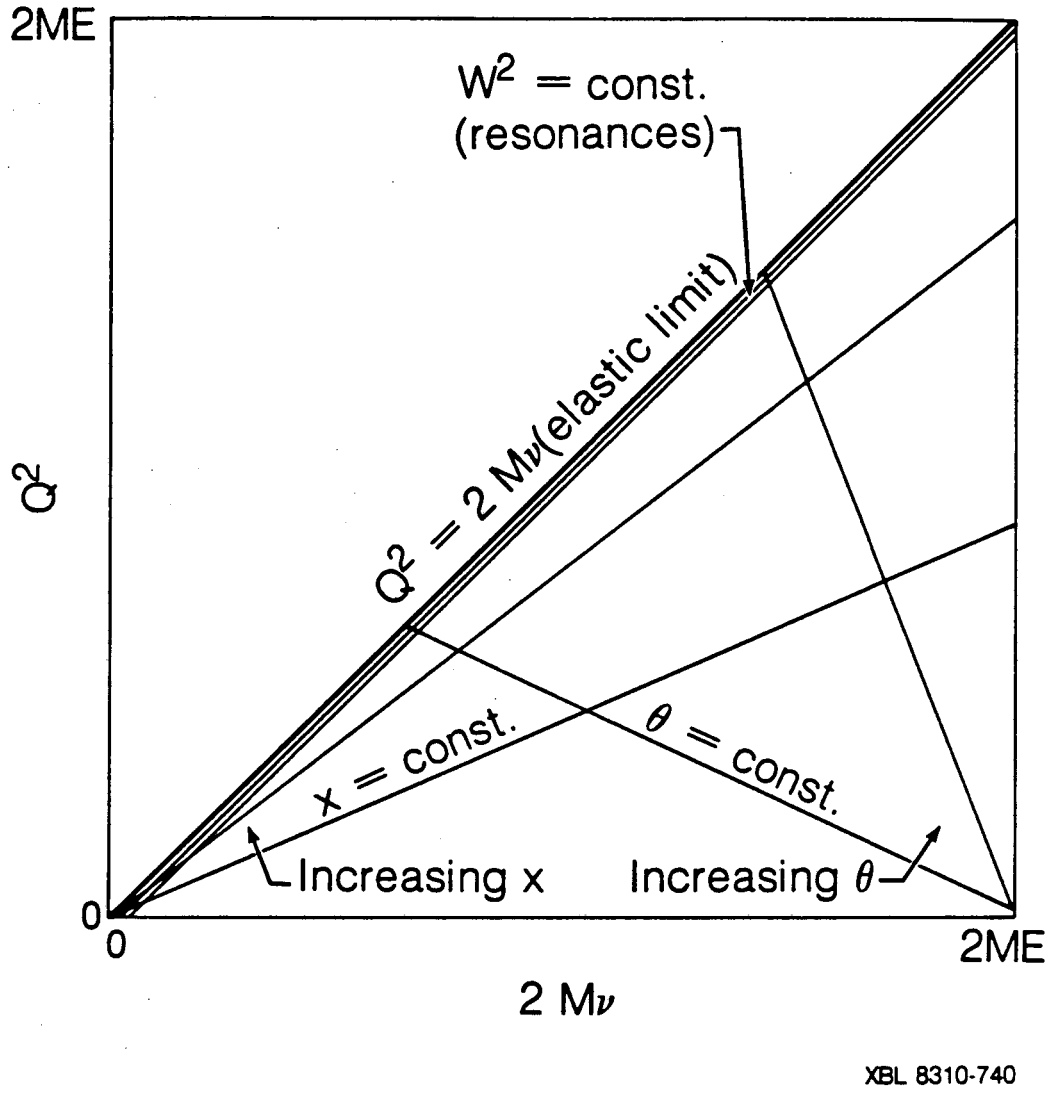

Fig. 2.2. Deep inelastic scattering kinematics. The region below the diagonal is accessible. Lines of constant W^2, x, and θ are indicated.

It is convenient to describe another set of variables which are Q^2 and ν scaled by their maximum values, neglecting lepton masses:

$$\begin{aligned} x &= Q^2/2M_N\nu \leq 1, \\ y &= \nu/E \leq 1, \\ v &= Q^2/2M_N E = xy. \end{aligned} \tag{2.2}$$

2.2 Cross section and structure functions

We can translate[17] the diagram of Fig. 2.1 directly into an expression for the spin-averaged inclusive cross section:

$$d\sigma = \frac{1}{v_{\text{rel}}}(2\pi)^4\delta^4(k+p-k'-p')\frac{(4\pi\alpha)^2}{Q^4}\frac{d^3\mathbf{k}'}{(2\pi)^3} \times \frac{m^2}{EE'}\frac{1}{4}\sum_{\text{spins}}\sum_X |(\bar{u}_{k'}\gamma_\mu u_k) < X \mid J^\mu(0) \mid p >|^2. \tag{2.3}$$

In this expression, m is the lepton mass, $\bar{u}_{k'}\gamma_\mu u_k$ is the known lepton electromagnetic current, and $J^\mu(0)$ is the unknown hadron electromagnetic current. Despite this ignorance, much further progress can be made in reducing this expression.[18] We start by isolating the unknown part of the square of the matrix element and defining the "hadron tensor"

$$W^{\mu\nu} = \frac{1}{2\pi}\frac{E_N}{M_N}\sum_X \frac{1}{2}\sum_{\text{spins}} < p \mid J^\mu(0) \mid X >< X \mid J^\nu(0) \mid p > (2\pi)^4\delta^4(p+q-p'). \tag{2.4}$$

Lorentz covariance demands that this tensor be constructed of the available tensor quantities with scalar coefficients. Because the corresponding lepton tensor (with which the hadron tensor will be contracted) is symmetric under interchange of μ and ν, we keep only symmetric terms:

$$W^{\mu\nu} = -W_1 g^{\mu\nu} + \frac{W_2}{M_N^2}p^\mu p^\nu + \frac{W_3}{M_N^2}q^\mu q^\nu + \frac{W_4}{M_N^2}(p^\mu q^\nu + p^\nu q^\mu). \tag{2.5}$$

The structure functions W_i are scalar functions and therefore depend only on Q^2 and ν. Gauge invariance requires that $q_\mu W^{\mu\nu} = q_\nu W^{\mu\nu} = 0$. With these constraints we can eliminate W_3 and W_4, leaving

$$W^{\mu\nu} = W_1\left(-g^{\mu\nu} + \frac{q^\mu q^\nu}{q^2}\right) + \frac{W_2}{M_N^2}\left(p^\mu - \frac{p\cdot q}{q^2}q^\mu\right)\left(p^\nu - \frac{p\cdot q}{q^2}q^\nu\right). \tag{2.6}$$

Contracting this with the lepton tensor, we get a compact expression for the differential cross section:

$$\frac{d^2\sigma}{dE'd\Omega'} = \frac{EE'}{\pi}\frac{d^2\sigma}{dQ^2d\nu} = \frac{4\alpha^2E'^2}{Q^4}\left[2W_1(Q^2,\nu)\sin^2\frac{\theta}{2} + W_2(Q^2,\nu)\cos^2\frac{\theta}{2}\right], \tag{2.7}$$

in terms of the two unknown structure functions W_1 and W_2.

2.3 Virtual photons

Further enlightenment comes from a complementary approach to the same process.[19] We treat the incident muon as a source of virtual photons and write the cross section as $d\sigma = \sum_\epsilon d\Gamma_\epsilon \sigma_\epsilon$, where Γ_ϵ and σ_ϵ are the flux and absorption cross section, respectively, for virtual photons of polarization ϵ. Using the Feynman rules for the reduced diagram of $\gamma^* N \to X$,

$$\sigma_\epsilon = \frac{4\pi^2\alpha}{K}\epsilon_\mu W^{\mu\nu}\epsilon^*_\nu, \tag{2.8}$$

where K is the virtual photon flux factor.

We now apply the gauge invariance condition in the form $q^\mu \epsilon_\mu = 0$. This is easiest in the "virtual photon rest frame" (indicated with primes), where we choose the basis polarizations

$$\begin{gathered}\epsilon'_1 = (0,1,0,0), \quad \epsilon'_2 = (0,0,1,0), \quad \epsilon'_3 = (0,0,0,1), \\ q' = (\sqrt{Q^2},0,0,0).\end{gathered} \tag{2.9}$$

Boosting into the lab frame with the z-axis chosen along the virtual photon direction gives

$$\begin{gathered}\epsilon_1 = \epsilon'_1, \quad \epsilon_2 = \epsilon'_2, \quad \epsilon_3 = \frac{1}{\sqrt{Q^2}}(\sqrt{Q^2+\nu^2},0,0,\nu), \\ q = (\nu,0,0,\sqrt{Q^2+\nu^2}).\end{gathered} \tag{2.10}$$

Explicitly contracting $\epsilon_\mu W^{\mu\nu}\epsilon^*_\nu$ we find

$$\begin{aligned}\sigma_T &\equiv \frac{1}{2}(\sigma_{\epsilon_1} + \sigma_{\epsilon_2}) = \frac{4\pi^2\alpha}{K}W_1, \\ \sigma_L &\equiv \sigma_{\epsilon_3} = \frac{4\pi^2\alpha}{K}\left[W_2\left(1+\frac{\nu^2}{Q^2}\right) - W_1\right],\end{aligned} \tag{2.11}$$

where T and L refer to transversely and longitudinally polarized virtual photons. Defining $R \equiv \sigma_L/\sigma_T$ we can eliminate W_1 in favor of R in the cross section Eq. 2.7. The advantages of this substitution will be described in the next section where it is shown that for some cases of interest R is expected to be small. For now we record the cross section in its new form,

$$\begin{aligned}\frac{d^2\sigma}{dQ^2 d\nu} &= \frac{4\pi\alpha^2}{Q^4}\left[1 - y + \frac{y^2 + 2M_N xy/E}{2(R+1)} - \frac{M_N xy}{2E}\right]W_2(Q^2,\nu) \\ &\approx \frac{4\pi\alpha^2}{Q^4}\left[1 - y + \frac{y^2}{2(R+1)}\right]W_2(Q^2,\nu).\end{aligned} \tag{2.12}$$

The approximate form comes from taking the Bjorken limit where energies $(E, Q^2, \nu) \to \infty$ with x and y finite.[10] In the kinematic region covered by our data, making such an approximation has a maximum effect of $< \frac{1}{3}\%$ on our measured structure function.

Chapter 3

Theory

The old lady crowed triumphantly. "It's no use, Mr. James—it's turtles all the way down!"
Discussion following a lecture by William James.

3.1 The parton model

The early experiments in the deep inelastic continuum showed that the nucleon behaves as if it contains pointlike constituents. That one could detect such structure meant that these constituents were interacting only weakly with each other, a fact not easily understood in the context of the strong interaction which presumably bound them together. Understood or not, this behavior is formalized as the parton model, the success of which is gratifying, if sometimes baffling.

In the parton model, the process of Fig. 2.1 is understood as the incoherent sum of diagrams such as Fig. 3.1. The nucleon is resolved into a swarm of partons, one of which is responsible for the scattering. During the scattering the parton is assumed to be free. The scattering itself is simple. If the parton has spin $\frac{1}{2}$, the virtual photon-parton vertex is calculated exactly as the lepton vertex was. Our ignorance about strong interactions is now relegated to the processes that determine the spectrum of partons in the nucleon and produce the splash of hadrons in the final state.

The parton model allows us to rewrite the hadron tensor of Eq. 2.4. We consider the process in the frame where the nucleon momentum is large.[9] We neglect the transverse momentum of the partons and assign to each parton of type i a fraction of the nucleon's momentum x_i from the unknown distribution $f_i(x_i)dx_i$. The hadron tensor is rewritten as

$$W^{\mu\nu} = \frac{1}{2\pi}\frac{E_N}{M_N}\sum_i \int f_i(x_i)\,dx_i \int \frac{d^3\mathbf{p}_i'}{(2\pi)^3} \times \left[\frac{1}{2}\sum_{\text{spins}} < p_i \mid J^\mu(0) \mid p_i' >< p_i' \mid J^\nu(0) \mid p_i > (2\pi)^4\delta^4(p_i + q - p_i')\right]. \tag{3.1}$$

The incoherent sum is now an integral over the initial distribution of partons, and the inclusive sum over final states is an integral over the final parton phase space. Aided by the momentum

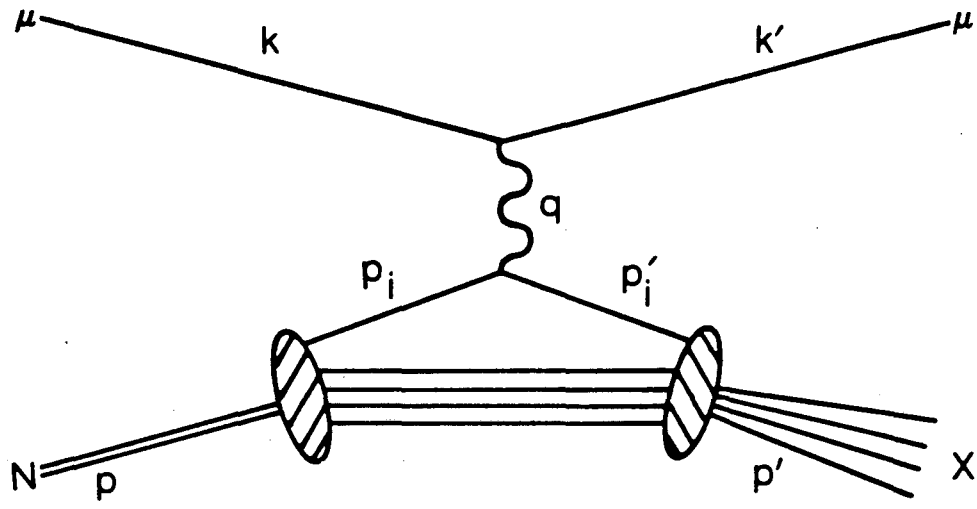

XBL 8310-709

Fig. 3.1. The parton model picture of deep inelastic scattering.

conserving delta function, we perform the final state momentum integration. Because the lepton-parton scatter is elastic and the partons are non-interacting, we are left with the elastic scattering condition in the form

$$\begin{aligned}\delta(2p_i \cdot q + q^2) &= \delta(2x_i p \cdot q - Q^2) \\ &= \frac{1}{M_N \nu}\delta(x_i - x),\end{aligned} \tag{3.2}$$

where $x = Q^2/2M_N\nu$ (see Eq. 2.2). We have neglected the masses and transverse momenta of the partons to allow the relation $p_i = x_i p$ to hold for all four momentum components. The measurable quantity x is thus the fractional momentum of the struck parton.

We now calculate the matrix elements, assuming the partons to be pointlike Dirac particles. Identifying the result term by term with the expression for $W^{\mu\nu}$ in Eq. 2.6 we find

$$\begin{aligned}F_1(x) &\equiv M_N W_1(Q^2, \nu) = \frac{1}{2}\sum_i f_i(x) e_i^2, \\ F_2(x) &\equiv \nu W_2(Q^2, \nu) = \sum_i x f_i(x) e_i^2.\end{aligned} \tag{3.3}$$

The structure functions F_i are seen to be functions of x only, with e_i the charge of type-i partons in units of the proton charge. This is the property known as "scaling."

Another property apparent from Eq. 3.3 is the relation $F_2(x) = 2xF_1(x)$. This is known as the Callen-Gross relation.[20] Inspection of Eq. 2.11 shows that, in the Bjorken limit ($\nu^2/Q^2 \to \infty$ with x fixed), the Callen-Gross relation implies $R = 0$. This result can be understood in the frame where the parton backscatters from the virtual photon. Since the electromagnetic Dirac (spin $\frac{1}{2}$) current is helicity conserving, this scattering can take place only through the absorption of helicity $= \pm 1$ photons, hence $\sigma_L = 0$ and $R = 0$. For scalar partons, $\sigma_T = 0$ and $R = \infty$. Allowing finite parton masses m_i and transverse momenta modifies these conclusions[21] and leads to corrections of order $(m_i^2 + p_{i\perp}^2)/Q^2$.

To summarize, in the parton model, a measurement of $F_2(x)$ is a determination of the momentum distribution of partons in the target nucleon – the nucleon's "structure" in momentum space. A measurement of R yields information on the spin of the partons themselves.

3.2 Quantum chromodynamics

At the beginning of the 1960's, Gell-Mann and Ne'eman[22] independently proposed $SU(3)$ symmetry as the underlying structure of the crowded spectrum of strongly interacting particles. While the classification of hadrons into $SU(3)$ multiplets was completely successful, it was puzzling that the fundamental 3 and $\bar{3}$ representations never appeared. Before long it was proposed independently by Gell-Mann[11] and Zweig[12] that all observed hadrons could be considered to be *composite* particles, made up of combinations of "quarks" which transformed under the fundamental representations. The actual existence of quarks as physical (as opposed to mathematical) entities was a point of speculation. In fact, Gell-Mann proposed searches that "would help to reassure us of the non-existence of real quarks".[11] The null results of such searches indicated that quarks were either very abstract or very tightly bound. In this environment, the experimentally-motivated parton model raised as many questions as it answered. If partons were quarks, then quarks had a rather robust (if restricted) physical existence inside nucleons and, furthermore, scaling implied that they were quasi-free.

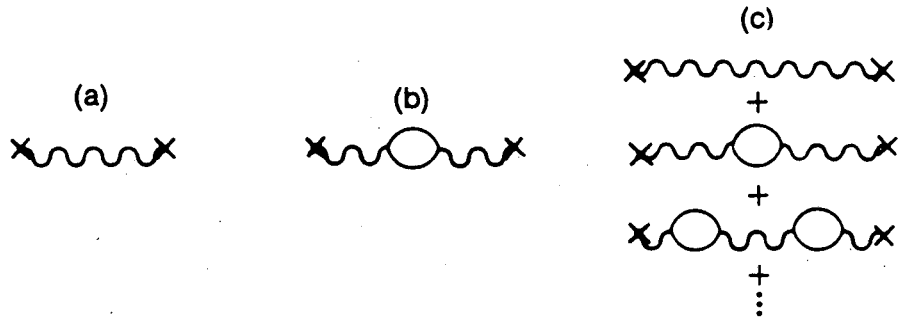

Fig. 3.2. The QED photon propagator with higher order corrections.

With the existence of partons as both mystery and clue, the development of a dynamical theory of the strong interactions proceeded. Euclid's geometry and Newton's mechanics were the explanatory standards of their day, and Kepler and Faraday felt compelled to try to cast their discoveries in terms of those successful structures. In high energy physics today, this role is played by quantum field theories, notably those with local gauge symmetry. The paradigm is quantum electrodynamics, which through a perturbation expansion in the fine structure constant $\alpha \approx \frac{1}{137}$ provides a powerful and remarkably accurate calculational tool. In creating a quantum field theory for the strong interactions of quarks one is in immediate difficulty. The coupling constant α_S is *not* small. In fact, the apparently permanent binding of quarks into hadrons casts doubt on the use of quarks as the fundamental fields to begin with. However, just as the existence of real electrons with finite mass and charge was the key to bypassing the divergences of QED's perturbation theory, the existence of quasi-free partons in the nucleon offered hope that, beyond the old-style strong interaction complexity, there was a usable field theory of quarks. In both cases, the restoration of finite physical behavior to the fundamental fields is through renormalization.

In QED, the lowest-order contribution to the photon propagator (see Fig. 3.2a) gives a $1/q^2$ dependence that is the Coulomb interaction.[23] The second-order contribution of Fig. 3.2b is infinite. Together, the expression for the propagator is[17]

$$\frac{-ig_{\mu\nu}}{q^2}\left[1 - \frac{\alpha}{3\pi}\ln\frac{M^2}{m^2} + \frac{2\alpha}{\pi}\int_0^1 dz\, z(1-z)\ln\left(1 - \frac{q^2 z(1-z)}{m^2 - i\epsilon}\right)\right], \tag{3.4}$$

where m is the electron mass and M is a large mass inserted as a cutoff. For $q^2 \to 0$ we restore the Coulomb potential by renormalizing the coupling constant (or, equivalently, the electron charge) to absorb the formally infinite factor

$$1 - \frac{\alpha}{3\pi}\ln\frac{M^2}{m^2}. \tag{3.5}$$

XBL 8310-710

Fig. 3.3. Corrections to the QCD gluon propagator.

This procedure is *defined* to yield the observed coupling constant

$$\alpha = \alpha_B\left(1 - \frac{\alpha_B}{3\pi}\ln\frac{M^2}{m^2}\right) \approx \frac{1}{137}, \tag{3.6}$$

where α_B is the unmeasurable "bare" coupling constant. The remainder of Eq. 3.4 is finite, q^2 dependent, and observable.[24] In the limit of small q^2 it gives a small contribution to the Lamb shift. If, instead, we look at the limit $Q^2 \equiv -q^2$ large, we find a correction to the propagator of

$$\frac{\alpha^2}{3\pi}\ln\frac{Q^2}{m^2}. \tag{3.7}$$

We can choose to redefine α to include this correction as well. We restore Coulomb's law, but at the expense of introducing a Q^2 dependent or "running" coupling constant

$$\alpha(Q^2) = \alpha\left(1 + \frac{\alpha}{3\pi}\ln\frac{Q^2}{m^2}\right). \tag{3.8}$$

We could, in a similar fashion, include higher order contributions from a series of loops (Fig. 3.2c). Summing this series gives

$$\alpha(Q^2) = \frac{\alpha}{1 - (\alpha/3\pi)(\ln Q^2/m^2)}. \tag{3.9}$$

The running coupling constant is seen to increase slowly with Q^2. This is interpreted as the penetration of the shielding due to vacuum polarization as one probes shorter distances, revealing more of the bare charge.

The theory of strong interactions was developed in analogy to QED, with an internal quantum number called "color" taking the part of the electric charge. The resulting theory is thus known as quantum chromodynamics (QCD). The primary difference between QCD and QED is that, while photons are neutral, the "gluons" of QCD carry color and thus couple directly to one another. This allows diagrams such as Fig. 3.3a to occur in addition to the QED-like diagram of Fig. 3.3b. Including the new QCD diagrams in the calculation of the running coupling constant

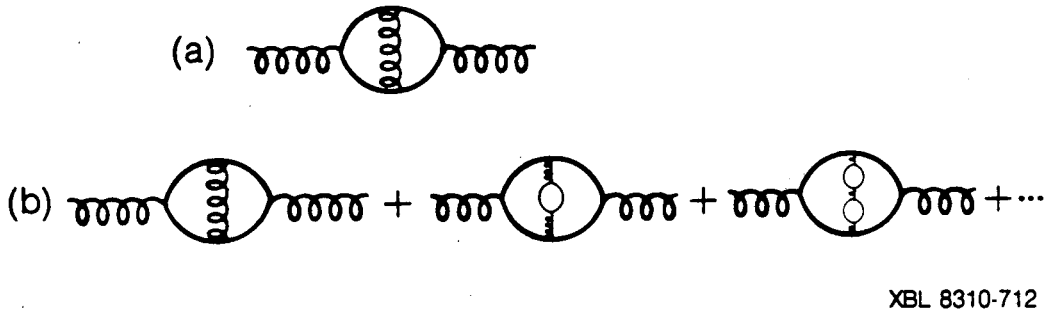

Fig. 3.4. (a) A non-leading-log diagram. (b) The effect of using the renormalized coupling constant in (a).

for the strong interaction gives

$$\alpha_S(Q^2) = \frac{\alpha_S(\mu^2)}{1 + [(33 - 2N_f)/12\pi]\alpha_S(\mu^2)\ln(Q^2/\mu^2)}, \tag{3.10}$$

where μ^2 is an arbitrary renormalization point and N_f is the number of quark flavors (up, down, strange...). This expression is distinguished from the QED case by two features: the QCD coupling constant runs much faster (due to the presence of α_S in the denominator) and it runs in the opposite direction, getting *weaker* as Q^2 increases, for $N_f < 17$. This latter property, known as "asymptotic freedom",[25] is the key to the success of the parton model, and hence to the success of QCD, as will be discussed further below. The restriction on the number of flavors arises because quark loop contributions behave like the electron loop terms of QED and run α_S up. They must be dominated by the remaining QCD terms to give asymptotic freedom. The expression Eq. 3.10 for α_S is an approximation based on ignoring diagrams such as Fig. 3.4a. In estimating its contribution we can use Eq. 3.10, or equivalently the renormalized gluon propagator, which automatically replaces Fig. 3.4a with the series of Fig. 3.4b. The asymptotically free running coupling constant increases the level of convergence and the resulting contribution is of the order $\ln(\ln(Q^2/\mu^2))$. The neglect of these terms compared with the $(\ln(Q^2/\mu^2))^n$ behavior of the terms in Fig. 3.3 is known as the "leading logarithm" approximation. We can remove the reference to the arbitrary renormalization point μ in Eq. 3.10 by introducing the parameter Λ such that

$$\alpha_S(Q^2) = \frac{12\pi}{(33 - 2N_f)\ln(Q^2/\Lambda^2)}. \tag{3.11}$$

While μ was arbitrary and unmeasurable, Λ is defined by Eq. 3.11 and is measurable. Other definitions of Λ differ from this one in the next order of α_S.[26] Keeping the next-to-leading logarithm gives such a correction. For this reason, Λ as defined in Eq. 3.11 is sometimes called Λ_{LO} for "lowest order."

Asymptotic freedom allows the understanding of the quasi-free appearance of partons in nucleons. As in QED, the renormalized coupling is indeed small. This permits meaningful

perturbation series calculations for strong interactions at large Q^2. At the low Q^2 end, it is hoped, but has not been proven, that the increasing α_S is a sign that the QCD interaction between quarks is *confining*, meaning that free quarks cannot be separated from their parent hadrons. Even without such proof, it is clear from Eq. 3.11 that perturbative QCD cannot work at low Q^2. For this reason, perturbative QCD cannot give predictions for such static properties of hadrons as the x distribution of partons. With low Q^2 information as input, however, QCD can calculate the Q^2 dependence of such quantities. (Recall that the parton model predicts scaling, that is, no Q^2 dependence at fixed x.)

The most direct prediction of QCD[13] is not of the Q^2 evolution of parton distributions, but rather of moments of those distributions, defined as

$$M_n(Q^2) = \int_0^1 dx\, x^{n-1} f_i(x, Q^2). \tag{3.12}$$

Given the moment at a reference $Q^2 = Q_0^2$, QCD predicts the evolution

$$M_n(t) = M_n(t=0)\left[\frac{\alpha_S(t=0)}{\alpha_S(t)}\right]^{d_n}, \tag{3.13}$$

with $t \equiv \ln(Q^2/Q_0^2)$ and the exponents d_n calculable in perturbative QCD. After calculating the moments to sufficiently high n, the set can be inverted to give results for the distributions themselves. When this is done, it is found that QCD predicts scaling violations which are logarithmic in Q^2.

Fortunately, Altarelli and Parisi[27] have given a more direct interpretation of QCD's predictions, an interpretation that is a natural extension of the parton model. Figure 3.5a shows the parton model diagram for deep inelastic scattering *via* a virtual photon. Allowing the partons to interact generates processes such as those in Figure 3.5b-d. These processes rob from the momentum fraction x carried by the struck parton. We therefore expect that these processes will reduce the structure function at large x and increase it at small x. Increasing Q^2 resolves finer and finer structure of this type, but asymptotic freedom slows the evolution, leaving soft (logarithmic) scaling violations. The method of Altarelli and Parisi accounts for the processes in Fig. 3.5b by writing a set of transport-like differential equations for the quark distribution functions:

$$\begin{aligned}
\frac{d\sum_{i=1}^{2N_f} f_i(x,t)}{dt} &= \frac{\alpha_S(t)}{2\pi}\int_x^1 \frac{dy}{y}\left[\sum_{i=1}^{2N_f} f_i(y,t)P_{qq}\left(\frac{x}{y}\right) + 2N_f G(y,t)P_{qG}\left(\frac{x}{y}\right)\right], \\
\frac{dG(x,t)}{dt} &= \frac{\alpha_S(t)}{2\pi}\int_x^1 \frac{dy}{y}\left[\sum_{i=1}^{2N_f} f_i(y,t)P_{Gq}\left(\frac{x}{y}\right) + G(y,t)P_{GG}\left(\frac{x}{y}\right)\right].
\end{aligned} \tag{3.14}$$

The sum is over quark+antiquark flavors, and couplings are assumed to be flavor independent. $G(x,t)$ is the distribution of gluons in the nucleon as a function of momentum fraction x. We have anticipated our use of a nuclear target with a nearly equal mix of protons and neutrons. This leads to a mixture of quarks which is nearly a flavor singlet. Since the gluon is also a flavor singlet, there is coupling between the quark and gluon evolutions. As the flavor independence of the couplings implies, the gluon does not couple to the difference between two quark types. For such a case ("non-singlet") the evolution is simpler:

$$\frac{d}{dt}[f_i(x,t) - f_j(x,t)] = \frac{\alpha_S(t)}{2\pi}\int_x^1 \frac{dy}{y}[f_i(y,t) - f_j(y,t)]P_{qq}\left(\frac{x}{y}\right). \tag{3.15}$$

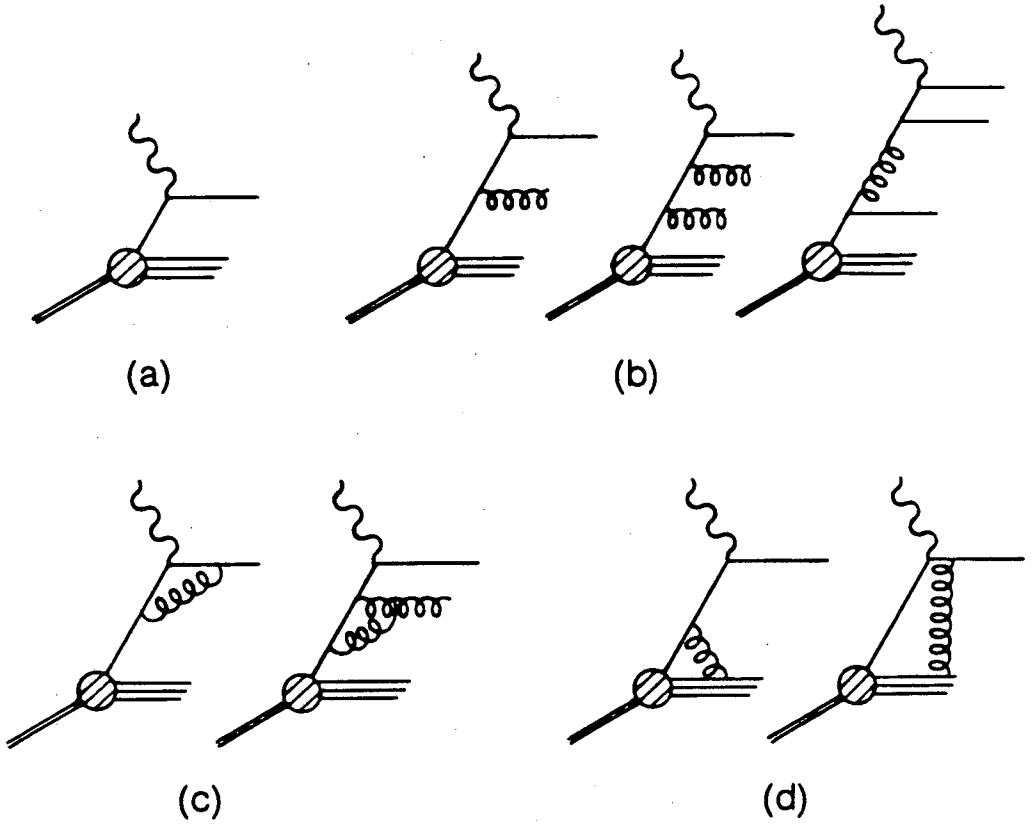

Fig. 3.5. QCD modifications to the parton model diagram (a) for deep inelastic scattering. (b) Logarithmic Q^2 evolution; (c) renormalization; (d) "higher twist".

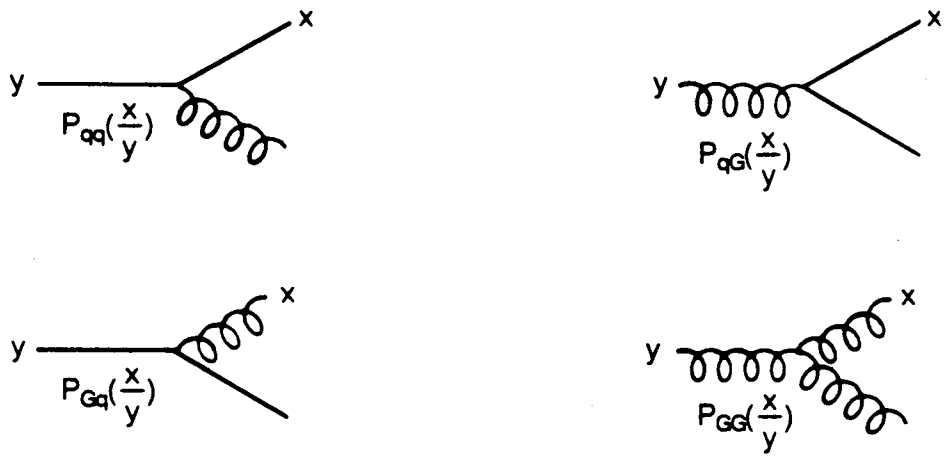

Fig. 3.6. QCD vertices governing the Q^2 evolution of the structure function.

The interpretation of Eqs. 3.14 is quite straightforward. The $P(z)$'s represent the probabilities of the processes in Fig 3.6, where a daughter parton (either quark or gluon) is split from a parent parton, taking a fraction z of its momentum. Thus partons of momentum fraction x (the left hand sides of Eq. 3.14) come from partons of larger momentum fraction y with probability $P(x/y)$. This approach is equivalent to the QCD calculation of moments, and the probabilities $P(z)$ can be calculated from the d_n of Eq. 3.13.

The diagrams of Fig. 3.5c and d still remain. Those such as that of Fig. 3.5c are taken into account automatically. They either cancel infrared divergences from the emission of soft real gluons and are handled by renormalization, or are contributions to the running coupling constant and thus are included in the leading log approximation by using $\alpha_S(Q^2)$.[28] The diagrams of Fig. 3.5d are another story. Though not calculable in detail, their general behavior is known. Since they involve interactions with more than one target quark, they resemble elastic scattering, where multiple gluon exchanges are required to keep the recoiling nucleon intact. This leads to a form factor-like suppression which goes as powers of $1/Q^2$. At sufficiently large Q^2, the logarithmic behavior discussed above should dominate these terms, which bear the unfortunate name "higher twist".

To test the predictions of QCD, one can measure the structure function as a function of Q^2 for various fixed values of x. This Q^2 dependence or scaling violation can be compared to QCD by using the measured x dependence at a fixed $Q^2 = Q_0^2$ as the initial condition and integrating Eq. 3.14 to get predicted values of the structure function for all Q^2. For the singlet case, it is also necessary to have $G(x, Q_0^2)$, the initial condition for the gluon evolution. This distribution is not directly measurable. Neutrinos, however, are sensitive to the difference between quarks and antiquarks. With this essentially non-singlet information, various QCD and phenomenological parameters can be determined without complications from gluons. With these values fixed, the singlet structure functions can be used to extract of the gluon distribution.[29] A hypothetically more direct but experimentally more difficult approach is to use the production of heavy flavors in the "photon-gluon fusion" diagram of Fig. 3.7 to tag interactions with gluons.[30]

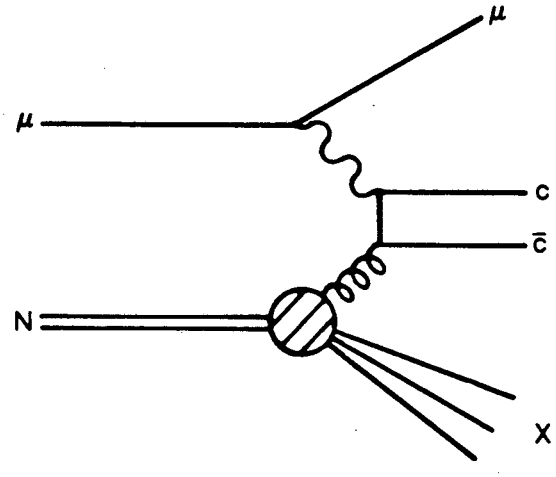

XBL 8310-713

Fig. 3.7. Photon-gluon fusion. The production of a heavy quark pair can be used to tag the interaction with a gluon.

3.3 Grand unified theories

The realization that asymptotic freedom brought the strong interactions (at least at high Q^2) under the hegemony of gauge theories brought a feeling of warm comfort to high energy physics. All the forces of concern to high energy physicists (except the one that holds them to the planet, and the peculiar one that draws them to Batavia, Illinois) were now described using the same basic tools. The weak and electromagnetic interactions had been unified and understood as one gauge theory with a spontaneously broken symmetry.[31] It was immediately hoped that the strong interactions could be added, making a "Grand Unified Theory" or GUT.

In a typical GUT (for a review, see Ref. 32.) quarks and leptons are placed in the same representation of a group ($SU(5)$ for the simplest theory[33]). Below some large energy scale characterized by the mass M_X of the bosons that mediate transitions among members of the representation, the symmetry between the strong and electroweak interactions is broken. At low energies symmetry breaking is complete and we observe the $SU(3)_{color} \times SU(2) \times U(1)$ structure of the standard model. The mass M_X is determined by following the three running coupling constants up to the energy where they become equal. Using α and α_S for this determination in one of the simpler models gives[32]

$$M_X \approx 15 \times 10^{14} \Lambda(\text{GeV}). \tag{3.16}$$

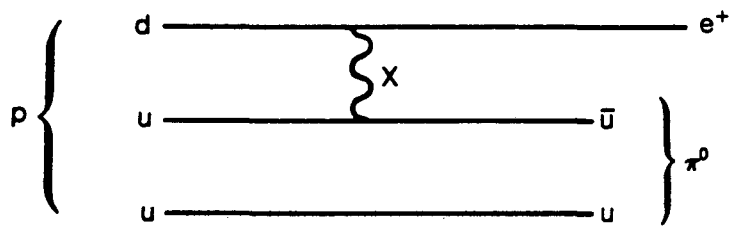

XBL 8310-714

Fig. 3.8. Proton decay mediated by X boson exchange.

The symmetry that allows transitions between leptons and quarks *via* the exchange of X-bosons means that baryon number is not conserved and hence protons are no longer stable. Proton decay can proceed through the diagram of Fig. 3.8 and others. The predicted lifetime is

$$\tau_p \sim \frac{1}{\alpha_{\mathrm{GUT}}} \frac{M_X^4}{M_p^5} \approx 5 \times 10^{32} [\Lambda(\mathrm{GeV})]^4 \text{ yr}, \tag{3.17}$$

with over an order of magnitude of theoretical uncertainty. The existence of this lepton-quark symmetry and its breaking has a number of other uses. It explains the apparently exact equality of the magnitude of the charges of the electron and proton. Baryon number violation is necessary, but not sufficient, to explain in a dynamical way the observed matter-antimatter asymmetry in the universe.[34] Some speculative theories use the "super-saturated" state of the universe in the false vacuum prior to the spontaneous breakdown of symmetry to give a cosmological constant that generates the entire observable universe out of virtually nothing.[35]

Although GUT's have had some theoretical successes, the prediction of proton decay is one of the few that may be verifiable. Early determinations of Λ indicated values on the order of several hundred MeV. The resulting proton lifetimes were above, but close to, existing experimental lower limits of $\approx 10^{29}$ years.[36] A new generation of proton decay experiments designed to probe the GUT regime has recently begun running. Early results[37] for the decay mode $p \to e^+\pi^0$ yield limits in conflict with the simplest GUT models. The fourth-power dependence of τ_p on Λ makes a reliable determination of Λ essential to the confrontation of theory with experiment.

3.4 Theoretical summary and experimental program

In the brief time since this experiment was proposed, the emphasis of theoretical interest has changed a great deal. Through all these shifts, the importance of input from deep inelastic lepton nucleon scattering has persisted. The original measurements of this type were concerned with determining the geometrical structure of the target. Today the differential cross section Eq. 2.12 is dissected to give information on a variety of topics. At fixed Q^2, $F_2(x)$ gives the longitudinal momentum distribution of the nucleon's charged constituents. R, determined using $F_2(E)$ at fixed Q^2 and x (see Sec. 10.6), gives the spin of the constituents and can be affected by their transverse momenta. At fixed x, the Q^2 dependence of F_2 probes the interactions of quarks and gluons and determines the running coupling constant of QCD. Grand unification turns a measurement of $\alpha_S(Q^2)$ into a prediction for the proton lifetime.

The experimental program is clear: test this theoretical structure by making a precision measurement of the differential cross section of deep inelastic scattering over as broad a kinematic range as possible. This is especially important for Q^2, where the variation of interest is expected to be only logarithmic (on top of a $1/Q^4$ falloff) and the low Q^2 region may be obscured by nonperturbative effects. The experimental considerations for such a measurement will be discussed in the next chapter.

Chapter 4

The Multimuon Spectrometer

The mud elephant,
wading through the sea,
leaves no tracks.

The Fugs, c. 1970

4.1 Design constraints

Our goal is to measure the nucleon structure function $F_2(x, Q^2)$ over as large a range of Q^2 as possible, without being forced to include very low Q^2. The kinematic limit, $Q^2 < 2M_N E$ (see Eq. 2.2), requires us to have a high energy lepton beam. The desire to reach $Q^2 > 100$ GeV$^2/c^2$ rules out existing electron beams, so we use the high energy muon beam at Fermilab. The virtual photon propagator suppresses the large Q^2 cross section like $1/Q^4$. To reach high Q^2 we must therefore have high luminosity. We achieve high luminosity by using a high intensity beam incident on a long, heavy target. To maintain high acceptance throughout the long target, the target and the spectrometer used to analyze the final state are integrated into one package. The high magnetic fields required for momentum analysis above 100 GeV/c and the large magnetized volume require an iron magnet.

Along with deep inelastic scattering, the experiment is designed to observe multimuon final states: $\mu N \rightarrow \mu\mu X, \mu\mu\mu X, etc.$ An example is shown in Fig. 3.7, where the heavy quark state decays to one or more muons.[30,38] This imposes three constraints: suppression of low mass electromagnetically produced muon pairs; observation at the lower Q^2's typical of multimuon production (a few GeV$^2/c^2$), and thus at smaller scattering angles; and suppression of secondary muons from pion and kaon decay in hadronic showers. To meet the first requirement, we use a Cartesian geometry with a uniform vertical magnetic field for momentum analysis. Muon trajectories bend (and muon pairs separate) in the horizontal plane. For pair mass discrimination we demand a minimum *vertical* opening angle, which is unaffected by the magnetic separation. When the large ($\approx$ 20 cm) size of the beam is folded in, the second constraint requires that the spectrometer be active in the beam region and therefore that the magnetic field extend uniformly to the center of the beam. This dictates that the target material be the same iron used in the magnet. This target must be densely packed along the beam direction to suppress π and K decay.

The result is the Multimuon Spectrometer (MMS) illustrated in Fig. 4.1. The MMS is a horizontal stack of 91 4-inch thick steel plates, each eight feet on a side. The stack is

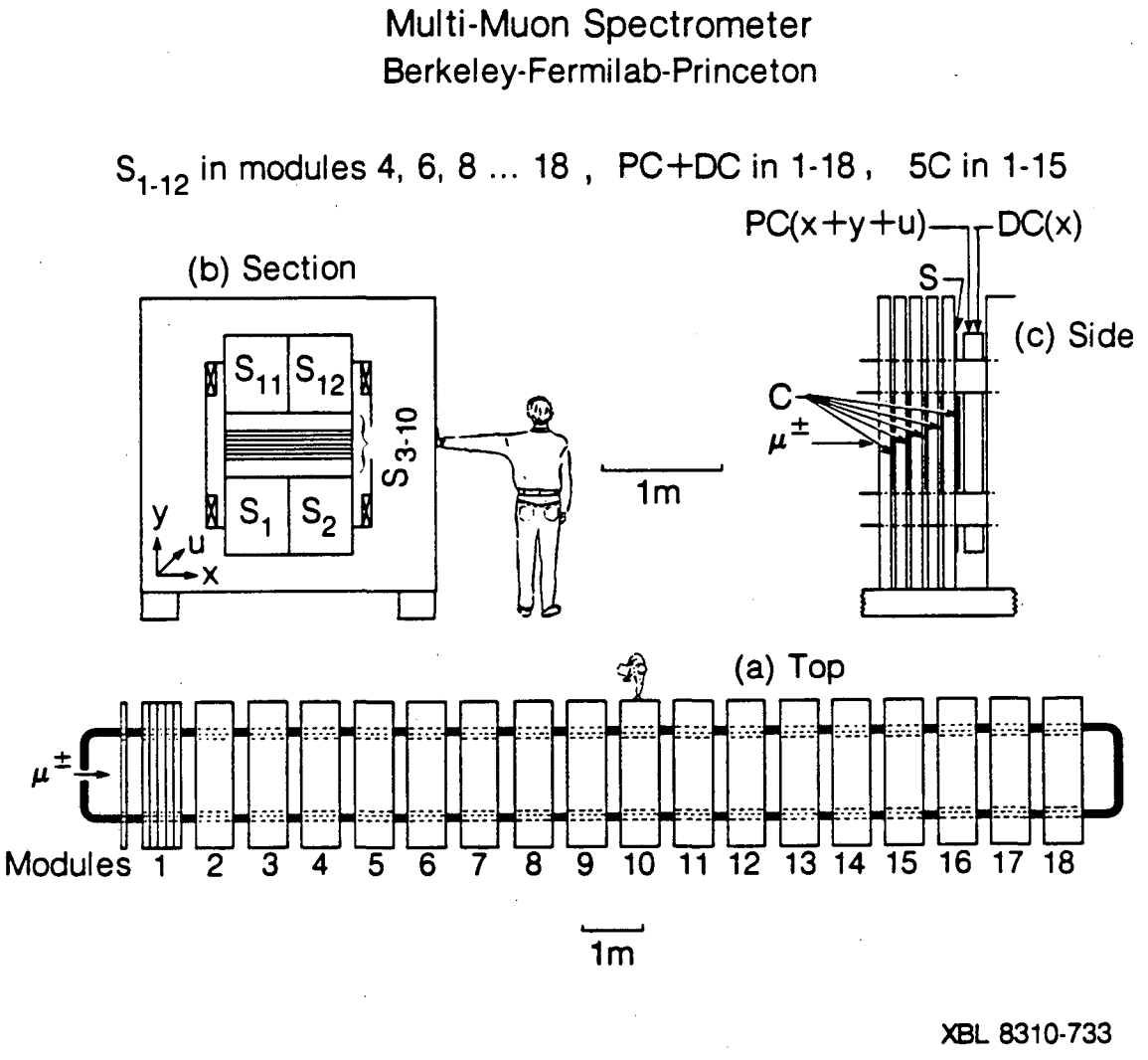

Fig. 4.1. The Multimuon Spectrometer (MMS). (a) Top view, showing the arrangement of iron plates into modules and the magnet coils running the length of the stack. (b) Section, looking into the beam, showing the coils in their slots, our coordinate system, and a trigger scintillator hodoscope. Paddles $S_{1,2,11,12}$ are used to signal a scattered muon, while staves S_{3-10} serve as a beam veto. (c) Side view of one module — detailed in Fig. 4.4.

magnetized by coils running the length of the stack through slots cut in the plates. The iron serves as target, analyzing magnet, hadron absorber/muon identifier, and hadron calorimetry medium. The spectrometer is instrumented with multiwire proportional and drift chambers for recording muon trajectories and with plastic scintillation counters for triggering and calorimetry. The various components of the MMS are described in the remaining sections of this chapter.

It should be noted that the MMS solution to these constraints represents a compromise and that other solutions have been designed and operated. The effectively solid-iron environment in which we work is a messy one, complicating the reconstruction of tracks and limiting our momentum resolution. An alternative design sacrifices luminosity for better resolution and a simpler target material by using a hydrogen or deuterium target followed by an air gap magnet, with muon identification postponed until after the magnet. Examples are the experiments done in the Chicago Cyclotron Magnet at Fermilab[16] and by the European Muon Collaboration at CERN.[39] For the reasons discussed above, these experiments are not suitable for the study of multimuon production. Another alternative is to use a neutrino beam. This probes somewhat different physics and is a complement to the muon program.

4.2 Operational summary

- Protons from the Fermilab synchrotron incident on a target produce pions which decay, giving a beam of muons. (Fig. 4.2)
- The last two magnets in the muon beam line are instrumented to record the beam track for momentum analysis. Beam muons are rejected if accompanied by a second muon. (Fig. 4.3)
- The beam muon enters the MMS. Three in a million scatter in the iron by enough to enter trigger counters above or below the beam, generating a signal to record an event. (The multimuon triggers operate in parallel.)
- The bending trajectories of the beam and scattered muons are recorded in proportional and drift chambers located at five plate intervals throughout the MMS. (Fig. 4.4)
- The pulse heights in plastic scintillators in the beam region after every plate are recorded to measure calorimetrically the energy of the final state hadronic shower.
- Our coordinate system is defined with z along the beam axis, y up, and x horizontal.

4.3 The muon beam

The production of the Fermilab muon beam begins with the continuous extraction of the 400 GeV proton beam during the 1.25 sec "flattop" of the accelerator. Typically 1.5-2 $\times 10^{13}$ protons were accelerated per cycle, with over half delivered to a 30 cm aluminum target for the N1 muon line. The pions and kaons produced in the target were focussed into a 400 m evacuated decay pipe (see Fig. 4.2) where the pions and kaons decayed to muons. The beam was sign- and momentum- selected in dipoles D1 and D2 and focussed into the aperture of D3 which contained 60 feet of polyethelene (CH_2) absorber to remove the remaining hadrons. The beam was then bent and focussed into the muon lab. The acceleration cycle was repeated at intervals of approximately 10 sec. The resulting beam yielded approximately 1 ($\frac{1}{3}$) μ^+ (μ^-) per 10^7 protons on target with a π/μ ratio of less than 10^{-7} and a momentum acceptance of $\pm 2.5\%$.[18]

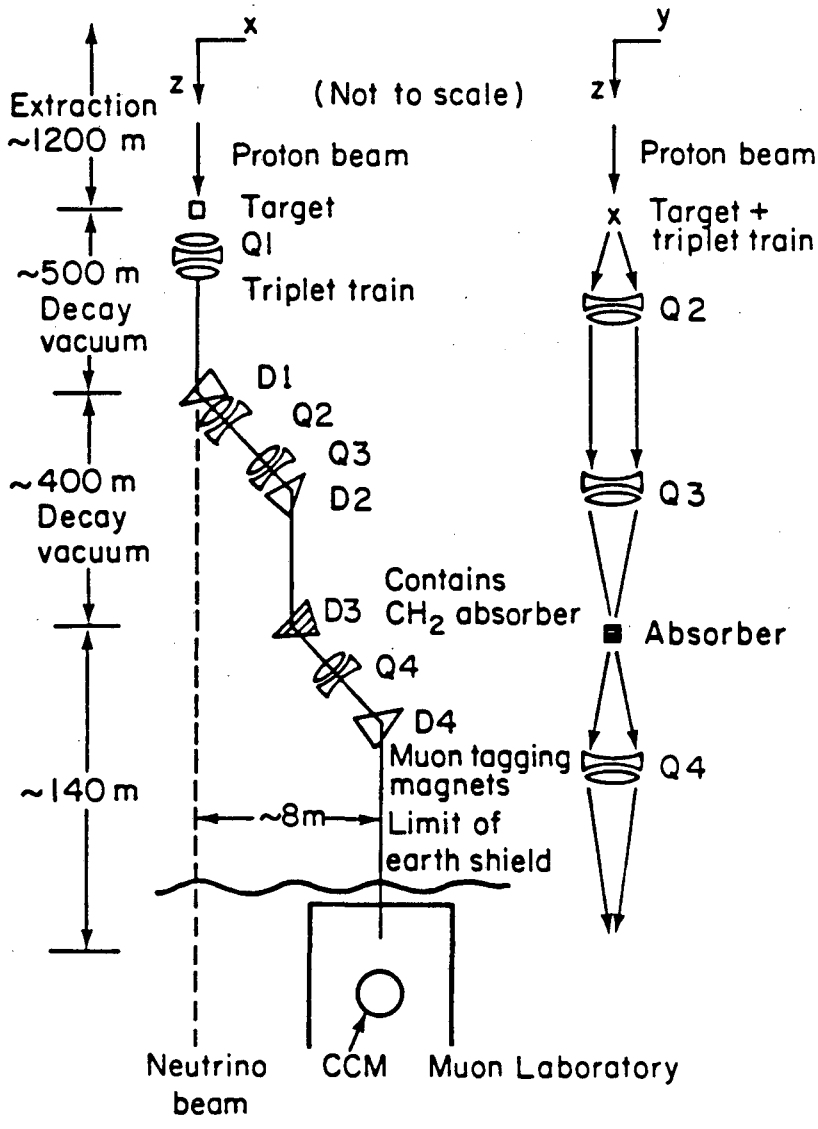

Fig. 4.2. The Fermilab muon beam.

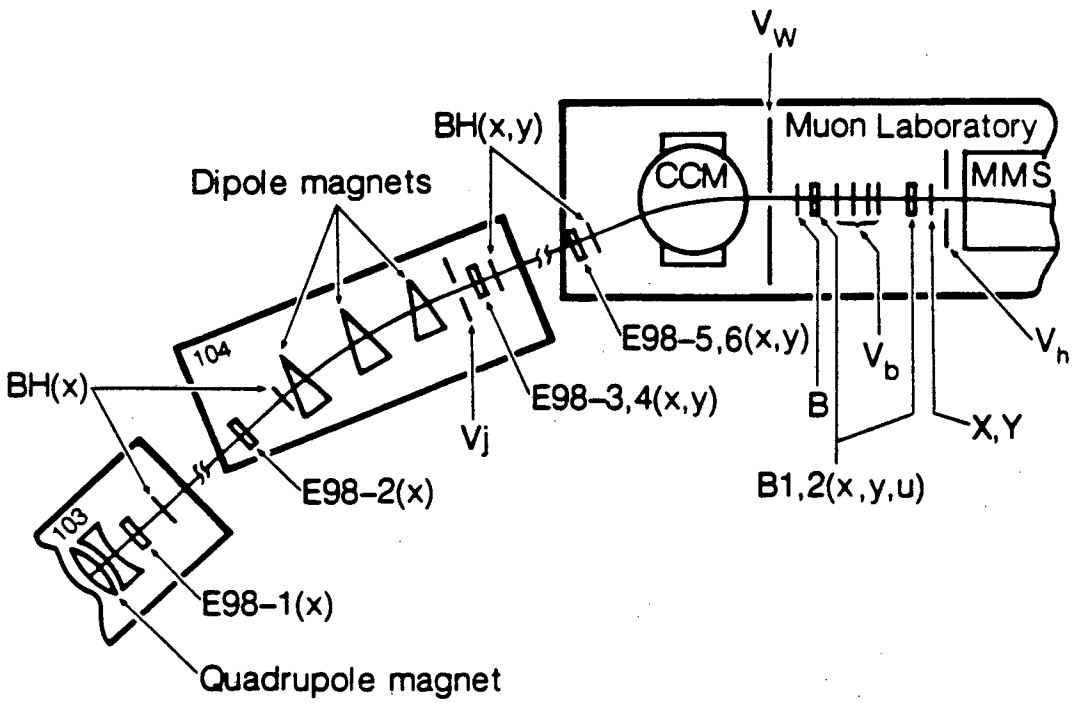

E98-n, B1, B2	Multiwire proportional chambers
BH,X,Y	Beam scintillator hodoscope
V_j	"Jaw" veto counter
V_W	Large veto wall
B	Beam defining scintillator
V_h	Halo veto hodoscope
V_b	Bucket occupancy veto counter
MMS	Multimuon Spectrometer
CCM	Chicago Cyclotron Magnet

XBL 8310-721

Fig. 4.3. The beam monitoring system used to define a valid beam muon and determine its momentum. Not to scale.

Beam instrumentation is shown in Fig. 4.3. Experiments using the Chicago Cyclotron Magnet (CCM) ran simultaneously with the MMS, which was positioned along the CCM-deflected beam line. The last N1 dipole and the CCM were instrumented with multiwire proportional chambers (MWPC) and scintillator hodoscopes, (E98-1...6, BH) giving four horizontal (x) and two vertical (y) measurements. These, in conjunction with two MWPC (B1 and B2) measuring x, y, and a diagonal (u) coordinate located in front of the MMS, were used to determine the momentum of individual beam muons, ideally to better than 0.5% (σ_p/p). In reality, the situation was complicated by material placed in the beam by the upstream experiment, including borax (to clean up the beam) and a lead-glass shower counter 20.5 radiation lengths thick. With enough MWPC information we could fit the Coulomb scattering angle in the lead-glass, but at the cost of redundancy in the momentum fit. Energy loss in material upstream of the MMS could be corrected for in an average sense only. Straggling was accounted for by including it in the simulation used for acceptance and resolution modeling (see Chap. 8).

A system of scintillator hodoscopes (see Fig. 4.3) was used to define the beam size and choose usable beam muons. The last focus of the beam was in the aperture of the last beam line dipole. At the front of the MMS, the counter B and the hodoscopes X and Y defined the beam to be 35.1 cm (x) by 22.9 cm (y). A usable muon was defined to be one unaccompanied by a second muon, either in or out of the beam. This was especially important to protect the multimuon triggers. The muon beam retained the 53 MHz signature of the synchrotron, leading to a time structure of 18.9 ns "rf buckets." Signals from counter B were put into advanced or delayed anticoincidence to veto muons which had another muon in either the preceding or following bucket. If another muon was in bucket ± 2 or ± 3, the track was used but tagged. Tracks with accompanying muons in the same bucket were rejected on the basis of pulse height information from scintillators B and V_b and from hodoscope information from X and Y. A 1.4 $\times$ minimum ionizing signal from any three of the five pulse heights or more than one count in either hodoscope plane vetoed the track. Muons out of the defined beam area are known as "halo." In the Fermilab muon beam, total intensity outside our defined beam was roughly equal to the intensity in the beam. Beam muons with an in-time halo muon were rejected by three layers of veto scintillators, one at V_w and two at V_h. The signal for a usable beam track was called BV (for "vetoed beam"):

$$\mathrm{BV} = \left(\mathrm{B} \cdot \sum \mathrm{X} \cdot \sum \mathrm{Y}\right) \cdot \overline{\mathrm{ADJ}} \cdot \overline{\mathrm{SAME}} \cdot \overline{\mathrm{V}}_\mathrm{w} \cdot \overline{\mathrm{V}}_\mathrm{h}, \tag{4.1}$$

where ADJ is a signal from an adjacent bucket and SAME is a second muon in the same bucket. BV was required in coincidence with all physics triggers, and a prescaled number, typically 1/350 000, was recorded with no further trigger requirements for calibration and use as a unbiased input for the simulation programs. The counter B, designed to give large, well behaved signals, was used further as the main timing element for the entire experiment. It was fanned out and used repeatedly in all triggers as a strobe to maintain the critical timing required by our complex trigger.

The intensity of the muon beam was $\approx 3 \times 10^6$ muons per pulse or, equivalently, a bucket occupancy probability of 0.07. This meant that there was typically one muon in the muon lab at a time. The vetoes rejected from $\frac{1}{3}$ to $\frac{1}{2}$ of the muons, leaving a usable flux of $1.5\text{-}2 \times 10^6$ muons per pulse. For μ^- running, the beam intensity was a factor of three lower, but the lower intensity meant less veto rejection, giving a usable flux of around 0.9×10^6/ pulse.

4.4 Target and magnet

The 91 steel plates of the Multimuon Spectrometer were rolled and cut at the Danly Steel Mills of Chicago from AISI 1018 steel with a carbon content of $(0.17 \pm 0.03)\%$. The

average thickness of the plates was 10.28 cm. The plates were grouped into 18 modules of five, with 3 cm gaps separating the plates. The remaining plate, known as plate 0, was placed at the front of the stack where the last plate of an otherwise nonexistent module 0 would have been. Following each module was a large gap for the insertion of an instrumentation package. This package was designed to be as thin as possible to minimize total module length and thus maximize high Q^2 acceptance and average target density. The large gaps were typically 25.4 cm thick. This dimension was adjusted to give a module length of 88.90 ± 0.04 cm. A module with instrumentation is shown in Fig. 4.4. The mass of the entire spectrometer was 4.3×10^5 kg or 475 tons.

The target was restricted by trigger geometry to be the first 13 modules plus plate 0. This gave 678.3 cm or 5.34 kg/cm^2 of iron. Including scintillator, chambers, and support structures gave a total target thickness of 5.61 ± 0.01 kg/cm^2, where the error is combined uncertainty due to measurement error in the plate thickness and an estimate of uncatalogued material in the beam. This target thickness and our integrated flux of muons gave the experiment a sensitivity of nearly 1 event/femtobarn for unit acceptance.

The iron target was magnetized by 4000 amperes $\times$ 18 turns of water-cooled copper running the entire length of the MMS through slots cut in the plates. The configuration is shown in Fig. 4.5. The configuration and shape of the slots were designed to give an approximately uniform vertical magnetic field in the 107 cm wide by 179 cm high active area filling the region between the coils. The MMS was run for roughly equal durations in both field polarities to cancel any systematic left-right asymmetries in the apparatus. This cancellation was only approximate because the CCM was required by the alignment of the MMS and the location of downstream shielding always to bend the beam to the East. This meant that the low momentum tail of the beam was treated asymmetrically by the two polarities of the MMS. The benefits of field reversal were nonetheless substantial, especially because once the MMS is magnetized there can be no zero field running. The polarity was typically changed once a day.

The magnetic field was mapped and calibrated using three sets of measured information. Flux loops spanning 12 sections of each module and one large loop enclosing the entire magnet gave absolute measurements of the flux of **H** in the iron. Hall probe and flip coil measurements between plates mapped the x and y components of **B** in the air gaps. Precision measurements of iron samples removed from the coil slots gave B *vs.* H.[40] These measurements were turned into an absolutely calibrated field map for the MMS by constraining the field to agree with both the measurements (used as boundary conditions) and the Maxwell equations.[41] The field integral for an average module was 9.998×10^5 Gauss-cm for an average field of 11.25 kG (19.46 kG in the iron). The transverse momentum kick of the magnet was 0.300 GeV/c per module. The field was mapped to 0.2% and observed to be uniform to 3% in the active region of the spectrometer.

4.5 Trigger

Trigger hodoscopes of 12 scintillation counters were located after each even numbered module starting with module 4. There were eight trigger banks in all, separated by 102.8 cm of iron. Figure 4.6 shows a trigger bank, along with the rest of a large-gap instrumentation package. The central section of each trigger bank was a set of six narrow staves, each 3.9 cm high and extending the width of the active area. These staves covered the beam region and were used primarily for multimuon triggering. Above and below the set of narrow staves was a single wide (15.2 cm) stave. These, along with the narrow staves, made up the beam veto for the deep inelastic scattering trigger. The regions above and below the staves were each divided vertically into two "paddles." These paddles, each 60.5 cm high by 52.7 cm wide, signaled the

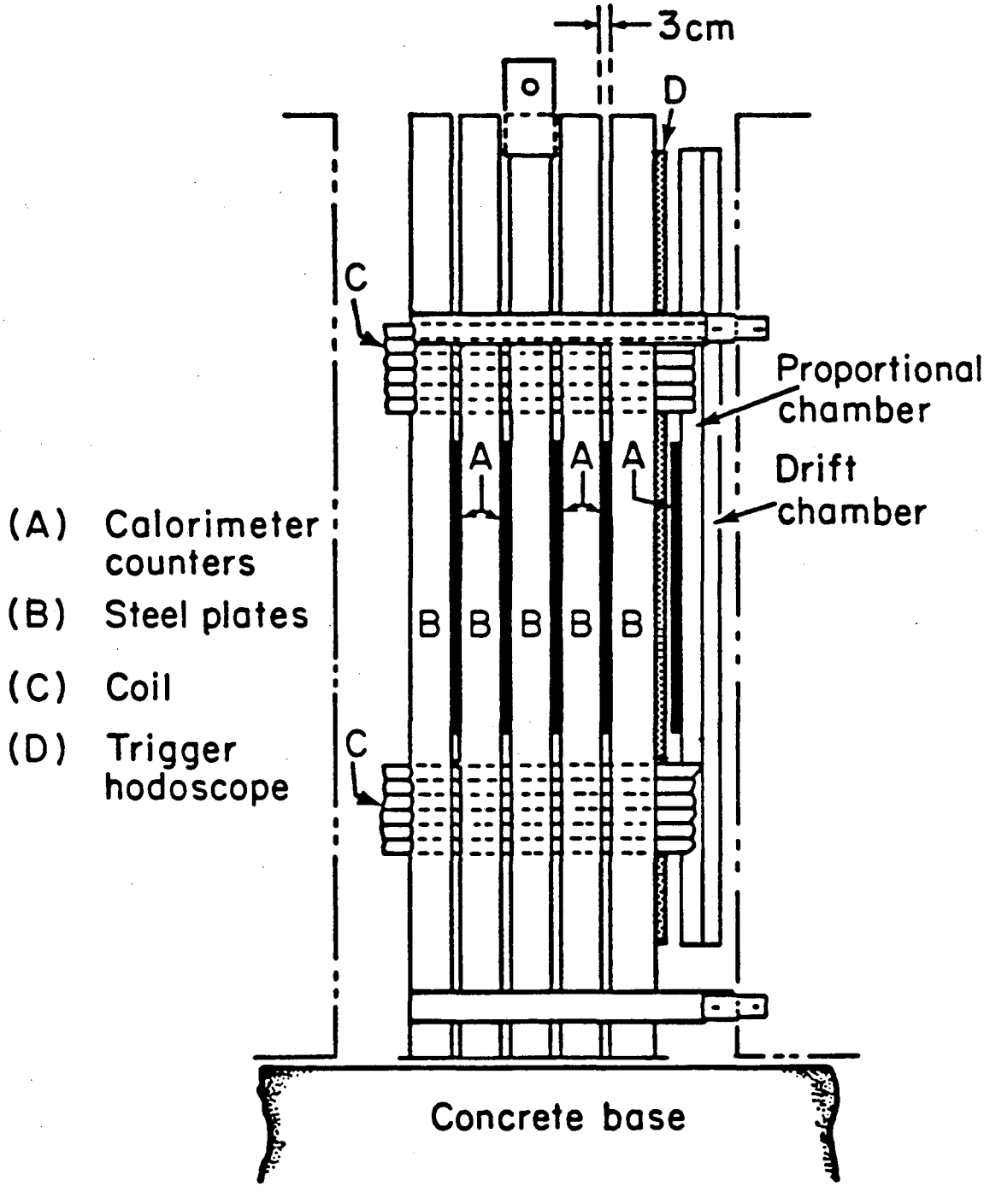

Fig. 4.4. An MMS module showing the location of the calorimeter scintillators and a large gap instrumentation package including a trigger hodoscope, a proportional chamber, and a drift chamber.

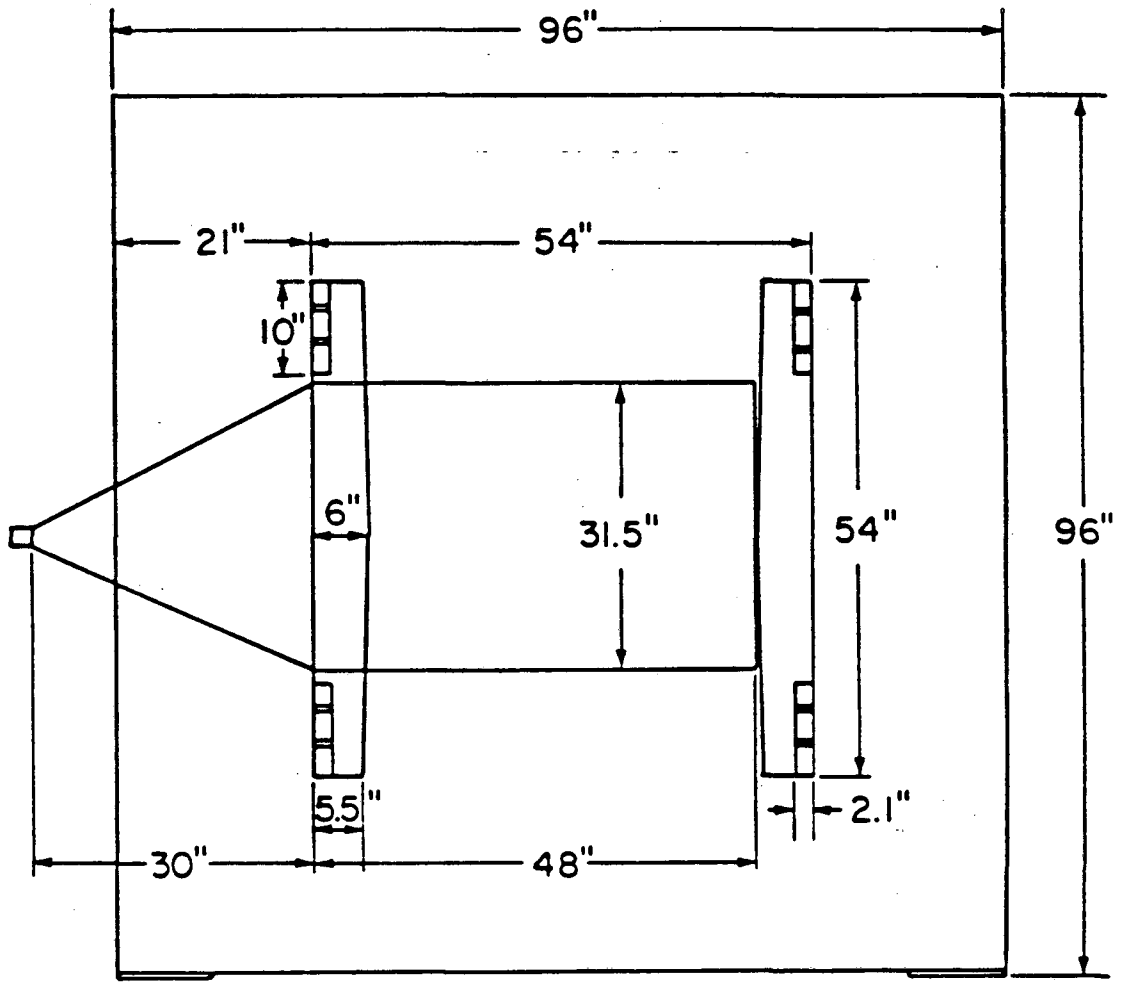

Fig. 4.5. The layout of coil slots and coils in a single iron plate. Also shown is a calorimeter counter.

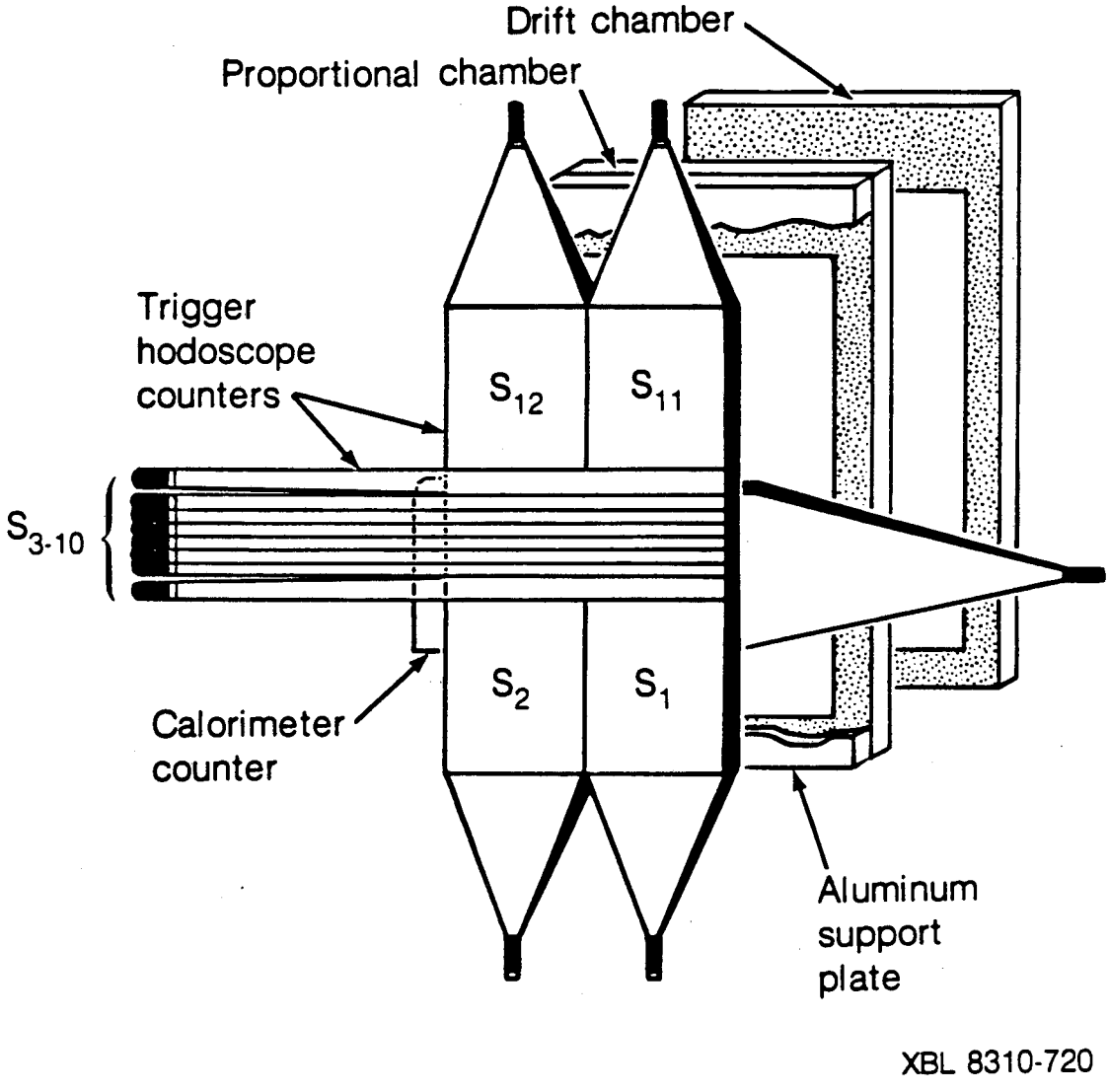

Fig. 4.6. A large gap instrumentation package. Trigger hodoscopes were located in even numbered gaps only, starting with module 4.

presence of a scattered muon. The deep inelastic trigger required a signal from any paddle and no signal in the beam veto (staves) in each of three or more consecutive trigger banks. There was no requirement made on hadronic energy deposition. The eight trigger banks made up six overlapping subtriggers of three banks each. These operated independently and a signal from any of them in coincidence with a BV signal from the beam logic (Eq. 4.1) created a full trigger signal which initiated the readout of the spectrometer information and the recording of an event. Along with chamber and calorimeter information, the logical status of each trigger and beam counter and each subtrigger were recorded. The trigger rate for the deep inelastic trigger was 3×10^{-6} per usable beam muon.

The wide staves between the paddles and the beam region imposed a minimum vertical scattering angle requirement of 12 mr. This minimum could only be reached by a scatter in module 1 triggering the last subtrigger. Moving the interaction vertex downstream increased the minimum accepted scattering angle. The acceptance of the MMS in Q^2, x, and E', averaged over the length of the spectrometer, is shown for beam energies of 93 and 215 GeV in Fig. 4.7. Since the cross section goes to infinity and the acceptance goes to zero as $Q^2 \rightarrow 0$ the absolute value of the acceptance for a kinematic region that includes very low Q^2 is arbitrary. The plots assume $v > 0.015$, or $Q^2 > 2.5, 5.9$ GeV$^2/c^2$ for the two beam energies. Figure 4.8 shows the acceptance in the Q^2-x plane. Finally, Fig. 4.9 shows the acceptance as a function of vertex z location for several ranges of Q^2. All of these results are from the Monte Carlo simulation discussed in Chap. 8.

The deep inelastic trigger was relatively free from background. The primary source of non-physics background, that is, triggers not involving an actual scattered muon, was a stopping or decaying beam muon (to give a BV signal, yet avoid the beam-vetoing staves) in coincidence with a halo muon, lobbed over or under the halo veto and entering the MMS from the top or bottom, directly into the paddles. The chief source of this component of the halo was believed to be otherwise harmless halo muons deflected back toward the beam by the return yoke of the Chicago Cyclotron Magnet. Approximately 1.6% of the triggers were from this source. They were easily eliminated in analysis by the failure of the beam and "scattered" tracks to meet at a consistent vertex.

During the data analysis, we discovered that some of the paddle counters were quite inefficient. Worse, the inefficiency was spatially non-uniform. Since the x and y positions of a track at the back of the MMS translate quite directly into E' and θ due to the Cartesian geometry of the spectrometer, this position dependent efficiency was a disaster. Fortunately, the redundant nature of the trigger with its overlapping subtriggers, allowed us to use the data to completely map the trigger efficiency. This crucial saga is related in Sec. 7.5. The stave counters were measured to be $> 99\%$ efficient.

4.6 Proportional and drift chambers

Muon trajectories in the MMS were determined from positions measured after every module in packages containing three multiwire proportional chamber (PC) planes and one drift chamber (DC) plane (see Figs. 4.1,4, and 6). There were 19 such packages, including one following plate 0, and the entire system contained over 14 000 channels. The chambers covered an area 106.7 cm wide by 178.8 cm high, slightly larger than that covered by the trigger hodoscopes.

Each PC was built on a 1/2 inch aluminum jig plate kept at ground potential, which formed the entry window. Continuing in the beam direction, the jig plate was followed by a cathode plane of wires oriented at 60 degrees from vertical, an anode plane of vertical wires, a second cathode plane of horizontal wires, and a 1/16 inch aluminum window at ground. The

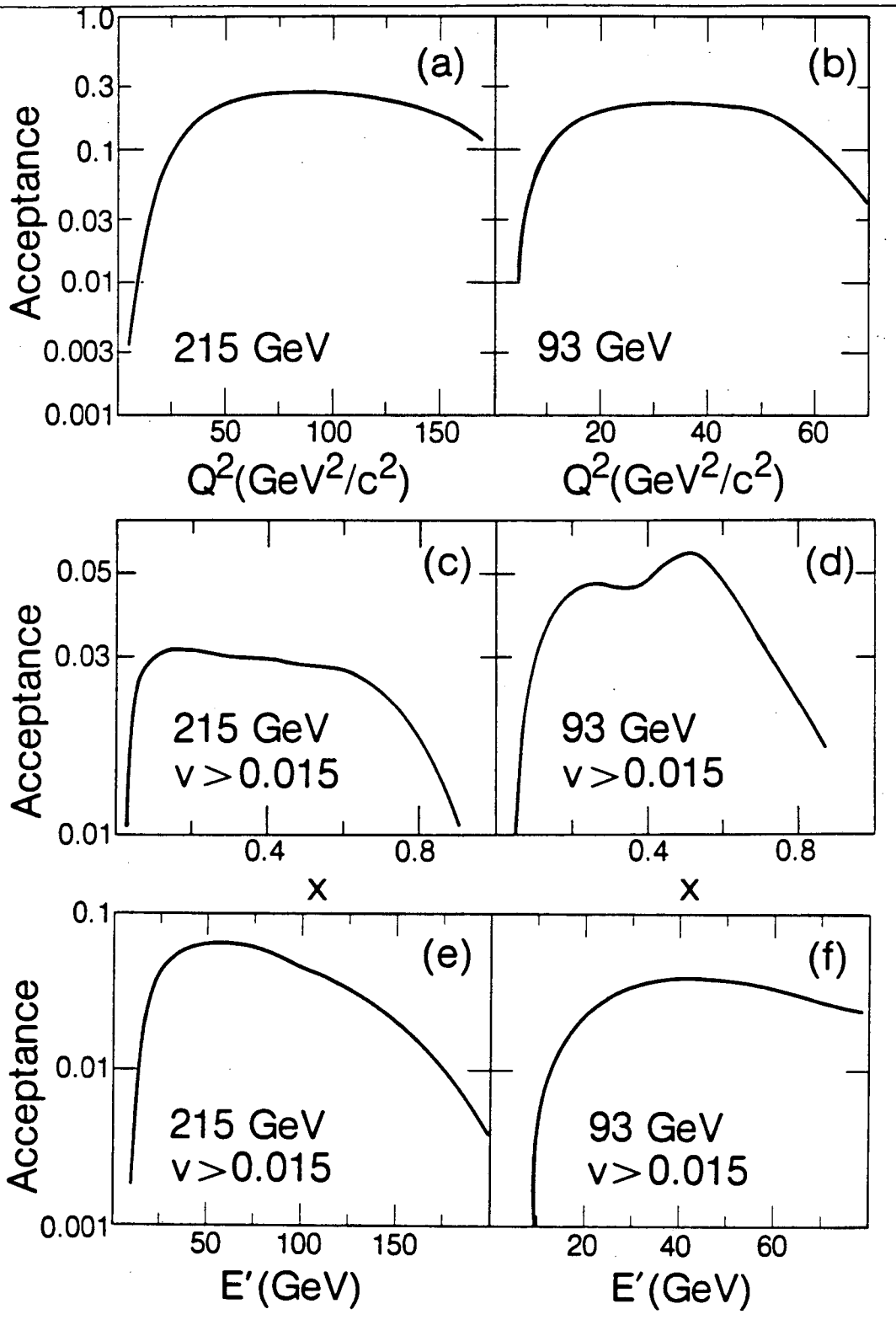

Fig. 4.7. MMS acceptance at 215 and 93 GeV *vs.* Q^2 (a, b), x (c, d), and E' (e, f).

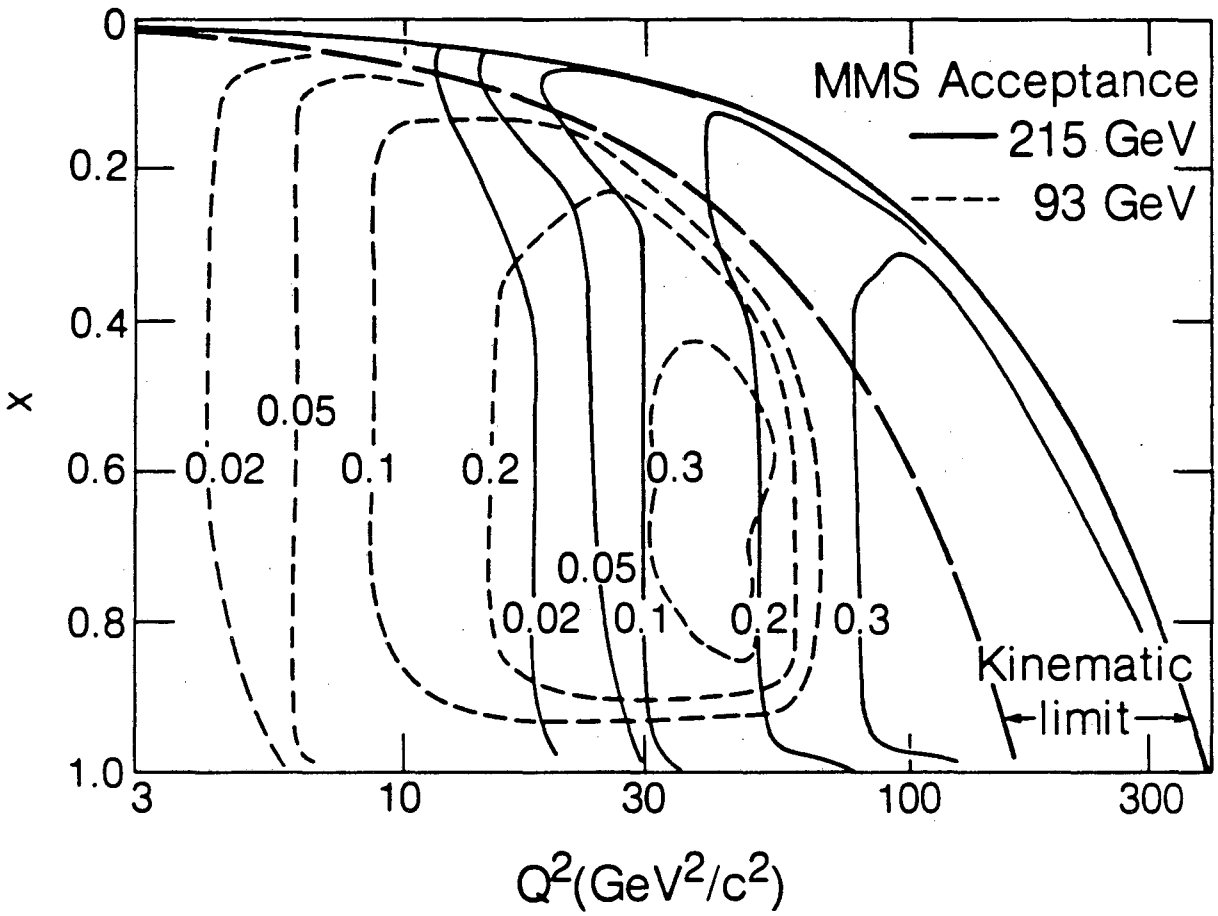

Fig. 4.8. Contours of constant MMS acceptance *vs.* Q^2 and x. The x axis origin is at the top to facilitate comparison with the $F_2(x, Q^2)$ plots of Chap. 10. Solid (dashed) contours are for a beam energy of 215 (93) Gev.

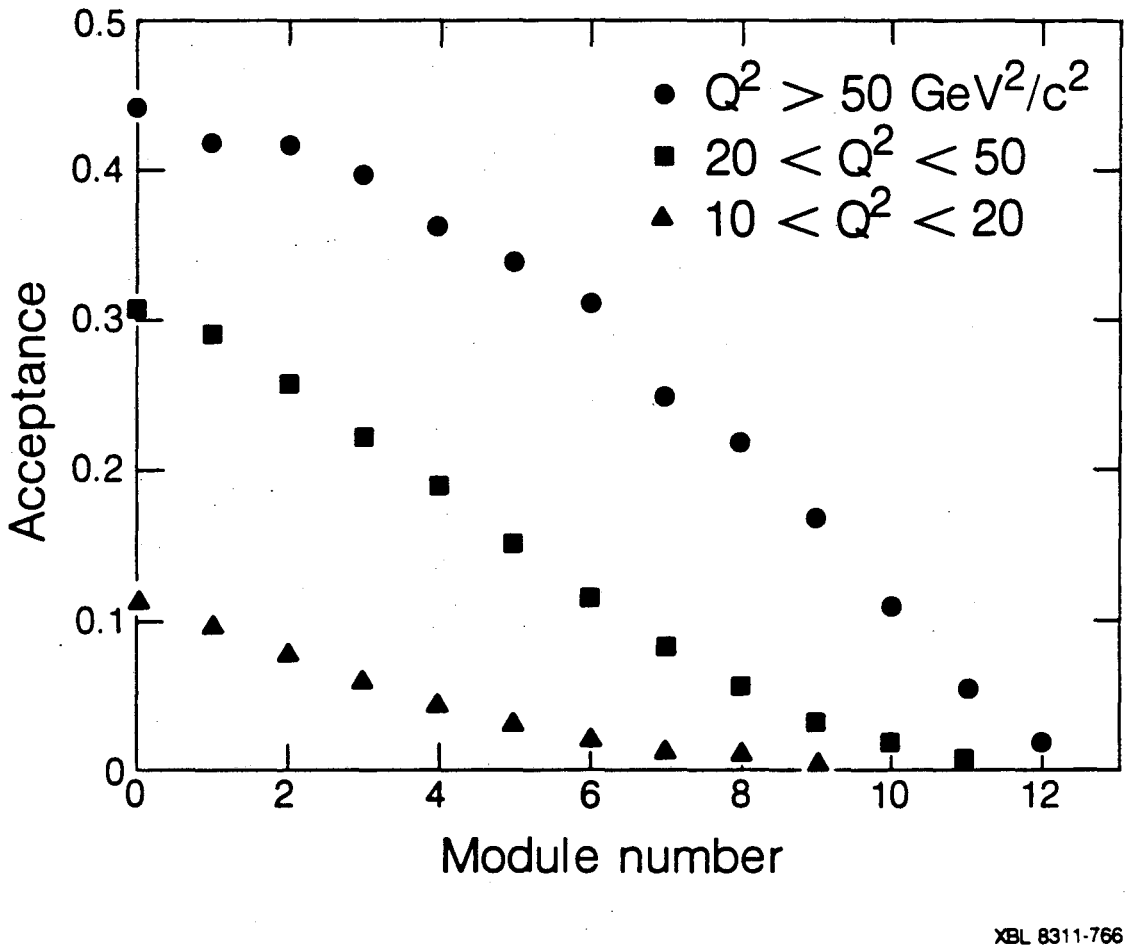

Fig. 4.9. MMS acceptance at 215 GeV *vs.* vertex location.

anode (sense) plane, measuring the x coordinate, was formed of 336 wires with 0.125 in spacing. Each wire was dc coupled to an amplifier/discriminator. The boundary between modules was defined to be at the sense plane, and the sense plane in PC 0 was defined as the origin in z. The signals induced on the cathode planes were read out to measure y and a diagonal u coordinate. The cathode wires were 0.050 inches apart and ganged together in groups of four. The broad induced signals were discriminated only after passing through a center-finding circuit (Fig. 4.10) with an output that was the second difference of the input. (Returning to our vision analogy, this is the same circuit used for pre-processing of visual signals in the retina (Fig. 4.10c).[42] It is apparently used for edge-enhancement and is generally unnoticable except in the visual illusion known as Mach bands.[43]) Although there are only half as many output channels as input channels, resolution equivalent to the input channel spacing is restored by the design, which gives signals on either one or two output channels, depending on which of the two input channels is hit (compare Figs. 4.10 a and b). There are 176 y and 192 u output channels per chamber. Further details on the PC design and construction are given by Markiewicz.[30]

The use of the induced signals allowed a thinner design than would three sense planes plus associated high voltage planes. The design also gave a distinct advantage in matching the various coordinates to give points in space. Because the signals on all three planes resulted from the single avalanche on the sense wire, the matching of the planes was independent of the angle of the initial ionizing track. This decoupled the matching process from the track finding process, an immense simplification. The u coordinate was used to resolve ambiguities in matching x with y caused by multiple tracks.

From the amplifier/discriminator cards, signals entered 60-90 m of ribbon cable to bring the signals from different chambers into synchronicity and to allow time for a trigger decision to be made. A trigger signal opened a 70 ns write gate, and chamber signals arriving during this interval were latched to await readout by the computer.

The resolution of the PC's was close to the expected $\sigma = (\text{wire spacing}/\sqrt{12})$ or 920 μm and 1500 μm for the sense and induced planes. The sense planes, which measured positions in the magnetic bending direction and thus momentum, were designed to give sufficient position resolution so that the multiple Coulomb scattering (MCS) in the 29 radiation lengths between chambers would limit momentum resolution for average length tracks at the highest momenta. The efficiency of the PC's was $> 90\%$ away from the beam. However, at our high intensities the efficiency in the beam suffered, dropping to an average of 83% and 59% at beam center for x and y, respectively. This was a greater factor in the analysis of multimuon events than in deep inelastic scattering, where the scattered muon rapidly leaves a beam region already obscured by the hadronic shower.

High momentum tracks at large angles can be shorter than average. In order to maintain MCS-limited resolution for these high Q^2 tracks, the x position measurement was augmented by following each PC with a drift chamber (DC). Each DC had 56 3/4-inch wide cells with sense wires in the center. A trigger signal initiated a string of 31 time bins during which the ionization electrons drifted to the nearest sense wire. Up to four occupied time bins could be recorded per cell. A uniform drift velocity would have meant a time bin width of 300 μm or $\sigma = 90\mu$m. In fact, the bulk of the signals arrived within 20 time bins and the velocity was not exactly uniform. This nonlinear time-distance relation was included in the analysis, and the resulting measured position resolution was better than 250 μm. The efficiency of the drift chambers was good, better than 98% in the beam area, but their (31 time bins / 120 MHz clock) meant they were active for 260 ns or 13 rf buckets. Extra beam tracks were often recorded. These were eliminated, and the left-right ambiguities in the cells were resolved, by referring to the PC system. For further discussion of the drift chamber system, see Ref. 44.

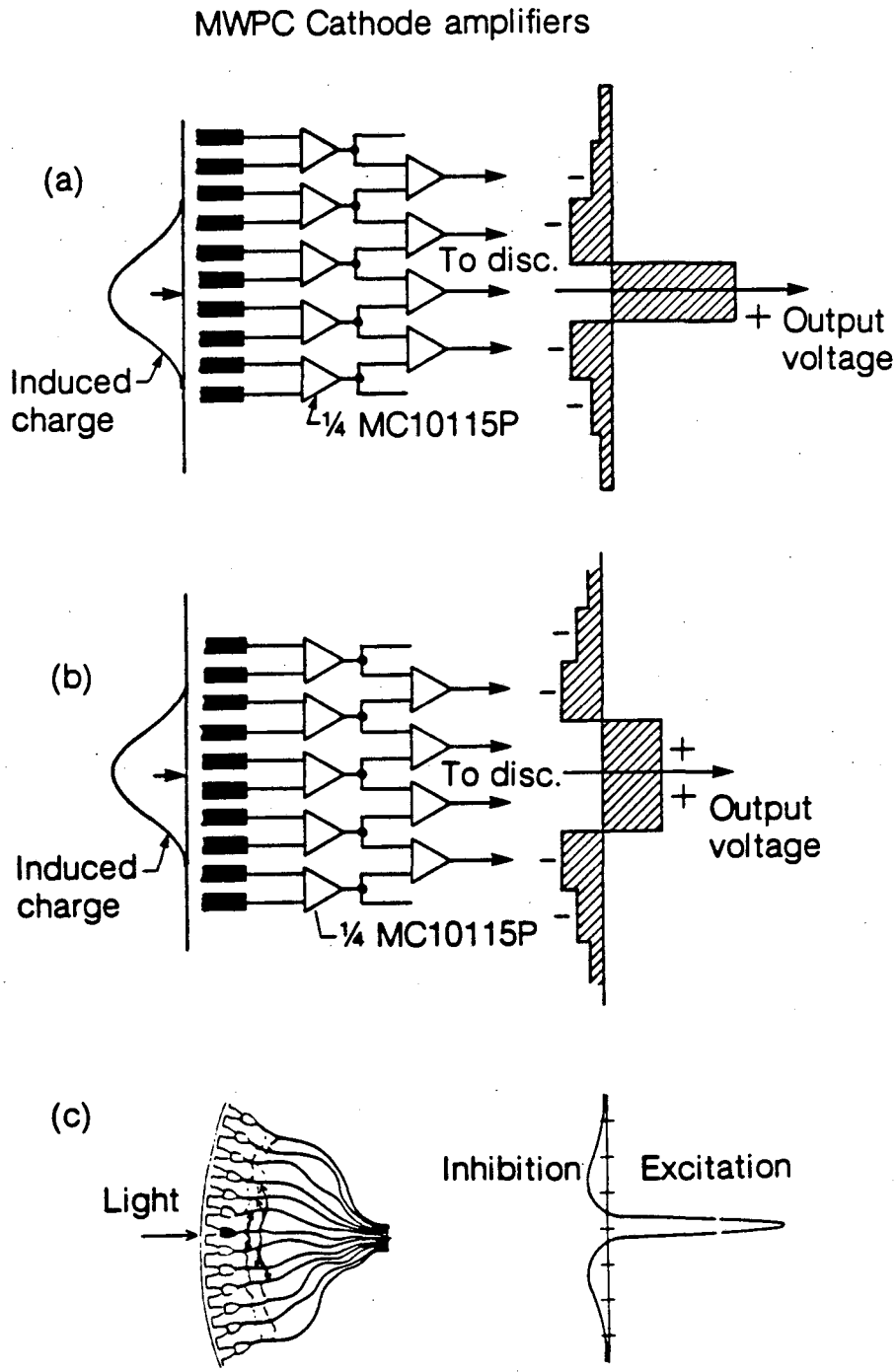

Fig. 4.10. Proportional chamber induced signal readout. The center of the broad input signal is found before a threshold is applied. Although there are only half as many output as input channels, full input resolution is restored by distinguishing between one (a) and two (b) output channels above threshold. (c) Similar circuitry in the eye of the horseshoe crab *Limulus* (from Ref. 42.).

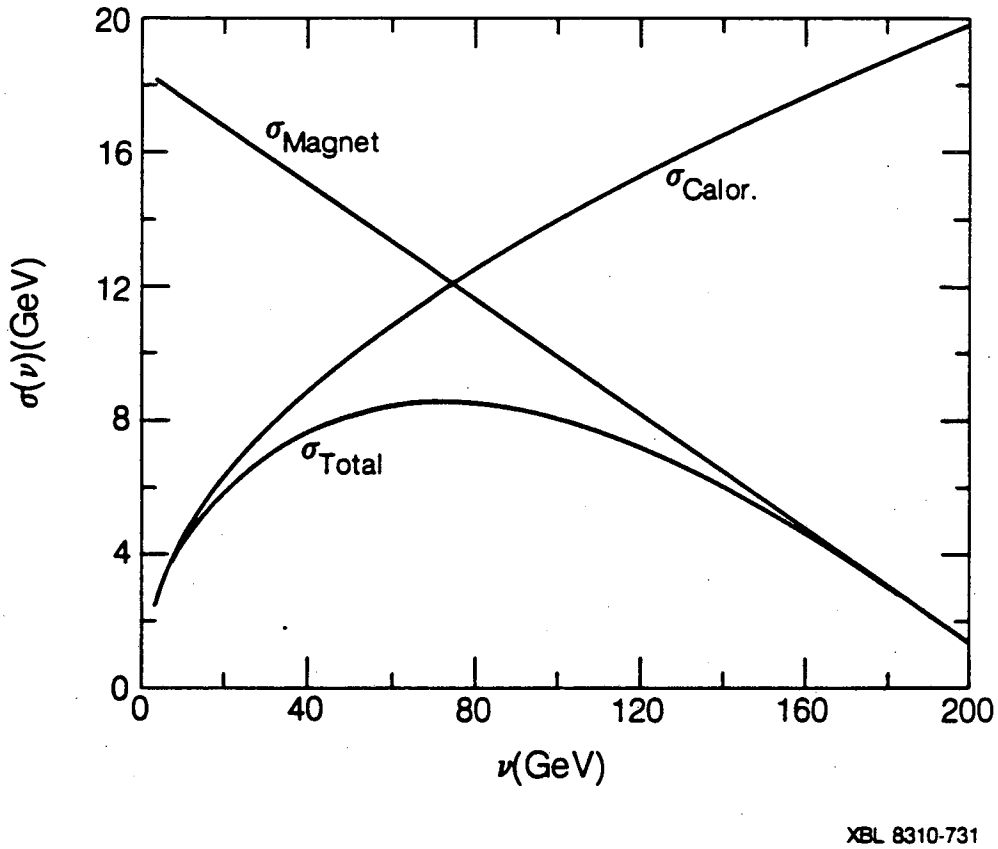

Fig. 4.11. Calorimeter and magnetic resolution in ν showing the improvement possible at low ν using the direct calorimetric measurement.

The average momentum resolution for deep inelastic scattering events in the MMS was $\sigma_{p'}/p' = 8.6\%$ at a beam energy of 215 GeV and 9.0% at 93 GeV. The average resolution is worse at the lower energy because the tracks are typically shorter.

4.7 Calorimeter

Although the kinematics of an inclusive deep inelastic scattering event can be determined entirely from the initial and final 4-momenta of the scattered muon (Eq. 2.1), there are experimental advantages in measuring $\nu = E - E'$ directly by measuring the energy of the hadronic final state. This we do calorimetrically by sampling the hadronic shower between the 10.28 cm iron plates in plastic scintillator. This is useful because, at low ν, $E' = E - \nu$ with E from the beam system and ν from the calorimeter gives better resolution than the magnetic determination of E'. The energy resolution of the calorimeter is $\sigma_\nu \approx 1.4\sqrt{\nu(\text{GeV})}$. Neglecting the beam momentum resolution, the magnetic and calorimetric resolution of E' are equal when

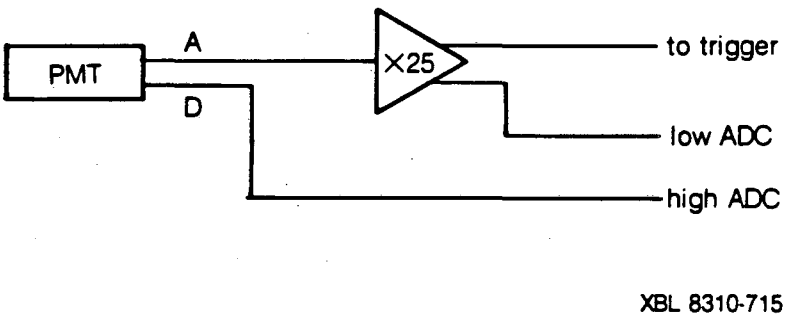

Fig. 4.12. Calorimeter counter readout. The signals on both the anode (A) and the last dynode (D) of the photomultiplier tube (PMT) are read out to give two overlapping scales.

$1.4\sqrt{E-E'} = 0.086E'$ at a beam energy of 215 GeV. The calorimeter thus gives better E' resolution for $E' > 140$ GeV or $\nu < 75$ GeV (see Fig. 4.11).

Calorimeter counters were placed to cover the beam area after each of the first 75 plates, not including plate 0. A counter is shown in place in Fig. 4.5. The scintillation light was detected and the resulting signal amplified at one end of each counter by an RCA 6655 photomultiplier tube. The triangular light guides were made of ultraviolet absorbing (UVA) lucite to absorb short wavelength light from the near end of the counter. Short wavelength light has a short attenuation length in the scintillator and cannot reach the phototube from the far end of the counter. The UVA light guide thus makes the response of the counter more spatially uniform. Overall uniformity was achieved by inserting the counters from alternate sides of the spectrometer. The read-out scheme for one counter is shown in Fig. 4.12. The anode signal is amplified $\times 25$ and sent both to a discriminator for use in the two-muon trigger and to a 1024 count analog-to-digital converter (ADC) for pulse measurement. For larger pulses, the ac signal on the last dynode (about 0.6 $\times$ the anode signal) was read directly by a second ADC. The amplified-anode and dynode ADC's (LRS 2249's) were known as the low- and high-ADC's, respectively.

The calorimeter works by sampling the shower produced when the primary hadrons from the event vertex interact in the iron between the counters. A typical shower reaches a maximum in the first or second plate following the vertex and extends 5-15 plates, with the mean length depending logarithmically on the shower energy. The individual counters and the calorimeter as a whole were calibrated in terms of "equivalent particles" (EP), the most probable pulse height produced in one counter by a minimum ionizing particle. This, rather than the mean, is used because the most probable pulse height is independent of the energy of the particle at large energies.[45] Our source of minimum ionizing particles is, of course, the muon beam. A

single muon gives a most probable signal in each low ADC of about 20 counts. The low ADC thus saturates at $\approx$50 EP, corresponding to the maximum of a 30 GeV shower. The high ADC saturates at $\approx$2000 EP. The analysis of the calorimeter signal is described in Sec. 6.4. Calibration is discussed in Sec. 7.3.

Chapter 5

Data Taking and Data Sets

"Dress warm," said the mother, who seemed to know.
Joseph Heller, *Catch 22*

5.1 Operation of the MMS

The operation of the MMS was synchronized with the beam cycle through timing signals sent by the accelerator control system. Immediately prior to the one second beam spill, the on-line computer sent out test pulses and then generated a trigger to record the resulting MMS signals as in a normal event. During a test event, chamber planes were pulsed and, on alternate spills, either a pedestal level or the response to an LED flash was measured for each calorimeter counter.

During the spill, control of the experiment was handed back and forth between trigger and computer. The more complicated multimuon triggers, notably the dimuon trigger which required input from the calorimeter, necessitated a two-level structure of pretrigger and full trigger. For the deep inelastic trigger, pre- and full trigger were identical. An event which satisfied the deep inelastic trigger generated a pretrigger signal which initiated the latching of chamber information and the digitization of calorimeter pulses and started the drift chamber clock. The pretrigger signal also inhibited further pretriggers for 3 μsec. If during that time no confirming full trigger signal arrived, digitization was aborted and the latches cleared. For deep inelastic events, a full trigger always arrived. This signal blocked further triggers for 300 μsec and informed the computer that there was an event to record. At this point, the computer took over, ignoring triggers until it was through reading out the chamber systems, the ADC's and the trigger latches ($\approx$ 1 msec). At full intensity, typically 50 events were recorded per spill of which four were deep inelastic triggers. Total deadtime was under 10%. Events were stored in computer memory during the spill, then written to tape between spills.

The beam flux was recorded by simply counting BV signals with a computer-read scaler gated by the same signal as the trigger. It was intended that this scaler would provide the normalization for all absolute measurements. Unfortunately, several supposedly redundant counts of the flux were found to be at variance at a level of several per cent. This was traced to an unexpected operating mode of one of the 1000 logic elements used in the trigger and meant that the BV scaler did not accurately reflect the livetime of the triggers. Fortunately, there was one count of BV that did identically match the trigger livetime. This was the prescaled BV trigger mentioned in Sec. 4.3. When multiplied by the known prescale value, the number of recorded BV

triggers, which was typically about the same as the number of deep inelastic triggers, provided the beam flux normalization for the experiment.

The rigors of handling and writing to tape 50 events per spill strained the capabilities of our PDP-15 computer to the extent that only minimal on-line analysis was possible. This was restricted to histogramming raw information from the MMS to check that various components were operating. A somewhat more detailed diagnostic package was run on randomly selected data tapes several times daily, but we had very little ability to analyze events until after the data taking was completed. This was a severe disadvantage, as was brought home in the late discovery of the trigger counter inefficiency and other problems.

5.2 Chronology

This experiment was originally advanced in a series of proposals submitted between March 1973 and December 1974. All proposed using roughly the same apparatus for measurements of rare muon-induced processes with one or more muons in the final state. These were combined into a single experiment with the various processes triggered in parallel and Fermilab Experiment 203/391 was approved in March 1975.

Magnet construction began in Spring 1977. After a period devoted to magnetic measurements, instrumentation of the MMS began at the end of the summer. As installation progressed, low intensity muon running was used to tune up the trigger. Data taking began on 20 January 1978 with all subsystems fully operational by 16 March (after a two week shutdown during a coal strike). Muon running continued until 9 May 1978. During this time 1239 magnetic tapes were written. A typical tape contained one run of approximately 13 000 events, about 1200 of which were deep inelastic triggers. Major analysis began in the summer of 1978 and concluded with production running early in 1980 of the final versions of the track finding and momentum fitting programs on all analyzable data. Results of the multimuon analysis were published first.[46—49] The analysis reported here represents the end of Experiment 203/391.

5.3 Data sets

The deep inelastic scattering analysis used a somewhat restricted data sample, corresponding to about 70% of the analyzable data. Of concern was our ability to simulate and make corrections for data with marginal analyzability or resolution. Runs previously deemed usable were rejected due to various forms of hardware failure, primarily in two classes. The first included data taken without drift chambers. The drift chambers contributed to the resolution of the MMS not only through their superior spatial resolution, but also by filling gaps in tracks due to PC inefficiency. The second class of rejected data included runs where the E98 beam chambers (Fig. 4.3) were operating poorly. The frequent failure of the beam chambers B1 and B2 in front of the MMS made the use of the E98 chambers crucial. Although it was often possible to identify a hit in MMS chamber 0 with the beam track, this was not sufficient to provide an independent measurement of the beam momentum in the CCM unless multiple scattering in the material downstream of the CCM was ignored. The use of measured beam tracks as the parent beam distribution for our simulation required confidence that the measured parameters of reconstructed beam tracks were negligibly different from the true values. For this reason, in the runs retained for analysis, we eliminated events where the beam track was missing more than one of the possible four x hits in the E98 chambers (a 10% loss) or for which no beam track could be reconstructed at all (8%). Events of the latter type were mostly background, with an off-axis muon entering the MMS.

Table 5-I. Data sets. Columns (d)-(g) refer to events with reconstructable beam tracks.

(a) Beam	(b) $<E>$ (GeV)	(c) Intensity (μ/spill)	(d) Incident μ	(e) Triggers	(f) Track found	(g) Event fit
215 GeV μ^+	209.	3.0×10^6	1.91×10^{11}	560 872	555 346	531 781
215 GeV μ^-	209.	1.0×10^6	2.61×10^{10}	58 365	58 110	56 615
215 GeV tot	209.	—	2.17×10^{11}	619 237	613 456	588 396
93 GeV μ^+	88.0	2.5×10^6	8.75×10^9	66 533	65 740	61 794

The data sets comprising events with good beam tracks as defined in the previous paragraph are summarized in Table 5-I. At 215 GeV, for both μ^+ and μ^-, roughly equal amounts of data were taken with each MMS magnet polarity. At 93 GeV, bending the muons to the west in the MMS was prohibited by radiation-safety considerations and all data were taken with the east-bending magnet polarity. Column (b) shows the average energy of beam muons at the interaction vertex. It differs from the nominal beam energy by the average energy loss (1.35 GeV/module at 215 GeV) suffered by beam muons in the MMS before scattering. Column (c) is the total number of muons penetrating the MMS in the beam area during a spill. Columns (d) and (e) are the totals of incident and scattered muons used in this analysis. Columns (f) and (g) show the fates of these events up to the beginning of physics analysis and will be discussed in the next chapter.

Chapter 6

Event Reconstruction

6.1 Overview

Reconstruction takes the events observed in the MMS from raw, hardware-produced signals (wire numbers, pulse heights, *etc.*) recorded on magnetic tape to measured kinematics. This procedure has two major phases: track finding and momentum fitting. In both phases, for reasons that seemed good at the time, an effort was made to treat all types of triggers identically. Track finding was optimized using trimuon events with the expectation that these would be the most challenging for the programs. As an unfortunate side effect, we did not capitalize upon the simplicity of the deep inelastic events, and their analysis was not what it might have been. In any case, the track finding program was quite successful, as can be seen in columns (e) and (f) of Table 5-I.

Event reconstruction proceeds along the following path:

- Track finding begins with a preliminary vertex z position which is found by using calorimeter information to locate the beginning of the hadronic shower.
- The beam track is reconstructed.

  Hits in the beam chambers are used to determine the beam track trajectory and momentum.

  The beam track is then projected into the MMS and PC hits are added. This continues until the preliminary vertex is reached.
- Scattered tracks are reconstructed.

  Starting from the back of the spectrometer, combinations of hits in three chambers are tried until one that gives a sensible momentum and direction is found.

  The candidate track is extended a module at a time. After each added hit, a new trajectory and momentum are calculated to project into the next module. This procedure is continued until no hit can be added or the vertex is reached.

  New track candidates are tried until all starting combinations up to the vertex are exhausted.

  Drift chamber hits are added to each successfully found track.

- Event fitting starts with a more sophisticated momentum fit of each track, using drift chamber hits when available.
- The x, y, and z positions of the vertex are determined.
- All tracks are re-fit, this time with all tracks constrained to meet at the common vertex.
- Using information from the calorimeter counters near the vertex, the hadronic energy is calculated.
- The calorimeter measurement of ν is used to refine the magnetic determination of E'.
- Kinematic quantities such as Q^2, θ, and x are calculated.

In the following sections of this chapter, these steps are discussed in more detail. A final section deals with the performance of these routines on our data sample. A discussion of the calibration and alignment procedures necessary to the analysis is deferred until the next chapter.

6.2 Track finding

Track finding was the most difficult part of the analysis of the experiment. The simple geometry of the MMS makes it quite easy for the human eye to identify tracks. Our task was to automate this procedure to handle the more than 15 million events recorded during the experiment. Unfortunately, pattern recognition is one of the areas where the combination of eye and brain can be vastly superior to machine computation. The track finding task was complicated further by several factors, some inherent to the distributed-target design of the MMS and some due to imperfections in the instrumentation. In the MMS, muons travel in nearly solid iron. We must therefore allow for substantial multiple Coulomb scattering and energy loss between position measurements. The energy loss distribution has a tail which extends all the way up to the muon energy. In more than 20% of our single-muon events either the beam or scattered track suffered an energy loss of over 5 GeV in a single plate. This energy appeared as an electromagnetic shower, fouling the calorimeter and chambers. Delta rays which escape into a chamber without showering can degrade track-finding by giving signals on wires adjacent to the one hit by the muon. These complications are compounded by instrumental effects, primarily the livetime and inefficiency of the proportional chambers. The 70 ns PC write window extended beyond the ± 1 rf-bucket beam veto. This permitted the recording of out-of-time "ghost tracks," $\approx$20% of which showered.

The inefficiency was a more serious problem. To allow for missing hits, it was necessary to allow projection through more than one module in extending a candidate track. The momentum uncertainty (initially very large) and multiple Coulomb scattering then demanded large search windows, increasing the probability of picking an incorrect hit to add to the track. Inclusion of a nearby wrong hit was often sufficient to derail the extension of the track. Figure 8.9a shows a typical deep inelastic scattering event. Although its overall pattern is unambiguous, there is clearly a fair amount of electromagnetic hash obscuring the tracks.

The track finding algorithm was basically a brute force trying of combinations of hits. Cleverness and endless testing were applied primarily toward reducing the number of available combinations. During the testing, a tremendous number of decisions of no general interest, but of crucial importance to the track finder, had to be made. Such questions as how many consecutive missing chambers to allow in a track had to be answered empirically. Our solutions to these questions are described in Ref. 38. For completeness, I will describe the general operation of the

track finder and discuss its limitations, which were most apparent in the attempt to measure precisely the low-background deep inelastic signal.

The first step in track finding was to convert the raw list of hit wires into spatial coordinates. To do this, hits on adjacent wires due to, say, a muon plus a δ-ray or small shower were first coalesced into a single hit. The position of the new hit was defined to be the center of the group of hit wires and the width set equal to the (number of hit wires) $\times$ (channel spacing). This redefinition of the width is incompatible with the output scheme of the induced electronics, which half the time gave two adjacent hits for single tracks. Although the result was to inflate mistakenly the error on some of the y positions by a factor of two, the central position was calculated correctly. Studies showed no significant degradation of angular resolution due to this problem, but the χ^2's for our fits of trajectories in the y view come out unnaturally small.

These redefined hits are then used in the matching of the independently recorded x, y, and u coordinates into "triplets," each with a unique x-y position. The poor efficiency of the PC induced planes required the retention of unmatched hits as "singlets," also available for use on tracks. Triplets, which were needed to tie the x and y views of the tracks together, were given higher priority in the reconstruction.

The search for hits to attach to beam and scattered tracks was limited along the beam direction by a preliminary vertex z position found using individual calorimeter pulse heights to locate the beginning of the hadronic shower. The determination of this vertex was begun by finding the largest single pulse height. In large hadronic showers, the mean location of the shower maximum occurs after more than 10 cm of iron. More important, hadronic showers have notorious fluctuations. It was therefore necessary to look upstream of the maximum to find the beginning of the shower. With A the maximum pulse height, a threshold of $0.08A$ was chosen empirically to define shower activity. To avoid missing the beginning of a shower with a large downward fluctuation in pulse height before the maximum and also to avoid incorporating electromagnetic splashes from the beam track into the shower, all pulse heights upstream of the maximum were compared to the threshold. The vertex was placed in the middle of the plate that maximized $N =$ (the number of pulse heights $< 0.08A$) $-$ (the number of pulse heights $> 0.08A$) upstream of the vertex. The operation of this algorithm is illustrated in Fig. 6.1.

The most frequent failure of the calorimeter vertex finder occurred when the largest single pulse height was due to an electromagnetic shower away from the true vertex. Electromagnetic showers give more pulse height per GeV than hadronic showers. They are also shorter, and thus can have very large maxima. When the vertex finder was fooled by an electromagnetic shower, either the beam or scattered track finding was stopped short. Even if the vertex was moved to the proper location during fitting (see the next section), the event was sometimes rejected for having a large gap in the track. Approximately 0.6%(1.3%) of the 215 (93) GeV events were lost in this way.

With the calorimeter vertex dividing the event into two sections, track finding proceeded with the separate reconstruction of the beam and scattered tracks. The beam track was begun in the beam chambers upstream of the MMS. Its momentum and trajectory in x and y (including, if possible, the scattering in the lead glass) were fitted. The track was then projected to the front of the MMS and the momentum was corrected for energy loss in the lead glass and other material in the beam. From there, the beam track was extended, one module at a time, by using the track as reconstructed up to that point to predict a central position in the next proportional chamber. The position, angle, and momentum uncertainties for the track and the predicted magnitude of multiple scattering were used to open a search window. A PC hit within the window was added to the track, and this was continued until the last chamber before the vertex. Only one beam track was sought.

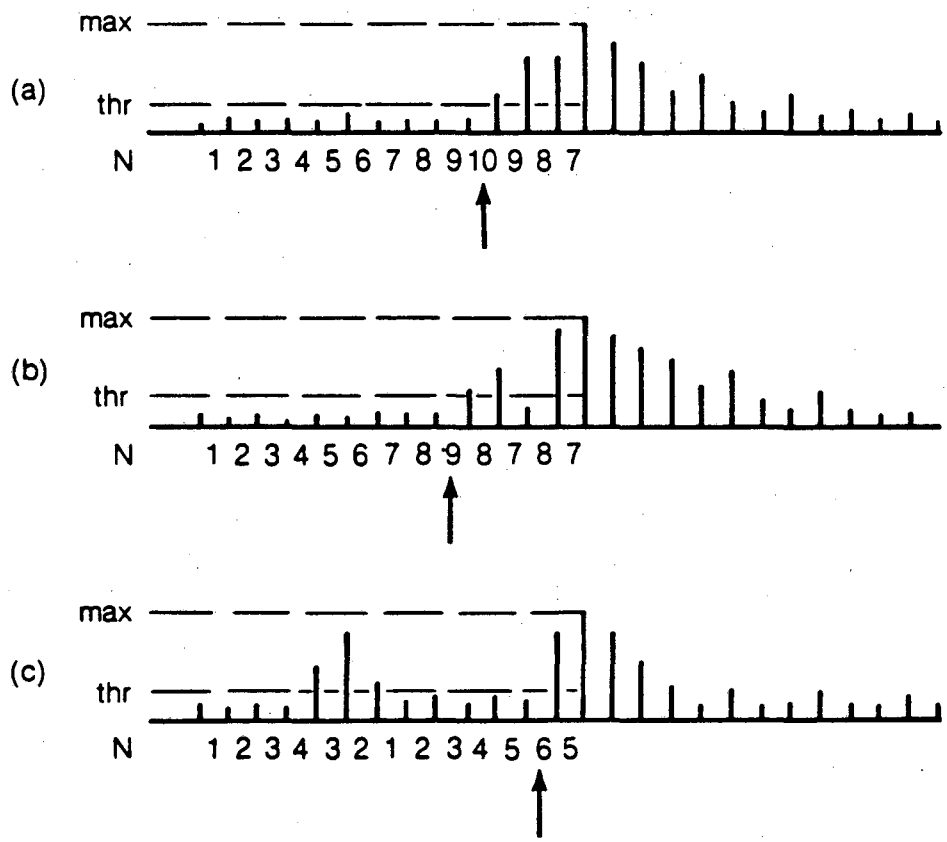

XBL 8310-717

Fig. 6.1. The calorimeter vertex-finding algorithm. The vertical bars indicate the pulse heights in individual counters. Each pulse height is compared to a threshold of 0.08 times the maximum pulse height. The result for each counter of the algorithm discussed in the text is shown as N. The vertex is assigned to the plate following the maximum of N (arrow). The point of the algorithm is to allow for fluctuations before the shower maximum (b), without including separate electromagnetic showers (c).

From the back of the spectrometer, starting combinations of three triplets or two triplets plus an unmatched x and y were investigated. One empty chamber was allowed between hits, but the combination had to meet angle and linearity requirements in y and angle and minimum momentum requirements in x. Valid starting combinations were pursued upstream module by module in the same fashion as for the beam track until the vertex was reached. The track was then projected to pick up hits downstream of the starting segment. Accepted tracks had x and y hits in at least four chambers, separated by no more than two consecutive empty chambers. At least two of the (x, y) pairs were required to be triplets. All possible starting combinations made up from hits downstream of the calorimeter vertex were investigated. All valid tracks of either charge were retained.

For all valid tracks, including the beam track, drift chamber hits were added after track finding was complete. In each drift chamber, the two hits closest to the track position were saved. These two hits could be the left-right ambiguous options of the same hit. The choice of which to use was postponed until a better fit of the trajectory could be performed.

6.3 Momentum fitting

Our momentum fitting algorithm took the measured positions of a found track and calculated the 3-momentum of the track at some reference point (usually the vertex) and a detailed trajectory of the track through the spectrometer. The calculated trajectory included the effects of magnetic deflection, energy loss, and multiple Coulomb scattering (MCS). The magnetic deflection was treated as a single transverse impulse between position measurements. It used the detailed field map produced during the MMS calibration, which included the small x component of the field. Energy loss was included as a continuous correction to the muon energy along the track. For a muon of energy E (GeV), the energy loss in MeV/(g-cm^{-2}) is

$$\frac{dE}{dx} = 1.825 + 0.0716 \ln\left(\frac{E^2}{E + 10.9}\right) + 0.0045E. \tag{6.1}$$

Besides the ionization loss, this expression includes terms due to δ-rays, bremsstrahlung, and pair production. The terms for these processes, which do not occur smoothly, represent averages integrated up to some maximum allowed energy loss. It is presumed that energy losses larger than this maximum would disrupt the track and confound the track finder, and thus would not appear within a single found track. MCS is handled by actually fitting the residual deflections between chambers after removing those due to the magnetic field.

Three variations of the fitting routine were used. These were applied to the x view of scattered tracks, the y view of scattered tracks, and either view of beam tracks. The first of these, the bending view, was the most general. For a track with N transverse position measurements $x_i \pm \sigma_i$ at z_i $(i = 1, \ldots, N)$, we define a_0, a_1, and a_2 as the x position, slope, and inverse momentum at the reference point z_0. The predicted positions ξ_i of the track are then[50]

$$\xi_i = a_0 + a_1(z_i - z_0) + \sum_{j=1}^{i-1} a_2 q_j (z_i - w_j) + \sum_{j=1}^{i-1} a_2 p_j (z_i - w_j). \tag{6.2}$$

Here the q_j are the unknown MCS $p_\perp$'s that occur at w_j between z_j and z_{j+1}, the p_j are the known magnetic deflection $p_\perp$'s, and, for demonstration purposes, energy loss has been neglected. In this expression there are N equations corresponding to the N measurements and $N+2$ (three a's and $N-1$ q's) unknowns. This distasteful situation is rectified by the constraint

that the average MCS $p_\perp$ is zero. This constraint is applied by adding $N-1$ "measurements" $q_j = 0$ with a "measurement uncertainty" equal to the expected rms value of the MCS $p_\perp$, $\delta = 15\sqrt{X}$ MeV/c, with X the path length in radiation lengths. The χ^2 of the fit is then

$$\chi^2 = \sum_{i=1}^{N} \frac{(x_i - \xi_i)^2}{\sigma_i^2} + \sum_{j=1}^{N-1} \frac{q_j^2}{\delta^2}. \tag{6.3}$$

The value of χ^2 is minimized to give the best values of the fit parameters a_0, a_1, a_2 and $q_{1,\ldots,N-1}$. For the y view of scattered tracks, a_2, the inverse momentum, was not fitted. Instead, the value from the x fit was used. For beam tracks, both the inverse momentum a_2 and the slope a_1 were fixed at the front of the spectrometer to the values determined with higher resolution in the beam system. In each fit, the routine was permitted to discard a limited number of hits if the χ^2 was poor.

Each track was fitted several times in the course of fitting an event. In the first fit, only proportional chamber hits were used. Using the initial fitted trajectory as a guide, the x view of each track was refitted, this time with the routine choosing the best hit in each chamber from the one PC and two DC hits provided by the track finder. If the track finder got confused, it was common for it to find two or more segments of a long track and call them separate tracks. To undo this damage, after the fitter had the chance to eliminate any wrong hits that might have misdirected the track finder, an attempt was made to rejoin tracks that appeared similar. Successful matches were consecrated by refitting them as one track. At this time, "ghost tracks" made of hits due to out-of-time muons were eliminated. This was done by requiring that the trigger counters, which had output pulse lengths less than the width of an rf bucket, register the passage of all fitted tracks.

The next step in event fitting was to require that all tracks intersect at a common vertex. The position of this vertex was determined by using the preliminary (calorimeter) vertex and the tracks themselves. For each outgoing track, the point of closest approach to the beam track was calculated. Tracks with too large an impact parameter were eliminated. The vertex was constructed from the remaining tracks and the calorimeter vertex by finding the z position which minimized

$$\chi^2 = \sum_i \frac{[x_i(z) - x_b(z)]^2}{\sigma_x^2} + \sum_i \frac{[y_i(z) - y_b(z)]^2}{\sigma_y^2} + \frac{(z - z_{\text{calorimeter}})^2}{\sigma^2_{\text{calorimeter}}}, \tag{6.4}$$

where i refers to outgoing tracks, b refers to the beam track, and $\sigma_{\text{calorimeter}}$ is the estimated uncertainty in $z_{\text{calorimeter}}$. If χ^2 was too large, the calorimeter vertex was ignored and, if necessary, tracks were eliminated. The x and y positions of the vertex were then the weighted averages of the positions of the surviving tracks at z_{vertex}. All tracks were then refit with the new requirement that they pass through the vertex. Tracks which could be successfully fit in this fashion were called "vertex enabled." The distribution of vertex z positions from our 215 GeV data set is shown in Fig. 6.2. Note that the large gaps between modules are easily resolved.

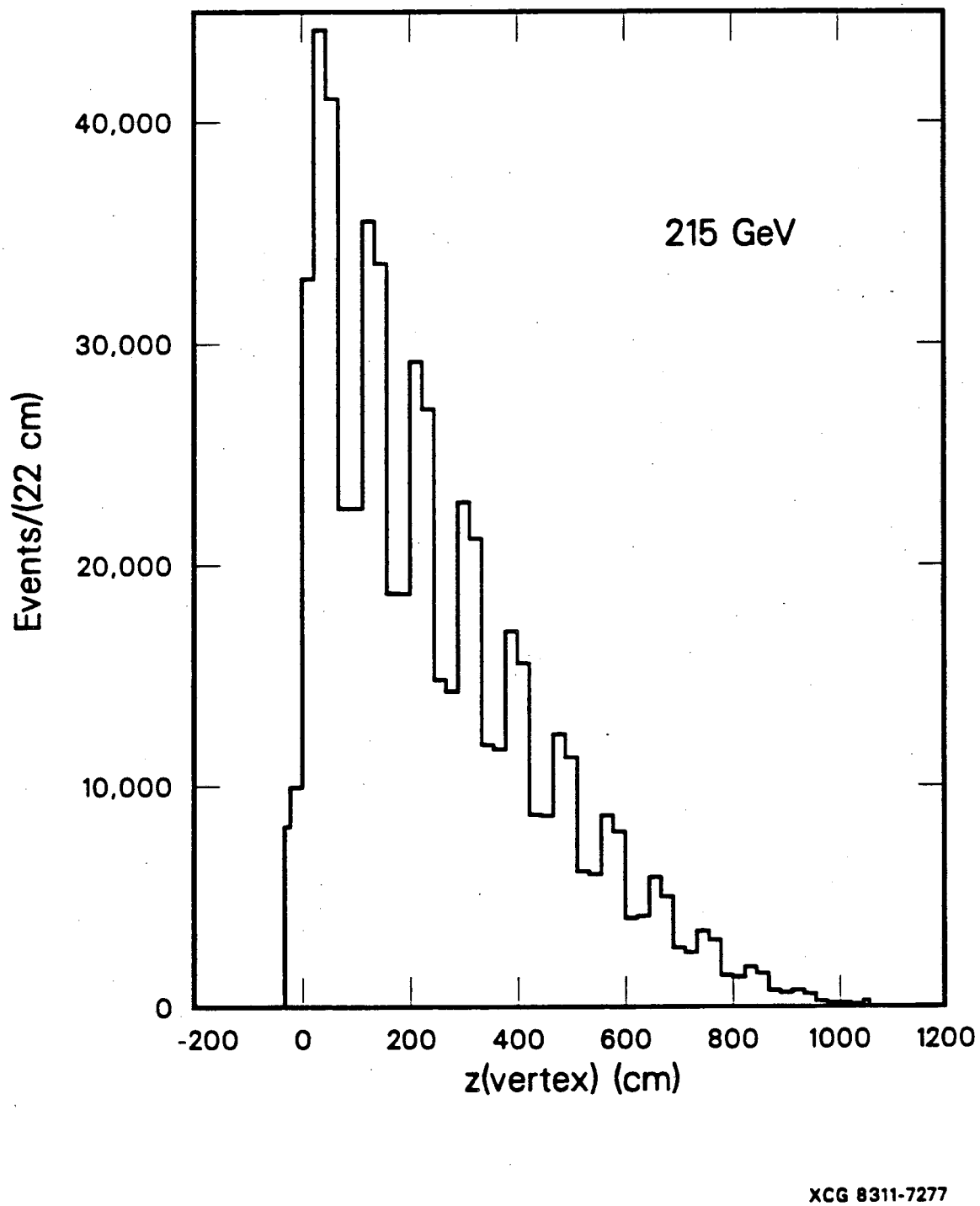

Fig. 6.2. The distribution of event vertices along the beam direction for the 215 GeV data.

6.4 Calorimetry

Once the vertex was located, the pedestal-subtracted signals (calibrated in equivalent particles, see next chapter) from calorimeter counters in the surrounding region were summed to give a direct measurement of ν, the energy of the hadronic final state. The summed region started five counters upstream of the estimated vertex position and extended to ten counters downstream of the vertex. This interval was extended if the counters at the ends showed more pulse height than expected from a single muon. In the sum, each counter signal had subtracted from it the *mean* pulse height from a single muon ($\approx$2.6 EP). This summed pulse height was turned into GeV *via* the calibration procedure described in the next chapter. The conversion was approximately 6 EP/GeV.

With ν determined independently, we could measure the missing energy of events, $E_{\rm miss} = E - E' - \nu$ (Fig. 6.3). For deep inelastic scattering events, this was due entirely to instrumental resolution. As discussed in Sec. 4.7, the otherwise redundant calorimeter information can be used to improve the E' resolution of individual tracks. The procedure assumed that the resolution on the beam energy measurement was negligible. E', previously determined from the momentum fit, was redefined to be the weighted average of the original value and $E - \nu$. The individual components of $\mathbf{p}'$ were then adjusted using the correlations determined in the momentum fit. Events with large $|E_{\rm miss}|$ were suspect. Large positive $E_{\rm miss}$ could mean that the shower was missed completely. Large negative $E_{\rm miss}$ could accompany a wide angle bremsstrahlung event with an electromagnetic shower (see Appendix A). For this reason, the calorimeter information was used only in events with $|E_{\rm miss}| < 52$ (26) GeV for the 215 (93) GeV data sets. These cuts correspond to approximately 2.5-3σ in $E_{\rm miss}$, independent of E'.

6.5 Performance

Table 5-I, columns (e), (f), and (g) summarize our success in reconstructing events. All entries refer to events with successfully reconstructed beam tracks. For the 215 (93) GeV data sets, the scattered track was found in 99.1% (98.8%) of the events. Of these events, 95.9% (94.0%) were successfully momentum- and vertex-fitted. Losses through this stage of the analysis were thus 5.0% (7.1%), of which inspection showed 1.9% (1.3%) to be background.

Momentum resolution in the MMS was limited by multiple Coulomb scattering to about 8%. The resolution for short, low momentum tracks was somewhat worse – about 10%. Using the calorimeter improved the resolution at high E' dramatically. In the 215 GeV data, the resolution for $E' > 150$ GeV without the calorimeter was $\sigma_{E'} = 0.08E'$. Using the calorimeter improved the resolution to $\sigma_{E'} = 0.05E'$. Figure 6.4 shows our resolution in Q^2 and x at various locations in the Q^2-x plane. The inner and outer bars indicate σ with and without calorimetry. The largest improvement occurs at low ν, that is, the lowest Q^2 for each value of x. This figure includes the effects of radiative corrections which, in effect, change the internal kinematics of an event without changing its appearance to the outside world. The Q^2 resolution was roughly constant at 13%. The x resolution varied between 13% and 30%.

These values for the resolution come from a program which simulates deep inelastic scattering events in the MMS. At 215 GeV, the width (σ) of the distribution of $(E'_{\rm measured} - E'_{\rm generated})/E'_{\rm generated}$ is between 0.074 and 0.083, depending on how much of the tail is included. Another estimate of the resolution comes from the momentum uncertainty calculated by the fitting routine, combined with the calorimeter resolution. For the same simulated events, the mean uncertainty is 0.077. This is a useful quantity because it can also be calculated for real events, where the result is 0.076.

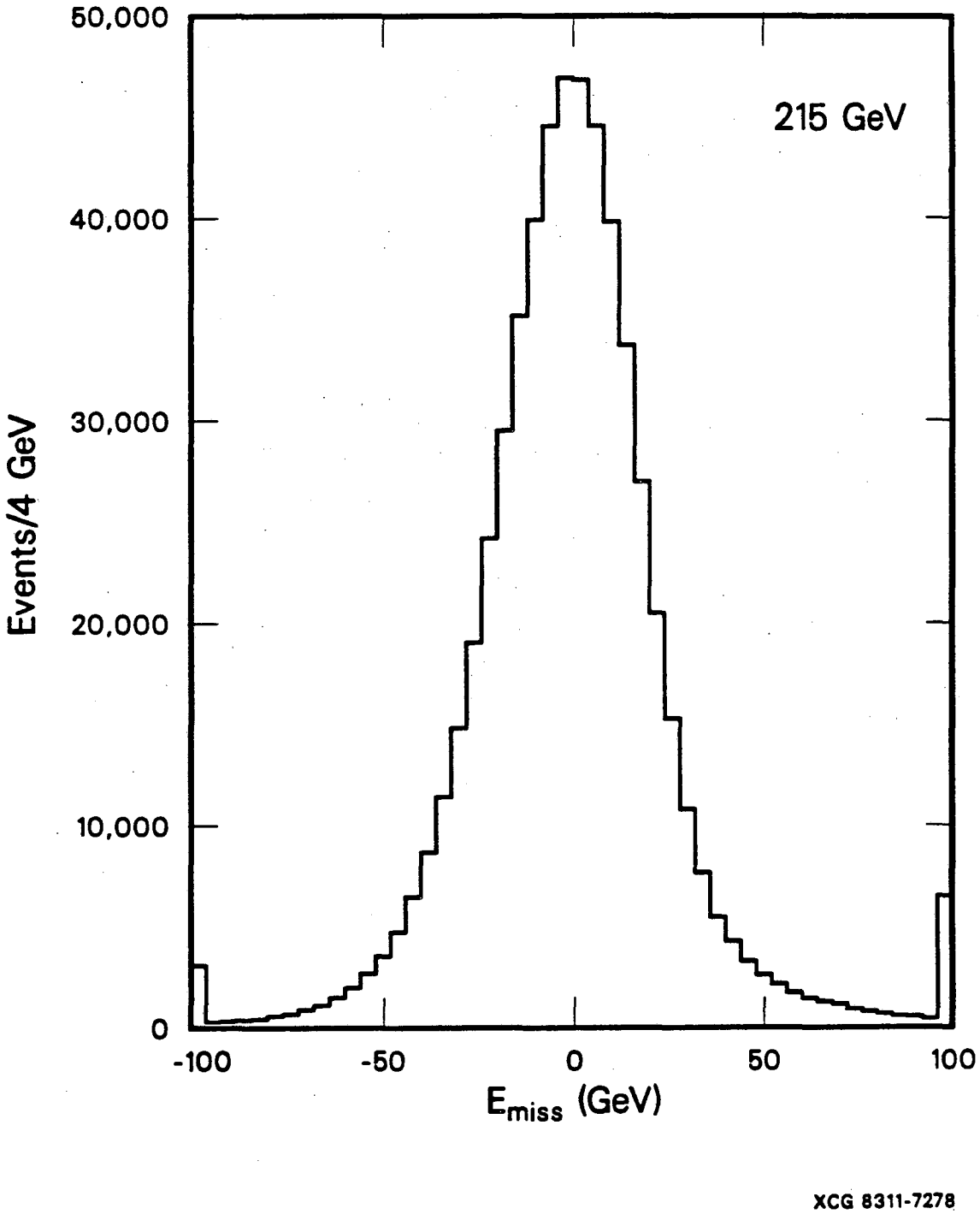

Fig. 6.3. The missing energy distribution of the 215 GeV data. The mean is calibrated to be zero, and the width ($\sigma = 21$ GeV) is consistent with our expected beam, momentum, and calorimeter resolution.

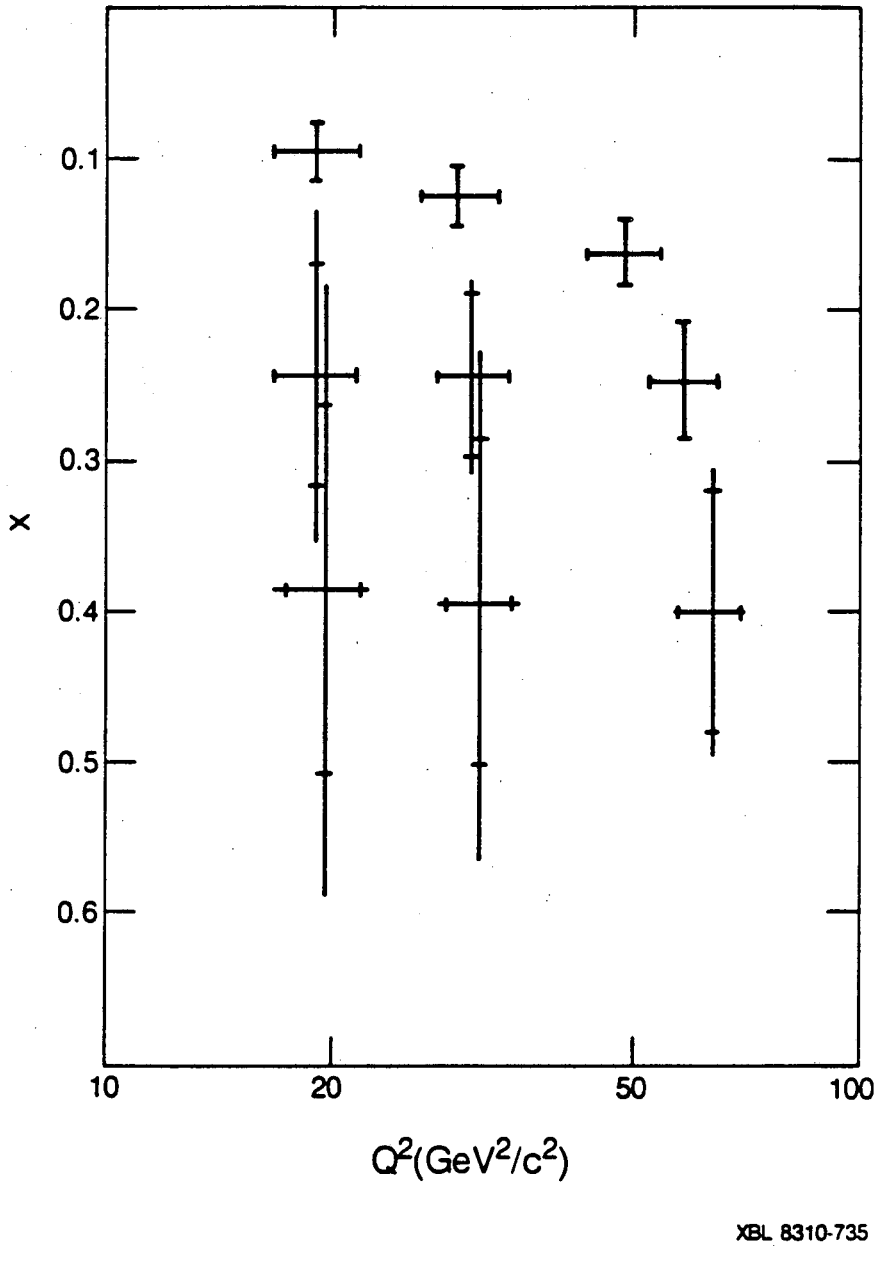

Fig. 6.4. MMS resolution in x and Q^2. The inner and outer bars indicate the resolution ($\pm\sigma$) with and without the use of the calorimeter. Note that the origin in x is at the top.

The results of the data reduction are shown in Fig. 6.5, where the measured spectra of reconstructed events in Q^2, x, and E' are plotted for both the 215 and 93 GeV data samples. The production running of the event reconstruction routines on our large amount of data was an arduous task that was performed only once on the full set of analyzable data. The effects of minor mistakes found after that point were corrected by subjecting the simulated events used in the acceptance calculation to the same errors in reconstruction.

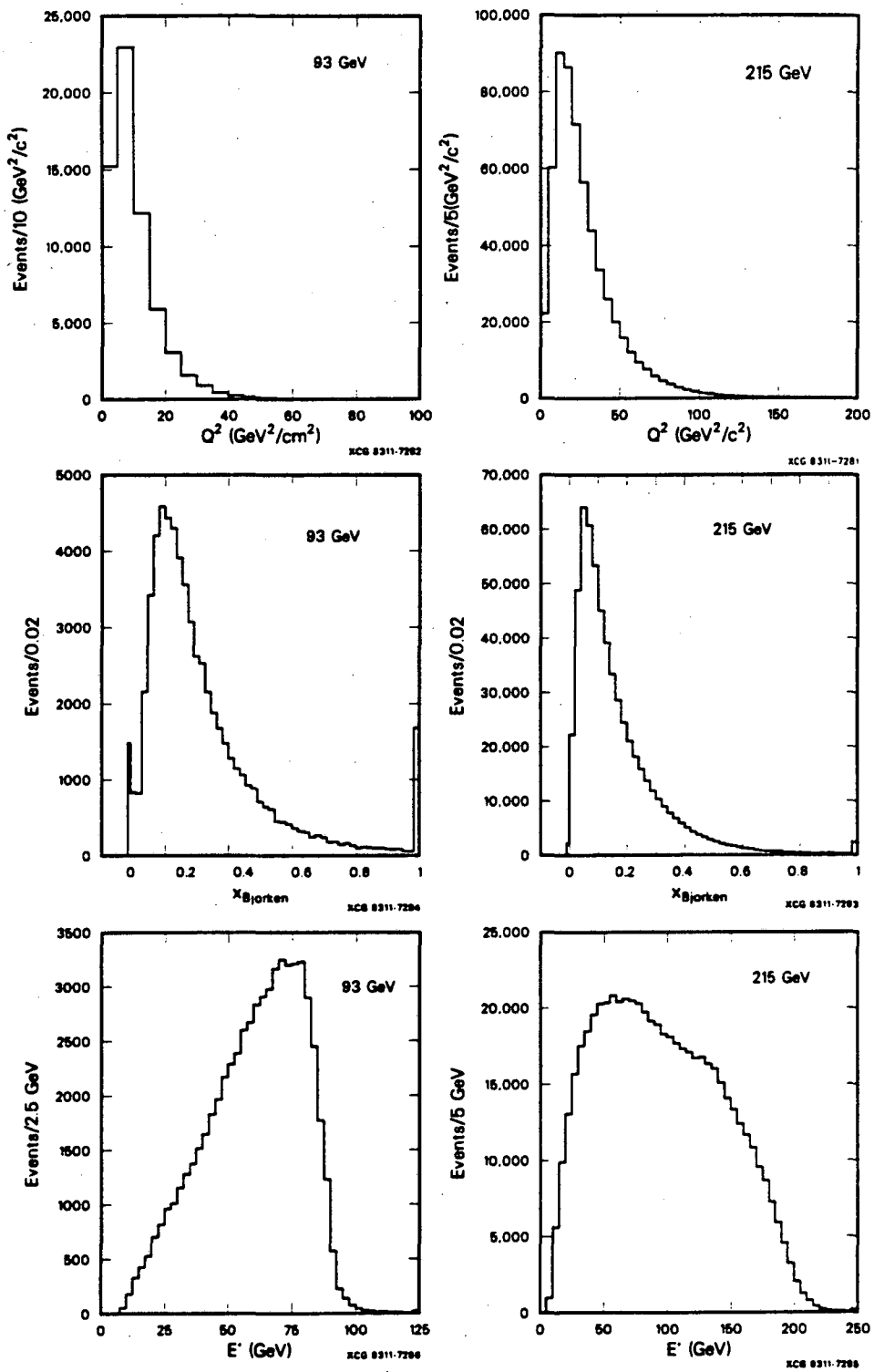

Fig. 6.5. Spectra of all reconstructed events in Q^2, x, and E'.

Chapter 7

Alignment and Calibration

In this chapter I discuss the various auxiliary measurements necessary to event reconstruction and analysis. This discussion follows that of reconstruction because of the iterative nature of most of these calculations. Although this information is used as input to the reconstruction and simulation programs, it was often derived using these same programs.

7.1 Chamber alignment

Surveying instruments were used to align both proportional and drift chambers in the MMS to an estimated 130μm accuracy. The alignment was checked and improved during data reduction by using muon trajectories from BV triggers to determine alignment constants, offsets to be added to raw coordinates in each chamber. This task was complicated by three factors: 1) the rms multiple scattering of 180μm/module at 215 GeV, 2) the large residual magnetic field ($\approx \frac{1}{2} \times$ full field), 3) the lack of confidence in the knowledge of the beam system alignment at that time. These factors meant that: 1) the average of many tracks had to be used, 2) the tracks curved (we left the magnet at full field), and 3) the momentum which determined the curvature was unknown.

The alignment procedure was to fit a large sample of tracks, ignoring the information from a single chamber. The initial position, angle, and momentum of the track were determined from the fit. The fitted position of the track at the ignored chamber was compared to the position of the hit in that chamber. An offset was then added to the chamber position to make the mean residual equal to zero. This was repeated for each chamber, and the whole procedure was iterated to produce a set of self-consistent alignment constants. The drift chambers were aligned to about 80μm accuracy for the event reconstruction. After the production running, the DC offsets were remeasured to 20μm and these locations were put into the apparatus simulation, the events from which were reconstructed with the same set of constants used on the real data.

With the position, angle, and curvature (momentum) of the tracks left free in the fit, constant systematic offsets in alignment or those that go as z or z^2 are not detectable in the residuals. The assumption used in the alignment procedure was that there were no such effects and the mean offset, angle, and curvature of the alignment constants was zero. Yet it is precisely the last of these terms that can systematically affect the momentum measurement. In fact, after the initial alignment, it was found that the average fitted momenta for east- and west-bending 215 GeV tracks differed by 1.06 GeV, indicating that a finite curvature did exist in the alignment,

corresponding to a radius of curvature of 214 miles. A quadratic correction was thus applied to the drift chamber offsets. This correction was everywhere less than 60μm.

The horizontal positions of the top and bottom of each chamber were surveyed separately. Thus the possibility that the chambers were rotated about their centers had to be investigated. A comparison of residuals for tracks scattered up and down in the MMS showed indications of random rotations at the level expected from the surveying precision. Fortunately, the effects of such rotations on the fitted momentum are negligible for deep inelastic scattering events. To produce a systematic effect on the momentum, an offset which is quadratic in z is required. A systematic rotation (due to systematic effects in the survey or to chance) that varies linearly with z will combine with the vertical scattering angle to give such an effect. If the chamber rotation is $\alpha(z) = az$, and θ is the scattering angle of a track, the chamber offset seen by the track is

$$\delta(z) = \alpha(z)y(z) = a\theta z^2. \tag{7.1}$$

This effect might manifest itself as a difference in the fitted momentum between high momentum tracks scattering up and down at large angles. High momentum is required to give the track a curvature small enough so that the chamber offset is noticeable. The kinematic limit $Q^2 \leq 2M_N\nu$ (or Bjorken $x \leq 1$) gives a maximum scattering angle that varies inversely with E'. Given our survey precision, this restricts the possible systematic effect on the momentum at 215 GeV to less than 0.1%.

7.2 Magnetic field integrals

The absolute calibration of the MMS magnet was described in Sec. 4.4. In the beam system, both the last dipole (actually three magnets labeled D4 in Fig. 4.2) and the Chicago Cyclotron Magnet (CCM) were used for the momentum measurement of beam muons and had to be calibrated. The field integrals of the D4 and CCM magnets were numerically integrated from flip coil measurements of the field along the path of the beam. At 215 GeV, the D4 magnets were operated at 4515 amp, giving a field integral of 205.9 kG-m. The CCM field integral at 3100 amp was 59.70 kG-m. At 93 GeV, the field integrals were 88.84 kG-m and 29.60 kG-m.

The beam chambers were aligned in a similar fashion to those in the spectrometer. Here we were aided by the fact that some of the chambers were on a direct unobstructed line and could be aligned with magnets off and no bending. With both the beam and spectrometer aligned and calibrated, BV triggers could be used to compare the two systems. BV triggers were treated differently from deep inelastic triggers by the track finder. No calorimeter vertex was found for BV triggers. Instead, the beam track was allowed to continue to the back of the spectrometer. Then a "scattered" track was found from the back in the usual fashion and allowed to continue to the front. When these two versions of the same track were fit, two values of the momentum at chamber 0 were produced, the first from the beam system, the second from the MMS. Using equal amounts of 215 GeV east- and west-bending MMS data, a discrepancy of $p_{\text{beam}} - p_{\text{MMS}} = 2.39$ GeV/c was found, a value that was constant throughout the experiment. This 1.1% difference was attributed to calibration or alignment errors in the beam system. There were two pieces of evidence backing this interpretation. The first was the estimated error in the MMS magnet calibration of 0.2%. This was confirmed at a level smaller than 1% by our measurement of the ψ mass using muon pairs in the MMS.[30] For the elastic, inelastic, and total ψ samples, the differences between the measured and true mass were 0.7%, −0.9%, and 0.2%, with statistical errors of about 0.2%. We thus applied −2.39 and −1.67 GeV/c corrections to the measured momenta of individual beam tracks in the beam system for the 215 and 93 GeV/c beams.

7.3 Calorimeter calibration

The calibration of the calorimeter had three distinct phases. The first was an ADC counts to equivalent particles (EP) calibration which gave the 75 counters a common scale in the low ADC's. Next was a high ADC to low ADC calibration to match the two scales in each counter. Last was an EP to GeV calibration of the summed counters in a shower.

Using the definition of EP, the single muon pulse height spectrum for each counter was inspected by eye to determine the location of the peak, after pedestal subtraction. As an (apparently cursory) study revealed no time variation of this calibration, only one set of constants was used. Single muons gave no appreciable signal in the high ADC's. The high scale was calibrated by comparing large low ADC signals from showers with their high ADC counterparts. Two problems arose, both worsening with increasing intensity: the relation between high and low broadened with intensity, and events with a random high/low ratio appeared at the few percent level at the highest intensities. With no further information to go on, these problems were ignored and low intensity data was used to fit (high) $= a$(low) $+ b$.

The energy calibration was performed in two steps, each of which compared the summed calorimeter signal to $\nu_{\rm mag}$, the value of the shower energy measured magnetically as $E - E'$. The first calibration simply fit $S = c\nu_{\rm mag}$ where S is the sum of calorimeter signals in EP described in Sec. 6.4. The value found for c was 5.965 EP/GeV. This linear fit was adequate only as a starting point. Problems with it included a possible offset due to inadequacies in the muon pulse height subtraction and an observed anti-saturation (more than 5.965 EP/GeV) at large ν. The muon subtraction used the mean pulse height for 215 GeV muons. Unlike the most probable pulse height, the mean is energy dependent, and a correct subtraction should depend on ν. The anti-saturation is believed to be due to radiative corrections, especially wide angle bremsstrahlung events, which add a large pulse height electromagnetic component to the showers and which trigger the MMS only at large ν. The final energy calibration was also the catch-all for curing the deficiencies in the previous calibration stages.

The final calibration was a correction derived from another comparison of $\nu_{\rm calor}$ with $\nu_{\rm mag}$, which, by definition, has its worst resolution where we need the calorimeter the most. At low ν (or high E', see Fig. 6.5c) the spectrum of triggered events drops off rapidly. Thus a bin of low measured $\nu_{\rm mag}$ has $\langle\nu_{\rm true}\rangle > \langle\nu_{\rm mag}\rangle$ due to smearing. This bias must be removed from the calorimeter calibration. This was done using the apparatus simulation (see next chapter) which produced events with known values of both $\nu_{\rm true}$ and $\nu_{\rm mag}$.

Before proceeding with the calibration, an important correction was made. The calorimeter, like the chambers, had a write gate that extended over several rf buckets. Since a muon contributes a mean pulse height of several EP in each of the ≥ 15 summed counters in a shower, a muon from another rf bucket could add several GeV to the apparent shower energy. Fortunately, this effect decreased with the number of buckets separating the ghost muon from the triggering muon. We vetoed buckets ± 1 and tagged buckets $\pm 2, 3$. To events with such a tag, a correction was applied. The largest correction was -5.6 GeV for bucket $+2$ in the 215 GeV data.

The final calorimeter calibration began with samples of real and simulated data, each divided into bins of measured $\nu_{\rm mag}$. For each bin, we produced histograms of $\nu_{\rm calor}$ for the real data and $\nu_{\rm gen}$, the true value of $E - E'$, for the simulated data. We then plotted $\langle\nu_{\rm calor}\rangle - \langle\nu_{\rm gen}\rangle$ *vs.* $\langle\nu_{\rm gen}\rangle$. One such plot is shown in Fig. 7.1. These points were then fit, using a fourth- or sixth-order polynomial with only even powers of $\langle\nu_{\rm gen}\rangle$. The fit was then used to correct the original linear calibration. Inspection of the calibration plots for different blocks of data showed significant time dependence. Much of this was found to be synchronized with the field reversals of the MMS, an effect traced to magnetic field sensitivity in individual photomultiplier

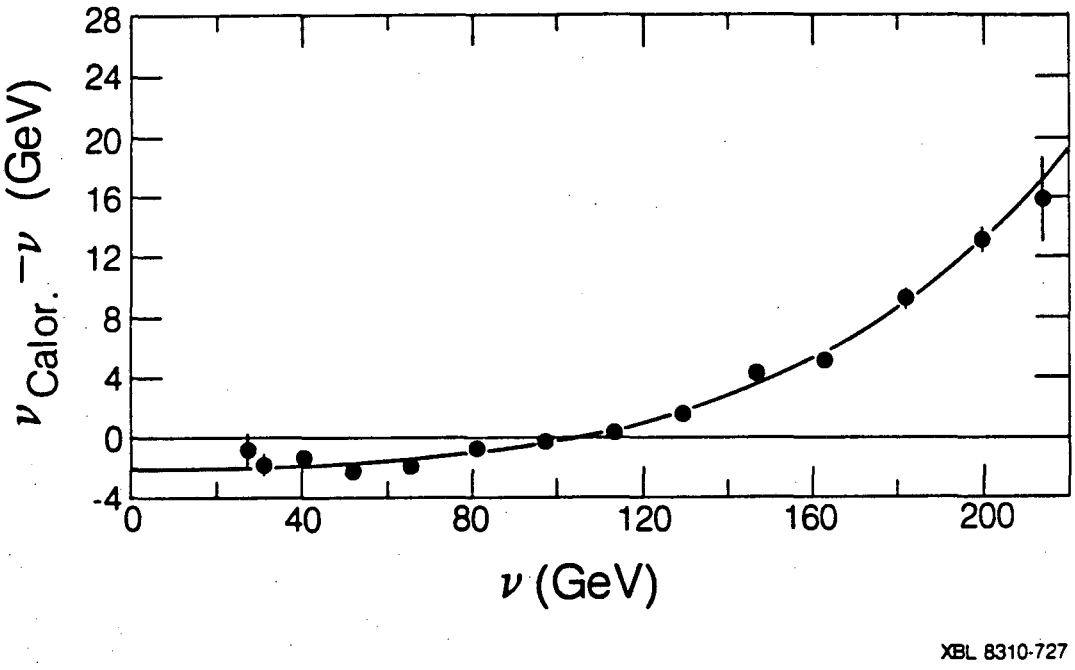

Fig. 7.1. Typical calorimeter final calibration plot. Uncorrected ν(calorimeter)—ν(true) is plotted *vs.* ν(true) determined bin by bin using our Monte Carlo simulation. The curve is the fit to be subtracted from the uncorrected measurements to give the final calorimeter energy.

tubes. These effects were corrected in an average sense only by separately calibrating blocks of data, each spanning only one MMS polarity. We also looked for the effects of transverse shower containment on the calibration. Fortunately, large shower recoil angles are correlated with small shower energies and thus shorter showers. A look at the least favorable combinations of ν, θ_{shower}, and the vertical position of the vertex showed no visible effect. An empirically-motivated search for Q^2 dependence showed an effect at large ν (see Fig. 7.2), beyond where the calorimeter contributes to the ν resolution. This effect, visible also in the simulated data sample, is due to radiative events which occur preferentially at large ν and low Q^2.

By methods similar to those used in the calibration, we determined the resolution of the calorimeter. Using the same binned data, we used the widths of the histograms to compute

$$\sigma^2_{\text{calor}} = \sigma^2_{\nu\text{calor}} - \sigma^2_{\nu\text{gen}}, \tag{7.2}$$

with $\sigma_{\nu\text{calor}}$ and $\sigma_{\nu\text{gen}}$ from the histograms. The results are plotted as $\sigma_{\text{calor}}/\sqrt{\nu_{\text{gen}}}$ *vs.* $\langle\nu_{\text{gen}}\rangle$ in Fig. 7.3. This procedure was very susceptible to disruption by tails in the histograms. For this reason, in Fig. 7.3 we show also for comparison σ_{calor} extracted by this method from simulated data generated with $\sigma_{\text{calor}} = 1.5\sqrt{\nu(\text{GeV})}$. From measurements such as this we estimate that $\sigma_{\text{calor}}/\sqrt{\nu} = 1.35$ to 1.7 at $\nu \leq 80$ GeV for various blocks of data, with a typical value of 1.4. This was substantially worse than the current state-of-the-art resolution for similar systems

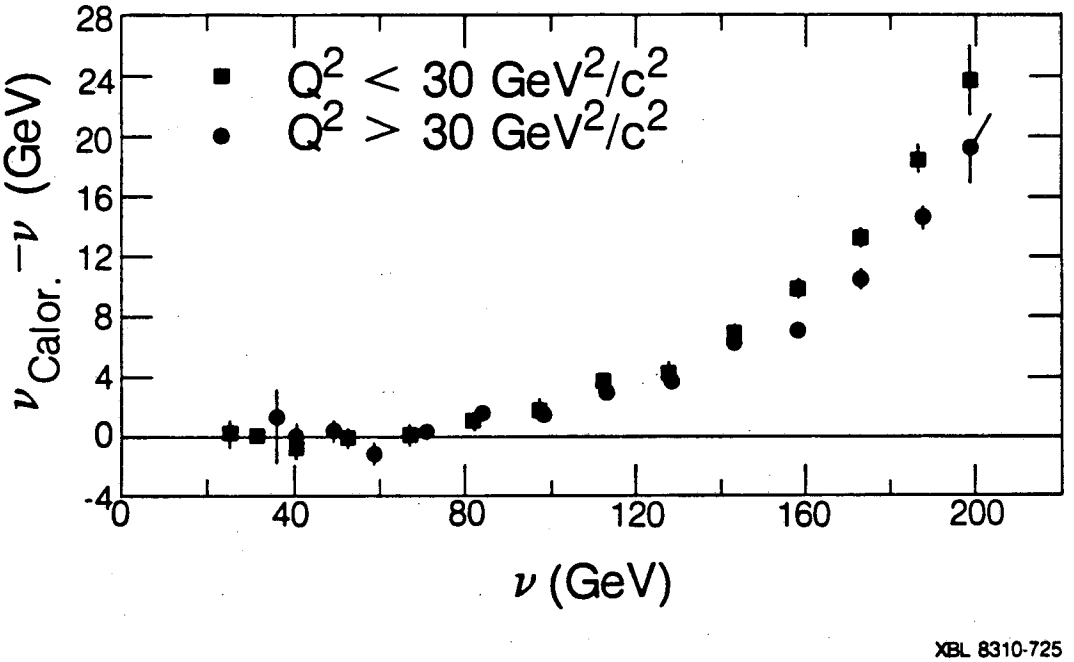

Fig. 7.2. Q^2 dependence in the calorimeter calibration. The larger pulse height at low Q^2, high ν is due to the electromagnetic showers in radiative events. Note: this is a different sample of events than in the calibration example of Fig. 7.1.

of $\sigma = 1.0\sqrt{\nu}$, a value which we approached in early small-scale tests in a pion beam. The reasons for this degradation are thought to lie primarily in the early calibration stages (counter-to-counter and ADC high-to-low), but include also an inherent component from fluctuations in the background energy loss of the muon (or muons).

The use of the calorimeter information to improve the energy resolution of the MMS was described in Sec. 6.4. The relative values of the calorimetric and magnetic resolutions in ν naturally restrict the effect of the calorimeter to low values of ν (see Fig. 4.11). At large ν, several problems appeared in the calorimetry including the radiative effects mentioned above, other poor calibration behavior, and lack of agreement between real and simulated calorimeter resolution. For these reasons, we quenched the calorimeter's contribution to ν by unweighting the contribution of the calorimeter by a further factor of $(\nu/\nu_c)^2$ for $\nu \geq \nu_c$. For the 215 (93) GeV data, ν_c was 80 (40) GeV.

7.4 Chamber efficiency

Missing chamber hits can seriously degrade the reconstruction and fitting of tracks. To model correctly the acceptance and resolution of the MMS, the efficiencies of the proportional

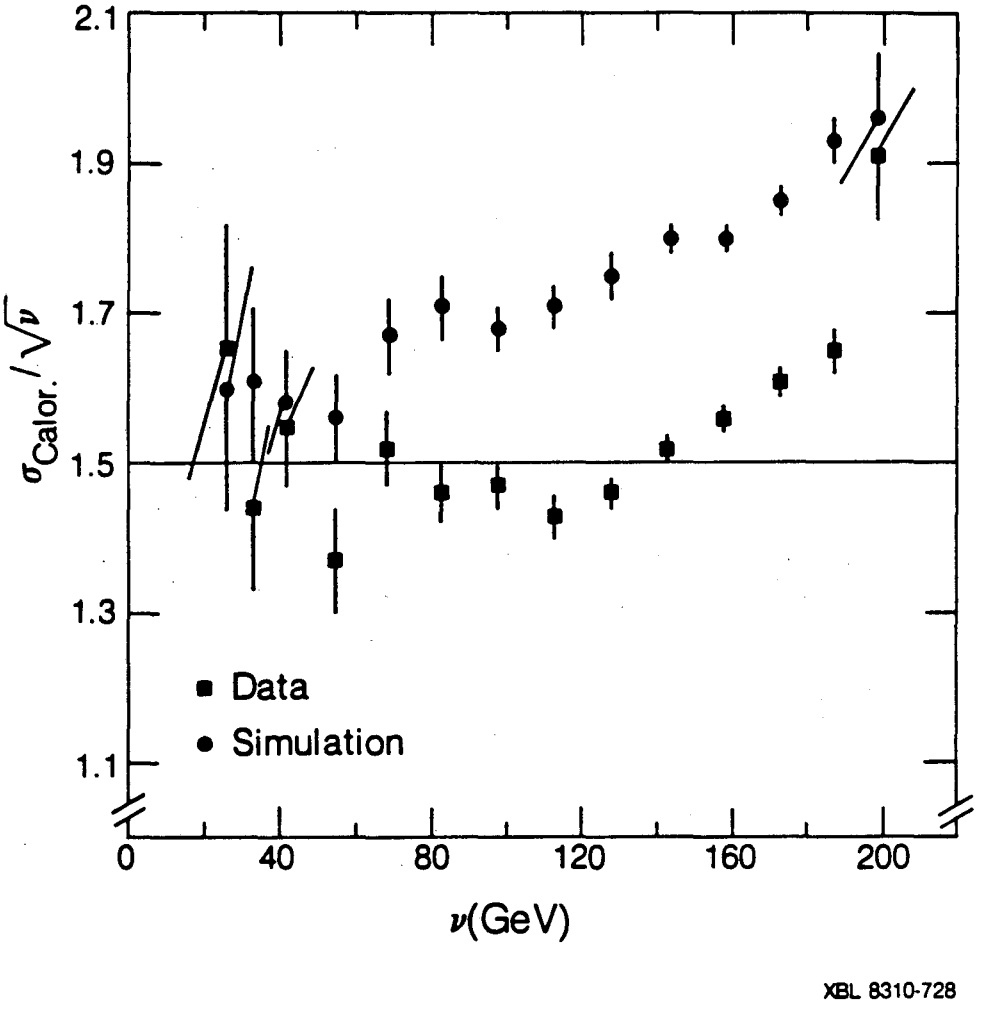

Fig. 7.3. Calorimeter resolution. The circles show the results of the calculation when applied to simulated events generated with $\sigma_{calor} = 1.5\sqrt{\nu}$. The method thus somewhat overestimates the resolution. The simulated resolution was later adjusted to match that of the data.

and drift chambers had to be measured and incorporated into our simulation programs. This was done in a track-oriented fashion by counting the missing chambers on successfully reconstructed tracks. This method inadvertantly includes in the chamber inefficiency track finding deficiences due to other causes. We iteratively corrected for this by using the raw measured inefficiencies in the simulation program, measuring the resulting rate of missing hits on tracks, comparing the result to the rate in real data, and making appropriate adjustments. Each wire plane in each proportional chamber was measured separately, with allowance for correlations within a chamber due to the induced signal read out. In each case, the result was fitted to

$$\epsilon(x,y) = a - be^{-r/s}, \tag{7.3}$$

where a, b, and s are fitted parameters and r is the radial distance from the beam center in that chamber. The fits were performed separately for μ^+ and μ^- running because the lower intensity of the μ^- beam led to improved efficiency. The average PC efficiencies were quoted in Sec. 4.6. The drift chambers suffered no loss of efficiency in the beam. A constant efficiency of 0.98 was used for all drift chambers.

7.5 Trigger counter efficiency

The discovery of a large, position-dependent inefficiency in some of the paddle counters that make up the deep inelastic trigger was a crucial one. The systematic pattern of inefficiency, largest near the beam and decreasing (improving) toward the top and bottom was almost exactly that needed to create spurious Q^2 dependence – a disaster for an experiment attempting to measure precisely logarithmic scaling violations. Fortunately, the existence of parallel subtriggers in the deep inelastic trigger allowed this discovery and also the measurement and mapping of the inefficiency with triggered (*i.e.*, recorded) events. The existence of the inefficiency was verified by hand-scanning a sample of events suspected to contain missing paddle counters. The possibility that the inefficiency was in the recording of the hits, and not in their contribution to the trigger, was eliminated by the insufficient rate of events with a recorded pattern of trigger counters which failed to satisfy the trigger. Eventually the evidence was incontrovertible, as in Fig. 7.4 which shows horizontal scans across pairs of paddle counters at two locations in the spectrometer. Two common features are visible. In Fig. 7.4a, the vertical edge between a good and bad counter is shown. In b, a depression at the center of a paddle is obvious. The calibration of this efficiency was of extreme importance and will be discussed in some detail.

The method used to measure the efficiency took advantage of the fact that, for a muon penetrating more than three paddles, those paddles outside of any satisfied subtrigger are redundant and can be checked in an efficiency measurement. Thus the events satisfying any subtrigger provide an unbiased sample for the study of the five other trigger banks. In this discussion, "penetrated" means the muon passed through the counter; "lit" means that the passage was observed by the phototube and available to the trigger. Using such events, most of the active region of the paddles could be mapped. The exceptions were those regions which could not be penetrated by a muon that also penetrated three other counters. There were two such regions: the outer edges (away from the beam) of paddles in the first three trigger banks, and, more importantly, the inside edges of the last three trigger banks. Of these, the most crucial was the inside edge of bank 6, through which every low Q^2 event in the experiment passed. How these regions were filled in is described below.

Using the entire sample of 800 000 analyzed deep inelastic events, efficiency maps of each paddle counter were prepared on a grid with 6 cm spacing in x and five cells in y ranging from 3 cm high near the beam to 18 cm high at the top and bottom of the spectrometer. Since

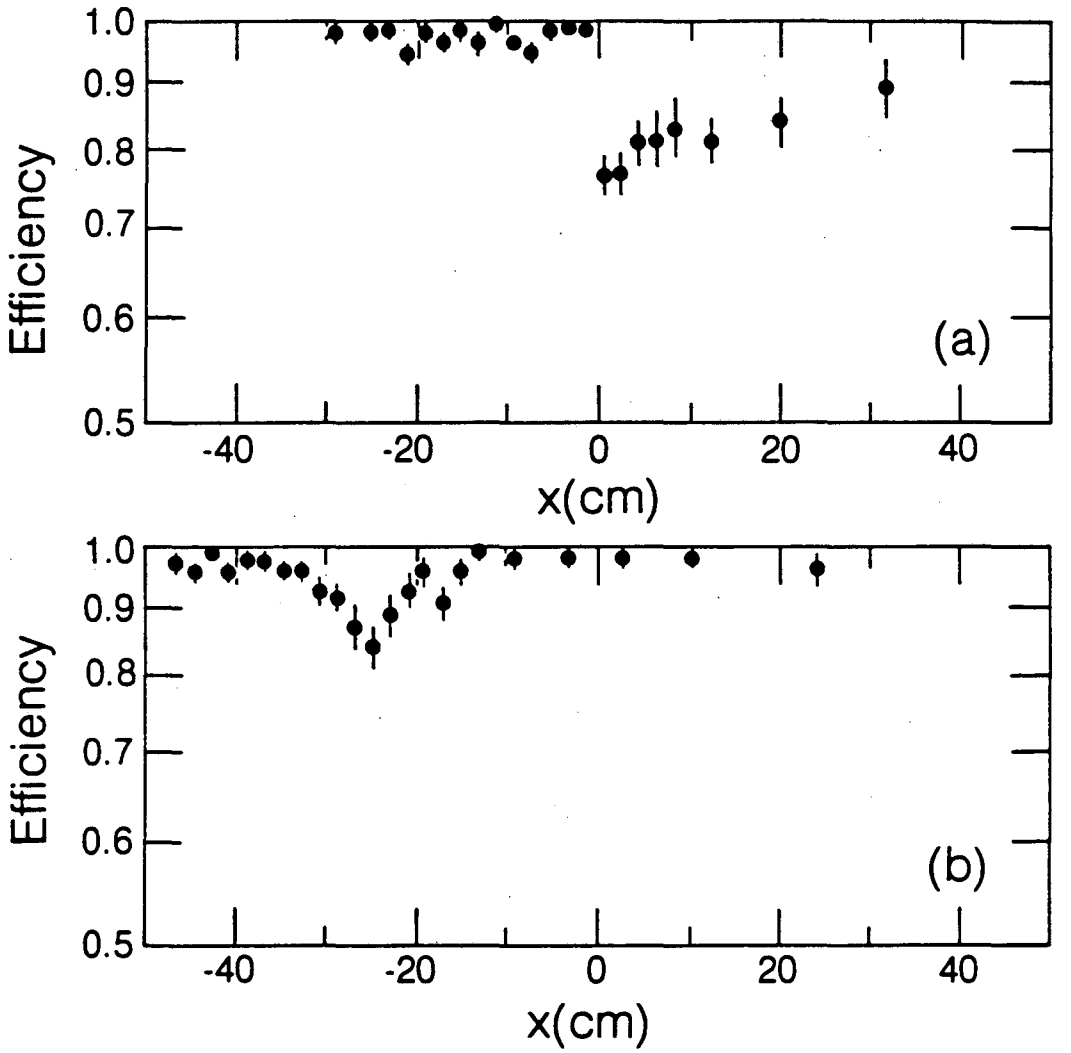

Fig. 7.4. Examples of paddle counter inefficiency.

time dependence was observed in the efficiency of several counters, the data set was divided into four blocks and four separate maps were produced. Where no time dependence was noticeable, the total sample was used for each map. Much of the time dependence was abrupt, and most occurred between the first block, which was not used in the deep inelastic analysis, and the rest. In regions where mapping was possible, the efficiency in each cell was typically measured to better than 5%.

Originally, the unreachable regions at the inside edges of the back counters were filled in by linearly extrapolating in y. This was checked using a small sample of trimuon triggers that triggered in the staves upstream. This test showed no systematic problems with the extrapolation. Further tests with a large sample of multimuon triggers still showed no systematic differences between the multimuon and deep inelastic maps in the extrapolation region, but several individual cells showed large discrepancies. Although these discrepancies were of random sign, in the MMS the relationship between geometry and kinematics is such that these did not average out. After this realization, which was the key to the successful analysis of the experiment, each muon from every multimuon event was used to make another set of paddle efficiency maps. Fortunately, those multimuon events which reached the paddles did so predominantly in the critical region missing from the deep inelastic map. Before including the multimuon data, the two sets of maps were compared in the regions where both measured the efficiency well. This was done to check for a possible bias due to fake tracks in the high background multimuon sample, the fear of which originally prevented their use in the maps. The 180 cells that had multimuon and deep inelastic efficiency measurements with a precision of better than 5% indicated that the multimuon map was low by $\frac{1}{2}$%. With this correction, the hypothesis that the two maps were the same yielded a χ^2 of 184 for 179 degrees of freedom. The maps were then averaged, giving complete coverage of the critical regions of the spectrometer to better than 10% and typically to 4%. Figure 7.5 is a contour map of a trigger bank, showing typical good and bad counters. The completed maps were included in the apparatus simulation for the calculation of the acceptance of the MMS.

Knowing the trajectory of a scattered muon, one can calculate the trigger efficiency for that track using the information from the maps. For muons penetrating more than the required three paddles, the efficiency of course goes up. The statistical uncertainties attached to the penetrated map cells can be similarly combined to give an uncertainty in the trigger efficiency for a single event. The distributions of trigger efficiency and uncertainty for the events used in the deep inelastic analysis are shown in Fig. 7.6. The mean efficiency and uncertainty are 0.83 and 0.057, respectively, with the efficiencies of 94.5% of the events known to better than 10%. Although counting on averaging to smooth statistical errors in the paddle maps is risky, one can count on at least a four-fold averaging from the four quadrants of the MMS which, after adding the two magnet polarities are identical except for paddle efficiency. (For the 93 GeV sample, the symmetry is only two-fold because only one MMS polarity was permitted.) Looking at events from individual x-Q^2 bins used in the F_2 analysis shows that at least five map bins in each quadrant of each trigger bank are illuminated in the worst (lowest Q^2) case. Thus, even in the worst case, the efficiency measurements for events in a single x-Q^2 bin are uncorrelated enough to reduce the effects of statistical errors by a factor of four or five. Allowing for different combinations of map cells in different trigger banks reduces the correlation further. The residual uncertainty in our results due to trigger counter efficiency will be discussed further in the section on systematic errors.

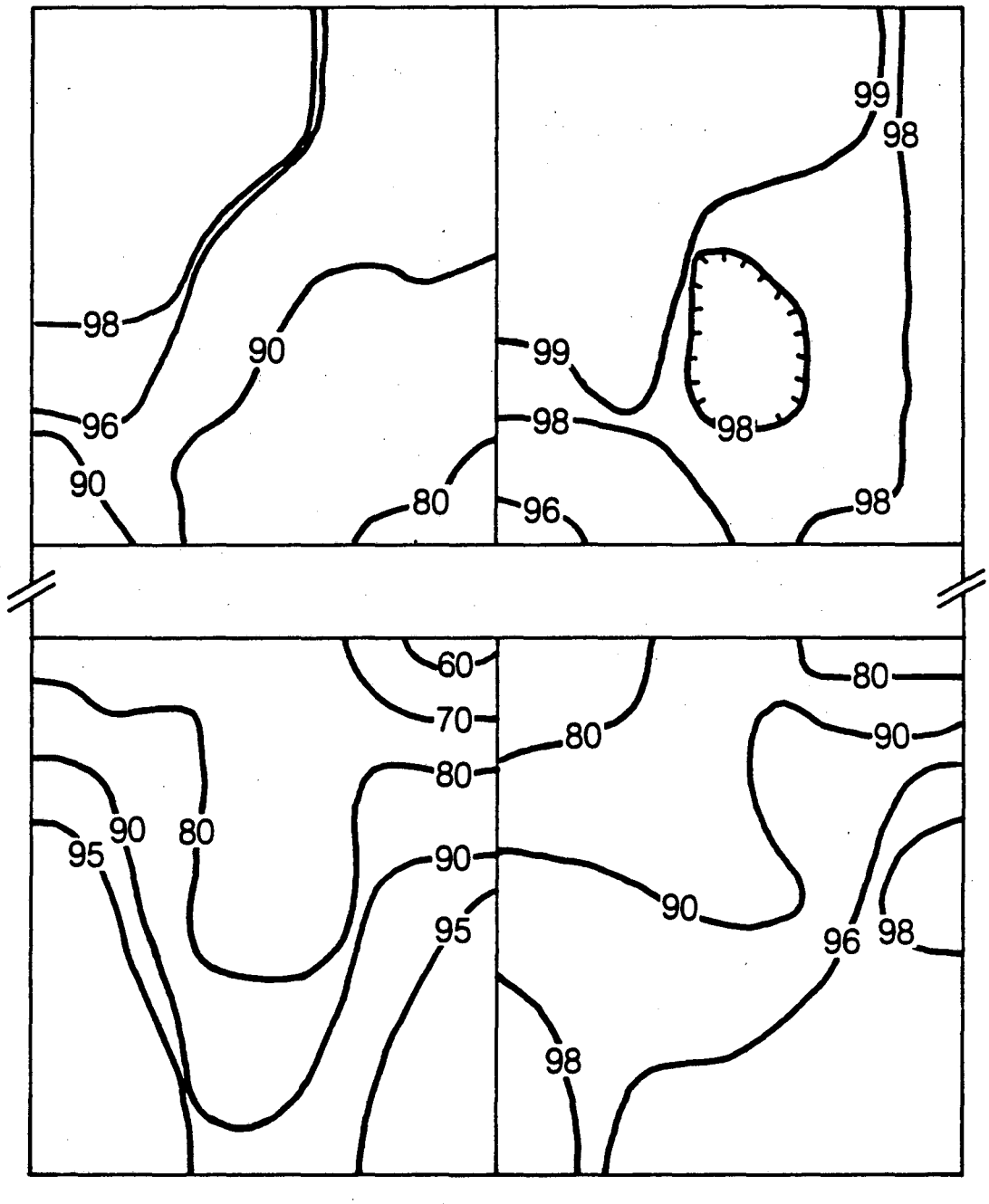

Fig. 7.5. Efficiency contour map of one trigger hodoscope showing counters of varying quality.

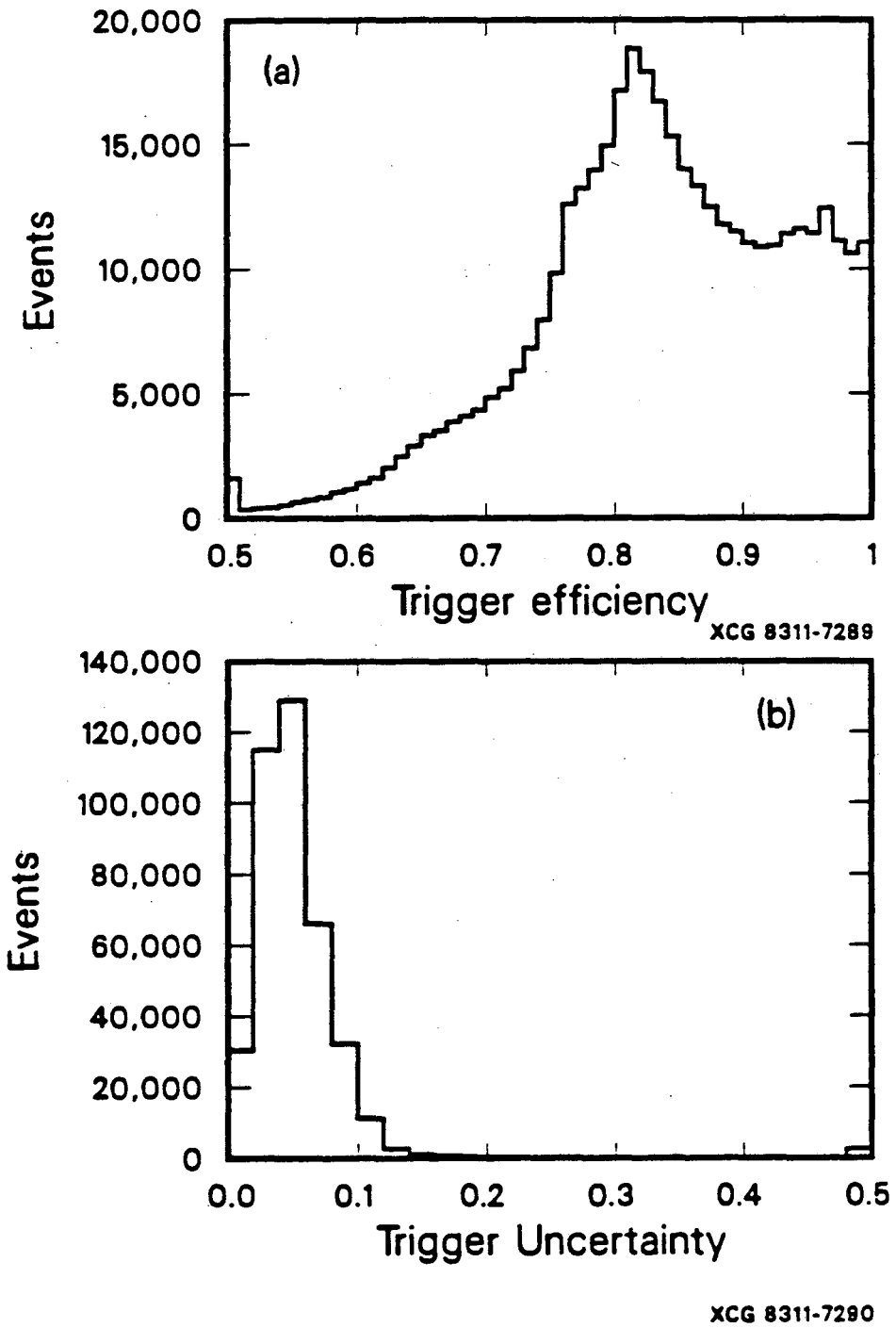

Fig. 7.6. Total triggering efficiency (a) and its uncertainty (b) calculated for individual events in the 215 GeV data.

Chapter 8

The Apparatus Simulation

ROS: *Seventy-six — love.*
GUIL *(musing): The law of probability, it has been oddly asserted, is something to do with the proposition that if six monkeys ... if six monkeys were ...*
ROS: *Game?*
GUIL: *Were they?*
ROS: *Are you?*
Tom Stoppard, *Rosencrantz and Guildenstern are Dead*

8.1 Acceptance calculation

After event reconstruction, both the number of incident muons and the number of detected scattered muons as a function of Q^2 and x, or any other set of variables, are known. From direct measurement of the various components of the MMS, the number of target nucleons is also known. To turn these numbers into a scattering cross section, one further quantity is needed. This is the acceptance of the MMS

$$A(x,Q^2) = \frac{N^{\rm trig}(x,Q^2)}{N^{\rm scat}(x,Q^2)}, \tag{8.1}$$

which is the fraction of the scattered muons which successfully trigger the apparatus. This is primarily a geometrical quantity depending on what range of angles and energies will project scattered muons into the paddle counters of the trigger banks. It also includes the efficiency of the trigger counters and can be extended to include the efficiency of the reconstruction programs. With these latter quantities measured, a simple apparatus might allow the acceptance to be calculated analytically, say as a multiple integral over allowed solid angle and energy. The MMS does not represent such a case. The integration over the large beam size, distributed target, energy loss, and multiple scattering, as well as scattered energy and angle make such an analytic or even numerical integration difficult. When variables affecting reconstruction efficiency such as PC efficiency, δ-rays, and the splashes from hadronic and electromagnetic showers are added to the integrals, the task becomes impossible.

Instead of integrating over the huge phase space defined by all of these variables, we use a Monte Carlo simulation to sample the various regions of this space with frequencies proportional to their likelihood. To do this, simulated events are generated and propagated through a computer

representation of the MMS. For each process of interest, a random value of the relevant variable, say an MCS angle in a single steel plate, is chosen at each occurance from a measured or calculated distribution of that variable. With a large number of generated events, it is hoped that even the more obscure neighborhoods of the phase space will be sampled. In the deep inelastic simulation, muons were propagated through more than 2×10^9 steel plates.

With the acceptance known, the cross section can be calculated from

$$d\sigma(x,Q^2) = \frac{D(x,Q^2)}{ITA(x,Q^2)}, \tag{8.2}$$

where I and D are the numbers of incident and triggered muons and T is the number of target nucleons per unit area. There is a more convenient form of this expression that allows full advantage to be taken of the details of the simulation. Writing A as it is calculated in the simulation as

$$A(x,Q^2) = \frac{M^{\rm trig}(x,Q^2)}{M^{\rm gen}(x,Q^2)} = \frac{M^{\rm trig}(x,Q^2)}{I^{\rm gen}T\,d\sigma^{\rm gen}(x,Q^2)}, \tag{8.3}$$

with $M^{\rm gen}$ and $M^{\rm trig}$ the numbers of generated and "triggered" events, $I^{\rm gen}$ the flux of muons represented by the simulated sample, and $d\sigma^{\rm gen}$ the cross section used to generate the events, we write

$$d\sigma^{\rm meas}(x,Q^2) = \frac{nD(x,Q^2)}{M(x,Q^2)} d\sigma^{\rm gen}(x,Q^2). \tag{8.4}$$

In this expression, $d\sigma^{\rm meas}$ is our measured cross section, D and M are the numbers of triggered data and triggered Monte Carlo-generated events, and n is the normalization, the ratio of incident muons in the simulated and real samples. Equation 8.4 is the basis of our analysis. Its convenience stems from the fact that no reference is make to untriggered events, either real or simulated. Only triggered simulated events have to be saved, and they can then be recorded and reconstructed in the same format as data. With unit normalization and a perfect apparatus simulation, the interpretation of Eq. 8.4 is simple: $D(x,Q^2) = M(x,Q^2)$ implies $d\sigma^{\rm meas} = d\sigma^{\rm gen}$. This equation is also used to make important corrections for resolution smearing. This procedure is described in the next chapter.

It is absolutely crucial that our simulation accurately model the behavior of muons in the MMS in detail. We have no "clean" data sample. Our acceptance and resolution have long tails due to occurances that would be unlikely anywhere but in 5.34 kg/cm^2 of iron. In kinematic regions of small cross section, these tails can dominate the observed population of events. It is essential that we have confidence in our ability to model not just typical behavior, but these tails as well.

8.2 Overview

Each of the 578 runs used in the analysis was separately simulated. The Monte Carlo simulation of an event proceeds as follows:

- Choose a beam track from the sample of BV triggers taken during the data run being simulated.
- Choose the vertex z position randomly in the target.
- Propagate the beam muon from the front of the MMS to the vertex.

- Use the radiatively corrected deep inelastic cross section to choose the momentum vector of the scattered muon.
- Propagate the scattered track until it leaves the spectrometer, recording the positions in chambers and trigger counters.
- Test the trajectory for triggering.
- If the event triggers, generate the information that appears on a raw data tape: chamber hits, including those from δ-rays and showers, calorimeter pulse heights, *etc.*
- Write the event on a magnetic tape in the same format as raw data, with an additional block containing the true (generated) kinematics of the event.

This tape is then read by the data reduction programs which do not distinguish between real and simulated events except in certain calibration information.

8.3 Beam and target

The rapidly rising deep inelastic cross section as $Q^2 \to 0$ makes us quite sensitive to the details of the beam phase space. Our trigger makes us especially sensitive to the spatial and angular distributions of the beam in the vertical (y) coordinate. For this reason, and also because frequent adjustments were made in the beam line settings to improve the yield of muons, we did not try to simulate the beam. We instead used the random selection of beam tracks recorded along with the triggered events as the parent sample of incident muons for the simulation. For each event, the real beam chamber hits are copied to the simulation output tape and the beam track *as reconstructed* in position, angle, and momentum at the front of the MMS is propagated to the interaction vertex by the same routine used for scattered muons (see below). This method, the use of reconstructed values as actual values, supposes that the resolution of the beam system is negligible compared to the width of the beam in all relevant variables. This is calculated to be the case in general, and in Sec. 5.3 I discussed the elimination of data where the meeting of this criterion was suspect.

The vertex z position is chosen randomly in the material of the first 13 modules, including plate zero. The scatter may take place in any of the elements of the spectrometer (iron, scintillator, chamber windows, *etc.*), but the target is always treated as a nucleon in an iron nucleus. 95% of the scatters take place in the iron plates.

Although the simulation starts with an unbiased sample of the muon beam phase space, the demands of the trigger modify it substantially. Figure 8.1 shows the y position distribution of the beam tracks used as input to the simulation, the distribution of simulated events which satisfied the deep inelastic trigger, and the corresponding distribution of real events. The outer edges of the triggered distributions are enhanced by the large low Q^2 cross section. The fluctuations present in the data are due to problems in the beam chambers. Using the measured distribution as input to the simulation causes the same fluctuations to reappear.

8.4 Event generation

When the beam muon reaches the z position of the vertex, its energy (after dE/dx losses) is handed to the event generator which will determine the kinematics of the interaction and the 3-momentum of the scattered muon. The generator uses the deep inelastic cross section

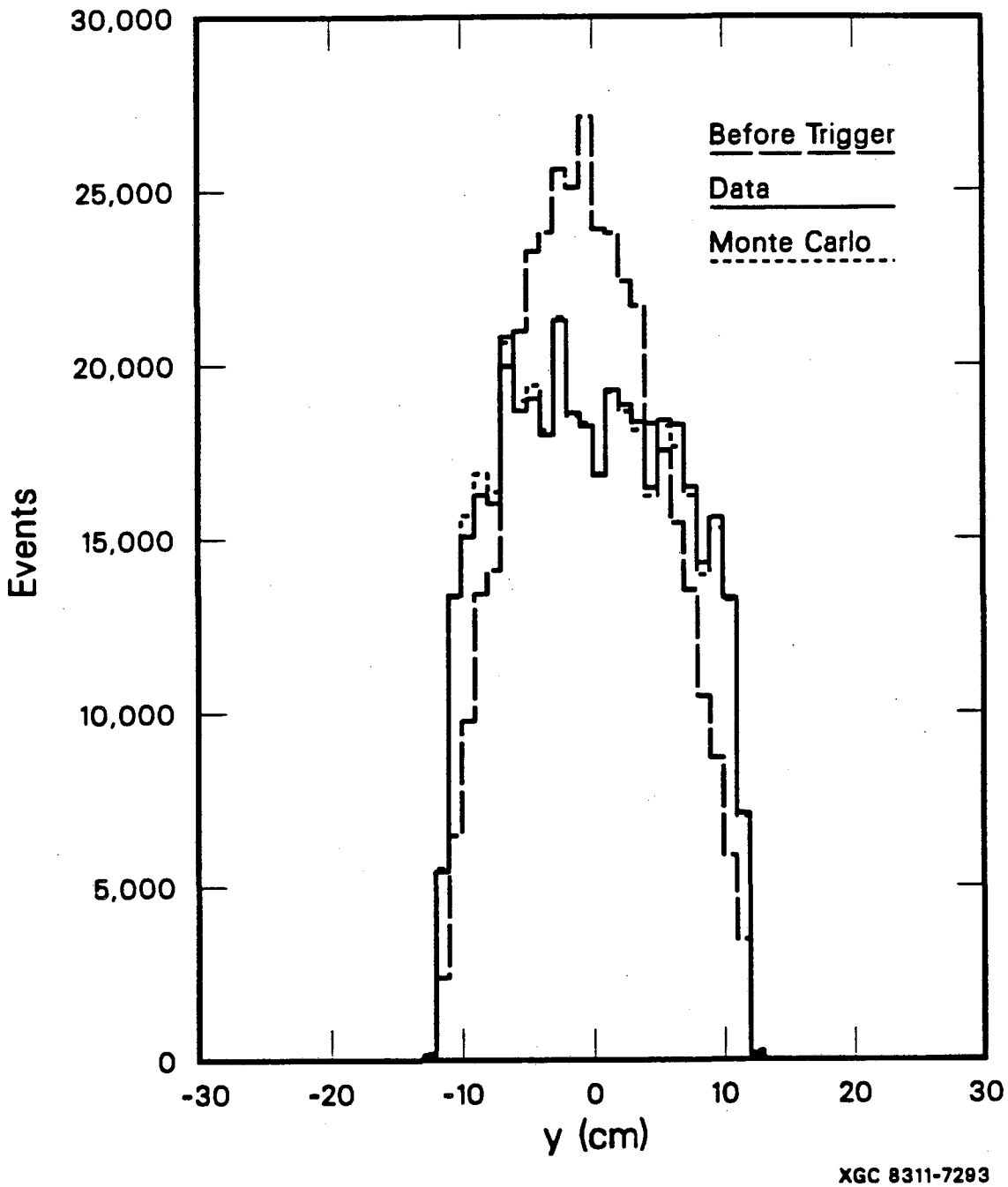

Fig. 8.1. Vertical distribution of beam muons entering the MMS, showing the input to the simulation (dotted) and the resulting distribution after triggering (dashed), normalized to the same total number of events. Also shown is the distribution of real events (solid line).

in the form (see Eqs. 2.2 and 2.12)

$$\frac{d^2\sigma}{dv\,dy} = \frac{4\pi\alpha^2}{2M_N E}\frac{1}{v^2 y}\left[1 - y + \frac{y^2}{2(1+R)}\right]F_2(x = v/y, Q^2 = 2M_N E v). \tag{8.5}$$

It starts by choosing v from a $1/v^2$ distribution. Since this is divergent, we choose v only above a value $v_{min} = 0.015$, low enough so that the acceptance is nearly zero below v_{min}. This v_{min} corresponds to $Q^2_{min} = 5.9$ (2.5) at the average energies at the vertex of the 215 (93) GeV data sets. Next, y is picked from a $1/y$ distribution with $y > v$. The remaining terms of the cross section are then calculated, using a nominal beam energy of 200 GeV and $R = 0$. For $F_2(x, Q^2)$ we use the parametrization of Buras and Gaemers.[51] This is a simple analytic form which approximates the predictions of QCD by adjusting the Q^2 dependence to match Eq. 3.13 before fitting the rest of the parametrization to data. The value of Λ used is 300 MeV/c. The chosen (v, y) pair is kept or rejected based on a random number comparison with the above cross section. The process is repeated until a valid (v, y) pair is found, at which point the initially chosen $1/v^2 y$ distribution has been shaped to reflect all of Eq. 8.5.

Once v and y are chosen and the nominal ($E = 200$ GeV) cross section for the event is known, the distribution is shaped once again to take into account the actual energy of the beam muon at the vertex and radiative corrections. Radiative corrections are treated in four parts, corresponding to the diagrams of Fig. 8.2. The first and last diagrams contain the radiation of a real photon in conjunction with the deep inelastic scattering. These are handled using the peaking approximation which assumes that the radiation leaves the muon direction unchanged and the method of equivalent radiators which treats the radiation as a separate energy loss due to a Q^2 dependent number of radiation lengths.[52] A new cross section is calculated for the actual beam energy, including energy loss in the target before the vertex and in the initial equivalent radiator. This cross section is then corrected for the contribution from the vertex and vacuum polarization diagrams of Fig. 8.2b.[52] To this cross section is added the cross section for the wide angle bremsstrahlung (WAB) process of Fig. 8.2c.[53] This can be viewed either as a background process or as a correction to the peaking approximation – a quasi-elastic scatter with most of the deflection of the muon occuring at the radiative vertex. WAB makes its largest contribution ($\approx 3\%$ after cuts) at large y and low Q^2. Radiative corrections are discussed further in Appendix A. The final shaping is done by comparing a random number to

$$\frac{(1+\delta)\sigma^{\mathrm{ACT}}(E) + \sigma^{\mathrm{WAB}}}{e\sigma^{\mathrm{NOM}}}, \tag{8.6}$$

where $\sigma^{\mathrm{ACT}}(E)$ is the actual cross section at the incident muon energy E (including radiative corrections), $(1+\delta)$ is the vertex and vacuum polarization correction (see Appendix A), σ^{NOM} is the uncorrected cross section at 200 GeV, and e is an enhancement factor, chosen to make this ratio usually less than 1.

For events successfully passing the final shaping, the outgoing muon's energy and polar angle with respect to the beam track are

$$\begin{aligned} E' &= E(1-y)(1-y_f), \\ \theta &= 2\arcsin\left[\frac{M_N v}{2E(1-y)}\right]^{1/2}, \end{aligned} \tag{8.7}$$

where y_f is the fractional energy loss in the final equivalent radiator. The azimuthal angle ϕ is chosen randomly. Even with the enhancement factor e in Eq. 8.6, events with a large upstream

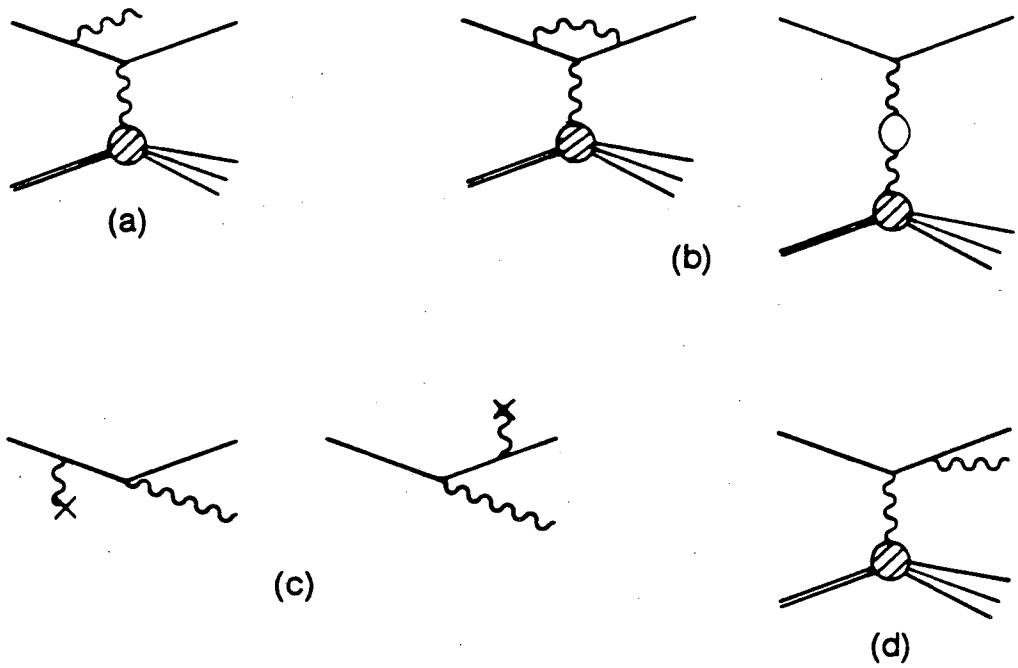

Fig. 8.2. Radiative corrections. (a, d) Internal bremsstrahlung; (b) vertex and vacuum polarization; (c) wide angle bremsstrahlung.

energy loss or a large WAB contribution will have a shaping ratio greater than one. These events are repeated the appropriate number of times, each time choosing a new y_f and ϕ. Finally, the outgoing track is rotated from the coordinate system of the beam track to that of the spectrometer and its 3-momentum is handed to the propagation routine.

8.5 Muon propagation

The propagation routine constructs the trajectory of the beam muon from the front of the spectrometer to the vertex, and that of the scattered muon from the vertex to where it exits the spectrometer. It projects the path through one element of the MMS at a time. In active elements (chambers, trigger counters, and calorimeter counters) the position of the trajectory is recorded. In these elements and in the air gaps the muon path is a straight line. In each iron plate the muon is subjected to energy loss, magnetic deflection, and multiple scattering. Although these processes are treated as occurring only in the iron, the amount of material or $\int \mathbf{B} \cdot d\mathbf{l}$ assigned to each plate includes that in the gaps. It should be noted that both the dE/dx and the MCS are generated in a form independent of that used to analyze them in the reconstruction programs.

The energy lost by the muon in an iron plate is calculated as the sum of five terms: average ionization losses (below $0.01E$), stochastically chosen ionization losses (to knock-on electrons above $0.01E$), average and stochastic losses to pair production (below and above $0.001E$, respectively), and stochastic losses to bremsstrahlung.[54] The probability distribution of energy losses above 5 GeV for a 200 GeV muon in one of our 4 inch iron plates is shown in Fig. 8.3. Muons are allowed to lose energy until their range in iron is less than one plate thickness. Their subsequent decay is not simulated. For use in the propagation routine, the energy loss in a plate is divided in half and the halves are applied before and after the deflections due to the magnet and MCS.

The magnetic deflection in each plate is calculated from the detailed field maps produced during the MMS calibration. Both the x and y components of the deflection are included. Each is treated as a single transverse impulse halfway through the plate.

Multiple Coulomb scattering $p_\perp$'s are chosen from a distribution calculated using the method of Molière as illuminated by Bethe.[55] In four inches of iron, the Rutherford scattering formula predicts a significant probability for scattering at quite large $p_\perp$'s, much larger than the $p_\perp$'s anticipated by Molière and Bethe. While the single scattering law used by these gentlemen includes a screening suppression at small $p_\perp$, it lacks a high $p_\perp$ roll-off due to the nuclear form factor. The Molière distribution thus has a tail extending to very large $p_\perp$ which is dominated by single scattering well beyond where the form factor should suppress it (see Fig. 8.4). To cure this, we subtract from the distribution the absolutely normalized Rutherford cross section for single scattering multiplied by $(1 - |F(p_\perp{}^2)|^2)$. The form factor we use is a Gaussian for the nucleus plus an incoherent sum of terms for the protons. The resulting suppression of the tail is also shown in Fig. 8.4. This procedure is of course only approximate in that it does not deal correctly with the plural scattering region.

The MCS distribution is important since it determines the momentum resolution of the MMS. Furthermore, at very low Q^2 where the cross section is large but the acceptance is small, most of the events that trigger do so with the help of multiple scattering. For this reason, doubling the width of the MCS distribution would raise our total trigger rate by over 20%. Figure 8.5 shows a measure of the MCS that can be observed directly in the data. In the non-bending (y) view in the MMS, the fitted position and angle of a track at the vertex are projected in a straight line to the back of the spectrometer and compared to the MCS-deflected position of the

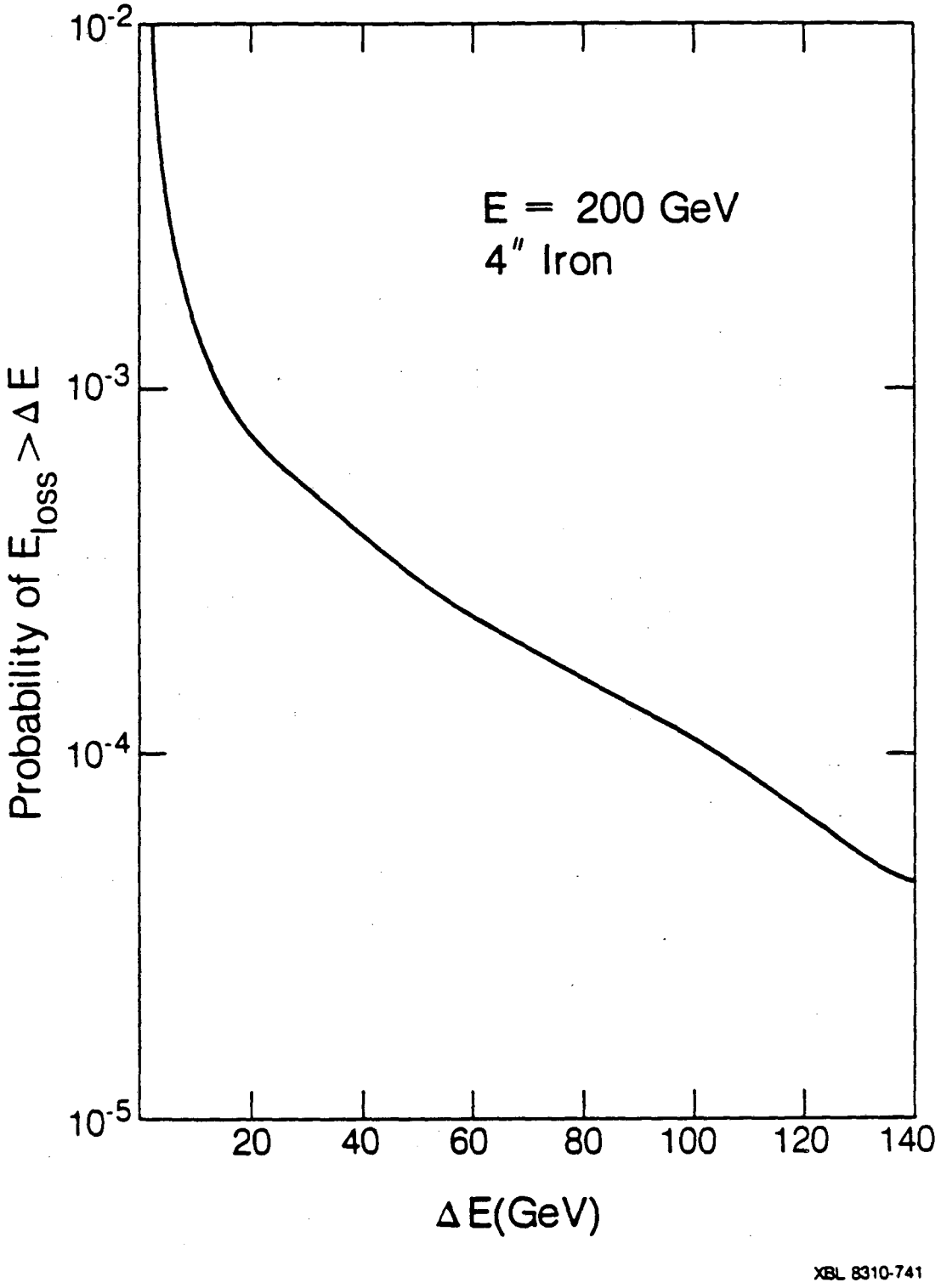

Fig. 8.3. Energy loss spectrum for 200 GeV muons in 4 inches of iron.

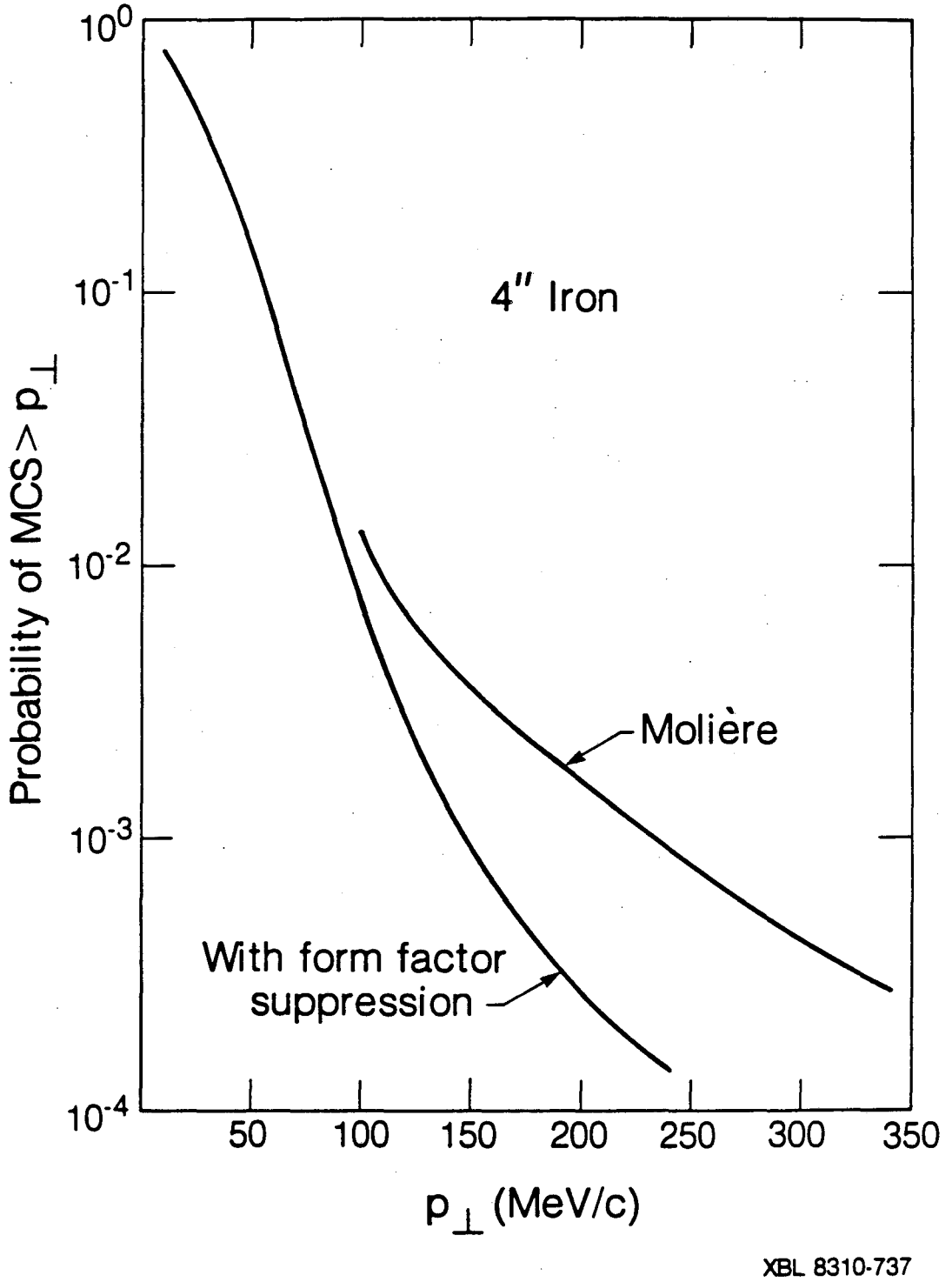

Fig. 8.4. Multiple Coulomb scattering $p_\perp$ spectrum for 4 inches of iron. The tail with and without form factor suppression of single scattering is shown.

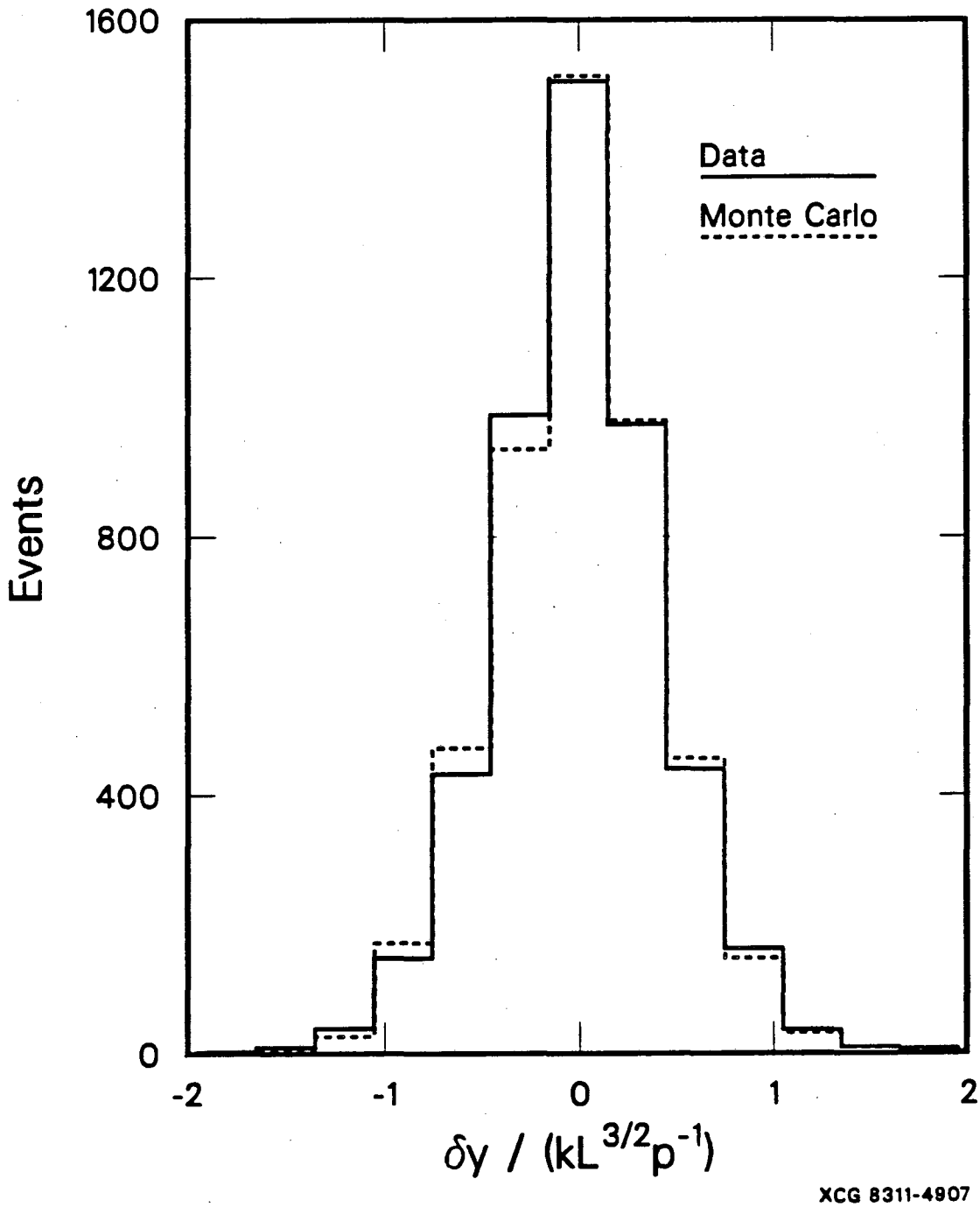

Fig. 8.5. Measured vertical multiple scattering deflection, normalized by the expected value, for real and simulated events.

track there. To remove path length and momentum dependence, this residual is divided by the expected value, proportional to $L^{\frac{3}{2}}/p$ where L is the track length. In the figure, distributions in this variable are presented for scattered tracks from our 93 GeV real and simulated data. Although our y position resolution is insufficient to resolve the MCS angles in individual modules (and thus the fitted MCS is somewhat suppressed), Monte Carlo study shows that the width of this distribution is sensitive to the width of the actual MCS distribution at the several percent level. The widths of the distributions for real and simulated events differ by less than 1.5%.

The propagation of the scattered muon continues until the muon leaves the spectrometer. The position of the muon in each trigger bank is inspected, and penetrated trigger counters are latched. If the counter is a paddle, the position is used to look up the efficiency in the maps constructed from the data. Only the appropriate fraction of penetrations result in latched counters. The pattern of latched counters is then tested against the deep inelastic trigger requirement.

8.6 Data simulation

Events which satisfy the trigger are turned over to a routine which simulates the information produced by the MMS, including its defects and blemishes. These blemishes—chamber hits from showers, missing hits, adjacent wires hit by δ-rays, *etc.*—are important. As an example, the track-finding failure rate doubles in data taken with any one of the proportional chambers in the middle half of the spectrometer switched off.

The routine begins by turning the positions of the muon in each chamber into wire and time bin numbers using the best available set of alignment constants. The measured efficiency of each plane is applied, and a history of the experiment is checked to blank out chambers which were switched off during the real run corresponding to that being simulated. Without regard to any specific physical process, positions were jittered before quantization, extra adjacent hits were added, and efficiencies were slightly adjusted to bring into agreement the distributions of χ^2, residuals, and fraction of missing chambers on tracks for real and simulated data. For hits in the induced PC planes, it was found that the ratio of double to single hits (ideally unity) was empirically reproduced by applying the measured efficiency to each channel of a double hit independently. Cases in which a double hit is changed to a single hit dominate the χ^2 of the y fits because they are interpreted as offset from their true locations and their weights are increased by a factor of four (see Sec. 6.2). The results of this tuning process are shown in Figs. 8.6 and 7. Figure 8.6a shows distributions of χ^2 per degree of freedom for fits of real and simulated tracks in the x and y views. Figure 8.6b shows an overall measure of chamber and track finding efficiency, the fraction of hits present on individual tracks in the DC's and the y view of the PC's. A value of 1.0 corresponds to a hit in every chamber penetrated by a track. In Fig. 8.7 we show the widths (σ) of the residual distributions ($x_{\rm meas} - x_{\rm fit}$) in the drift chambers, where the fit has been performed ignoring the information in each chamber in turn. These distributions give us confidence that our modeling of the resolution of the MMS is adequate.

Every deep inelastic event has a hadronic shower which produces a distribution of pulse heights in the calorimeter and also creates a splash of hits in nearby chambers. The response of the calorimeter must be modeled to give data and simulation the same resolution at low ν. The splash in the chambers must also be included in the simulation because it affects track finding and vertex resolution. The shower simulation was based on a parametrization of showers from our deep inelastic data. There was no physics input whatsoever.

To generate the total pulse height in a shower, the calorimetry simulation used a calibration of 6.0 EP/GeV and a resolution chosen to match that of the data. The parametrization

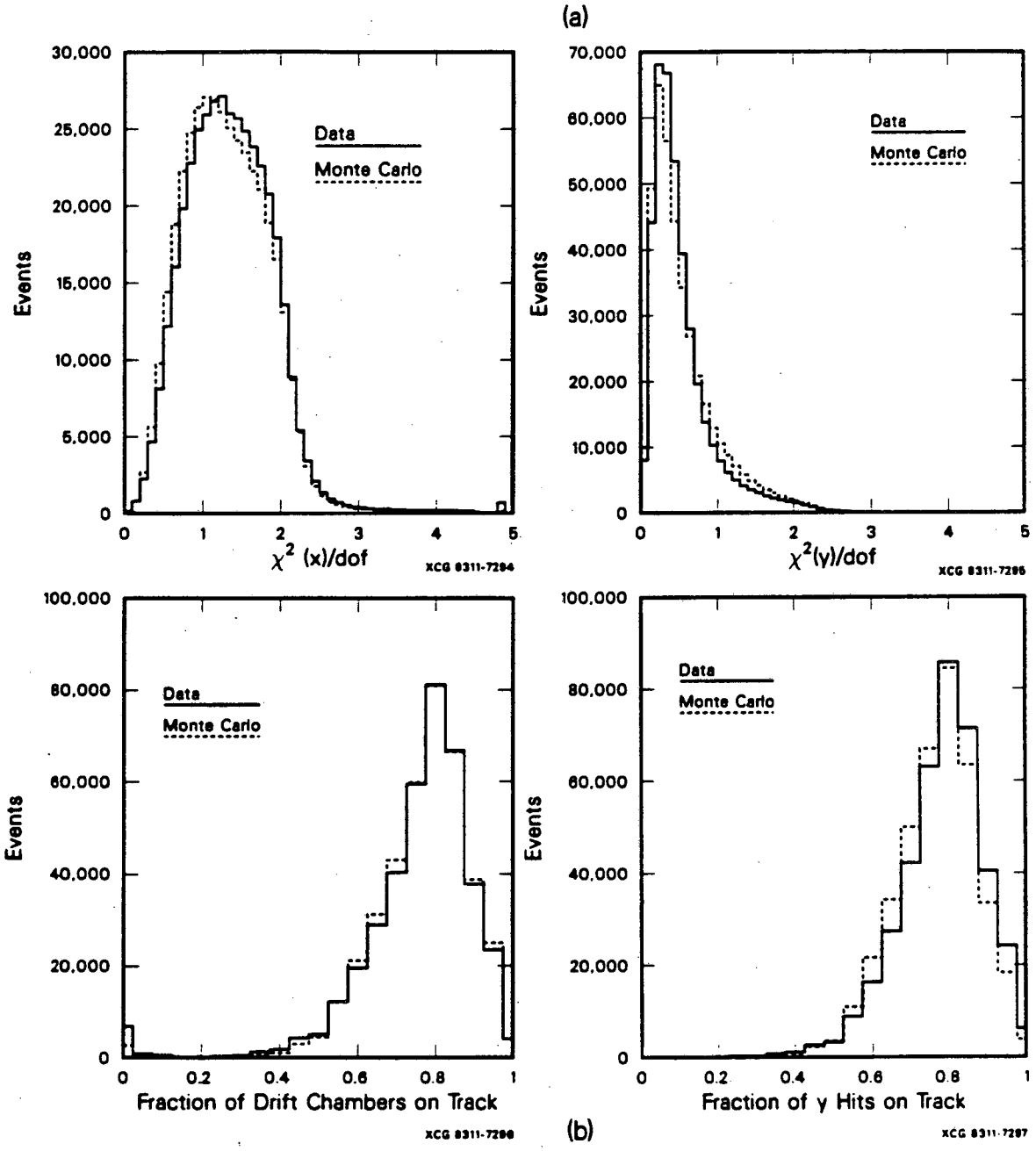

Fig. 8.6. Comparisons of real data and simulation in (a) momentum-fit χ^2 per degree of freedom and (b) fraction of chamber hits on tracks.

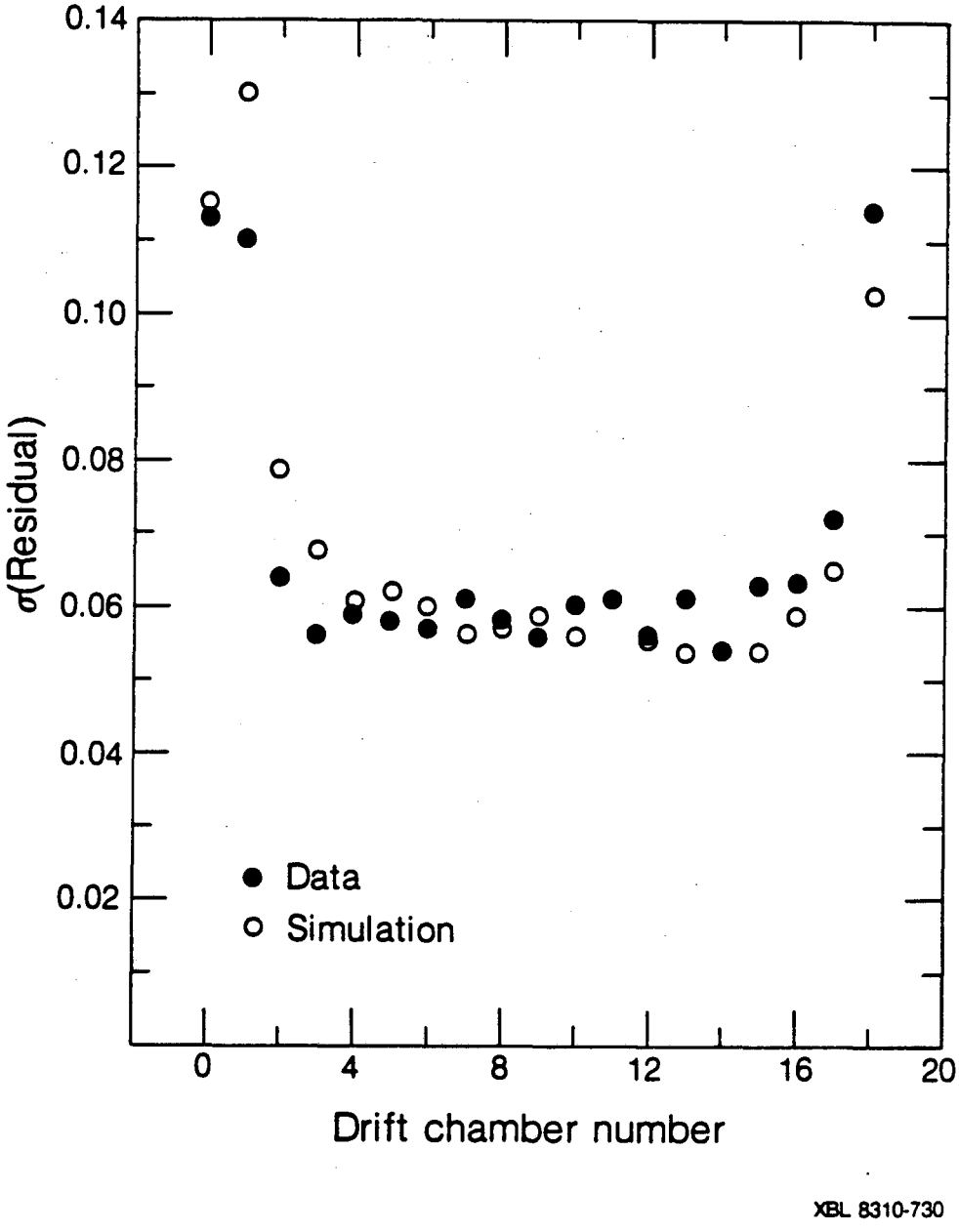

Fig. 8.7. Widths of the residual distributions in each drift chamber.

of the longitudinal shape began with the determination of the fraction of the energy appearing in each counter following the vertex. This fraction as a function of counter number at two energies is presented in Fig. 8.8 along with results from another calorimeter of similar construction.[45] To use this information to generate the individual pulse heights sequentially, it was cast in the form of fraction of remaining energy per counter. The extremely large fluctuations in these numbers were also measured and used in the shower generation. For reconstruction, the EP-to-GeV calibration of the simulated calorimetry is done with the same procedures used for data, as is the summing of the individual pulse heights to get the shower energy.

To put hadronic shower splashes into the chambers, the width of the splash, the number of hits, and its standard deviation were measured in real showers. The width was measured as a function of energy and distance from the vertex and was found to be consistent in the DC and various PC planes. Rather than parametrize the number of hits as a function of plane type, energy, and distance from the vertex, a shortcut was employed. The number of hits in a plane was plotted *vs.* the pulse height in the adjacent calorimeter counter for each plane type. The result was a family of rapidly rising, then saturating curves, with the level at saturation depending, as expected, on the wire spacing. After calculating the simulated calorimeter counter pulse heights, this relation and its standard deviation were used to choose a number of hits to put into each chamber plane. These hits were distributed in space as a Gaussian with a width as measured for that energy and distance from the vertex. The center of the shower in each plane was laid out along a line whose direction was determined by the shower's recoil from the scattered muon.

Electromagnetic showers were parametrized and simulated in a similar fashion. The sample of real showers used to determine the parameters was found in BV (random) triggers using the calorimeter. The showers showed about 10% more pulse height per GeV than hadronic showers, with a resolution of $\sigma_\nu \approx 2.3\sqrt{\nu}$. An electromagnetic shower was simulated for each energy loss exceeding 5 GeV in an iron plate. For wide angle bremsstrahlung events, an electromagnetic shower replaced the hadronic shower at the vertex.

8.7 Operation and performance

The use of real beam tracks as the beam sample for the simulation provided an automatic normalization, both between simulated samples and with the data, through the known sampling fraction in the BV trigger. The total Monte Carlo simulated data sample corresponds to 1 × the 215 GeV data and 2 × the 93 GeV data. These events were then reconstructed using the same routines used on the real data. Generating and reconstructing the total simulated sample consumed one week of CDC 7600 central processor time.

The remaining figures in this chapter are evidence of the success with which we can model the complex acceptance and resolution of the MMS. Figures 8.9a and b show typical real and simulated events. The simulation reproduces all the features of a real event except for hits not related to the beam or scattered muons and the details of low level fluctuations in the single muon pulse heights in the calorimeter. Distributions of real and simulated events in two variables that depend only indirectly on the details of the cross section are shown in Fig. 8.10. In the figure, the samples are those which result from the application of the analysis cuts and shaping procedure described in the next chapter. The numbers of events in the two samples have been normalized. Figure 8.10a is the distribution of events in ϕ, the azimuthal angle of the scattered muon with respect to the beam track's direction at the vertex. Bending of the beam in the spectrometer before the vertex correlates this coordinate system to that of the spectrometer and the distribution has peaks at $\frac{\pi}{2}$ and $\frac{3\pi}{2}$ corresponding to the vertical scatters required by

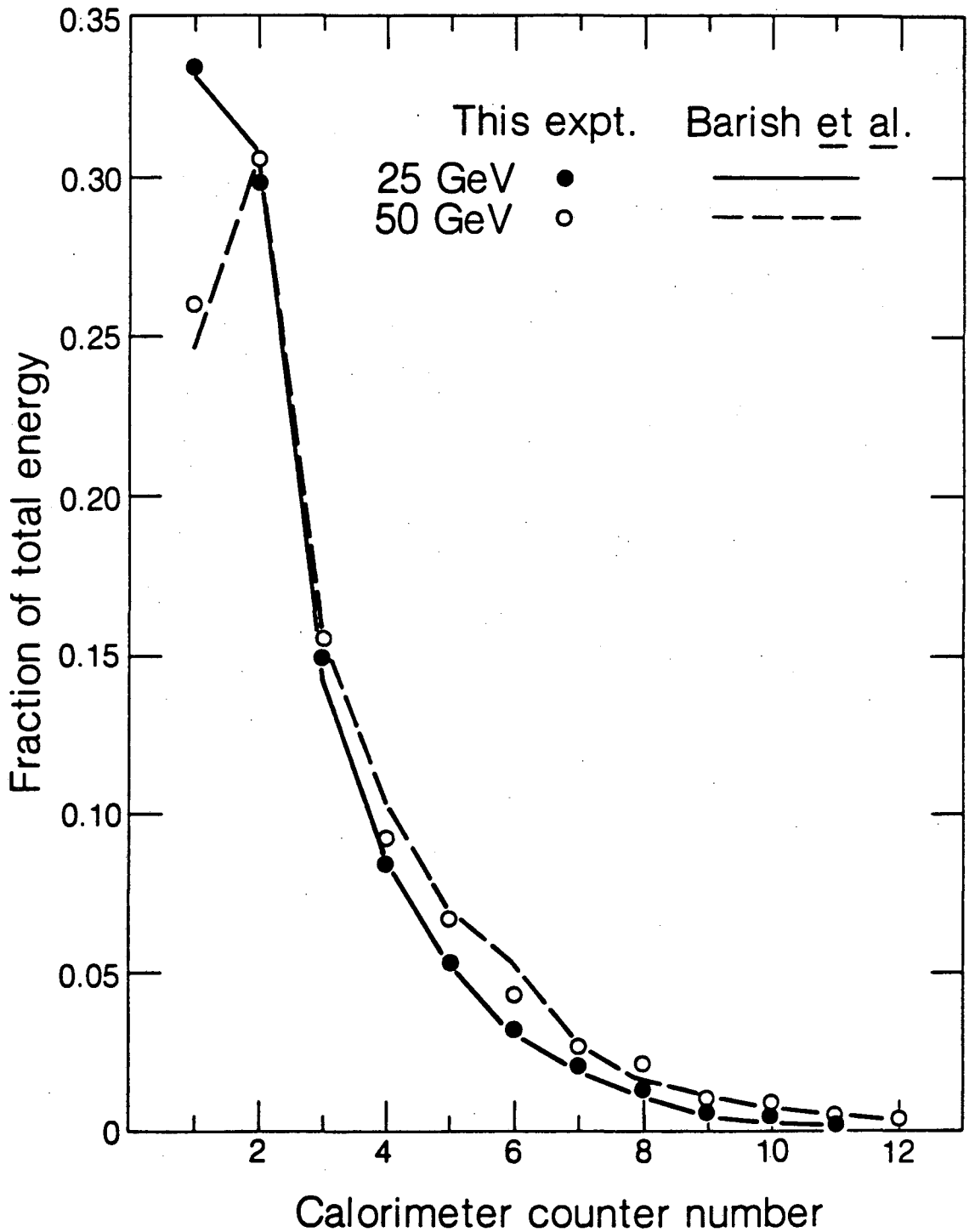

Fig. 8.8. Mean longitudinal distribution of hadronic energy deposition in the calorimeter at $\nu = 25$ and 50 GeV. At the higher energy, shower maximum is typically after more than 4 inches of iron. The curves show similar measurements from Ref. 45.

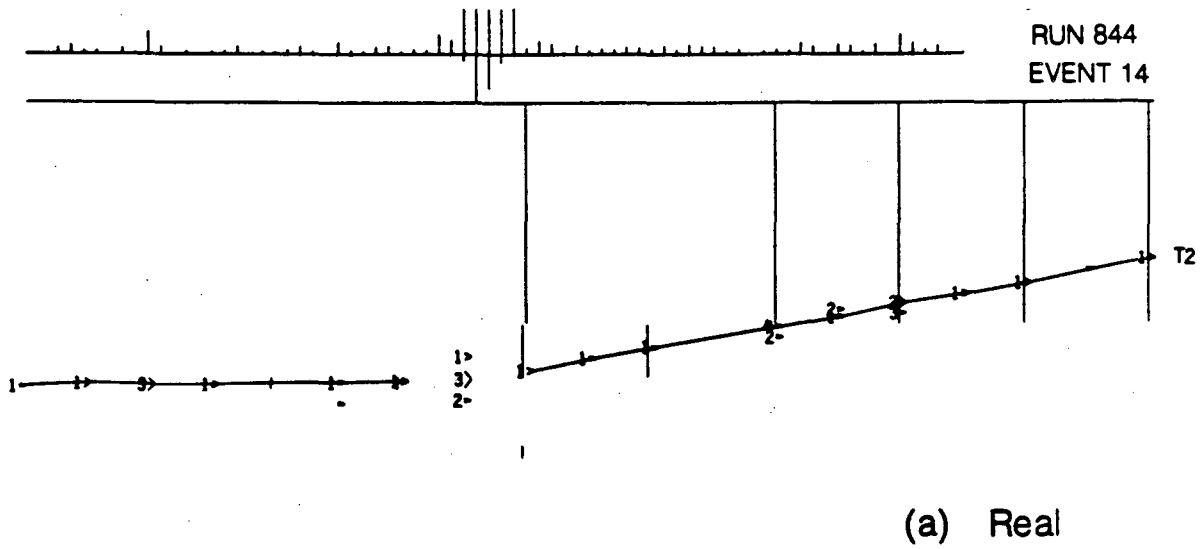

(a) Real

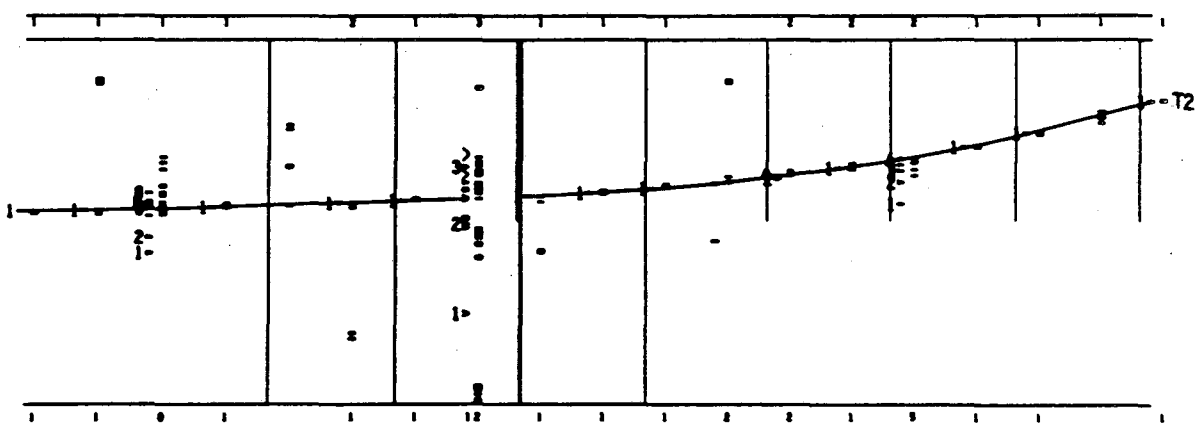

Fig. 8.9. Typical real (a) and simulated (b) event. Shown are computer displays of raw data from the track finding program with line segments connecting PC hits assigned to tracks. From top to bottom are: a bar graph of calorimeter pulse heights, low ADC above and high ADC below; the side view of the spectrometer; and the top view. The beam enters from the left. Vertical lines are hit trigger counters. In each chamber, the width of the caret indicates the span of consecutive hit wires. In the top view, the upstream and downstream hits in each module are those in the PC and the DC, where both of the left-right ambiguous solutions are shown. Note the electromagnetic splashes in both the chambers and the calorimeter, and the dense distribution of hits in the hadronic shower.

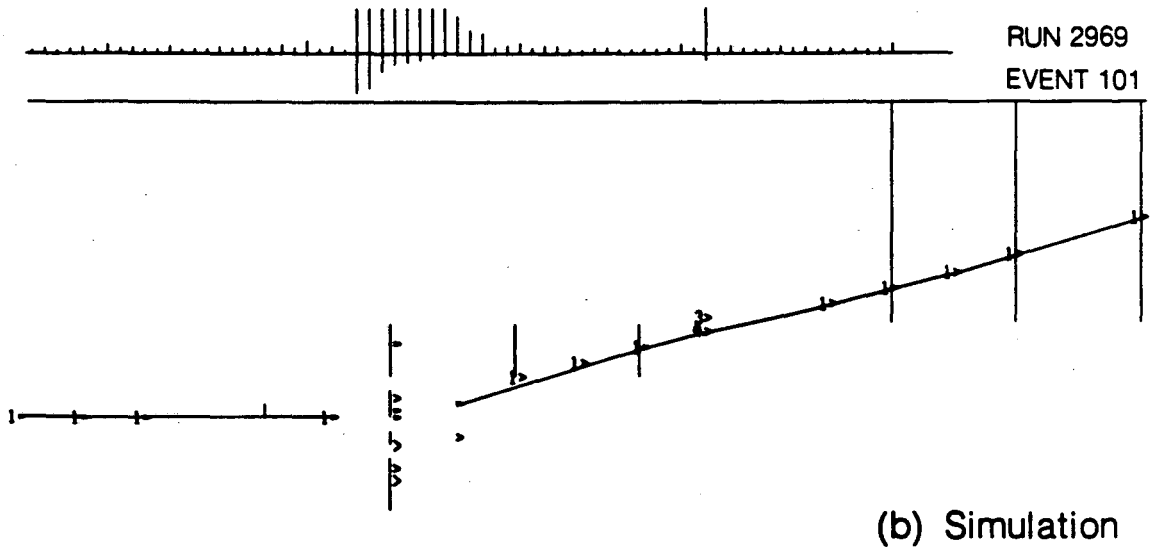

(b) Simulation

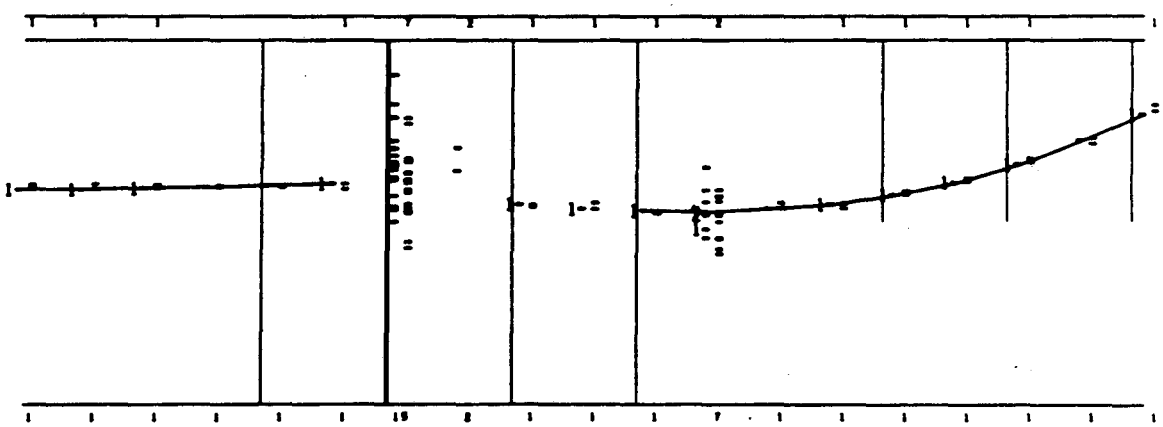

Fig. 8.9. – continued. (b) Typical simulated event.

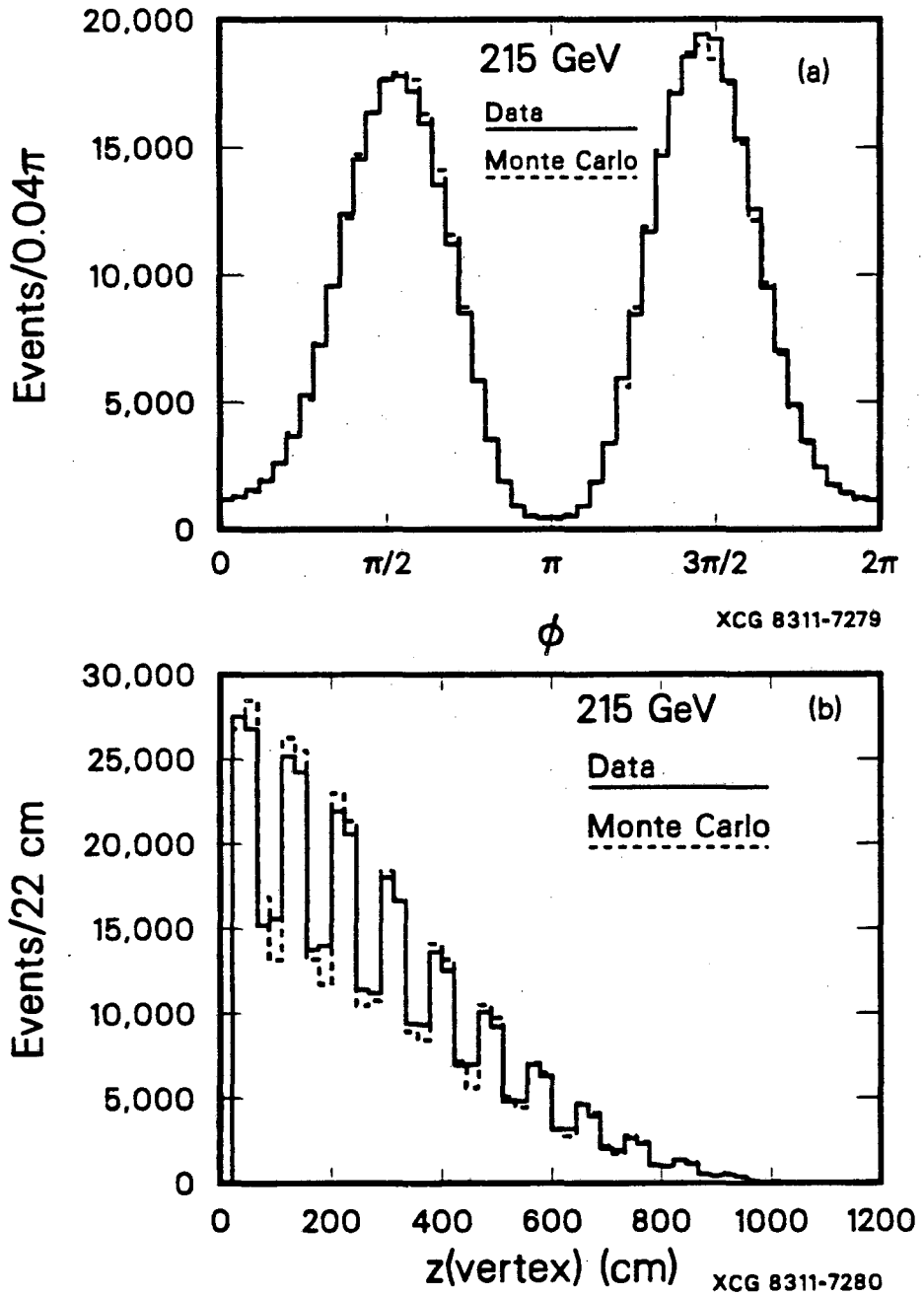

Fig. 8.10. Comparison of real and simulated distributions in (a) azimuthal scattering angle and (b) vertex position along the beam.

the trigger. Distributions of vertex z locations are shown in Fig. 8.10b. The mean z positions are 281.0 ± 0.3 cm and 280.7 ± 0.4 cm for the real and simulated samples.

Chapter 9

Analysis

I said, "No, it's not a case of being lonely we have here — I've been working on this palm tree for eighty-seven years."
Neil Young, "The Last Trip to Tulsa"

9.1 Cuts and the final data sample

Our analysis is based on the comparison of distributions of reconstructed real and simulated events with all differences attributed to differences between the actual cross section and that used in the simulation. In doing this, we are assuming that the effects of the apparatus and reconstruction on the distributions are adequately modeled. We apply cuts simultaneously to the real and simulated samples to insure that this is the case.

Our cuts fall into two general categories. The first set of cuts includes those that are necessary because of known limitations in the simulation. The event generator chose events only above $v_{min} = 0.015$ ($v \equiv Q^2/2M_N\nu$). We must therefore eliminate regions which in the data have a contribution from $v < v_{min}$. We choose a cut of $v > 0.025$. The data include events with scattering vertices upstream of the MMS. These are eliminated by a cut in $z_{\rm vertex}$ corresponding to the front of plate 0. Muons which penetrate a paddle counter near the edge adjoining the staves can veto themselves by producing a δ-ray which hits a stave. While some of the effects of δ-rays on track finding and resolution were empirically modeled, the effect on the trigger was neglected. For this reason an aperture cut of 0.5 cm was applied to the inside edges of the paddle counters. A study of real events whose muons passed near the edge of one paddle and triggered in three other paddles further downstream showed this to be adequate. These cuts remove about 20% of the data.

Additional cuts not absolutely required by the simulation are applied to remove events that are likely to have been badly misanalyzed or come from regions of poor resolution. We require that there be one and only one scattered track and that the reconstructed track be consistent with the recorded pattern of hit counters that triggered the event. Because there was no calorimeter counter in the gap following plate 0, the calorimeter cannot be used to improve ν resolution for events with vertices in plate 0. We eliminate these events and also, to allow for our finite vertex resolution, those in the first plate of module 1. Table 9-I shows the set of kinematic cuts applied before analysis. Cuts in parentheses removed only an infinitesimal number of events. The regions removed are populated by the extreme tails of the resolution and energy loss distributions. As an example, large missing energy indicates a catastrophic energy loss by

Table 9-I. Kinematic cuts. Those in parentheses remove a negligible number of events.

Variable	93 GeV	215 GeV
E	$75 < E < 96$ GeV	$196 < E < 217$ GeV
ν	> 10 GeV	> 20 GeV
E'	$(> 10$ GeV$)$	> 10 GeV
W^2	$(> 8$ (GeV/c^2)^2)	> 16 (GeV/c^2)^2
$E_{\rm miss}$	< 48 GeV	< 96 GeV

the beam muon before scattering. Although such losses were included in our simulation, these events are badly misanalyzed. This second set of cuts removes about 20% of the events surviving the first set. There remain 394 522 (39 061) events in the 215 (93) GeV sample.

9.2 Normalization correction and uncertainty

The normalization of the data is determined by the fixed relation between data and simulation achieved through the use of the prescaled sample of real beam tracks in the simulation. Deficiencies in the simulation are revealed by different losses to reconstruction failures and cuts in the real and simulated samples. This necessitates small corrections to the normalization. Before comparing real and simulated event losses, the number of rejected real events itself had to be corrected. This is because some rejection categories are dominated by background events which do not appear in the simulation. Thus samples of rejected events from each loss category had to be hand scanned to determine what fraction were real deep inelastic scattering events. This fraction ranged from 0.13 ± 0.11 for events rejected due to too large an impact parameter between the beam and scattered tracks to 1.00 ± 0.08 for events in which the beam track was badly reconstructed and missed the lit trigger counters. Losses to cuts were also investigated in the same way. Of course, no correction to the normalization was made for the losses due to the "necessary" cuts discussed in the previous section, which were expected to be different for the real and simulated samples. The corrections, accumulated into three major categories, are shown in Table 9-II. The final corrections to the 215 and 93 GeV samples were 0.020 ± 0.002 and 0.028 ± 0.003, respectively.

The uncertainty in this correction was but one of the systematic uncertainties in the normalization. Others include uncertainties in the target thickness, magnetic field calibration, beam energy, and trigger counter efficiencies. Some of these are discussed in more detail in the next chapter. We estimate that in total the normalization uncertainties for the 215 and 93 GeV samples are each 3%. Since some of these uncertainties are common to both samples, the uncertainty in the relative normalization between the two samples is smaller and is estimated to be 2.5%.

9.3 Extraction of $F_2(x, Q^2)$

The basis for the extraction of $F_2(x, Q^2)$ from the raw population of measured events is Eq. 8.4. Since our $d\sigma^{\rm gen}$ includes radiative corrections, with an assumption about R we can

Table 9-II. Normalization correction.

215 GeV losses

Source	Data	Simulation	Correction
Track finding	0.0015±0.0007	0.0050±0.0004	−0.0035±0.0008
Event fitting	0.0238±0.0020	0.0148±0.0003	0.0090±0.0020
Cuts	0.1789±0.0006	0.1644±0.0006	0.0144±0.0008
Total			0.0199±0.0023

93 GeV losses

Source	Data	Simulation	Correction
Track finding	0.0048±0.0007	0.0080±0.0003	−0.0032±0.0008
Event fitting	0.0247±0.0011	0.0059±0.0002	0.0188±0.0011
Cuts	0.2089±0.0018	0.1968±0.0015	0.0121±0.0024
Total			0.0277±0.0028

cancel all the kinematic factors in Eq. 8.4 and are left with an expression for F_2

$$F_2^{\text{meas}}(x,Q^2) = \frac{nD(x,Q^2)}{M(x,Q^2)} F_2^{\text{gen}}(x,Q^2). \tag{9.1}$$

The normalization n now includes the corrections of the previous section. Besides providing the acceptance and radiative corrections to the data, Eq. 9.1 is also used to correct for resolution smearing effects. The rapidly varying cross section and the poor x resolution at low ν (see Figs. 6.4 and 6.5b) make this resolution correction essential. This is illustrated in Fig. 9.1 where the knowledge of the true kinematics of Monte Carlo-generated events is used to show the average value of x_{true} for bins of x_{measured}. From this figure one can easily determine where data points will and will not appear in our final F_2 plots. For example, we cannot determine F_2 at $Q^2 = 128\ \text{GeV}^2/c^2$, $x = 0.75$, even though we have hundreds of events with (unsmeared) Q^2 and x in this bin and the acceptance of the MMS in this region is at its maximum. The resolution-induced feed down from the more populous low x region (see Fig. 6.5b) makes it impossible to isolate a subset of the data at this Q^2 with an average true x of 0.75. Even at smaller x, there is a discrepancy between the measured and average true values of x for the same reason.

We correct for this feed down by using Eq. 9.1 and information of the type used to make Fig. 9.1. With real and simulated data divided into bins of measured x and Q^2, (x_m, Q^2_m), the simulated events in each bin are used to determine $\langle x_{\text{true}}\rangle$ and $\langle Q^2_{\text{true}}\rangle$ for that bin. F_2^{gen} is calculated at these average true values of x and Q^2 and the resulting F_2^{meas} is assumed to refer to these same values. Eq. 9.1 thus actually reads

$$F_2^{\text{meas}}(x(x_m,Q^2_m),Q^2(x_m,Q^2_m)) = \frac{nD(x_m,Q^2_m)}{M(x_m,Q^2_m)} F_2^{\text{gen}}(x(x_m,Q^2_m),Q^2(x_m,Q^2_m)) \tag{9.2}$$

where x and Q^2 are the average true values for the bin of measured variables (x_m, Q^2_m).

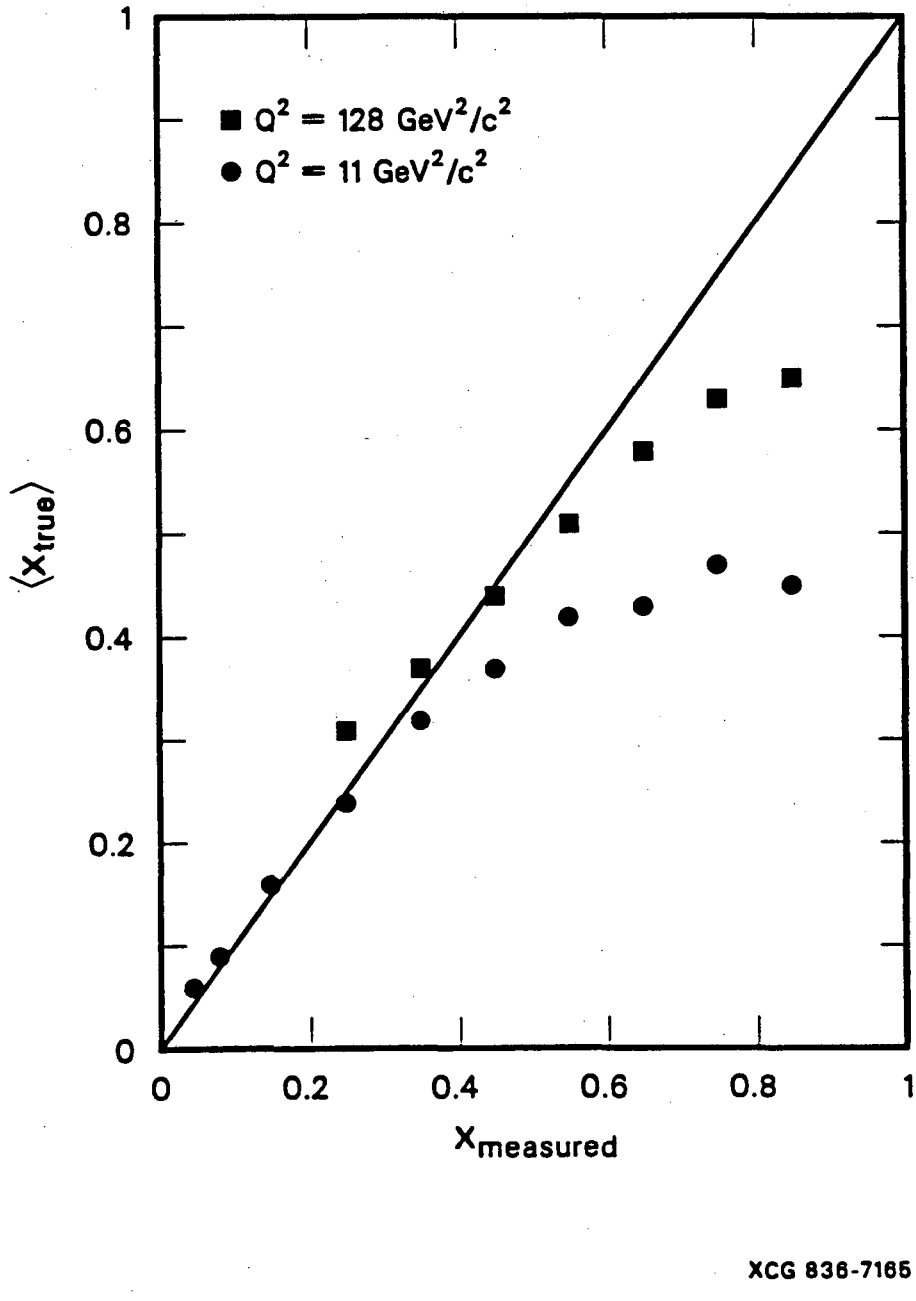

Fig. 9.1. Limiting effects of x resolution. Plotted is the average value of x_{true} for bins of $x_{measured}$ as calculated in our apparatus simulation.

The presence of F_2^{gen} in Eqs. 9.1 and 2 suggests that the F_2^{meas} yielded by this procedure is model dependent. Considering the simulation as merely an acceptance calculation or noting that $M(x, Q^2)$ is proportional to $F_2^{gen}(x, Q^2)$, demonstrates that, to first order, this is not the case, However, changing the model sufficiently could change the shapes of distributions enough to affect the smearing or the distribution of events within finite sized bins. We remove this model dependence by empirically fitting F_2^{meas} and using this as the F_2^{gen} for a next iteration. This is done by weighting the existing simulated events by the ratio of new to old F_2^{gen}. The normalization correction due to the final set of cuts must be recalculated for each iteration. The values presented above are for the final iteration. The signals that the iteration has converged are 1) stability against further change, and 2) identical distributions of data and simulation in many variables. In practice, one iteration satisfies both requirements. In Fig. 9.2 we show comparisons of data and Monte Carlo-simulated events in several variables before and after this iteration for the 215 GeV sample. Only the x and Q^2 dependence is explicitly changed. Most of the effect in all three variables shown is due to changing the x dependence of F_2. Note that the shaping is done in real (unsmeared) variables and that agreement in the resolution-dominated tails of measured distributions such as at large x depends on the accuracy of the apparatus simulation. The 93 GeV sample is done separately using the same procedure.

Other resolution unsmearing techniques were attempted in an effort to extend our measurements further into the high x region. Various global unfolding techniques were tried,[56] but none were reliable in the regions not covered by the scheme described above. It should be pointed out that the actual unsmearing power of our scheme resides equally in the use of Eq. 9.2 and in the iteration procedure. When the iteration is complete, our parametrization is in fact a determination of F_2 over the entire x range, since true values of x from the entire range are smeared to yield agreement with the measured distribution. Away from the directly measured region, however, this determination is limited by the form of the parametrization and is not very sensitive.

Table 9-III lists our measured values of F_2 in the raw form produced by Eq. 9.2, that is. with each point referred to its own average true x and Q^2. The entries have passed a final set of three cuts. We have eliminated points whose statistical uncertainty in F_2 is greater than 40%. We have eliminated points from regions with acceptance less than about 0.1 of the maximum, which corresponds to retaining the region $x > 0.06$ and $Q^2 > 15\,(5)$ GeV$^2/c^2$ for the 215 (93) GeV data. We have also eliminated measurements with minimal sensitivity in x by rejecting points for which smearing from other bins contributes greater than 90% of the events finally appearing in the bin. The correction to F_2 due to resolution smearing in the retained points is typically 10%, increasing at large x. Our results are not sensitive to the exact values of these cuts. The interpolation to our final grid of x and Q^2 is described in the next chapter.

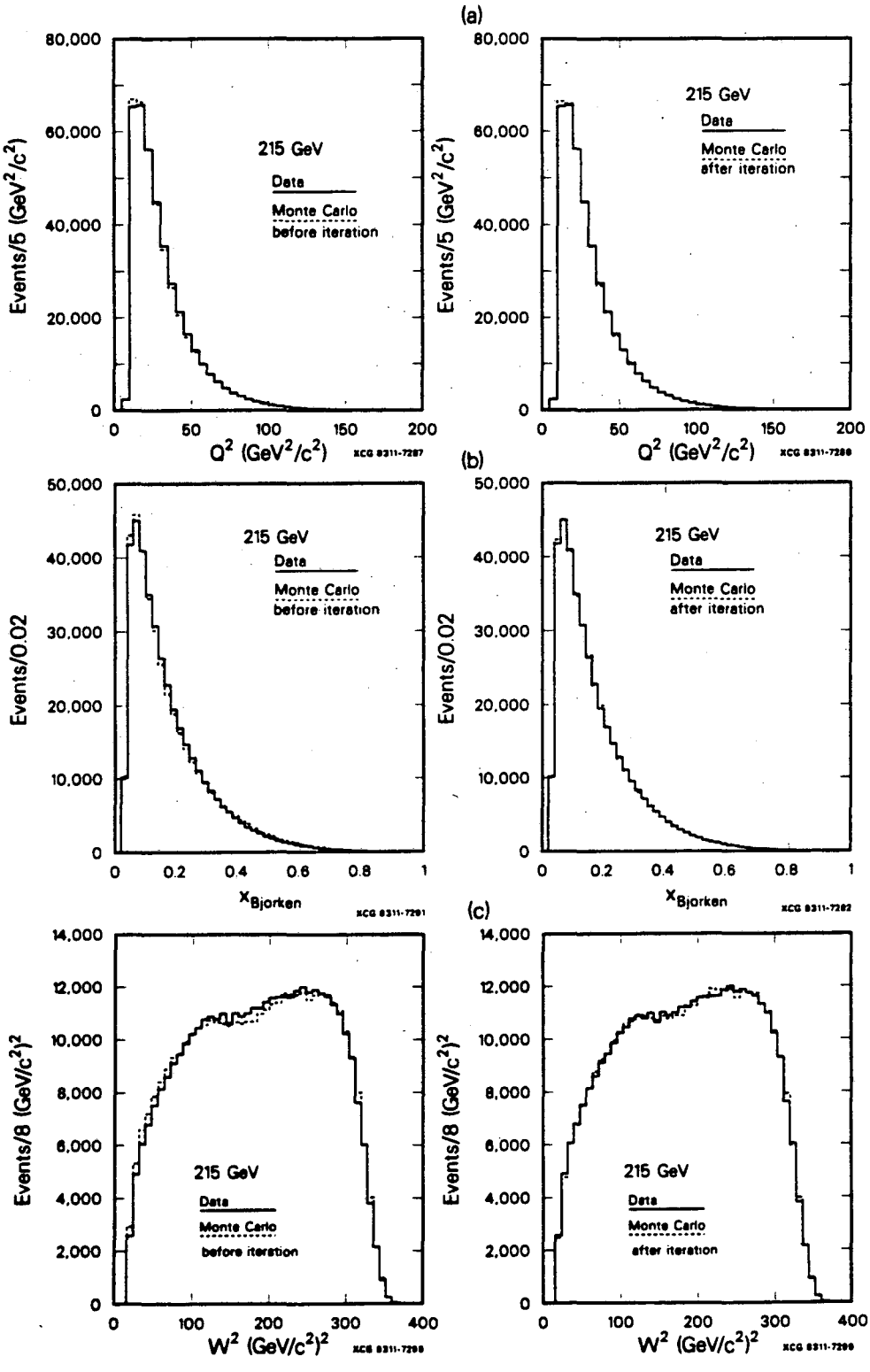

Fig. 9.2. Distributions of real and simulated events before and after the F_2^{gen} iteration procedure described in the text.

Table 9-III. Raw $F_2(x,Q^2)$ at 93 GeV. For each measured bin, $F_2(x,Q^2)$ is presented at the average true x and Q^2 of that bin. Errors are statistical.

x	Q^2 (GeV$^2/c^2$)	$F_2(x,Q^2)$
0.0965	5.30	0.3890 ± 0.0105
0.0992	7.13	0.3766 ± 0.0099
0.1050	9.53	0.3661 ± 0.0114
0.1161	12.36	0.3729 ± 0.0228
0.1591	5.29	0.3375 ± 0.0092
0.1584	7.26	0.3600 ± 0.0084
0.1575	9.78	0.3478 ± 0.0074
0.1601	13.30	0.3227 ± 0.0077
0.1703	17.67	0.3207 ± 0.0104
0.1904	22.25	0.2716 ± 0.0201
0.2343	5.33	0.2923 ± 0.0111
0.2384	7.15	0.2867 ± 0.0088
0.2401	9.74	0.2666 ± 0.0075
0.2398	13.28	0.2574 ± 0.0073
0.2403	17.94	0.2578 ± 0.0080
0.2435	24.22	0.2436 ± 0.0091
0.2647	31.06	0.2259 ± 0.0163
0.2802	5.69	0.2677 ± 0.0344
0.3067	7.16	0.2257 ± 0.0103
0.3131	9.62	0.2144 ± 0.0083
0.3189	13.13	0.2021 ± 0.0081
0.3284	17.94	0.1986 ± 0.0083

x	Q^2 (GeV$^2/c^2$)	$F_2(x,Q^2)$
0.3299	24.19	0.1722 ± 0.0082
0.3355	32.99	0.1601 ± 0.0098
0.3542	42.67	0.1187 ± 0.0168
0.3554	7.60	0.2337 ± 0.0294
0.3719	9.49	0.1773 ± 0.0093
0.3825	12.81	0.1602 ± 0.0089
0.3946	17.83	0.1495 ± 0.0085
0.4049	24.11	0.1374 ± 0.0088
0.4162	32.33	0.1169 ± 0.0090
0.4199	42.87	0.0964 ± 0.0112
0.4101	9.87	0.1240 ± 0.0132
0.4269	12.61	0.1141 ± 0.0085
0.4551	17.40	0.1092 ± 0.0090
0.4646	23.62	0.0911 ± 0.0085
0.4768	32.27	0.0764 ± 0.0086
0.4951	43.11	0.0542 ± 0.0082
0.5146	56.97	0.0499 ± 0.0176
0.4871	17.09	0.0888 ± 0.0096
0.5091	23.22	0.0830 ± 0.0105
0.5235	31.05	0.0550 ± 0.0090
0.5332	42.23	0.0467 ± 0.0093
0.5801	56.65	0.0444 ± 0.0138

Table 9-III. –continued. Raw $F_2(x, Q^2)$ at 215 GeV. For each measured bin, $F_2(x, Q^2)$ is presented at the average true x and Q^2 of that bin. Errors are statistical.

x	Q^2 (GeV$^2/c^2$)	$F_2(x, Q^2)$
0.0736	16.31	0.3852 ± 0.0053
0.0781	18.13	0.3967 ± 0.0652
0.0925	18.29	0.3794 ± 0.0028
0.1026	23.70	0.3667 ± 0.0028
0.1175	30.61	0.3603 ± 0.0045
0.1326	34.22	0.2972 ± 0.0306
0.1563	18.68	0.3261 ± 0.0037
0.1564	25.06	0.3246 ± 0.0029
0.1575	33.56	0.3257 ± 0.0027
0.1686	43.68	0.3146 ± 0.0030
0.1917	55.67	0.2765 ± 0.0055
0.2438	18.68	0.2466 ± 0.0044
0.2439	25.25	0.2428 ± 0.0034
0.2415	33.85	0.2469 ± 0.0030
0.2427	45.74	0.2446 ± 0.0029
0.2470	61.64	0.2336 ± 0.0030
0.2670	78.30	0.2113 ± 0.0045
0.2922	92.56	0.2120 ± 0.0410
0.3220	18.45	0.1940 ± 0.0052
0.3255	24.91	0.1852 ± 0.0040
0.3306	33.82	0.1830 ± 0.0034
0.3307	45.67	0.1762 ± 0.0031
0.3352	61.68	0.1644 ± 0.0030
0.3421	83.72	0.1589 ± 0.0033
0.3598	106.28	0.1427 ± 0.0054
0.3780	18.58	0.1514 ± 0.0063

x	Q^2 (GeV$^2/c^2$)	$F_2(x, Q^2)$
0.3920	24.60	0.1416 ± 0.0045
0.4049	33.48	0.1319 ± 0.0036
0.4091	45.32	0.1276 ± 0.0033
0.4149	61.01	0.1086 ± 0.0028
0.4163	82.30	0.1073 ± 0.0032
0.4303	111.10	0.0927 ± 0.0035
0.4431	136.49	0.0788 ± 0.0095
0.4175	19.48	0.1282 ± 0.0129
0.4313	24.12	0.1188 ± 0.0054
0.4514	33.04	0.1047 ± 0.0041
0.4684	44.44	0.0919 ± 0.0035
0.4855	60.45	0.0720 ± 0.0028
0.4822	80.84	0.0661 ± 0.0027
0.4933	109.42	0.0672 ± 0.0035
0.5148	143.17	0.0407 ± 0.0037
0.4815	32.60	0.0892 ± 0.0052
0.5159	44.07	0.0670 ± 0.0037
0.5255	59.27	0.0566 ± 0.0033
0.5353	79.92	0.0492 ± 0.0030
0.5575	107.94	0.0394 ± 0.0029
0.5812	142.99	0.0382 ± 0.0040
0.6056	186.69	0.0394 ± 0.0161
0.5880	79.71	0.0393 ± 0.0036
0.6187	107.23	0.0296 ± 0.0031
0.6026	137.44	0.0285 ± 0.0042
0.6511	182.23	0.0120 ± 0.0043

Chapter 10

Results

It's time to fish or cut bait ... or both.

T. Markiewicz (apocryphal)

10.1 $F_2(x, Q^2)$

The raw F_2 measurements of Table 9-III are interpolated onto a grid of fixed true x and Q^2 using the final fit (see next section) as an interpolating function. The grid is chosen to be the same as that used to bin the events initially in measured x and Q^2. In Q^2, the effects of resolution smearing, and thus of the interpolation, are minor. This is aided by the approximate scaling of F_2. In x, $\langle x_{\rm true}\rangle$ may bear little resemblance to the measured x bin it corresponds to. For this reason, the F_2 measurements were interpolated to the bin center of the bin in the final grid which contained $\langle x_{\rm true}\rangle$ for that point, independent of which bin of measured x the point came from. Thus a point from a bin of measured x between 0.6 and 0.7 with $\langle x_{\rm true}\rangle = 0.42$ would be interpolated to $x_{\rm true} = 0.45$. This procedure can result in several bins producing measurements at the same true x and Q^2. A minimum requirement on our extraction method is that these measurements give the same value of F_2, that is, that they have the same ratio of real to simulated events. Figure 10.1 shows the $x = 0.45$ section of our 215 GeV data. The agreement between points at the same Q^2 (originally from different bins of measured x) is good. These points are averaged after fitting to create our final $F_2(x, Q^2)$ results.

The resulting measurements of $F_2(x, Q^2)$ are presented separately for the two beam energies in Table 10-I and in Fig. 10.2. We have assumed $R = 0$ and have made no correction for Fermi motion. The F_2 values thus represent $F_2^{\rm Fe}/56$. The effects of Fermi motion and non-zero R are discussed below. As a consequence of the above procedure, the measurements refer to F_2 at the indicated true x and Q^2 and are not bin averages. Because of this fact, a few of the points appear to have $y > 1$. This is simply because the center of the Q^2 bin lies above the kinematic limit and the original $\langle Q^2_{\rm true}\rangle$ was near the lower edge of the bin. In using these measurements, these points can be ignored if the y dependence is important, or the raw measurements of Table 9-III can be used. The listed and plotted errors are statistical. As systematic errors cause correlated shifts in the data we do not attach systematic uncertainties to individual points – systematic errors are discussed in detail in a later section. One powerful test of the internal consistency of our data is the agreement of the 93 and 215 GeV measurements. Figure 10.2 shows this agreement to be quite good. Although the χ^2 for the overlap is 33 for 15 degrees of freedom (dof), over half of this comes from two points. When these are ignored, the χ^2 drops to 14/13 dof. In these

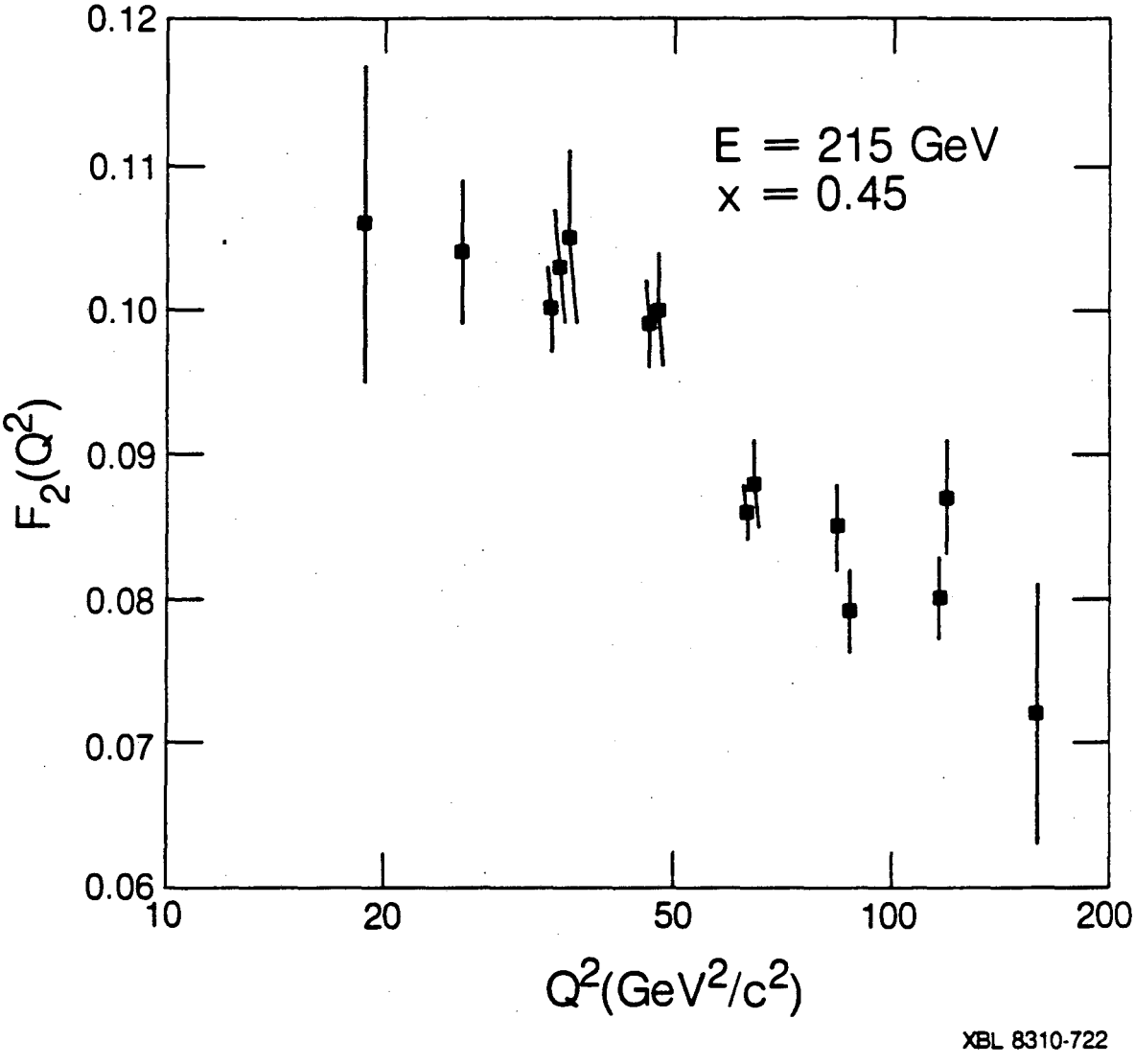

Fig. 10.1. The $x = 0.45$ bin of our 215 GeV $F_2(x, Q^2)$ measurement, after interpolation to the grid of true x and Q^2, but prior to averaging of measurements assigned to the same point. Values at the same point have been displaced slightly in Q^2 for clarity.

Table 10-L The structure function $F_2(x, Q^2)$ on a fixed grid of x and Q^2. $R = 0$ is assumed and no Fermi motion correction has been applied. (Table continued on next page.)

x	Q^2	F_2 (93 GeV)	F_2 (215 GeV)	F_2 (combined)
0.08	5.54	0.3997 ± 0.0108		0.3997 ± 0.0108
	7.52	0.3905 ± 0.0103		0.3905 ± 0.0103
	10.2	0.3855 ± 0.0120		0.3855 ± 0.0120
	18.8		0.3894 ± 0.0026	0.3894 ± 0.0026
	25.6		0.3906 ± 0.0030	0.3906 ± 0.0030
0.15	5.54	0.3430 ± 0.0094		0.3430 ± 0.0094
	7.52	0.3657 ± 0.0085		0.3657 ± 0.0085
	10.2	0.3531 ± 0.0075		0.3531 ± 0.0075
	13.9	0.3321 ± 0.0074		0.3321 ± 0.0074
	18.8	0.3364 ± 0.0109	0.3309 ± 0.0037	0.3315 ± 0.0035
	25.6	0.3017 ± 0.0223	0.3296 ± 0.0030	0.3291 ± 0.0030
	34.8		0.3330 ± 0.0023	0.3330 ± 0.0023
	47.2		0.3303 ± 0.0031	0.3303 ± 0.0031
	64.1		0.3148 ± 0.0062	0.3148 ± 0.0062
0.25	5.54	0.2811 ± 0.0102		0.2811 ± 0.0102
	7.52	0.2764 ± 0.0085		0.2764 ± 0.0085
	10.2	0.2576 ± 0.0072		0.2576 ± 0.0072
	13.9	0.2480 ± 0.0070		0.2480 ± 0.0070
	18.8	0.2481 ± 0.0077	0.2413 ± 0.0043	0.2429 ± 0.0038
	25.6	0.2365 ± 0.0088	0.2373 ± 0.0033	0.2372 ± 0.0031
	34.8	0.2351 ± 0.0170	0.2386 ± 0.0029	0.2385 ± 0.0029
	47.2		0.2370 ± 0.0029	0.2370 ± 0.0029
	64.1		0.2300 ± 0.0029	0.2300 ± 0.0029
	87.1		0.2253 ± 0.0048	0.2253 ± 0.0048
	118.3		0.2479 ± 0.0479	0.2479 ± 0.0479
0.35	7.52	0.1961 ± 0.0084		0.1961 ± 0.0084
	10.2	0.1874 ± 0.0059		0.1874 ± 0.0059
	13.9	0.1791 ± 0.0058		0.1791 ± 0.0058
	18.8	0.1808 ± 0.0061	0.1729 ± 0.0039	0.1752 ± 0.0033
	25.6	0.1578 ± 0.0076	0.1686 ± 0.0030	0.1671 ± 0.0028
	34.8	0.1500 ± 0.0091	0.1692 ± 0.0031	0.1672 ± 0.0029
	47.2	0.1192 ± 0.0168	0.1628 ± 0.0029	0.1615 ± 0.0029
	64.1		0.1545 ± 0.0028	0.1545 ± 0.0028
	87.1		0.1534 ± 0.0032	0.1534 ± 0.0032
	118.3		0.1475 ± 0.0056	0.1475 ± 0.0056

Table 10-I. – continued.

x	Q^2	F_2 (93 GeV)	F_2 (215 GeV)	F_2 (combined)
0.45	10.2	0.1009 ± 0.0107		0.1009 ± 0.0107
	13.9	0.0989 ± 0.0074		0.0989 ± 0.0074
	18.8	0.1092 ± 0.0071	0.1082 ± 0.0109	0.1089 ± 0.0059
	25.6	0.1032 ± 0.0055	0.1062 ± 0.0048	0.1049 ± 0.0036
	34.8	0.0929 ± 0.0059	0.1035 ± 0.0022	0.1022 ± 0.0021
	47.2	0.0756 ± 0.0070	0.1009 ± 0.0022	0.0986 ± 0.0021
	64.1		0.0882 ± 0.0019	0.0882 ± 0.0019
	87.1		0.0844 ± 0.0020	0.0844 ± 0.0020
	118.3		0.0833 ± 0.0025	0.0833 ± 0.0025
	160.7		0.0739 ± 0.0089	0.0739 ± 0.0089
0.55	25.6	0.0611 ± 0.0077		0.0611 ± 0.0077
	34.8	0.0444 ± 0.0072		0.0444 ± 0.0072
	47.2	0.0403 ± 0.0080	0.0522 ± 0.0028	0.0509 ± 0.0026
	64.1	0.0443 ± 0.0105	0.0469 ± 0.0027	0.0467 ± 0.0026
	87.1		0.0457 ± 0.0023	0.0457 ± 0.0023
	118.3		0.0412 ± 0.0030	0.0412 ± 0.0030
	160.7		0.0353 ± 0.0025	0.0353 ± 0.0025
0.65	118.3		0.0210 ± 0.0022	0.0210 ± 0.0022
	160.7		0.0171 ± 0.0025	0.0171 ± 0.0025
	218.3		0.0137 ± 0.0039	0.0137 ± 0.0039

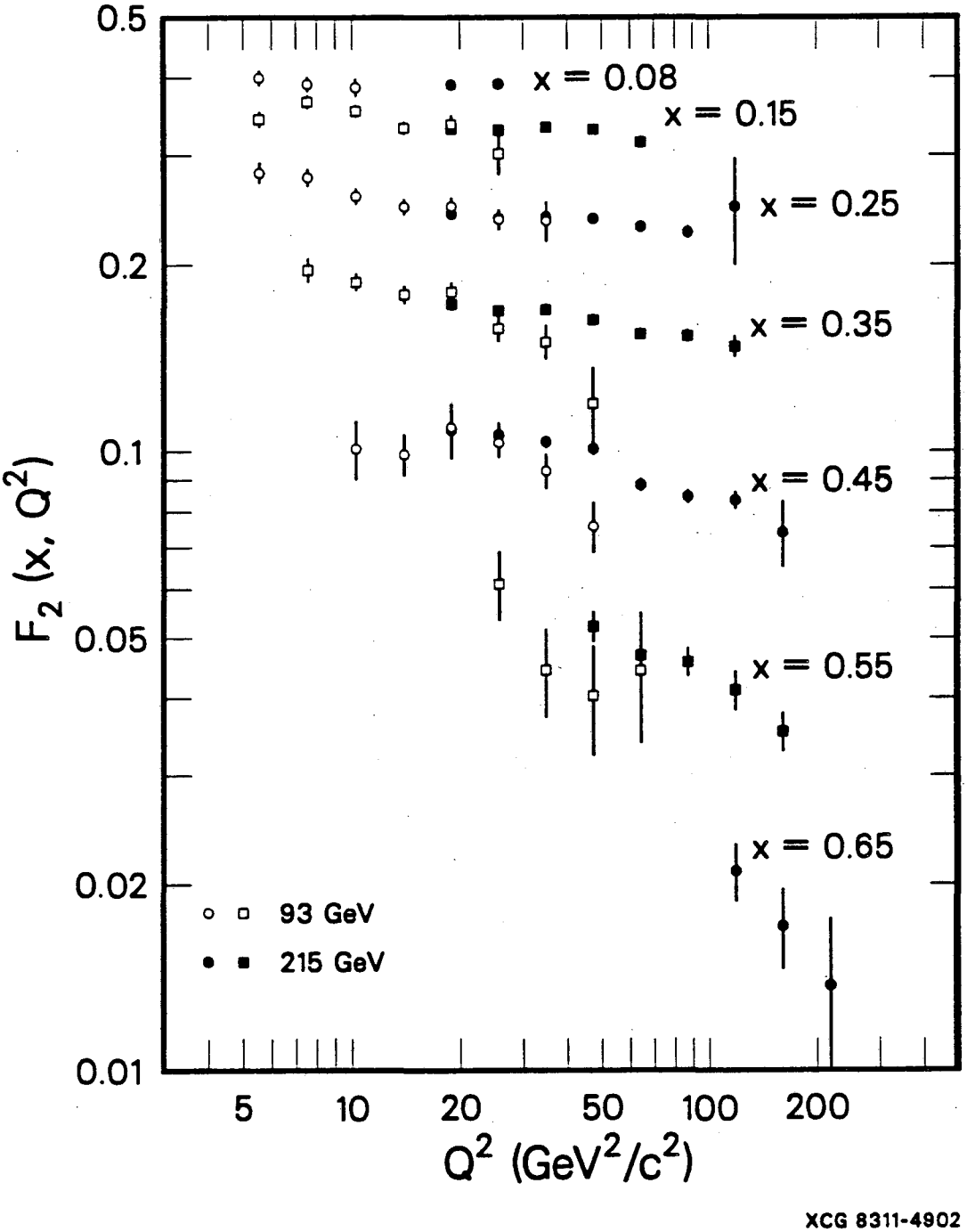

Fig. 10.2. F_2 for nucleons in iron as a function of Q^2 at various fixed values of x. 93 and 215 GeV data are shown separately. Errors are statistical.

data the scaling violation is plainly visible at $x > 0.2$. To treat this quantitatively, we fit the measurements using lowest order quantum chromodynamics.

10.2 Comparison to lowest order QCD

Fits are performed to the data of Table 9-III prior to the interpolation and coalescence of points in x. For convenience in fitting, the more gentle interpolation to Q^2 bin centers is performed before fitting. The core of our fitting program was modified from a routine kindly provided by R. M. Barnett. Its operation and use are described in Ref. 57. and summarized here.

The fitting program uses the Altarelli-Parisi method[27] to calculate the Q^2 dependence of F_2 at fixed x predicted by lowest order QCD for the flavor singlet case. Starting with parametrizations of $F_2(x)$ and $G(x)$ at a reference value of $Q^2 \equiv Q_0^2$ and an initial estimate of the QCD scale parameter Λ, the routine numerically integrates the set of simultaneous differential equations of Eq. 3.14 from Q_0^2 to each Q^2 at which there are F_2 measurements. There is one singlet-quark and one gluon equation for each bin of x with bin center x_i. At each Q^2, the predictions for $F_2(x_i, Q^2)$ are interpolated to the average true x of each measured point at that Q^2 using a cubic spline. The predicted and measured values are compared and the minimization program MINUIT[58] is used to vary Λ and the Q_0^2 parametrization so as to minimize the χ^2. Note that operationally Q_0^2 is largely symbolic, as the data at all Q^2 are used to determine all the parameters.

Our parametrization at $Q_0^2 = 5.535\ \mathrm{GeV}^2/c^2$ is

$$\begin{aligned} F_2(x, Q_0^2) &= \frac{5}{18} \sum_{i=1}^{2N_f} x f_i(x) = A x^{\alpha}(1-x)^{\beta}(1+ax) + B(1-x)^{\gamma}, \\ G(x, Q_0^2) &= C(1-x)^{\delta}. \end{aligned} \tag{10.1}$$

The two terms of the F_2 parametrization are inspired by the conceptual division of the quarks into "valence" and "sea" distributions. The $\frac{5}{18}$ is the average charge squared of the $SU(2)$ singlet (valence) or $SU(4)$ singlet (sea) quarks. This interpretation is not essential, however, and all we actually demand of Eqs. 10.1 is that they be sufficiently general. In our standard fit, we fix $a = 0$, $\gamma = 8$, and $\delta = 5$. The variation of these parameters is discussed below. The parameters α, β, A, B, and Λ are fitted. The parameter C determines the fraction of the nucleon's momentum that is carried by gluons. With the other parameters known, C is fixed by normalization of the fractional momentum distributions

$$\int_0^1 \left[\frac{18}{5} F_2(x) + G(x)\right] dx = 1 \tag{10.2}$$

which gives

$$C = (1-\gamma)\left\{1 - \frac{18}{5}\left[AB(1+\alpha, 1+\beta)\left(1 + \frac{a(1+\alpha)}{2+\alpha+\beta}\right) + \frac{B}{1-\delta}\right]\right\}. \tag{10.3}$$

B is the beta function, $B(z,w) = \Gamma(z)\Gamma(w)/\Gamma(z+w)$. We fit the pure singlet case - no correction is made for the neutron excess in iron.

The result of the standard fit applied simultaneously to the 215 and 93 GeV measurements is shown in Fig. 10.3. The family of curves traces the Q^2 variation of F_2 at various values of x from the single global fit. We find a value for Λ of 225 MeV/c with a statistical error of 43 MeV/c. The values of the other fitted parameters and their statistical errors are listed as entry (a) of Table 10-II. Each error represents the allowed excursion of the parameters for a unit increase of χ^2. The marginal χ^2 of the fit (154/91 degrees of freedom) implies that this is an underestimate of the actual uncertainties, either due to the inadequacy of lowest order QCD, to our structure of assumptions, or to the presence of systematic errors. As discussed below, the uncertainties due to these possibilities outweigh those of a purely statistical origin. Entries (b)-(d) of Table 10-II show the minor effects of changing the form of the parametrization. The parameters are sufficiently correlated to allow a restructuring of the parametrization to give nearly the same $F_2(x, Q_0^2)$, without affecting Λ. Changing Q_0^2 from 5.535 to 25 GeV$^2/c^2$ has no effect on Λ.

We can ask whether the other fitted parameters give us any physically meaningful information. The experimental distinction between the charged quarks and the neutral gluons is clear. From the integral of the fitted distributions, we find that 48% of the nucleon's momentum is carried by gluons at Q_0^2. The separation between valence and sea quarks in our case is carried entirely by the parametrization. If we choose to interpret the second term of the F_2 parametrization (Eq. 10.1) as representing the sea, the standard fit tells us that 16% of the momentum of the target nucleon is carried by quark-antiquark pairs. However, an immediate problem occurs with the subsequent identification of the first term as the valance quark contribution. If we remove the charge-squared factor and one power of x from this term, we get back the "valence" quark momentum distribution. Integrating this over x counts the valence quarks. This is a weaker (model dependent) version of the Gross-Llewellyn Smith sum rule for F_3 in neutrino scattering.[59] Unfortunately, performing these operations with the results of our standard fit gives 2.04 valence quarks instead of three. If we constrain the parameter A in Eq. 10.1 to give three valence quarks, we get the fit labeled (e) in Table 10-II. The sea momentum fraction in this fit is 11%; Λ and the gluon fraction are virtually unchanged. Even with this constraint, my confidence in this valence-sea separation is minimal. On the other hand, the constrained results are in remarkably precise agreement with more direct neutrino results.[29] Using the neutrino's ability to distinguish between quarks and antiquarks, an antiquark structure function $\overline{q}(x)$ ($\approx \frac{1}{2} \times$ the sea) can be measured. With this additional input, the neutrino measurements yield a gluon momentum fraction of 55%, an antiquark momentum fraction of 5.5%, and $\Lambda_{\rm LO} = 180$ MeV/c.

10.3 Systematic uncertainties

We define systematic uncertainties to mean uncertainties whose origins are purely experimental and affect the measured cross section. Uncertainties that affect the interpretation of the measured cross section, say in terms of Λ, will be discussed in the next section. Neither the estimation nor the presentation of systematic effects is an exact science. We begin by making a catalog of possible sources of experimental uncertainty. An example would be the MMS magnetic field calibration. We next estimate the magnitude of the uncertainty in each source and how it would affect our analysis. We then reanalyze the data with each source in turn changed to reflect its uncertainty, and we observe the effect on our measured and fitted $F_2(x, Q^2)$. We also make various tests of internal consistency to reveal possible problems. The changes to $F_2(x, Q^2)$ from systematic effects are typically correlated. Thus assigning errors to individual measured points is misleading. Showing bands of uncertainty on our F_2 plots is also unsatisfactory – the top of one band may correspond to the bottom of another. We will thus give only a representative example

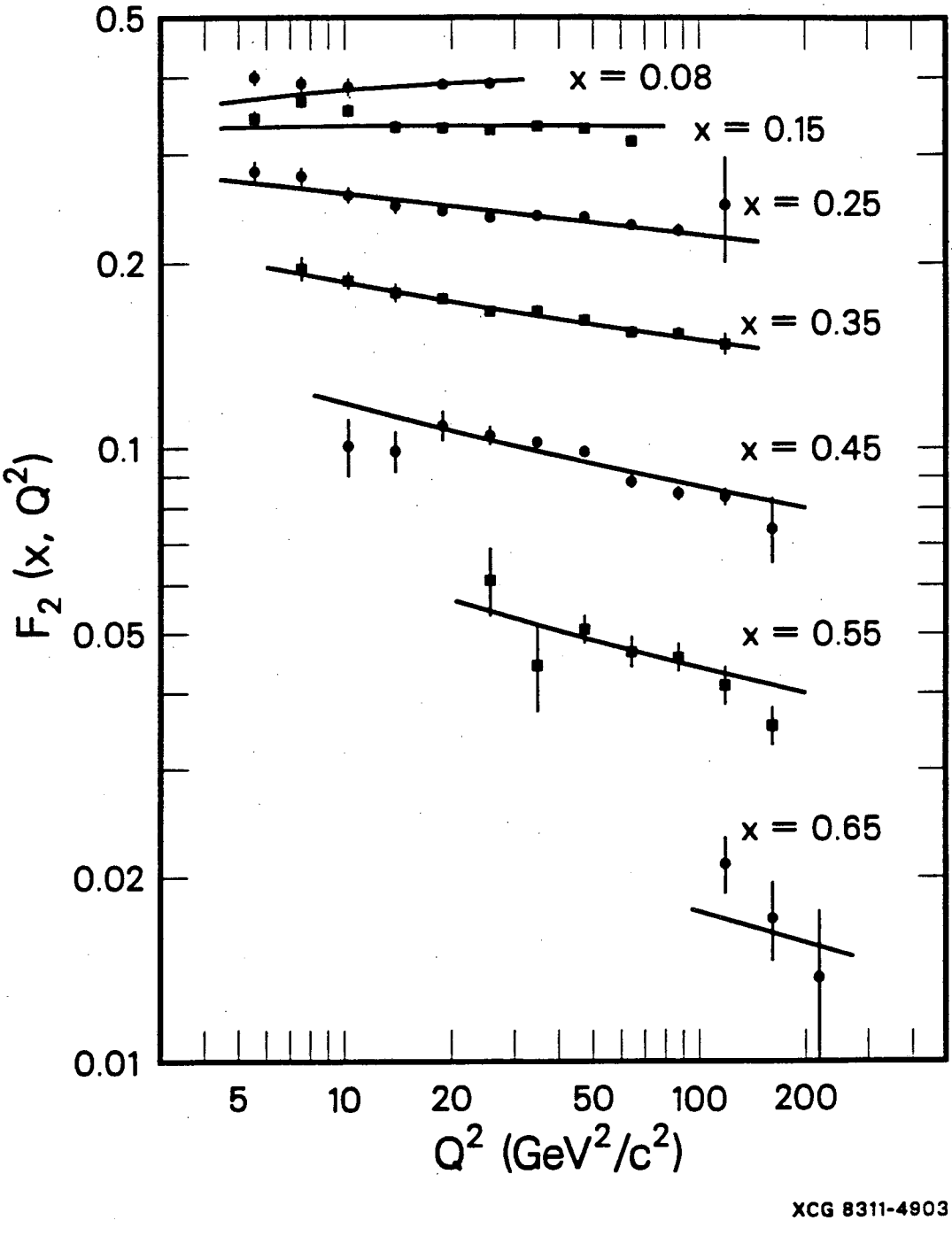

Fig. 10.3. Results of the lowest-order QCD fit applied simultaneously to the 93 and 215 GeV measurements of $F_2(x, Q^2)$. These measurements have been averaged after fitting. The curves represent the Q^2 dependence of F_2 at various fixed values of x predicted by the single global fit.

Table 10-II. Results of lowest order QCD fits to $F_2(x, Q^2)$. $F_2(x, Q_0^2) = Ax^\alpha(1-x)^\beta(1+ax) + B(1-x)^\gamma$; $G(x, Q_0^2) = C(1-x)^\delta$; a, γ, δ fixed; C from momentum sum rule; α, β, A, B, and Λ fitted. Errors are statistical and represent $\Delta\chi^2 = 1$ excursions in the fit.

Fit	Λ (MeV/c)	α	β	A	B	a	χ^2/dof	Comment
a. Std: $\gamma = 8$, $\delta = 5, a = 0$	225 ± 43	1.00 ± 0.10	3.80 ± 0.15	2.74 ± 0.44	0.410 ± 0.036	—	154/91	$Q_0^2 = 5.535$ GeV$^2/c^2$
b. Fit a	225 ± 43	0.51	3.97	0.84	0.948	3.24	153/90	
c. $\gamma = 12$	230 ± 44	0.71	3.56	1.92	0.350	—	153/91	
d. $\alpha = B = 0$, fit a	217 ± 43	—	3.43	0.37	—	3.73	160/92	
e. Sum rule normalization	222 ± 43	0.67	3.35	1.61	0.265	—	164/92	
f. Fit 93 GeV normalization	176 ± 43	0.99	3.83	2.67	0.409	—	148/90	normalization lowered by $2.0 \pm 0.8\%$
g. Standard, EMC data (Ref. 67)	159 ± 25	0.65	3.29	1.41	0.258	—	230/153	$Q_0^2 = 5.50$ GeV$^2/c^2$

Table 10-III. Systematic uncertainties in Λ. The total indicates the sum of the other entries in quadrature.

Source	Uncertainty	$\delta\Lambda$ (MeV/c)
MMS B-field calibration	0.5%	< 10
Beam energy	0.5%	10
Trigger efficiency (systematic)	0.5%	16
Trigger efficiency (statistical)	(see text)	10
Resolution smearing	(see text)	50
93/215 GeV normalization	2.5%	60
Total		82

of the effect on $F_2(x, Q^2)$, but concentrate on the global effects on our fitted results, notably on Λ. Our catalog of systematic effects is listed in Table 10-III.

The first source of systematic uncertainty to be checked was the MMS magnetic field calibration. From the evidence presented in Sec. 7.2 we conclude that the uncertainty in the field is, conservatively, ±0.5%. What would the effect of a 0.5% miscalibration be? Since both the beam system and the calorimeter were calibrated to the spectrometer, the result is an overall shift in the measured energy scale. This would be easy to simulate – change the incident beam energy and MMS field by 0.5% in the simulation and analyze with the original values – but time-consuming and expensive. Instead, we reason backwards from the existing simulated events, a procedure to be used often in this section. By using the existing simulated events we have fixed the trajectory, that is, the angle, curvature and triggering probability of each track in the MMS. We reinterpret the true momentum of both the incident and scattered tracks in accordance with the new assumed field value. If $\overline{B} = \epsilon B$ (with $\epsilon = 1.005$), we find $\overline{Q^2} = \epsilon^2 Q^2$, $\overline{x} = \epsilon x$, and $\overline{y} = y$. Had we actually redone the simulation, this change in kinematics would have caused a corresponding change in the cross section for each event. We therefore assign each simulated event a new true x and Q^2 and a weight given by

$$\frac{\overline{d\sigma}}{d\sigma} = \frac{1}{\epsilon^3} \frac{F_2(\epsilon x, \epsilon^2 Q^2)}{F_2(x, Q^2)} \tag{10.4}$$

as implied by Eq. 8.5. This method is not exact. Radiative corrections, MCS, *etc.* are left at the old energy scale and $\overline{x} = \epsilon x$ must break down at the kinematic limit. For small adjustments in B, however, it should be adequate. It has the advantage that by using the same events, the modified results are highly correlated to the original set, and thus small changes are readily visible in spite of statistical fluctuations. The most notable change caused by the adjustment in B is the shift in normalization. This, as well as the other effects of this section, has been taken into account in the estimate of the normalization uncertainty quoted earlier. The changes in shape are minor, as expected from an overall scale change. As indicated in Table 10-III, the uncertainty in Λ from this source is less than 10 MeV/c.

We expect more substantial effects from a differential shift of the beam energy (measured exclusively in the beam system) relative to that of the scattered track. The precision of the calibration of beam to spectrometer rules out such a relative shift of greater than a few tenths of a percent. We consider a total uncertainty of ±0.5% to allow for uncertainty due to the discrepancy between the two MMS polarities and for possible effects in the analysis of the average

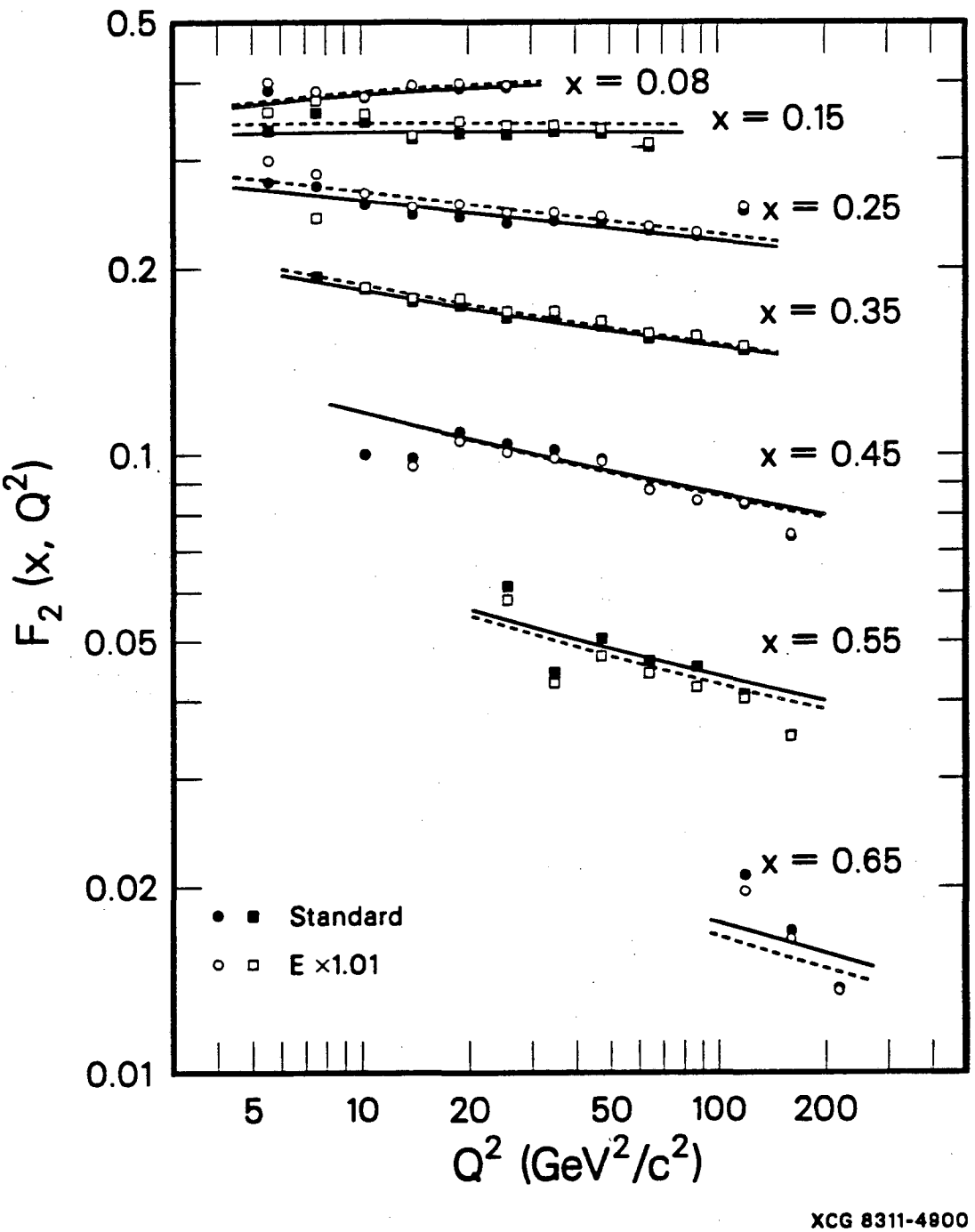

Fig. 10.4. Systematic effects of a 1% shift in beam energy ($\approx$ 2 $\times$ the estimated uncertainty). The normalization of the 93 GeV data has been allowed to float in each case. The solid (dashed) curves are the QCD fit to the standard (shifted) data. The difference in Λ between the fits is 20 MeV/c.

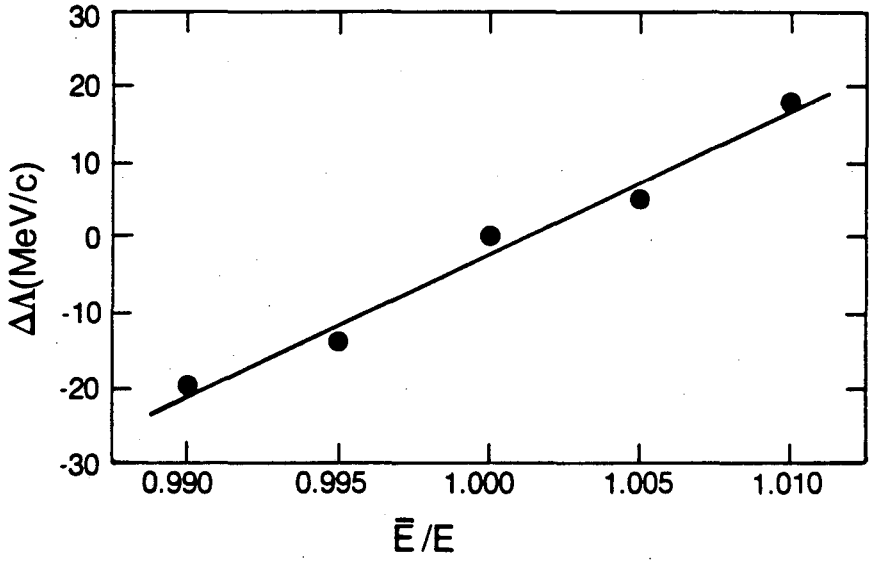

Fig. 10.5. The dependence of Λ on systematic error in the beam energy calibration relative to that of the MMS. The estimated uncertainty is 0.005. The line is a fit to the points with slope (19 MeV/c) per (1% shift).

energy loss of the beam muon en route to the vertex. The effect of beam energy shifts was determined in the same fashion as the previous case. To use existing events, we neglect the shift of less than 1 mm in the vertex position and have $\overline{E} = \epsilon E$, $\overline{E'} = E'$, and $\overline{\theta} = \theta$. This gives $\overline{Q^2} = \epsilon Q^2$, $\overline{y} = 1 - (1-y)/\epsilon$, $\overline{x} = xy/\overline{y}$, and

$$\frac{\overline{d\sigma}}{d\sigma} = \frac{1}{\epsilon}\left(\frac{y}{\overline{y}}\right)^2 \frac{(1-\overline{y}+\overline{y}^2/2)}{(1-y+y^2/2)} \frac{F_2(\overline{x},\overline{Q^2})}{F_2(x,Q^2)}. \tag{10.5}$$

Figure 10.4 shows the effect of such an energy shift, magnified to $\epsilon = 1.01$ for clarity. We have allowed the 93 GeV normalization to adjust to that of the 215 GeV data. As mentioned above, the corresponding points of each set are highly correlated and only their separation is meaningful. The error bars have thus been suppressed. The curves show the fit to each case. They also demonstrate the effect of changing Λ, in this case by 20 MeV/c, on the slope of $F_2(Q^2)$. Figure 10.5 shows the response of Λ to beam energy miscalibration. Our estimate of the uncertainty in Λ from this source is ± 10 MeV/c.

After mapping the efficiency of the trigger counters, there are residual uncertainties, both statistical and systematic. We can estimate the global systematic uncertainty in the trigger efficiency by comparing events that trigger in different parts of the spectrometer or events that penetrate different numbers of paddle counters. We feel that any global efficiency offset is limited

to $\pm 0.5\%$. Even a uniform offset in efficiency can affect the shape of the cross section because the number of paddles penetrated, and thus the sensitivity to the efficiency of individual paddles, varies with Q^2. We find that a 0.5% change in efficiency changes Λ by 16 MeV/c. Even if there is no systematic offset in the efficiency maps, the statistical errors in the maps may affect our results. In any kinematic region with a large geometrical acceptance, the statistical errors in many map cells are averaged and there is no effect. However, at low Q^2 only small portions of the spectrometer are illuminated and only a limited amount of averaging takes place. This was the problem with the penultimate set of maps, which were not systematically biased, but had large statistical errors in the crucial regions. We probed this possibility in the new maps by varying by one statistical standard deviation the efficiency of the single most critical map cell (or rather, the corresponding cells in each paddle of trigger bank 6). From this worst case, we estimate that the statistical uncertainty in the efficiency maps leads to an uncertainty in Λ of ± 10 MeV/c. As an overall check, we compare results extracted separately from the events entering the four quadrants of the apparatus as seen by the beam. In Fig. 10.6, we show Λ as separately fitted in the four quadrants using our 215 GeV data. This figure should be considered in the light of Fig. 7.5, which indicates how different the quadrants actually are. Another indication of the sensitivity of this test is to note that with our previous set of maps, which for two years was believed to be quite adequate, Λ from the various quadrants varied by over three orders of magnitude.

Another source of systematic uncertainty is resolution smearing, or rather our ability to model and correct for it. We include here effects due to the use of the calorimeter for resolution improvement, and thus possible calorimeter miscalibration. We study this by varying the degree to which the calorimeter is used. We relax the missing energy requirement (see Sec. 6.4) and use the calorimeter in all events (with the same weighting scheme as before). We also try ignoring the calorimeter information totally. The kinematic cuts described in the previous chapter were chosen to minimize the effects of these changes. The uncertainty in Λ from this source is estimated to be ± 50 MeV/c.

The major source of uncertainty in Λ is the relative normalization of our 93 and 215 GeV data sets. Since Λ determines the slope of the Q^2 dependence of F_2 at fixed x, and our low Q^2 data comes from one set and high Q^2 from the other, this is no surprise. We estimate the uncertainty in the relative normalization to be $\pm 2.5\%$. This causes a ± 60 MeV/c uncertainty in Λ. We can also allow the relative normalization to float in the global fit. Table 10-II, entry (f) shows the result of this fit. The result is to lower the 93 GeV normalization by $2.0 \pm 0.8\%$, within the estimated uncertainty. Alternatively, we can normalize directly by comparing the 15 points where the data sets overlap. The first normalization check is, of course, model dependent; the second is more sensitive to R. The direct normalization indicates that the 93 GeV event sample should be increased by $2.9 \pm 1.5\%$. Eliminating the same two points that contributed the most to the χ^2 of the comparison between the two data sets reduces the normalization shift to $1.5 \pm 1.5\%$. Unless otherwise indicated, all results of the chapter refer to the original (separate, absolute) normalizations, including the corrections discussed in the previous chapter.

As another consistency check, we can separately fit the 93 and 215 GeV measurements. Unfortunately, the resulting smaller Q^2 ranges and our limited 93 GeV statistics reduce the significance of this comparison. The results are not terribly satisfying. The fit of the 93 GeV data gives $\Lambda = 633 \pm 148$ MeV/c, 2.6 statistical standard deviations higher than the 215 GeV value of 227 ± 55 MeV/c. Inspecting Fig. 10.2, it is apparent that the slopes of the 93 GeV data are somewhat steeper. In fact, there has been some attempt[60] to attribute physical significance to a similar effect in the data of the European Muon Collaboration (though not by the experimenters). My opinion is that systematic errors must be reduced in all of the experiments before such effects are to be considered significant. On the positive side, the agreement between the result of the combined fit and that of the 215 GeV data alone is excellent. The effects of shifting the relative

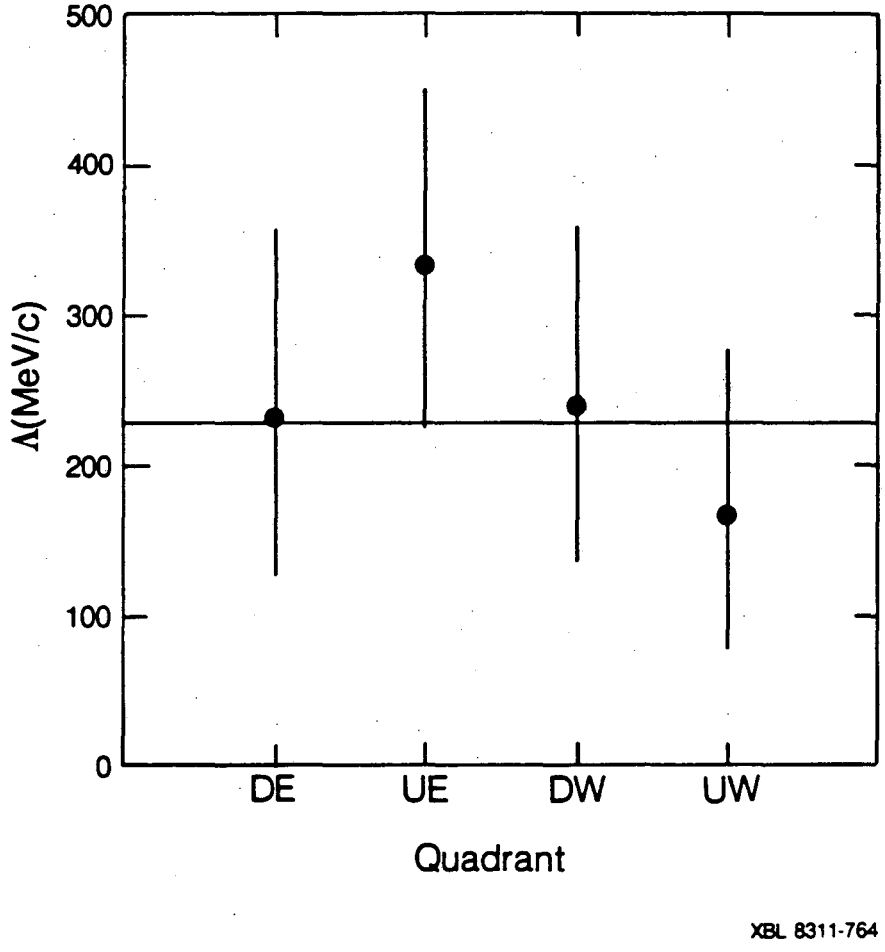

Fig. 10.6. Λ by quadrant. The 215 GeV data has been sorted by quadrant and $F_2(x, Q^2)$ extracted and fit separately for each. The line shows the value of Λ fit to the total 215 GeV sample (227 MeV/c).

normalization indicate that this agreement is not simply due to the 215 GeV data dominating the combined fit.

Table 10-III concludes with an estimate of our total systematic uncertainty in Λ of 82 MeV/c, the sum in quadrature of the individual entries. This estimate is obviously accurate only to the extent that our catalog of sources is complete. It is apparent, however, that the systematic uncertainty already dominates the statistical uncertainty.

Table 10-IV. Effects of various phenomenological assumptions on the fitted value of Λ.

Assumption	$\Delta\Lambda$ (MeV/c)	χ^2/dof
Standard	($\Lambda = 225$)	154/91
$R = 0.1$	-100	142/91
Fermi motion correction	$+20$ to $+60$	149 to 151/91
$x > 0.15$	$+5$	134/81
Gluon exponent = 6	-25	152/91
Higher order QCD	$+50$ (estimated)	—
Target mass correction	$+15$	155/91
Include $1/Q^2$ term	-25 or more (see text)	152/91

10.4 Phenomenological uncertainties

Beyond the experimental uncertainties discussed in the previous section lie questions of interpretation. We have measured Λ by assuming that the cross section (Eq. 8.5 with $R = 0$), the parametrization (Eq. 10.1), and lowest order perturbative QCD are a complete description of deep inelastic scattering. In this section we explore the effects of relaxing or varying the various pieces of this assumption. Table 10-IV summarizes the results.

We start with the cross section and begin by varying R. In this exercise, the measured cross section remains constant; the measurement is simply apportioned differently between F_2 and R. We choose $R = 0.1$ as an upper limit based on the measurements of R to be discussed below. Even this small change decreases Λ by 100 MeV/c.

Another matter of interpretation concerns Fermi motion. As we have defined it in Eq. 8.5, our measured $F_2(x, Q^2)$ refers to an average over the nucleons in an iron nucleus. To translate this into F_2 for a free nucleon, we can try to remove the known effects of the nuclear environment such as binding energy and its manifestation as Fermi motion. This correction has been demoted in importance by the discovery[61] of another nucleus-dependent effect which is larger in the x region covered by our data. This "EMC effect" is discussed in the next section. The situation of Fermi motion itself is surprisingly murky. The models we use are described in Appendix B. In brief, Fermi motion is primarily an x dependent phenomenon, and thus has a limited effect on Λ. Depending on the model used, we find that Λ increases by 20 to 60 MeV/c when Fermi motion corrections are applied. Above the very low Q^2 region ($Q^2 < 2$ GeV$^2/c^2$), the EMC effect has no observed Q^2 dependence.[62]

Our data extend into the kinematic region known to contain scaling violations due to the crossing of the charm threshold.[49] We have made no detailed attempt to correct for this, but rather try removing the region in question and observe the effect. Before the interpolation to x bin centers, we eliminate all measurements with $x < 0.15$. This results in an increase in Λ of only 5 MeV/c.

We have already discussed the minor effects of varying some of the more arbitrary features of our parametrization at Q_0^2. One feature, however, has an unambiguous physical interpretation. This is the exponent δ which determines the "hardness" of the gluon momentum spectrum. In inclusive muon scattering we cannot directly measure the gluons. This is unfortunate, because it has been noted[63] that Λ and this exponent can be strongly correlated. As

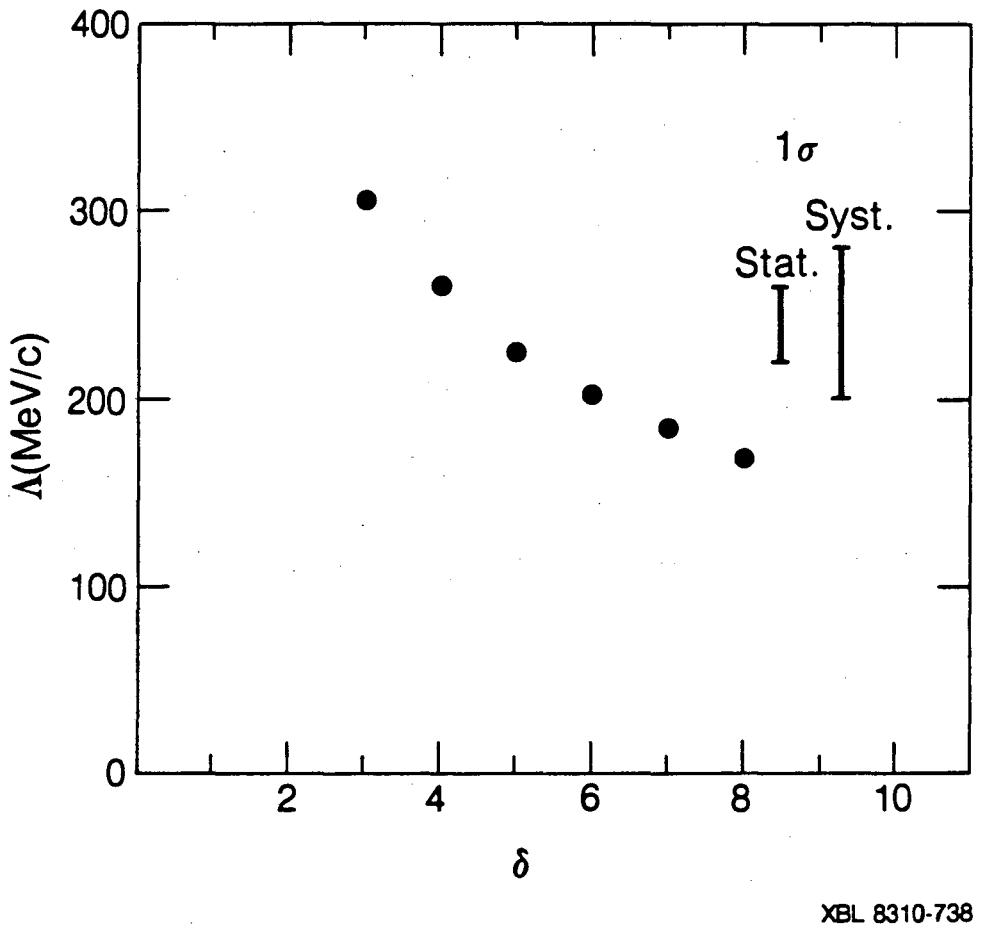

Fig. 10.7. The correlation between our best-fit value of Λ and the value assumed for δ, the exponent of $(1-x)$ in the gluon distribution. For comparison, the statistical and systematic uncertainties in our standard fit of Λ are shown.

mentioned earlier, the non-singlet information available from neutrino scattering allows a more constrained determination of the gluon sector. The CERN-Dortmund-Heidelberg-Saclay (CDHS) neutrino collaboration[29] has found the exponent δ to lie in the range 5 to 7, but the actual precision of this result has been questioned.[64] Our standard fit uses $\delta = 5$. Raising this to $\delta = 6$ decreases Λ by 25 MeV/c. Figure 10.7 traces further the dependence of our best fit value of Λ on the assumed value of δ.

As discussed in Chap. 3, our lowest order QCD fits neglect the contribution of higher powers of $\ln Q^2$ and powers of $1/Q^2$ to the Q^2 dependence of F_2 at fixed x. This is known as the "leading-log, leading twist" approximation. The next-to-leading-log contribution can be incorporated into the Altarelli-Parisi evolution equations, but we have not done so. From the work of others[64,65] we estimate that these higher order corrections increase Λ by approximately 50 MeV/c. The $1/Q^2$ terms are, in general, not calculable. An exception is the "target mass correction" which can be taken into account[66] by replacing the variable x with

$$\xi = \frac{2x}{1+\sqrt{1+4x^2M_N^2/Q^2}}. \tag{10.6}$$

In our Q^2 and x range, this effect should be small. When this transformation is made we find that Λ increases by 15 MeV/c. Considerably more freedom in Λ is allowed if we include an arbitrary $1/Q^2$ dependence in our parametrization. We first simply multiply our F_2 parametrization by $(1 + k/Q^2)$ with k determined by the fit. Λ drops by 100 MeV/c, with a moderate improvement in χ^2 from 154/91 dof to 130/90 dof. To gain sensitivity, the EMC investigated $1/Q^2$ terms by combining their muon-proton data with lower Q^2 electron-proton data from SLAC.[65] They allowed the x dependence of the $1/Q^2$ term to vary and found that this dependence was consistent with $kx^2/(1-x)^2$. If we use this form and fix $k = 0.45$, which is the approximate level observed by the EMC, Λ drops by 25 MeV/c with a negligible improvement in χ^2. If we instead try to use our data to determine k, we find $k \approx 4$, $\Lambda = 30$ MeV/c, and $\chi^2 = 144/90$ dof. It is not clear that anyone is doing anything but quantifying systematic errors with these fits. The fact remains that our experiment alone cannot rule out large $1/Q^2$ corrections to lowest order QCD.

10.5 Comparison with other experiments

The most direct comparison we can make is to data from the European Muon Collaboration (EMC).[67] Part of their data was taken on an iron target at beam energies similar to ours. Their spectrometer, however, was completely different from the MMS, and thus we can hope that some of the sources of systematic error are different for the two experiments. Figure 10.8 shows a comparison of our results with the EMC's iron target measurements. Both measurements are averaged over the various beam energies, both assume $R = 0$, and neither has been corrected for Fermi motion. For purposes of this comparison only, our values of F_2 have been multiplied by a factor of 0.94, determined from the x dependence comparison discussed below. This normalization is consistent with the 3% systematic uncertainty quoted by each experiment. Except for the region of $Q^2 < 10$ GeV$^2/c^2$, the agreement is excellent. Table 10-II includes an entry for a fit to the EMC's data using our fitting routine and assumptions. These fitted parameters are consistent with the EMC's published results,[65] although the assumptions made here are slightly different. It should be noted that while the individual parameters of $F_2(x)$ at Q_0^2 appear different in fits (a) and (g), the actual values of $F_2(x, Q_0^2)$ are quite similar after the 6% shift indicated above.

In Fig. 10.9 the ratio of our F_2^{Fe} (multiplied by 0.94) to that of the EMC for $Q^2 >$ 20 GeV$^2/c^2$is displayed as a function of x. Fits (a) and (g) of Table 10-II have been used to

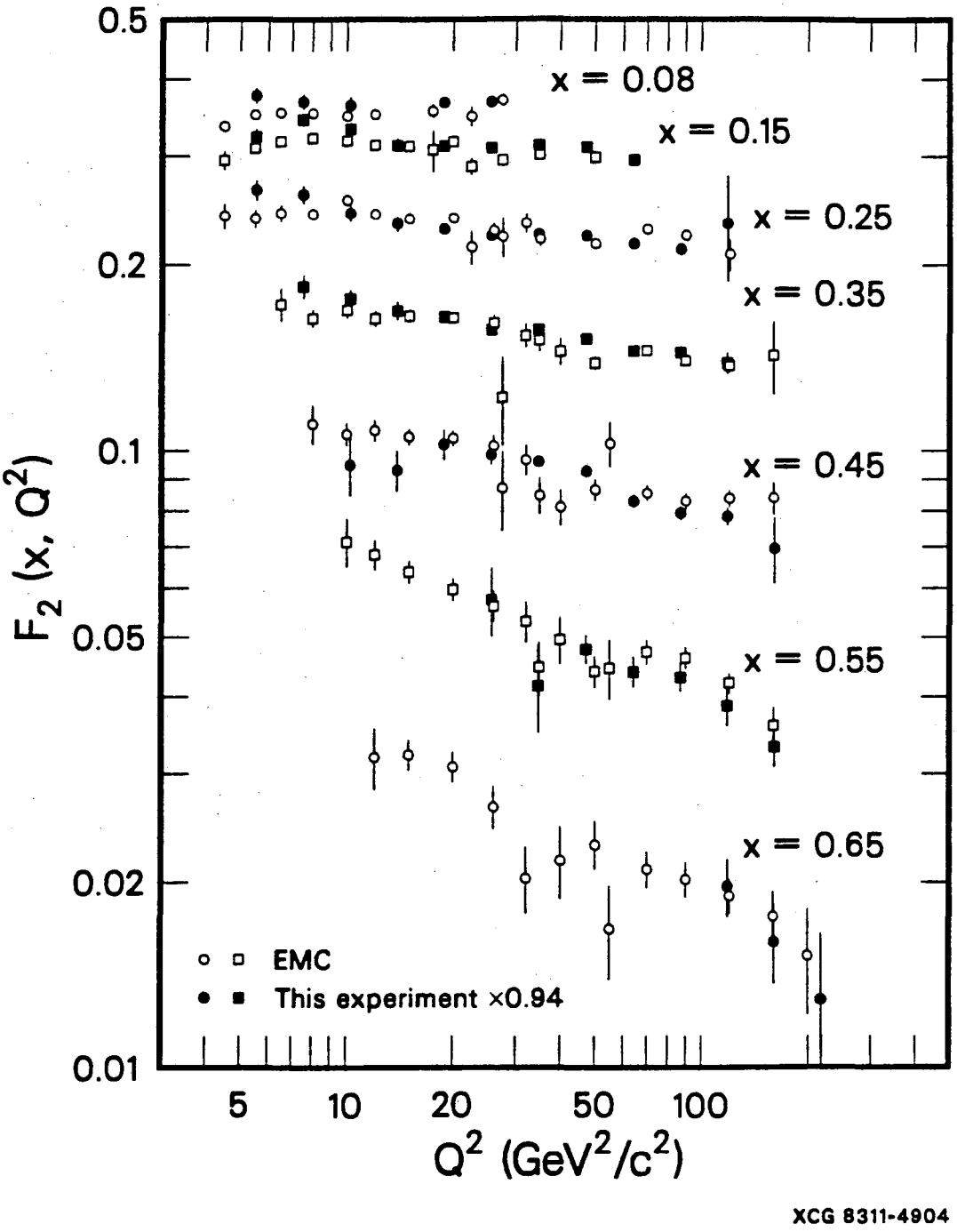

Fig. 10.8. A comparison of our measured $F_2(x, Q^2)$ (multiplied by 0.94) to the EMC's iron target measurement (Ref. 67.).

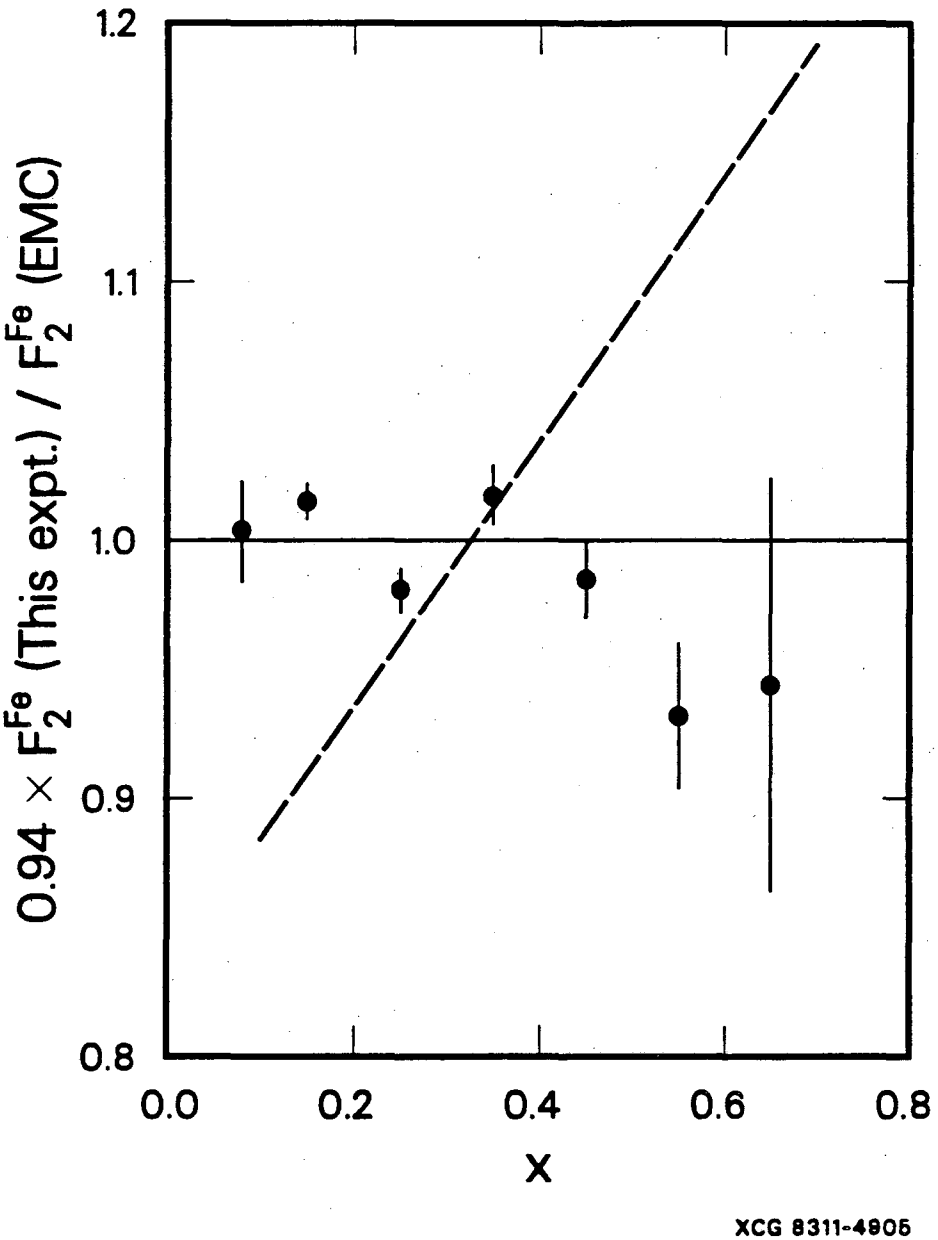

Fig. 10.9. The ratio of our F_2(Fe) measurements (multiplied by 0.94) to the EMC's (Ref. 67.) as a function of x, for $Q^2 > 20$ GeV$^2/c^2$, interpolated to $Q^2 = 50$ GeV$^2/c^2$. The dashed line shows the trend of EMC's F_2(deuterium)/F_2(Fe) from Ref. 61.

interpolate each data point to $Q^2 = 50$ GeV$^2/c^2$ prior to averaging. The errors shown are statistical; systematic uncertainties from our data alone are of comparable magnitude. The EMC has reported differences of up to 15% between deuterium and iron in the x dependence of F_2.[61] These discrepancies, not explained by Fermi motion, have been confirmed using resurrected data from old experiments at SLAC.[62] The dashed line in Fig. 10.9 shows the trend of $F_2(d)/F_2(\mathrm{Fe})$ for the EMC's measurements. We, of course, cannot make the deuterium-iron comparison directly. However, from the evidence of Fig. 10.9, we can provide support for the existence of the discrepancy by noting that our measurements agree quite well with the EMC's iron measurements, but are distinctly different from their deuterium measurements.

We can also compare our results to those of charged current neutrino experiments. Here the comparison is somewhat less direct, due to the difference in the coupling to quarks between the weak and electromagnetic probes used. The parton model predicts that

$$F_2^{\mu N}(x) = \frac{5}{18} F_2^{\nu N}(x) + \epsilon(x), \tag{10.7}$$

where the 5/18 factor is the average electric charge squared of the quarks and ϵ represents a residual difference in the coupling to the sea of heavy quarks and antiquarks. This ϵ term, expected to be positive, is complicated by the threshold behavior in the neutrino interaction where an s quark must be turned into a massive c quark. Figure 10.10 shows our results compared to $\frac{5}{18} \times F_2^{\nu N}$ from the CDHS collaboration, which also has an iron target.[68] For the comparison, our F_2 has been multiplied by 0.89. Both sets assume $R = 0$ and neither has been corrected for Fermi motion. Although CDHS fits a similar value of Λ to ours,[29] the agreement with our x dependence (see Fig. 10.11) is not as good as that between the two muon experiments. The difference at low x is not in the direction expected from the heavy quark sea contribution mentioned above. This discrepancy has been noted before[69] and will have to be resolved by future experiments. Figure 10.12 shows the x dependence of the three experiments, again for $Q^2 > 20$ GeV$^2/c^2$ and interpolated to $Q^2 = 50$ GeV$^2/c^2$, with the arbitrary normalizations mentioned above.

We can compare our measurement of $\Lambda_{\mathrm{LO}} = 225 \pm 43^{stat} \pm 82^{syst}$ MeV/c to the results of other investigations of the strong coupling constant $\alpha_S(Q^2)$. In e^+e^- annihilation, α_S appears whenever gluons are present. For example, the value of α_S can be determined by observing the modifications due to gluon emission to the two-jet structure of events. There are various methods of characterizing this modification, but all appear to be subject to substantial uncertainties from the (non-perturbative) fragmentation of the primary quarks and gluons into the observed hadrons. At a center of mass energy $\sqrt{s} \approx 30$ GeV, values of α_S typically between 0.13 and 0.20 are found.[70] If we use Eq. 3.11 with $Q^2 = s$ and $N_f = 5$ to turn these results into measurements of Λ_{LO}, we find $\Lambda_{\mathrm{LO}} = 60$ - 400 MeV/c. The expectation that the hadronic decay of the Υ is dominated by by $\Upsilon \rightarrow 3$ gluons allows a determination of α_S from the observed decay widths of the Υ.[71] It is found that $\alpha_S(M_\Upsilon) = 0.158 \pm 0.011$. This translates into $\Lambda_{\mathrm{LO}} = 80 \pm 30$ MeV/c. One of the interpretational difficulties here is the appropriateness of using M_Υ as the argument of α_S. It is apparent that in e^+e^- annihilation, as in deep inelastic scattering, the confrontation of theory with experiment is limited as much by questions of interpretation as by experimental precision.

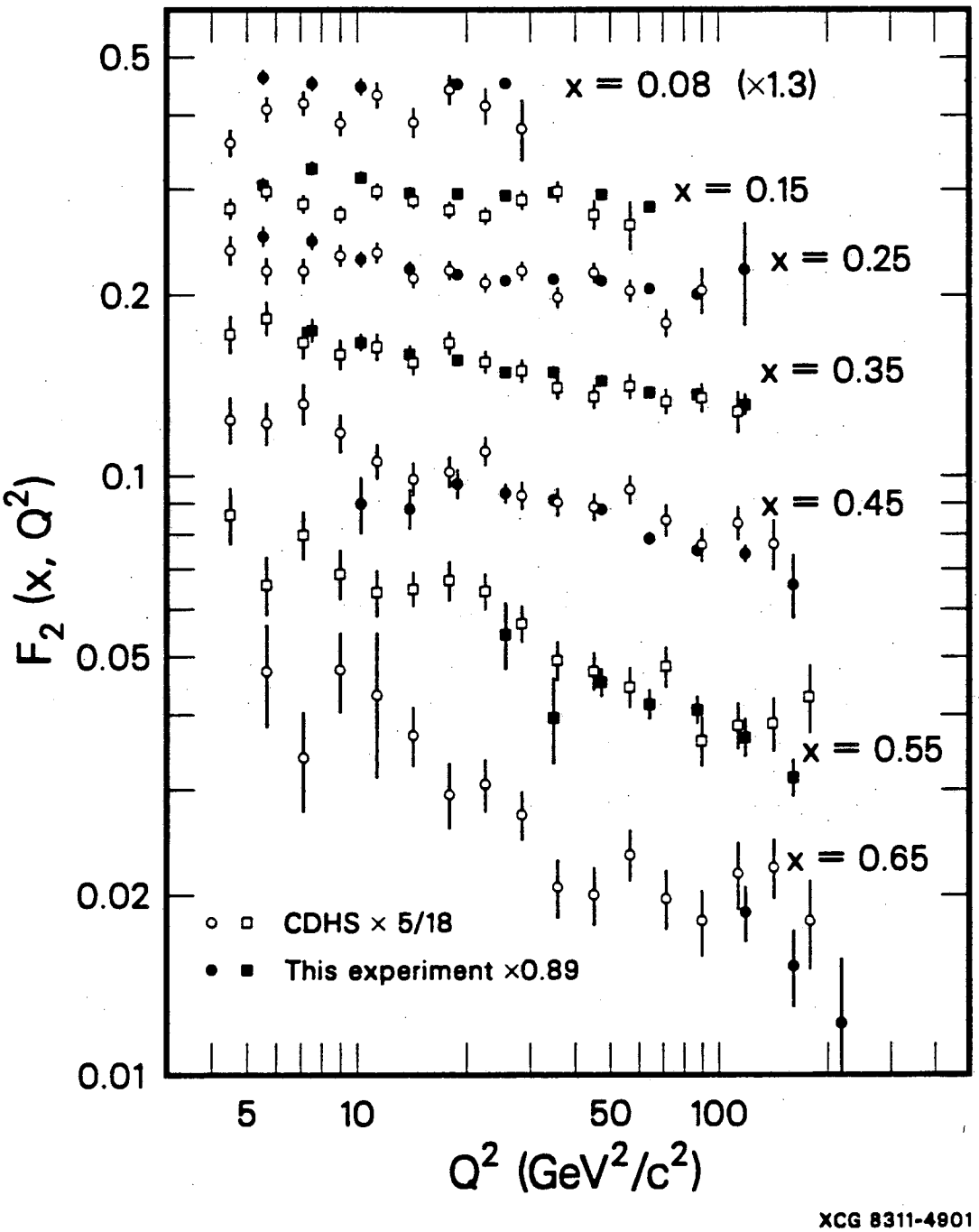

Fig. 10.10. Our measured $F_2(x, Q^2)$ (multiplied by 0.89) compared to $\frac{5}{18} \times F_2^{\nu\mathrm{Fe}}$ from CDHS (Ref. 68.). For clarity, the $x = 0.08$ bin has been raised by a factor of 1.3.

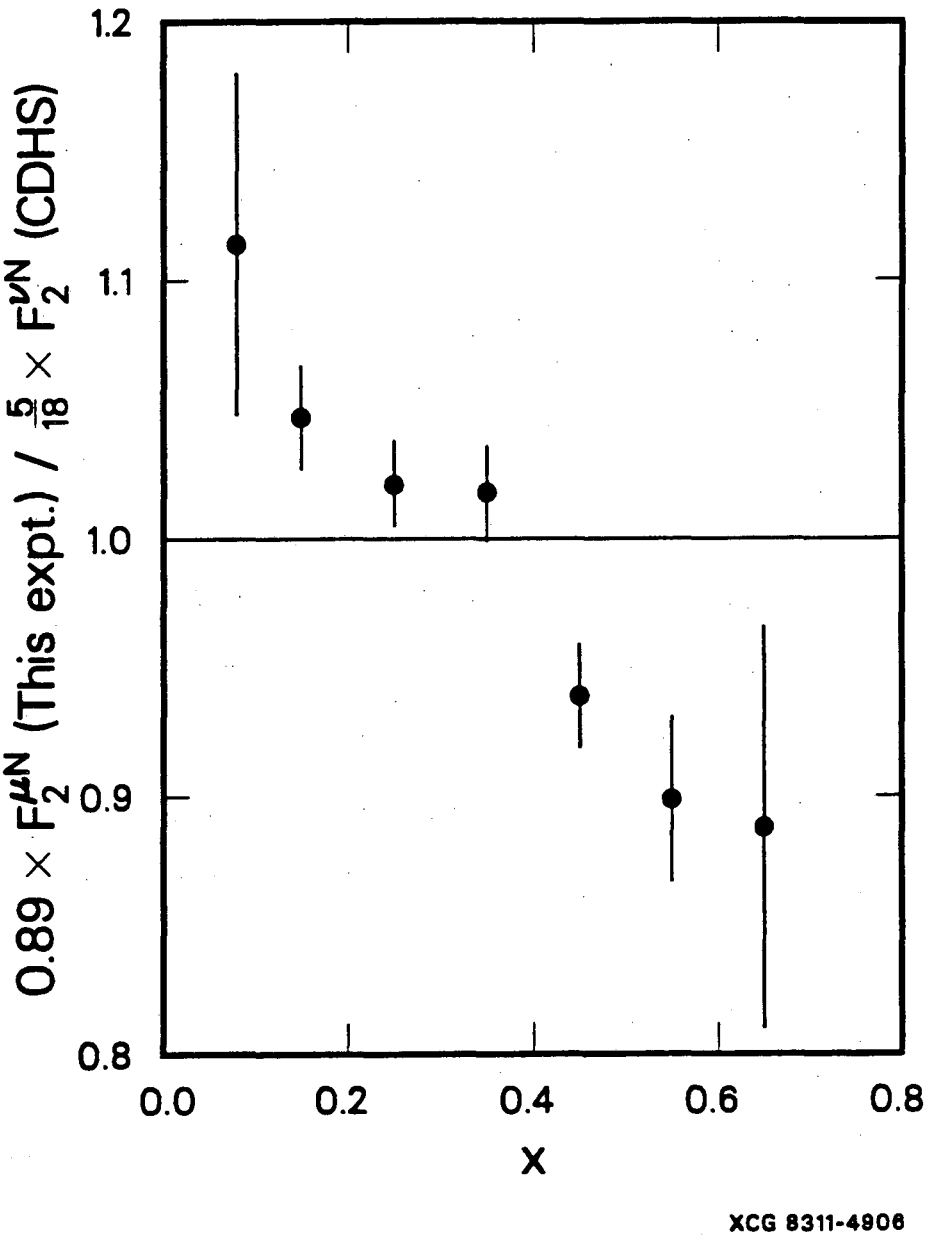

Fig. 10.11. A comparison of the x dependence of our $F_2^{\mu Fe}$ and $\frac{5}{18} \times F_2^{\nu Fe}$ from CDHS (Ref. 68.). Measurements for $Q^2 > 20$ have been averaged after interpolation to $Q^2 = 50$ GeV$^2/c^2$.

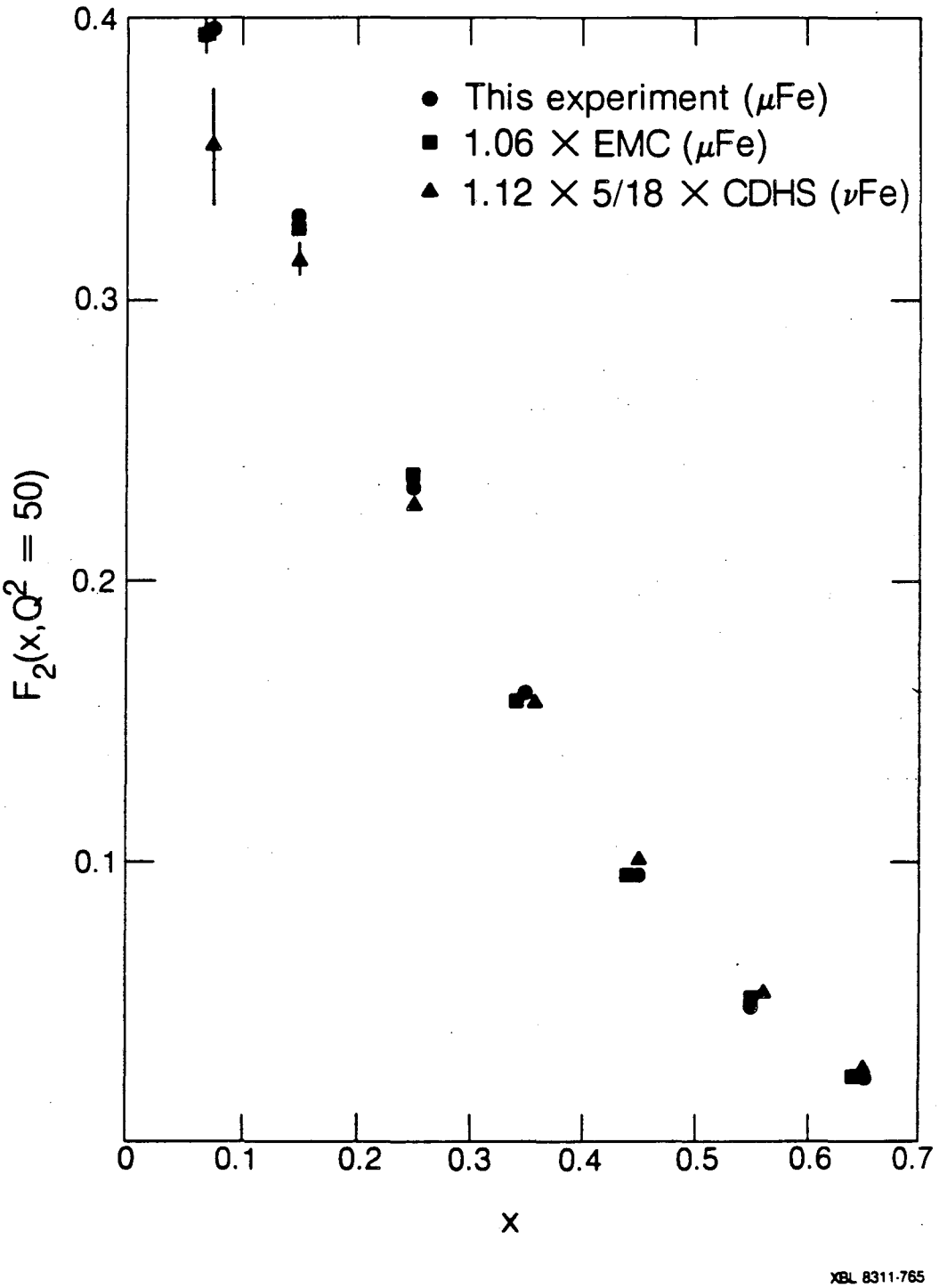

Fig. 10.12. The x dependence of $F_2(Q^2 = 50)$ determined from our measurements and those of the EMC (Ref. 67.) and CDHS (Ref. 68.). All experiments had iron targets, made no Fermi motion correction, and assumed $R = 0$. Some points have been displaced slightly in x for clarity.

10.6 Measurement of R

Although previous results have assumed a fixed value of $R \equiv \sigma_L/\sigma_T$, usually $R = 0$, our overlapping measurements of $F_2(x, Q^2)$ taken at different beam energies allow us to measure R. At fixed Q^2 and ν (*i.e.*, at fixed Q^2 and x) we have fixed the 4-momentum of the virtual photon, independent of the muon beam energy. However, this does not exhaust the photon's quantum numbers; it also carries polarization. We can isolate the dependence on the virtual photon polarization by writing the differential cross section in two forms:

$$\begin{aligned}\frac{d^2\sigma}{dQ^2 d\nu} &= \frac{4\pi\alpha^2}{Q^4}\frac{E'}{E}\cos^2\frac{\theta}{2}\left(2W_1\tan^2\frac{\theta}{2}+W_2\right)\\ &= \Gamma_T\sigma_T + \Gamma_L\sigma_L \equiv \Gamma_T(\sigma_T + \epsilon\sigma_L).\end{aligned} \tag{10.8}$$

$\Gamma_{T,L}$ and $\sigma_{T,L}$ represent the fluxes and cross sections for transversely and longitudinally polarized virtual photons; the polarization $\epsilon \equiv \Gamma_L/\Gamma_T$. Using the expressions for W_1 and W_2 in terms of σ_L and σ_T (Eq. 2.11), we can identify

$$\begin{aligned}\epsilon &= \frac{1}{1+2(1+\nu^2/Q^2)\tan^2(\theta/2)} = \frac{1-(\nu/E)-(Q^2/4E^2)}{1-(\nu/E)+(\nu^2/2E^2)+(Q^2/4E^2)},\\ \Gamma_T &= \frac{K\alpha}{2\pi Q^2}\frac{1}{E^2}\frac{1}{1-\epsilon}.\end{aligned} \tag{10.9}$$

K is a factor that must approach ν as $Q^2 \to 0$ to agree with real photoproduction.[19,72] From this expression for ϵ we see that, at fixed ν and Q^2, varying the muon beam energy changes the polarization of the "beam" of virtual photons.

Inserting R into Eq. 10.8, we define

$$S \equiv \frac{1}{\Gamma_T}\frac{d^2\sigma}{dQ^2 d\nu} = \sigma_T(1+\epsilon R). \tag{10.10}$$

R is thus the slope of S *vs.* ϵ. To extract R, we recall that our measurement of F_2 is actually a measurement of the cross section coupled to an assumption about R. By restoring the kinematic factors of Eq. 2.12 with $R = 0$ to F_2, we get a measured cross section independent of R. For measurements at different beam energies E_i, but at the same ν and Q_2,

$$S_i(x, Q^2) = \frac{4\pi^2\alpha}{K}\frac{(\nu^2+Q^2)}{Q^2\nu}F_2^i(x, Q^2), \tag{10.11}$$

where F_2^i is the measured F_2 with $R = 0$. Using Eqs. 10.8–11 we get a measurement of R for each point where the two data sets overlap:

$$R(x, Q^2) = \frac{S_2 - S_1}{S_1\epsilon_2 - S_2\epsilon_1} = \frac{F_2^2(x, Q^2) - F_2^1(x, Q^2)}{F_2^1(x, Q^2)\epsilon_2 - F_2^2(x, Q^2)\epsilon_1}, \tag{10.12}$$

where the indices 1 and 2 refer to the 93 and 215 GeV beam energies, respectively.

It is clear that this measurement of R will be sensitive to systematic experimental differences between the data sets. Beginning with the F_2 measurements of Table 9-III, we find

Table 10-V. R measurements. Errors are statistical. The final entry is a global average.

x	Q^2 (GeV$^2/c^2$)	ϵ(93 GeV)	ϵ(215 GeV)	R
0.1633	18.18	0.5870	0.9464	-0.057 ± 0.085
0.2421	18.31	0.8359	0.9772	-0.160 ± 0.185
0.3252	18.20	0.9184	0.9880	-0.378 ± 0.291
0.3863	18.20	0.9445	0.9916	-0.550 ± 0.325
0.2437	24.73	0.6682	0.9564	0.011 ± 0.138
0.3277	24.55	0.8390	0.9776	0.758 ± 1.071
0.3985	24.35	0.8996	0.9855	-0.269 ± 0.461
0.4480	23.87	0.9265	0.9891	-5.002 ± 23.776
0.2531	32.45	0.4220	0.9258	-0.003 ± 0.137
0.3331	33.41	0.6766	0.9574	0.659 ± 0.518
0.4106	32.91	0.8104	0.9739	0.610 ± 1.164
0.4641	32.66	0.8603	0.9803	-4.844 ± 11.585
0.5025	31.83	0.8904	0.9842	-1.857 ± 0.975
0.3425	44.17	0.4131	0.9246	1.045 ± 0.727
0.4145	44.10	0.6269	0.9512	1.557 ± 1.732
0.4818	43.78	0.7436	0.9656	-4.027 ± 3.908
0.5246	43.15	0.7975	0.9723	-4.764 ± 11.744
0.5001	58.71	0.5274	0.9389	0.732 ± 1.821
0.5528	57.96	0.6382	0.9526	-0.316 ± 0.525
0.2278	22.80			-0.064 ± 0.057

Table 10-VI. R vs. Q^2, R vs. x

Q^2 (GeV$^2/c^2$)	R		x	R
18.2	-0.120 ± 0.073		0.194	-0.055 ± 0.067
24.7	-0.004 ± 0.130		0.274	0.02 ± 0.12
32.5	0.034 ± 0.133		0.392	-0.37 ± 0.25
44.2	0.95 ± 0.65		0.541	-0.57 ± 0.43
58.0	-0.27 ± 0.47			

that the average true x and Q^2 can be different for the two beam energies due to differences in smearing, energy loss, *etc.* To correct for this, we interpolate each measurement to the average x_{true} and Q^2_{true} of both measurements using the final F_2 fit for each energy. We eliminate measurements for which Δx_{true} or ΔQ^2_{true} is greater than 10% to minimize the sensitivity to this procedure.

The resulting measurements of R are listed in Table 10-V and shown in Fig. 10.13. Points with uncertainties greater than 10 units of R have not been plotted. In Table 10-VI and Fig. 10.14 we show separately the dependence of R on Q^2 and x. Because no strong dependence is apparent,

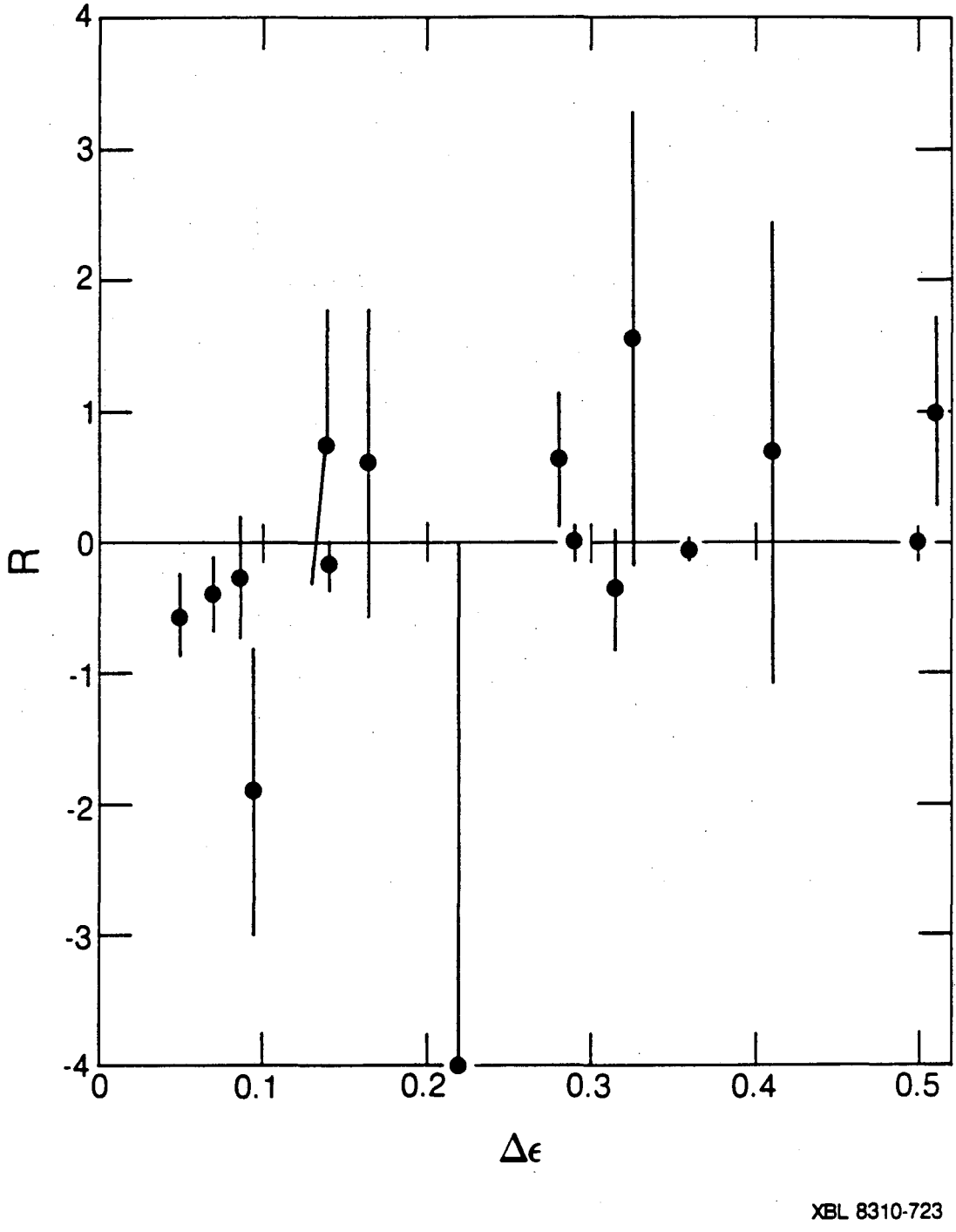

Fig. 10.13. Measurements of R from the comparison of our 93 and 215 GeV data. All measurements with statistical uncertainties less than 10 are shown *vs.* $\Delta\epsilon$, the difference in virtual photon polarization due to the different beam energies at each fixed (x, Q^2). Errors are statistical.

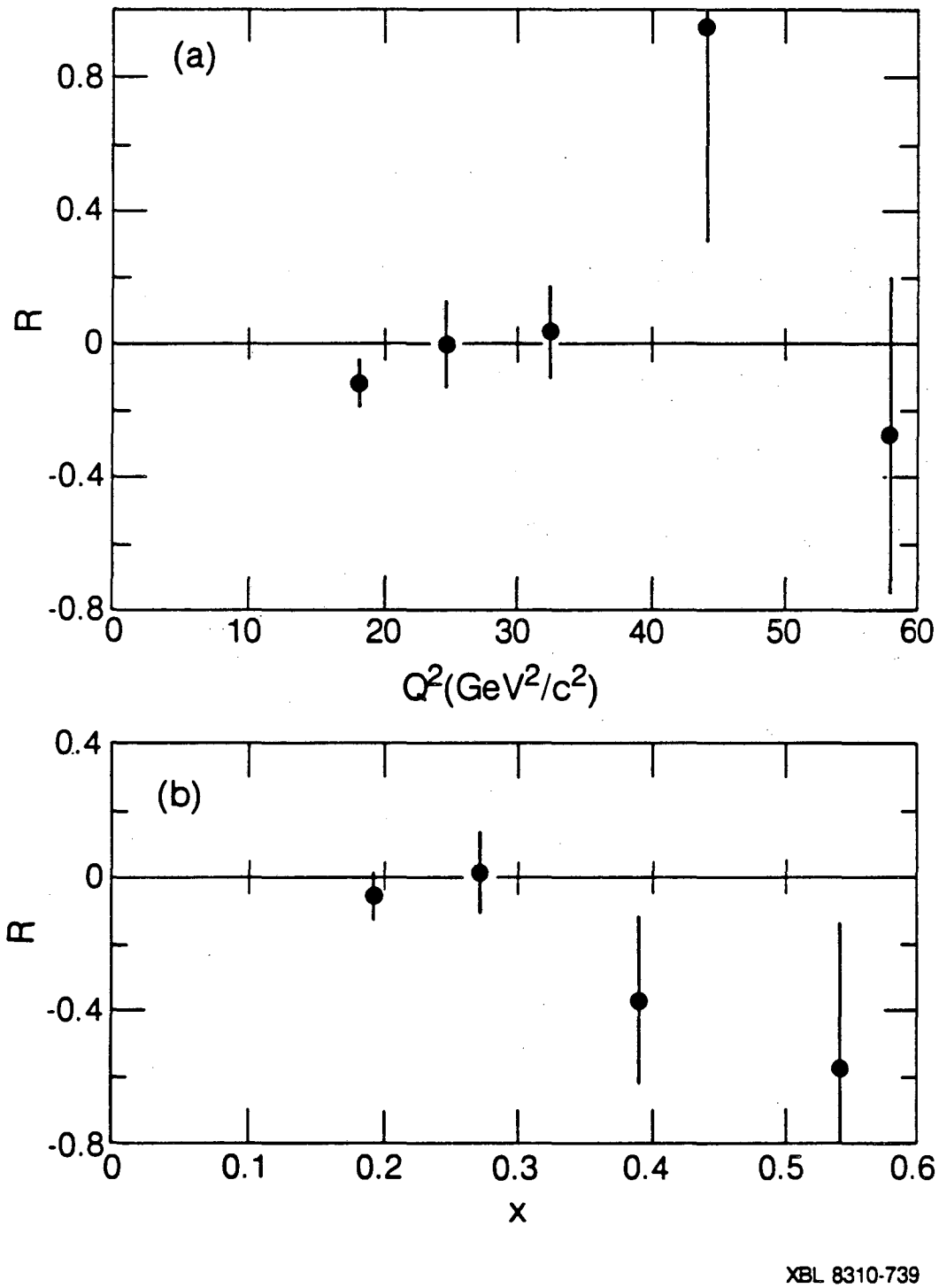

Fig. 10.14. (a) R *vs.* Q^2; (b) R *vs.* x.

Table 10-VII. Systematic uncertainty in R. The total shows the sum of the other entries in quadrature.

Source	Uncertainty	δR
MMS B-field calibration	0.5%	0.0049
Beam energy	0.5%	0.0644
Trigger efficiency (systematic)	0.5%	0.0102
Trigger efficiency (statistical)	(see text)	0.0018
Resolution	(see text)	0.0509
93/215 GeV normalization	2.5%	0.0743
Total		0.1113

we average all the measurements and find $R = -0.06$ with a statistical error of 0.06. The kinematic range covered by the measurements is $20 < \nu < 70$ GeV and $18 < Q^2 < 60$ GeV$^2/c^2$, with $\langle\nu\rangle = 53$ GeV and $\langle Q^2\rangle = 23$ GeV$^2/c^2$. In Sec. 10.4 we observed the effect of varying R on our fitted results. This procedure can be used to infer a model dependent value of R. We find that, at fixed normalization, the χ^2 of our QCD fits is minimized for $R \approx 0.1$ (see Table 10-IV).

The greatest contribution to the systematic uncertainty in R comes from the uncertainty in the relative normalization of the 93 GeV and 215 GeV data sets. This uncertainty was estimated in Sec. 9.2 to be 2.5%. In Sec. 10.3, we calculated a model dependent correction to the relative normalization by including it as a variable in our QCD fit (with $R = 0$). The result was a -2.0% correction to the 93 GeV normalization. We can attempt a model- and R-independent normalization as suggested in Ref. 73. by looking in the low ν region where both polarizations are near 1. Unfortunately, if we restrict ourselves to $\epsilon_{1,2} > 0.9$, we are left with only three points and a correction to the 93 GeV normalization of $(-2.8 \pm 3.6)\%$. If we make these corrections, R becomes 0.01 ± 0.06 or 0.04 ± 0.06 for the -2.0% or -2.8% corrections, respectively.

We also estimate the contributions to the systematic uncertainty in R from the rest of the effects considered previously in fitting F_2. These uncertainties are shown in Table 10-VII. Included in the table is the contribution of a 2.5% relative normalization uncertainty. Our final result is $R = -0.06 \pm 0.06^{stat} \pm 0.11^{syst}$. For comparison, the EMC has reported $R = 0.00 \pm 0.10$ in muon-proton interactions for $60 < \nu < 160$ GeV and the same average Q^2.[73] Electron-nucleon scattering experiments at SLAC found $R = 0.22 \pm 0.1$ at lower Q^2.[74] Neither experiment observes any significant kinematic dependence in R.

10.7 Search for a μ^+-μ^- asymmetry

In considering only the radiatively-corrected process of Figure 10.15a, we have neglected both the higher-order QED process of Fig. 10.15b and the weak neutral current interaction of Fig. 10.15c. Although too small to measure directly, these processes can give measurable effects through their interference with the one-photon exchange diagram.[75] Weak interaction effects have been observed in eN interactions in atomic physics[76] and in high energy eN interactions[77] by searching for a parity-violating signal.

Recently the BCDMS Collaboration at CERN reported an asymmetry between the cross sections for μ^+N and μ^-N interactions:[78]

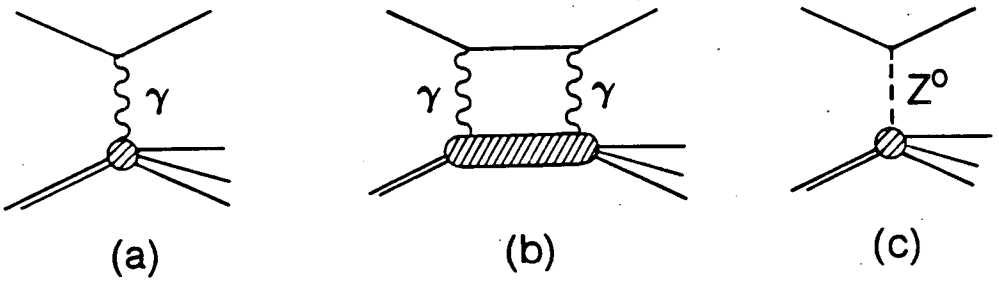

Fig. 10.15. Contributions to deep inelastic scattering. (a) One photon exchange; (b) two photon exchange; (c) weak neutral current.

$$A \equiv \frac{d\sigma_L^+ - d\sigma_R^-}{d\sigma_L^+ + d\sigma_R^-} \tag{10.13}$$

The L and R refer to the predominant helicities of the μ^+ and μ^- beams due to their production in the forward decay of pions. Because this asymmetry violates neither parity nor charge conjugation, both the two photon and weak neutral processes contribute. After correcting for the former, BCDMS finds an asymmetry consistent with the Weinberg-Salam model prediction.

Although all of our 93 GeV data and nearly all of our 215 GeV data was taken with a μ^+ beam, Table 5-I shows that we do have a small amount of μ^- data. While statistically insufficient to probe the expected level of asymmetry (see below), the measurement has value both as an exercise for the eager student and as a check of the systematic consistency of our data. It should be pointed out that a serious attempt to measure this asymmetry would require more than additional μ^- statistics. It would also demand better control of possible systematic differences. Although both the μ^+ and μ^- data sets represent roughly equal amounts of east and west bending spectrometer settings, the μ^- running was done all in one block and at a beam intensity of only about $\frac{1}{3}$ that of the μ^+ beam. Our Monte Carlo simulation takes into account known time-, intensity-, and beam phase space-dependent effects, but no attempt was made to make these the same for the μ^+ and μ^- running.

The expected asymmetry[79] using the parton and Weinberg-Salam models is

$$\begin{aligned} A_{WS} &= -4\sin^2\theta_W \left(\frac{9G}{20\sqrt{2}\pi\alpha}\right) g(y)Q^2, \\ g(y) &= \frac{1-(1-y)^2}{1+(1-y)^2}. \end{aligned} \tag{10.14}$$

Here θ_W is the Weinberg angle, $G \approx 10^{-5}/M_p$ is the weak interaction coupling constant, and $y = \nu/E$. This approximation assumes Bjorken scaling, an isoscalar target, and polarization of ± 1 for the beams. It neglects Cabibbo mixing and non-valence quarks. Because the currently accepted value of $\sin^2\theta_W \approx 0.23$ is near $\frac{1}{4}$, the asymmetry is nearly independent of the actual polarization of the beams. The expected asymmetry is then $A_{WS} = -1.45 \times 10^{-4} g(y)Q^2$. The two-photon asymmetry is expected to be smaller and opposite in sign.[78]

We measure the asymmetry by extracting $F_2(x, Q^2)$ for the μ^+ and μ^- samples separately following the procedures described in Sec. 9.3. For each bin of x and Q^2 for which there is an F_2 measurement from both samples, the μ^- measurement is interpolated to the average x and Q^2 of the μ^+ measurement. We then calculate $g(y)Q^2$ and A for each point. Figure 10.16 shows the asymmetry measurements after binning in $g(y)Q^2$. The line is the best fit of $A = a + bg(y)Q^2$ to all the points before binning. The result of this fit is $A = (6.9 \pm 6.7) \times 10^{-3} - (1.4 \pm 2.4) \times 10^{-4} g(y)Q^2$ with a χ^2 of 48 for 44 degrees of freedom. As the statistical error in the slope b indicates, setting $b = 0$ has a negligible effect on χ^2.

While, as expected, our lack of μ^- statistics bars us from the realm of the weak interaction asymmetry, this measurement adds to the confidence we have in our ability to correct for systematic effects due to beam intensity and phase space. It also rules out an unexpectedly large contribution from the one photon-two photon interference term in muon scattering from iron that might affect the deuterium-iron comparison. Figure 10.17 shows the asymmetry *vs.* x. There is no significant asymmetry at the 2% level out to $x = 0.5$.

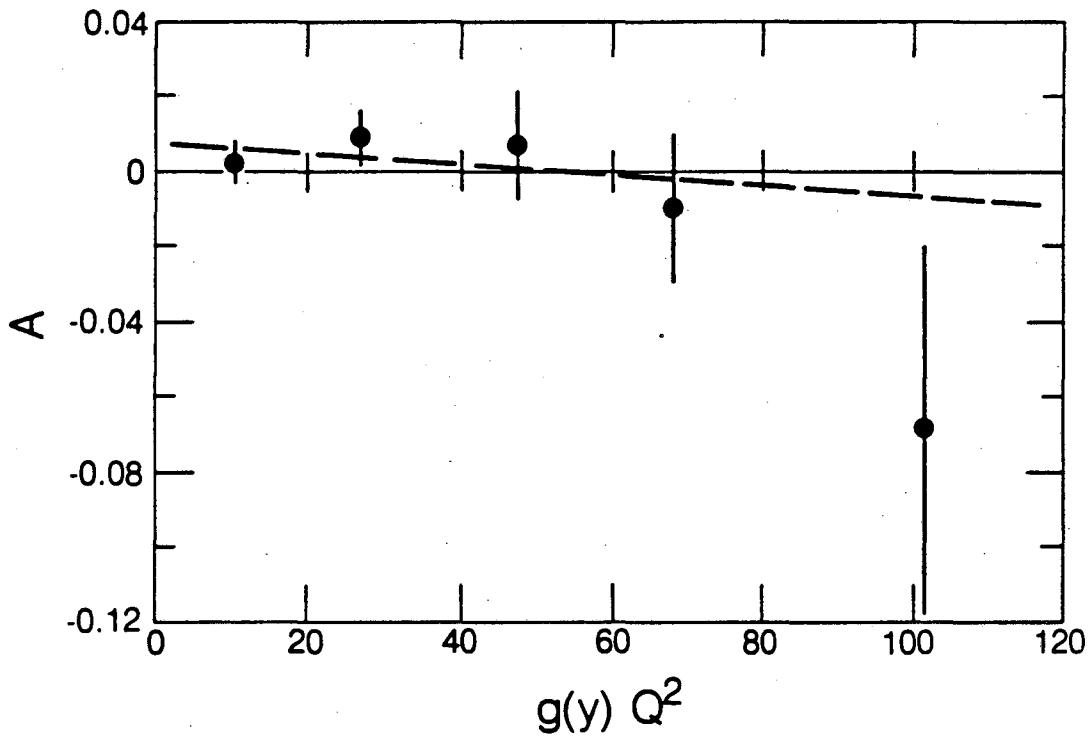

Fig. 10.16. The μ^+-μ^- asymmetry *vs.* $g(y)Q^2$. The dashed line is a linear fit. Errors are statistical.

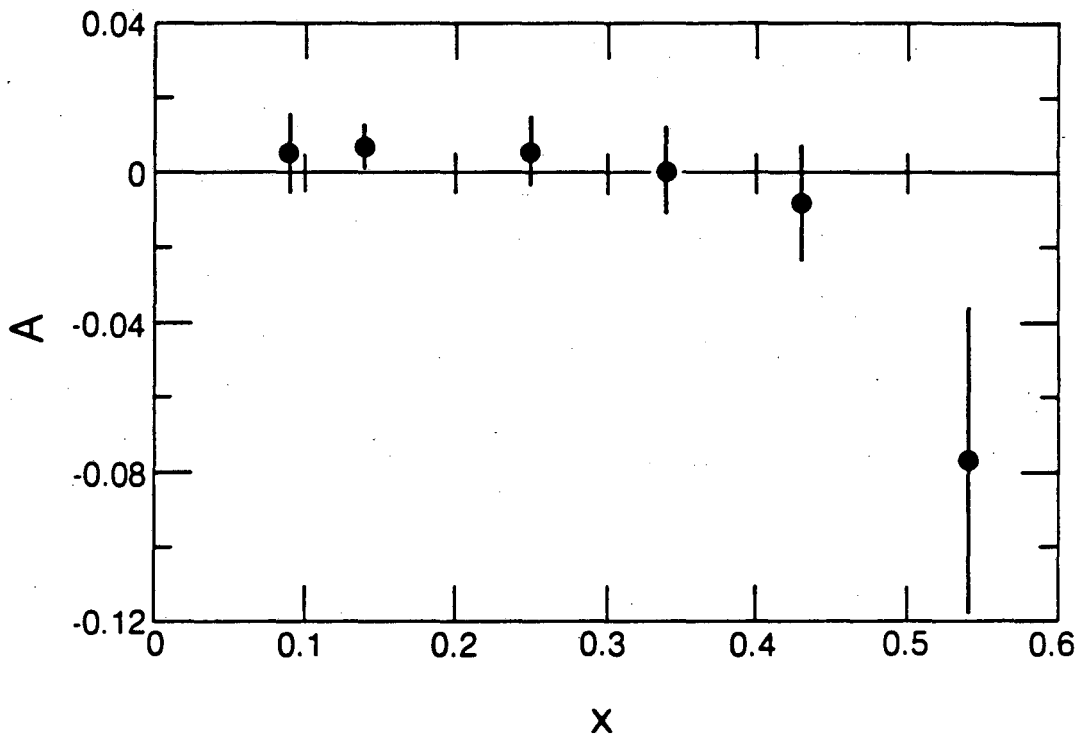

Fig. 10.17. The μ^+-μ^- asymmetry *vs.* x.

Chapter 11

Summary and Conclusions

Bomp bomp bomp—BOMP BOMP. Bomp bomp bomp—BOMP BOMP.
Bomp bomp bomp—BOMP BOMP ...

R. Berry, 1955

We have built and operated the Multimuon Spectrometer, an iron target-spectrometer-calorimeter in the muon beam at Fermilab, to observe muon-nucleon interactions with high luminosity and broad acceptance. We have measured the cross section for the deep inelastic scattering of muons on nucleons in iron at incident energies of 93 and 215 GeV. Using the known properties of the electromagnetic interaction, we have extracted from the measured cross sections measurements of the structure function $F_2(x, Q^2)$ with a statistical precision of better than 2% over a broad kinematic range. These measurements, extending in Q^2 from 5 to 200 GeV$^2/c^2$, are presented in Table 10-I and in Fig. 10.2. Figure 11.1 illustrates the factors limiting the kinematic coverage of our experiment. Our measurements are in good agreement with results from similar contemporary experiments. The agreement in x dependence between our data and that of the European Muon Collaboration's iron target experiments is especially notable in the light of the controversy surrounding the newly discovered A dependence of $F_2(x)$.

We have compared our measurements to the predictions of lowest order quantum chromodynamics (QCD) in which the Q^2 dependence of F_2 at fixed x is calculable. QCD reproduces the qualitative pattern of scaling violation seen in the data. Within our set of phenomenological assumptions, we measure the QCD scale parameter Λ_{LO} to be 230 ± 40^{stat} MeV/c. With the same assumptions, we estimate the systematic uncertainty in Λ_{LO} to be 80 MeV/c. This value of Λ agrees within quoted errors with the determinations from other deep inelastic scattering experiments using muons and neutrinos. While the statistical precision and Q^2 range of the new experiments represent an improvement over those of several years ago, systematic uncertainties still limit the precision with which we measure Λ to about 100 MeV/c. If we relax some of our assumptions about imprecisely known parameters, we can again generate $\approx$100 MeV/c uncertainties in Λ. These uncertainties will diminish as the quantities in question, notably R and the shape of the gluon spectrum, become better known, but progress in this direction has been slow and difficult. We have compared our F_2 measurements from the 93 and 215 GeV beam energies and measured $R = -0.06 \pm 0.06^{stat} \pm 0.11^{syst}$, a value consistent with zero, but with enough uncertainty to affect Λ substantially. Similarly, the rejection of large contributions to the observed scaling violations from $1/Q^2$ terms in favor of the logarithmic behavior predicted by QCD is difficult, especially with little constraint on the form of such terms. Although the confirmation from deep inelastic scattering of QCD as the theory of the strong interactions must

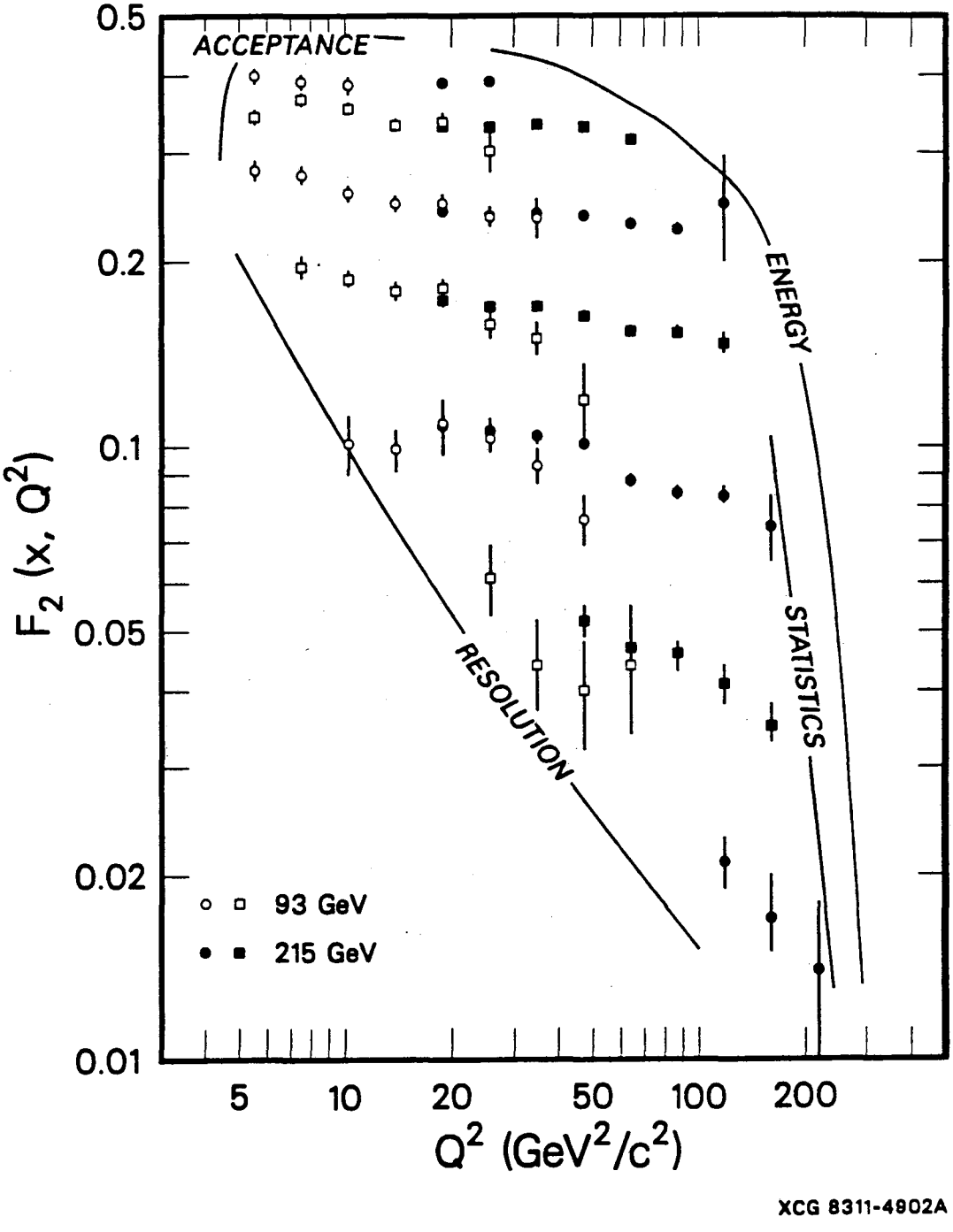

Fig. 11.1. The various factors limiting the kinematic range of our measurement of $F_2(x, Q^2)$.

still be considered somewhat qualitative, the improved agreement between the various experiments represents a distinct clarification of the experimental situation, without which no progress can be possible.

Appendix A

Radiative Corrections

As summarized in Chapter 8, we correct the deep inelastic scattering cross section Eq. 8.5 for processes involving the radiation of photons (Fig. 8.2a-d). We do this by using the method of equivalent radiators[52] in which these internal bremsstrahlung diagrams are replaced by an equivalent amount of radiation emitted separately from the primary (deep inelastic) scatter. The connection to the primary scatter remains in the amount of radiation, which is effectively that due to a Q^2 dependent number of radiation lengths

$$t = \frac{3\alpha}{4\pi}[\ln(Q^2/m_\mu^2) - 1]. \tag{A.1}$$

This radiation has the characteristic spectrum

$$P(y)dy = \left(1 - y + \frac{3}{4}y^2\right)\frac{dy}{y}, \tag{A.2}$$

where $y = (E - E')/E$ is the muon's fractional energy loss in the radiator. We radiatively correct the cross section in our event simulation by explicitly radiating a photon before the interaction with a probability and spectrum given by Eqs. A.1 and 2. Since the Q^2 of the interaction is not known before the interaction, we use a large limiting value, to be corrected later. The divergent spectrum is cut off at $y_{min} = 0.001$. We invoke the peaking approximation, in which the muon's direction is unaffected by the photon emission, and the incident muon, with its energy degraded, is handed to the deep inelastic generator. Besides the energy loss due to the process of Fig. 8.2a, the cross section is modified by the processes of Fig. 8.2b and c. The vertex and vacuum polarization corrections (Fig. 8.2b) have the effect of multiplying the cross section by[52]

$$1 + \delta(Q^2) = 1 + \frac{2\alpha}{\pi}\left[-\frac{14}{9} + \frac{13}{12}\ln(Q^2/m_\mu^2)\right]. \tag{A.3}$$

We cogenerate the wide angle bremsstrahlung (WAB) events of Fig. 8.2c using the per nucleon cross section[80]

$$\frac{d^2\sigma^{\mathrm{WAB}}}{d\nu\, dy} = \frac{1}{A}\frac{4Z^2\alpha^3}{2M_N E}\frac{y(1 - y + y^2/2)}{(1 - y)\nu^2}G(Q_\parallel^2) \tag{A.4}$$

where $G(Q_\parallel^2)$ is the nuclear form factor integrated over the component of q perpendicular to the incident muon direction. Finally, photon emission from the outgoing muon is simulated. The actual Q^2 of the event is then calculated and excess radiation is removed.

To investigate the effects of the radiative corrections, I have convolved numerically the deep inelastic scattering cross section with the radiative effects of Eqs. A.1-3. The cut off at y_{min} is imposed by calculating the total probability of the emission of a photon from a single radiator

$$k(y_{min}, Q^2) = \frac{\alpha}{\pi}[\ln(Q^2/m_\mu^2) - 1] \int_{y_{min}}^{1} P(y)\, dy. \tag{A.5}$$

The convolution then breaks into four terms:

1. an "unradiated" term with weight $[1 - \delta(Q^2)][1 - k(y_{min}, Q^2)]^2$.
2. an "initial radiator only" term with weight $[1 - k(y_{min}, Q^2)]$ (the probability of no *final* emission greater than y_{min}).
3. a "final radiator only" term with weight $[1 - k(y_{min}, Q^2)]$.
4. a "both radiators" term with weight 1.

As a point of reference, for $y_{min} = 0.001$, the probability of photon emission with $y > y_{min}$ in a single radiator is 0.082 at $Q^2 = 10$ and 0.125 at $Q^2 = 100$ GeV$^2/c^2$.

The results of this calculation are shown in Fig. A.1 for a beam energy of 200 GeV and the same $F_2(x, Q^2)$ used in the event simulation routine.[51] Plotted is $d\sigma^{\text{corr}}/d\sigma^{\text{uncorr}}$ as a function of Q^2 for fixed x. For a fixed observed cross section, $d\sigma^{\text{corr}}/d\sigma^{\text{uncorr}} > 1$ corresponds to a *downward* correction in measured F_2. Changing the beam energy to 100 GeV has an effect very similar to sliding the plot down by a factor of two in Q^2. Although it was not included in our event simulation, in this calculation I also studied the contribution of the radiative tail from elastic scattering. This correction turns out to be invisible where we have data, reaching a maximum of $< 1\%$ at the highest Q^2, lowest x point of the 93 GeV data.

After the cuts restricting the region over which we present $F_2(x, Q^2)$ are applied, the contribution of WAB is never greater than 3%. The number of simulated WAB events found in each bin of measured x and Q^2 is subtracted from both the real and simulated events before the F_2 extraction procedure of Section 9.3. The iteration of the F_2^{gen} used in the simulation does not modify the WAB events.

As an order of magnitude check on the presence of radiative events, I looked for the difference between hadronic and electromagnetic showers in the calorimeter. In Fig. 7.2 we see evidence in the calorimeter calibration for the expected electromagnetic events at low Q^2. For a given energy, electromagnetic showers are shorter than hadronic showers. Looking at a sample of deep inelastic events with $y > 0.67$, but short showers, showed them to occur at roughly the same rate as simulated WAB events and to have similar properties.

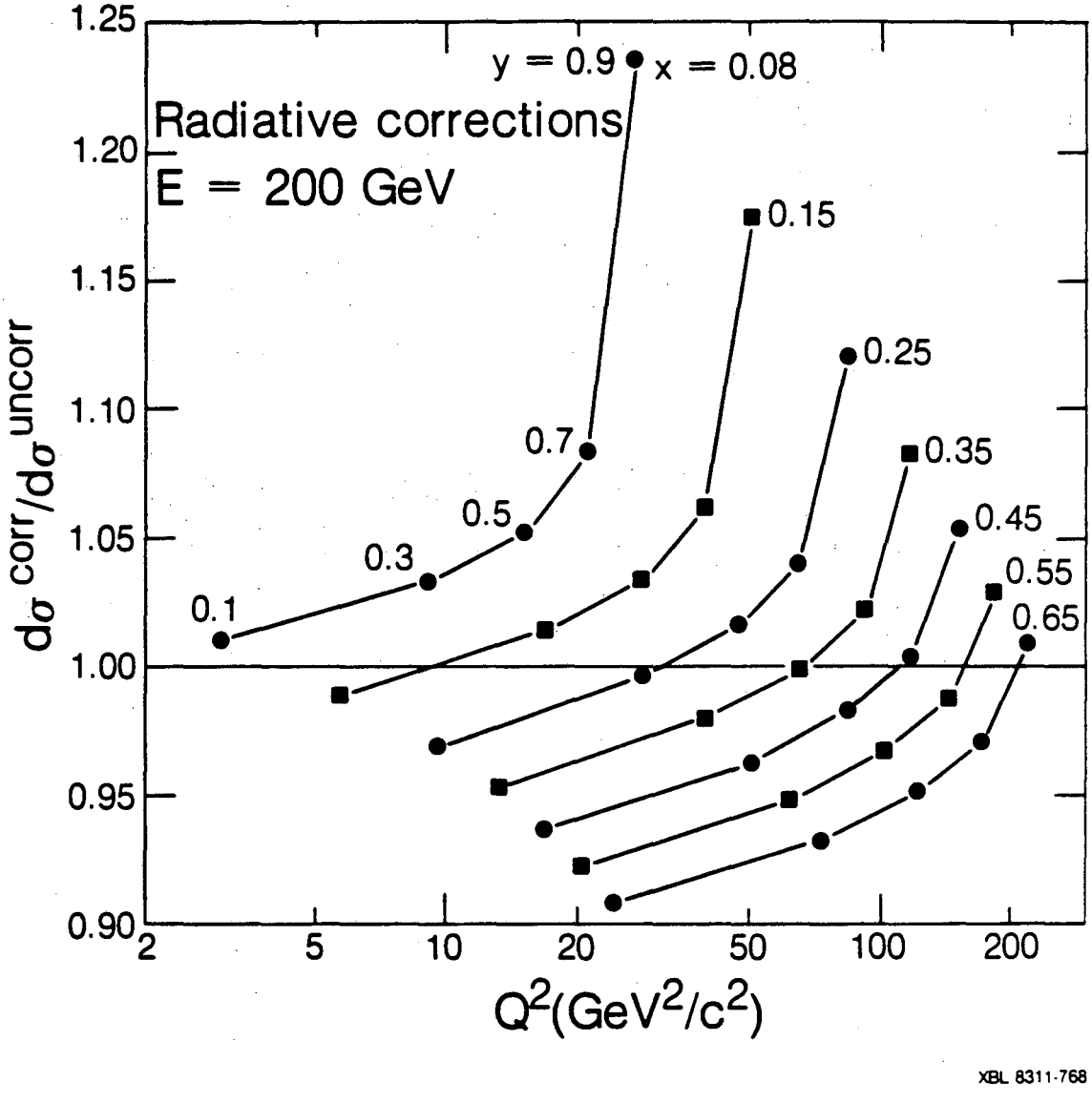

Fig. A.1. The effect of radiative corrections on the deep inelastic scattering cross section.

Appendix B

Fermi Motion

In analyzing our data we have calculated the various kinematic quantities using Eqs. 2.1 and thus have assumed that the laboratory frame and the target rest frame were the same. In our experiment, this is fine if the target is considered to be an iron nucleus, as in most of our results where we have presented $F_2^{Fe}/56$. In order to interpret our results in terms of F_2 for a single nucleon, we must remove the effects of nuclear binding, beginning with Fermi motion. Although the energy scale of Fermi motion seems negligible compared to that of our 200 GeV muons, a proton with a Fermi momentum of 240 MeV/c can change the effective beam energy by over 50 GeV. The treatment of Fermi motion and binding can be broken into three nearly independent phases. The first is the determination of the momentum spectrum of the target nucleons. The second is the treatment of binding energy. The third is the calculation of the effect on the cross section, and thus on the measurement of F_2.

The nucleon momentum spectrum we use is derived from measurements of the nuclear form factor,[81] augmented by a tail inferred from studies of antiproton production below threshold.[82] A zero-temperature, spherically symmetric Fermi gas has a kinetic energy (T) spectrum proportional to $T^{1/2}$ below the Fermi energy T_f. Our spectrum has a form corresponding to a finite temperature plus the tail:

$$\frac{dN}{dT} \sim \begin{cases} T^{1/2}/(1+e^{(T-36)/6.4}), & T < 70 \text{ MeV}; \\ T^{-2.6}, & 70 < T < 385 \text{ MeV}; \\ 0, & T > 385 \text{ MeV}. \end{cases} \tag{B.1}$$

This spectrum as a function of nucleon momentum is shown as the solid curve in Fig. B.1. Also shown in the figure is the spectrum used by Bodek and Ritchie.[83] The interpretation of the tails in these spectra is not entirely clear. Rather than single high energy nucleons, the tail may represent a collective effect in the nucleus, such as the scattering off a higher mass cluster of nucleons.

The treatment of binding is, in effect, the calculation of the energy component of the target nucleon's 4-momentum. The various models thus provide a function $E(p)$ giving the energy for any momentum chosen from the spectrum of the previous paragraph. I will consider two such models here. The first is an independent particle model – each nucleon in the potential well formed by the others.[84] We derive the parameters of this well from the known static properties of nuclei. From the table of nuclides we can define the separation energy S needed to remove

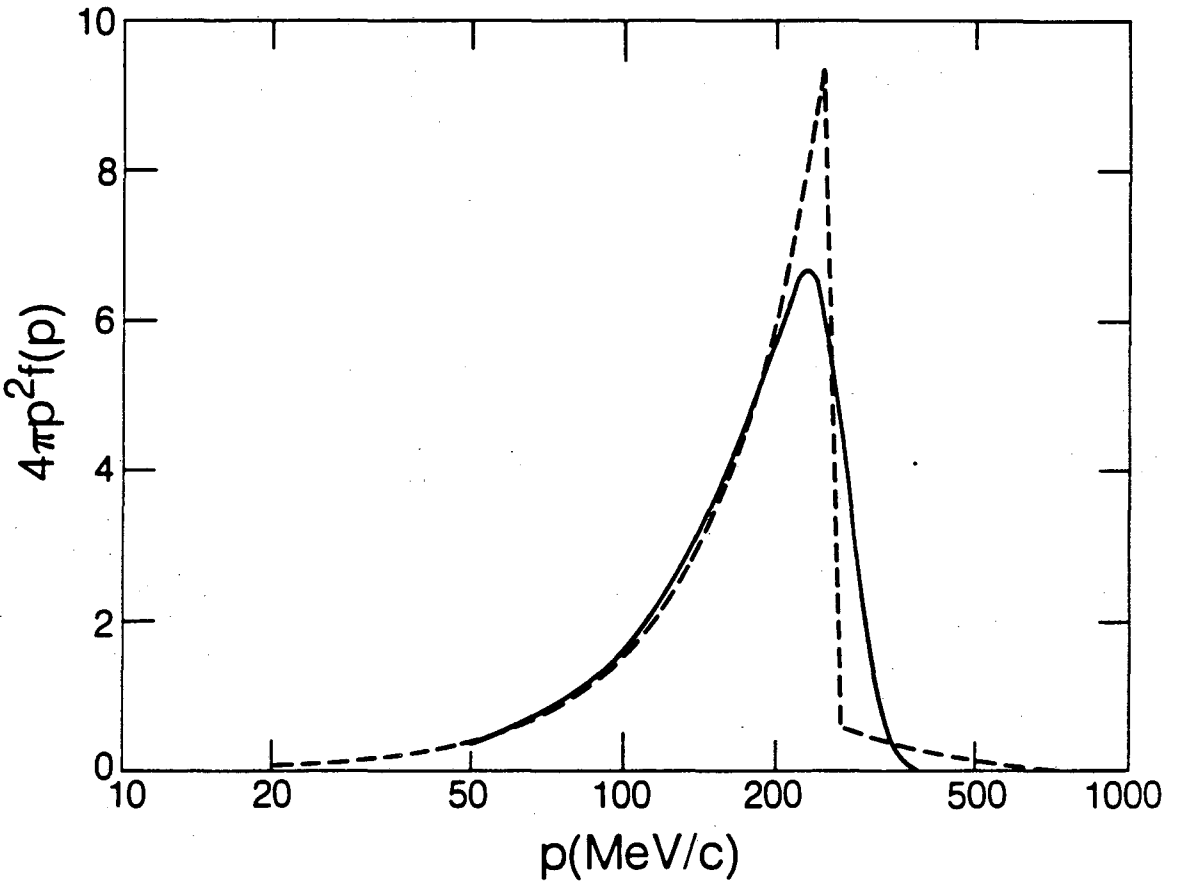

Fig. B.1. Fermi momentum spectrum of nucleons in iron (solid curve). Also shown is the spectrum used in Ref. 83. (dashed curve).

the most weakly bound nucleon (at zero temperature), and the binding energy per nucleon B/A

$$\begin{aligned} S &= M(A,Z) - M(A-1,Z) - M_n = V + T_f, \\ B/A &= (M(A,Z) - ZM_p - (A-Z)M_n)/A = \tfrac{1}{2}\langle V\rangle + \langle T\rangle, \end{aligned} \tag{B.2}$$

where V is the potential and the $\frac{1}{2}$ is necessary to avoid double counting since the potential seen by each nucleon is actually due to all the others. In the limit of "nuclear matter," that is, a collection of nucleons of arbitrary extent, $S = B/A$, and Weisskopf[85] has shown that a consistent picture demands a velocity dependent potential $V(T)$. For a linear $V(T) = V_0 + aT$ we can solve for V_0 and a and thus determine $E(T) = M_N + V_0 + (1+a)T$.

Bodek and Ritchie use an entirely different model which can be described as the spectator or coherent recoil picture. In their model, the target nucleon is required to conserve energy and momentum by recoiling against an on-shell spectator nucleus with mass number $A-1$. Thus the momentum of the spectator nucleus is equal and opposite to that of the target nucleon and $E = M_A - E_{\text{spectator}} = M_A - (p^2 + M_{A-1}{}^2)^{1/2} \approx M_N + S - (M_N/M_{A-1})T$. Note that in this case, the nucleon's energy *decreases* slowly as its momentum increases. The two models are shown in Fig. B.2 for iron ($T_f \approx 36$ MeV, $S \approx -11$ MeV, $B/A \approx -8$ MeV). Each of these models has advantages and disadvantages. The independent particle model arbitrarily invokes the existence of nuclear matter and the linear form of $V(T)$. The spectator model arbitrarily assumes the recoil of a real, on-shell nucleus of mass number $A-1$ (although Bodek and Ritchie modify this for $T > T_f$). I have been unable to choose between them, and have investigated the effects of each.

To apply these Fermi motion models to deep inelastic scattering, we follow the work of West.[86] The starting point is the impulse approximation in which the complicated interactions within the nucleus are considered to affect things only by determining the wave function of the target nucleon, that is, the momentum spectrum and $E(p)$. Hence

$$W^A_{\mu\nu}(P^A, q) = A\int_0^\infty 4\pi p^2 dp f(p) W^N_{\mu\nu}(p,q), \tag{B.3}$$

where $W_{\mu\nu}$ is the hadron tensor introduced in Eq. 2.4 and A and N refer to the nucleus and nucleon. Using Eq. 2.6 and inspecting the 3-3 component of Eq. B.3 we find

$$W^A_2(P^A, q) = A\int_0^\infty 4\pi p^2 dp f(p)\left[\left(1 + \frac{p_3 Q^2}{M_N \nu' q_3}\right)^2\left(\frac{\nu'}{\nu}\right)^2 + \frac{p_\perp^2 Q^2}{M_N^2 q_3^2}\right] W^N_2(p,q), \tag{B.4}$$

where we have chosen the 3-axis along the direction of $\mathbf{q}$, and $\nu' \equiv p\cdot q/M_N, \nu \equiv P^A \cdot q/M_A$. The remaining difficulty is that W_2^N in Eq. B.4 still refers to the structure function of an off-shell nucleon. That this might complicate the situation is evident. Our derivation of $W_{\mu\nu}$ was based on the presence of only two relevant scalars. Now, with $p^2 \neq M_N^2$, W_2^N can be a function not only of Q^2 and ν', but also p^2. Following Bodek and Richie, we identify the off-shell $W_2^N(p,q)$ with the on-shell version at the same Q^2 and invariant mass W^2. Hence

$$\begin{aligned} W_2^{N,\text{off-shell}}(p,q) &= F_2^N(x', Q^2)/\nu, \\ Q^2 &= -q^2, \\ x' &= \frac{Q^2}{2M_N\nu' + p^2 - M_N^2}, \end{aligned} \tag{B.5}$$

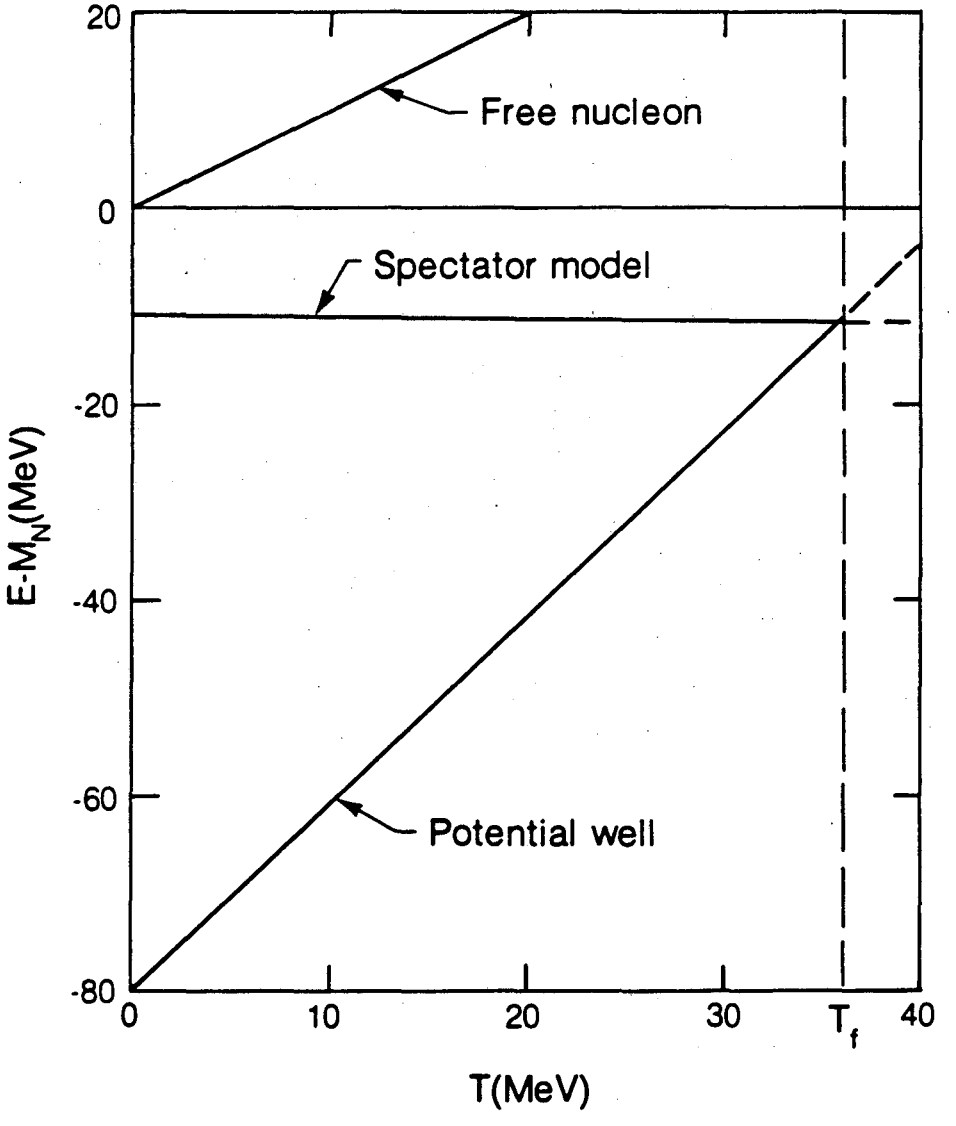

Fig. B.2. The effects of binding. Total energy *vs.* kinetic energy is shown for a free nucleon and for the two nuclear models of iron discussed in the text.

where F_2^N is the standard on-shell structure function.

With $f(p)$, $E(p)$, and an assumed $F_2^N(x,Q^2)$, one can perform the integral in Eq. B.4 numerically and calculate the Fermi motion correction defined as $F_2^N(x,Q^2)/(\frac{1}{56}F_2^{Fe}(x,Q^2))$. The results of such a calculation are shown in Fig. B.3 for the independent particle model and our spectrum. For comparison, the dashed curves are the results of Bodek and Ritchie using the spectator model. Both calculations used the Buras-Gaemers parametrization of F_2^N as input.[51] The two calculations agree fairly well in Q^2 dependence, which is minor below $x = 0.45$. However, the x dependence differs substantially above $x = 0.4$. It should be noted that a calculation which neglects the effects of binding entirely, that is, with $E(p) = \sqrt{(p^2 + M_N^2)}$, yields a correction with a similar shape to those shown, but which is everywhere less than one. Applying these corrections to our measured $F_2^{Fe}(x,Q^2)/56$ before fitting resulted in the changes noted in the text. The independent particle model yielded the smaller correction to Λ, although others have found corrections nearly as small using the model of Bodek and Ritchie.[67]

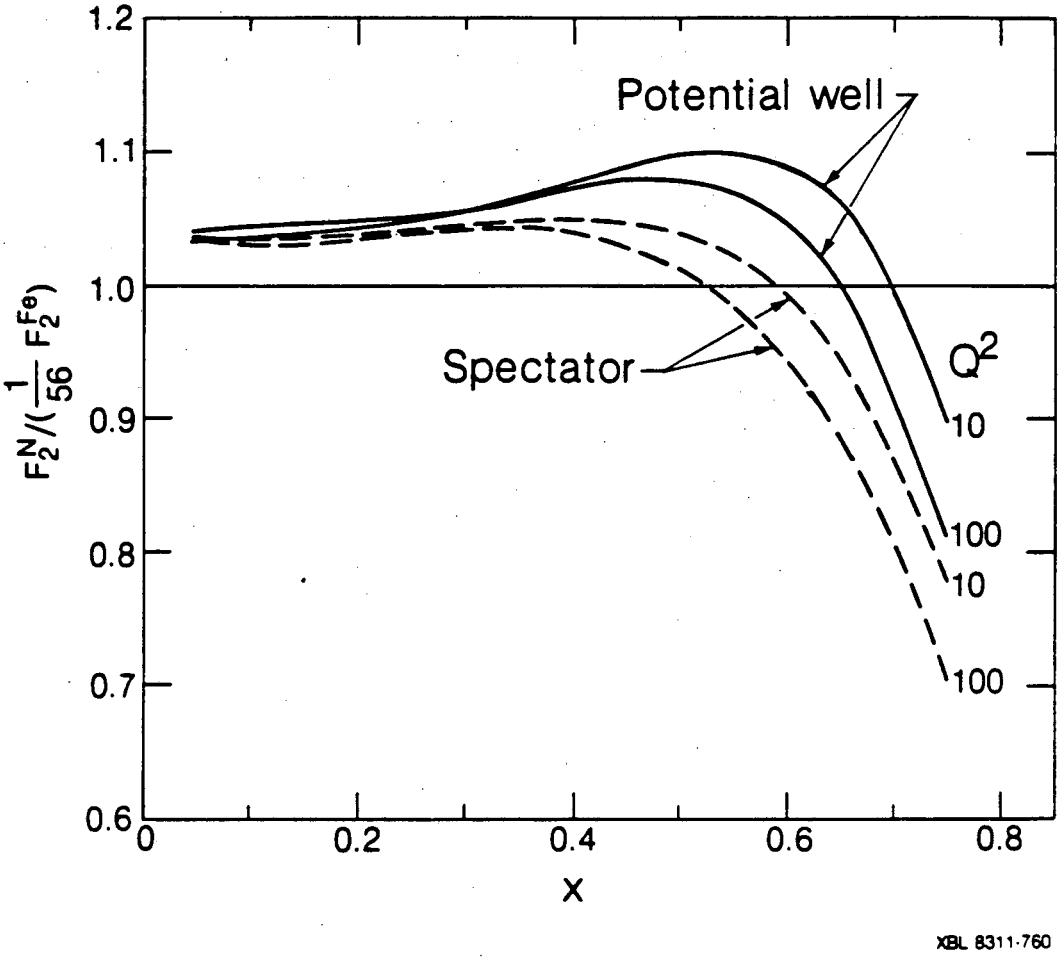

Fig. B.3. The effects of Fermi motion on F_2. The two nuclear models discussed in the text have been used to calculate F_2^{Fe} given F_2^N. The result is shown as a function of x for $Q^2 = 10$ and 100 GeV^2/c^2. The dashed curves are the results of Ref. 83.

References

1. J.J. Thomson, Philos. Mag., Ser. V **48**, 547 (1899).
2. J.J. Thomson, Camb. Lit. Philos. Soc. **15**, 465 (1910).
3. H. Geiger and E. Marsden, Proc. R. Soc. London, Ser. A **82**, 495 (1909).
4. E. Rutherford, Philos. Mag., Ser. VI **21**, 669 (1911).
5. H. Geiger and E. Marsden, Philos. Mag., Ser. VI **25**, 604 (1913).
6. R. Hofstadter, Ann. Rev. Nucl. Sci. **7**, 231 (1957).
7. W.K.H. Panofsky, in *Proceedings of the Heidelberg International Conference on Elementary Particles,* edited by H. Filthuth (North-Holland Publishing Co., Heidelberg, Germany, 1967), p. 371.
8. E.D. Bloom *et al.*, Phys. Rev. Lett. **23**, 930 (1969); M. Breidenbach *et al.*, Phys. Rev. Lett. **23**, 935 (1969).
9. J.D. Bjorken and E.A. Paschos, Phys. Rev. **185**, 1975 (1969).
10. J.D. Bjorken, Phys. Rev. **179**, 1547 (1969).
11. M. Gell-Mann, Phys. Lett. **8**, 214 (1964).
12. G. Zweig, CERN Reports TH-412 (1964) (unpublished).
13. H.D. Politzer, Phys. Rep. **14**, 129 (1974).
14. D.J. Fox *et al.*, Phys. Rev. Lett. **33**, 1504 (1974); C. Chang *et al.*, Phys. Rev. Lett. **35**, 901 (1975).
15. A. Bodek *et al.*, Phys. Rev. **D20**, 1471 (1979).
16. B.A. Gordon *et al.*, Phys. Rev. **D20**, 2645 (1979).
17. J.D. Bjorken and S.D. Drell, *Relativistic Quantum Mechanics,* (McGraw Hill Book Company, New York, 1964).
18. S.D. Drell and J.D. Walecka, Ann. Phys. (N.Y.) **28**, 18 (1964).
19. L.N. Hand, Phys. Rev. **129**, 1834 (1963).
20. C.G. Callen and D.J. Gross, Phys. Rev. Lett. **22**, 156 (1969).
21. F.E. Close, *An Introduction to Quarks and Partons,* (Academic Press, London, 1979), p. 221.

22. M. Gell-Mann and Y. Ne'eman, *The Eightfold Way*, (W.A. Benjamin, Inc., New York, 1964).

23. This heuristic approach is derived from a seminar given by I. Hinchliffe, Lawrence Berkeley Laboratory (1979).

24. Newsweek Magazine **30**, 60 (Sept. 29, 1947). It was from this article that Tomonaga and other Japanese physicists learned of the discovery of the Lamb shift. See Y. Nambu and K. Nishijima, Enrico Fermi Institute Preprint EFI 83/34, June 1983 (unpublished).

25. D.J. Gross and F. Wilczek, Phys. Rev. Lett. **30**, 1343 (1973); H.D. Politzer, Phys. Rev. Lett. **30**, 1346 (1973).

26. M. Bace, Phys. Lett. **78B**, 132 (1978).

27. G. Altarelli and G. Parisi, Nucl. Phys. **B126**, 298 (1977).

28. F.J. Ynduráin, *Quantum Chromodynamics: An Introduction to the Theory of Quarks and Gluons*, (Springer-Verlag, New York, 1983).

29. H. Abramowicz *et al.*, Z. Phys. **C12**, 289 (1982).

30. T. Markiewicz, University of California Ph.D. Thesis, (Berkeley, 1981).

31. S.L. Glashow, Nucl. Phys. **22**, 579 (1961); A. Salam and J.C. Ward, Phys. Lett. **13**, 168 (1964); S. Weinberg, Phys. Rev. Lett. **19**, 1264 (1967).

32. P. Langacker, Phys. Rep. **72**, 185 (1981).

33. H. Georgi and S.L. Glashow, Phys. Rev. Lett. **32**, 438 (1974).

34. A.D. Sakharov, JETP Lett. **5**, 24 (1967).

35. A.H. Guth, Center for Theoretical Physics (M.I.T.) Preprint CTP-1050 (Jan. 1983), to be published in the Proceedings of the XI Texas Symposium on Relativistic Astrophysics (Austin, Texas, 1982).

36. M. Goldhaber, P. Langacker, and R. Slansky, Science **210**, 851 (1980).

37. R.M. Bionta *et al.*, Phys. Rev. Lett. **51**, 27 (1983).

38. G.D. Gollin *et al.*, Phys. Rev. **D24**, 559 (1981).

39. O.C. Allkofer *et al.*, Nucl. Instrum. Methods **179**, 445 (1981).

40. D. Nelson, Lawrence Berkeley Laboratory Engineering Note MT-260, May 24, 1977 (unpublished).

41. D. Evans, Kerth Group Internal Note GIN-65, Lawrence Berkeley Laboratory, June 15, 1978 (unpublished).

42. F. Ratliff. Sci. Am. **226**, 90 (June,1972).

43. E. Mach, Sitzber. Akad. Wiss. Wien Math. Naturw. Kl.II **52**, 303 (1865).

44. G. Gollin *et al.*, IEEE Trans. Nuc. Sci. **NS-26**, 59 (1979).

45. B. Barish *et al.*, in *Proceedings of the Calorimeter Workshop*, edited by M. Atac, (Fermilab, May 1975), p. 229.

46. A.R. Clark *et al.*, Phys. Rev. Lett. **43**, 187 (1979).

47. A.R. Clark *et al.*, Phys. Rev. Lett. **45**, 682 (1980).

48. A.R. Clark *et al.*, Phys. Rev. Lett. **45**, 686 (1980).

49. A.R. Clark *et al.*, Phys. Rev. Lett. **45**, 1465 (1980).

50. M. Strovink, Kerth Group Internal Note GIN-100, Lawrence Berkeley Laboratory, December 18, 1978 (unpublished).

51. A.J. Buras and K.J.F. Gaemers, Nucl. Phys. **B132**, 249 (1978).

52. L.W. Mo and Y.S. Tsai, Rev. Mod. Phys. **41**, 205 (1969).

53. R.H. Siemann *et al.*, Phys. Rev. Lett. **22**, 421 (1969).

54. F.C. Shoemaker, Kerth Group Internal Notes GIN-153, April 7, 1980 and GIN-155, April 9, 1980 (unpublished).

55. G. Moliére, Z. Naturforsch. **3a**, 78 (1948); H.A. Bethe, Phys. Rev. **89**, 1256 (1953).

56. B.R. Frieden, "Image Enhancement and Restoration" in *Picture Processing and Digital Filtering*, Topics in Applied Physics, v.6, edited by T.S. Huang, (Springer-Verlag, New York, 1975), p. 177.

57. L.F. Abbott, W.B. Atwood, and R.M. Barnett, Phys. Rev. **D22**, 582 (1980).

58. F. James and M. Roos, Computer Phys. Comm. **10**, 343 (1975).

59. D.J. Gross and C.H. Llewellyn Smith,Nucl. Phys. **B14**, 337 (1969).

60. R.M. Barnett, Phys. Rev. Lett. **48**, 1657 (1982).

61. J.J. Aubert *et al.*, Phys. Lett. **123B**, 275 (1983).

62. A. Bodek *et al.*, Phys. Rev. Lett. **51**, 534 (1983).

63. R.M. Barnett and D. Schlatter, Phys. Lett. **112B**, 475 (1982).

64. A. Devoto *et al.*, Phys. Rev. **D27**, 508 (1983).

65. J.J. Aubert *et al.*, Phys. Lett. **114B**, 291 (1982).

66. H. Georgi and H.D. Politzer, Phys. Rev. **D14**, 1829 (1976).

67. J.J. Aubert *et al.*, Phys. Lett. **105B**, 322 (1981).

68. H. Abramowicz *et al.*, Z. Phys. **C17**, 283 (1983).

69. H.E. Fisk and F. Sciulli, Ann. Rev. Nucl. Part. Sci. **32**, 499 (1982).

70. S. Wu, in *Proceedings of the 1982 SLAC Summer Institute on Particle Physics*, (SLAC, Stanford, CA, 1982), and references therein.

71. P.B. Mackenzie and G.P. Lepage, Phys. Rev. Lett. **47**, 1244 (1981).

72. F.J. Gilman, Phys. Rev. **167**, 1365 (1968).

73. J.J. Aubert *et al.*, Phys. Lett. **121B**, 87 (1983).

74. M.D. Mestayer *et al.*, Phys. Rev. **D27**, 285 (1983).

75. E. Derman, Phys. Rev. **D7**, 2755 (1973).

76. E. Commins and P. Bucksbaum, *Weak Interactions of Leptons and Quarks*, (Cambridge University Press, Cambridge, 1983), pp. 343-52.

77. C.Y. Prescott *et al.*, Phys. Lett. **77B**, 347 (1978); **84B**, 524 (1979).

78. A. Argento *et al.*, Phys. Lett. **120B**, 245 (1983).

79. S.M. Berman and J.R. Primack, Phys. Rev. **D9**, 2171 (1974); **D10**, 3895(E) (1974).

80. M. Strovink, internal memorandum, July 22, 1974 (unpublished).

81. B. Hahn, D.G. Ravenhall, and R. Hofstadter, Phys. Rev. **101**, 1131 (1956).

82. D.E. Dorfan *et al.*, Phys. Rev. Lett. **14**, 995 (1965).

83. A. Bodek and J.L. Ritchie, Phys. Rev. **D23**, 1070 (1981); **D24**, 1400 (1981).

84. A. Bohr and B.R. Mottelson, *Nuclear Structure*, v.I, (W.A. Benjamin, Inc., New York, 1969), p. 146.

85. V.F. Weisskopf, Nucl. Phys. **3**, 423 (1957).

86. G.B. West, Ann. Phys. (N.Y.) **74**, 464 (1972).

This report was done with support from the Department of Energy. Any conclusions or opinions expressed in this report represent solely those of the author(s) and not necessarily those of The Regents of the University of California, the Lawrence Berkeley Laboratory or the Department of Energy.

Reference to a company or product name does not imply approval or recommendation of the product by the University of California or the U.S. Department of Energy to the exclusion of others that may be suitable.

TECHNICAL INFORMATION DEPARTMENT
LAWRENCE BERKELEY LABORATORY
UNIVERSITY OF CALIFORNIA
BERKELEY, CALIFORNIA 94720